UNIVERSITAT DE BARCELONA

Estudio teórico del transporte de ligandos en proteínas y de la afinidad ligando-receptor

Axel Bidon-Chanal Badia

Universitat de Barcelona

Facultat de Farmàcia

Departament de Fisicoquímica

Estudio teórico del transporte de ligandos en proteínas y de la afinidad ligando-receptor

Axel Bidon-Chanal Badia

Diciembre 2007

Programa de doctorat de Química Teòrica i Computacional, bienni 2003-2005
Departament de Química-Física, Facultat de Química, Universitat de Barcelona

Directores: Dr. F. Javier Luque Garriga y Dr. Modesto Orozco López

Departament de Fisicoquímica
Facultat de Farmàcia
Universitat de Barcelona

Estudio teórico del transporte de ligandos en proteínas y de la afinidad ligando-receptor

Esta tesis ha sido realizada por el licenciado Axel Bidon-Chanal Badia bajo la dirección del Dr. Francisco Javier Luque Garriga , catedrático del Departament de Fisicoquímica de la Facultat de Farmàcia de la Universitat de Barcelona, y del Dr. Modesto Orozco López, catedrático del Departament de Bioquímica i Biologia Molecular de la Facultat de Ciències Química i Física de la Universitat de Barcelona, para optar al título de doctor por la Universitat de Barcelona en el Programa de Doctorado en Química Teórica y Computacional.

Dr. F. Javier Luque Garriga

Dr. Modesto Orozco López

Índice

A todas aquellas personas que en algún momento durante estos últimos 5 años me han ayudado en modo alguno en la realización de esta tesis, quisiera darles las gracias. A mis padres, Carles y Teresa, mis hermanos, Kevin y Aidan, y a mi tío Santi, quien siempre me persigue para que le deje leer mis trabajos. A los que me ayudaron enormemente cuando empecé, Curu y Jordi, con los que disfruté en el trabajo y en los ratos libres jugando al curucasc. A mis compañeros de laboratorio, Ignacio, Óscar y Damián. A Ramón, con el que siempre se puede hablar, y a Xavi, que me ha ayudado estos últimos dos años preguntándome cosas que no sabía y que gracias a eso he acabado aprendiendo. A toda la gente de MMB, y en especial a Albert, con quien pude compartir parte de la carrera y los años de doctorado y que espero no cambie nunca, así como también a Manu y a Carles. A Yolanda, Montse y Assumpta, por aguantarme en el despacho que compartimos. A los de QBCE, que me acogieron durante mi estancia en Almirall, y a los del otro lado del Atlántico, que me acogieron en mi estancia en Buenos Aires, fue un placer poder trabajar con Darío, Marcelo, Lula y todos los del laboratorio. A mis amigos y a todos los que estuvieron a mi lado en algún momento.

Por otro lado, agradecer también el apoyo de las Dras. Ana Castro y Ana Martínez de Neuropharma S. A., y de los Drs. Pelayo Camps y Diego Muñoz-Torrero, del Departament de Química Farmacéutica.

Finalmente, quisiera agradecer de forma especial la oportunidad que me brindó el Dr. F. Javier Luque para poder realizar la tesis y la codirección de la misma por el Dr. Modesto Orozco. Trabajar con ellos significa aprender día a día y disfrutar. Muchas gracias.

Esta tesis ha sido realizada gracias a una beca predoctoral de la Universitat de Barcelona.

Barcelona, Diciembre de 2007.

Introducción

Introducción

1.1 Afinidad ligando-receptor

El reconocimiento molecular es clave para la comprensión de la mayoría de procesos biológicos. Hace más de 100 años Emil Fischer plasmó este hecho aseverando que "una enzima y un glucósido deben encajar como una llave en una cerradura para poder iniciar una reacción química entre ellos"[1]. En la actualidad sabemos que la formación de un complejo entre una proteína y una molécula pequeña subyace en la base molecular de procesos bioquímicos como la catálisis enzimática, el control alostérico, la señalización celular, o el transporte y almacenamiento de ligandos[2,3]. Diseñar moléculas que optimicen la interacción con macromoléculas diana constituye la estrategia más importante de cara al descubrimiento de nuevos medicamentos[4], pues la fijación selectiva a un único receptor asegura una respuesta farmacológica única y ayuda a disminuir efectos colaterales no deseados. Por ello, la identificación de los determinantes moleculares responsables de la interacción entre ligando y receptor es fundamental no solo para entender y modular la afinidad de dicha unión, sino también para establecer la selectividad y especificad de dicho reconocimiento[5].

La afinidad entre ligando y receptor depende de diversos factores de naturaleza entálpica y entrópica[6]. Por un lado, viene determinada por la naturaleza de las interacciones que se establecen entre ligando y receptor. Dichas interacciones suelen ser de tipo no covalente, aunque en determinados casos puede estar mediada por la formación de enlaces covalentes. La afinidad también depende del coste de desolvatación tanto del ligando como del receptor, así como del cambio energético asociado a modificaciones conformacionales inducidas en el ligando y el receptor a consecuencia de la unión entre ambos. Ambos términos tienen una naturaleza entálpica y contribuyen disminuyendo la intensidad de la unión. Por otra parte, el reconocimiento entre ligando y receptor implica una disminución en su flexibilidad conformacional, lo cual afecta negativamente a la afinidad al representar una disminución entrópica. Finalmente, la afinidad se ve incrementada por el aumento de desorden en las moléculas de agua que rodean al ligando y al centro de unión del receptor antes de la interacción. En conjunto, pues, la afinidad entre ligando y receptor refleja un delicado balance entre

dichos componentes y ser capaz de modularla requiere un profundo conocimiento sobre la fisicoquímica de la interacción.

En principio, cuanto mayor sea la complementariedad existente entre ligando y receptor, tanto mayor será la afinidad. Ello, pues, implica que debe existir una estrecha correspondencia entre la distribución tridimensional de los grupos químicos presentes en el ligando y el receptor, ya que ello redundará en un incremento del número de interacciones estabilizantes tanto electrostáticas como de van der Waals.

Entre las contribuciones de tipo electrostático, la formación de puentes de hidrógeno desempeña un papel crucial en el reconocimiento, debido especialmente a su direccionalidad, aunque no existe un consenso sobre su contribución energética[7-10]. La formación de un puente de hidrógeno es el resultado de la atracción electrostática entre un átomo de hidrógeno y un átomo electronegativo como por ejemplo un nitrógeno o un oxígeno. La fortaleza de la interacción depende de la distancia entre ambos (típicamente entre 2.5 y 3.2 Å entre los átomos pesados) y del ángulo formado por los tres (X-H···Y, habitualmente entre 130º y 180º). A distancias más cortas el puente de hidrógeno puede tomar un carácter más covalente que aumenta la energía de interacción.[11-13] Además, la fortaleza de un puente de hidrógeno dependerá del entorno en el que se encuentre, siendo más fuertes en las zonas internas de la proteína donde la constante dieléctrica es más pequeña que en las zonas expuestas a un solvente polar.[14,15] Los puentes salinos y las interacciones π-catión son igualmente importantes e incluso pueden llegar a ser determinantes para la formación del complejo.[16] La naturaleza ácida o básica de algunos aminoácidos como la arginina, la lisina, la histidina, el glutámico o el aspártico, hace que éstos puedan adoptar diferentes estados de protonación que les confieren carga positiva o negativa. De esta manera, un ligando con carga opuesta podrá interaccionar formando lo que se conoce como un puente salino con un residuo cargado de la proteína.[17] Las interacciones π-catión se producen entre las cadenas laterales aromáticas de los residuos de la proteína y/o anillos aromáticos del ligando y se han descrito como claves en la unión de algunos ligandos, caso por ejemplo de (-)-huperzina A al enzima acetilcolinesterasa (AChE, estructura 1VOT); véase Figura 1.

Finalmente, las interacciones de tipo *van der Waals* tienen protagonismo a distancias cortas dado que su intensidad decrece con la distancia a razón de $1/r^6$.[19] Este

tipo de interacciones se rigen por dos componentes diferentes, una de carácter atractivo y otra repulsivo. Desde un punto de vista clásico la contribución atractiva proviene de las fuerzas dispersivas debidas a la formación de dipolos instantáneos fruto de las fluctuaciones de las distribuciones electrónicas en las moléculas interaccionantes. La contribución repulsiva aparece a distancias muy cortas por debajo de los 3 Å de separación entre átomos cuando se produce el solapamiento de las partes internas de los átomos. Un ejemplo clásico de interacción de van der Waals especialmente intensa es el apilamiento de anillos aromáticos en interacciones π-π, que es una de las contribuciones dominantes en la unión de E2020 al enzima acetilcolinesterasa (código PDB: 1EVE[20]; véase Figura 1).

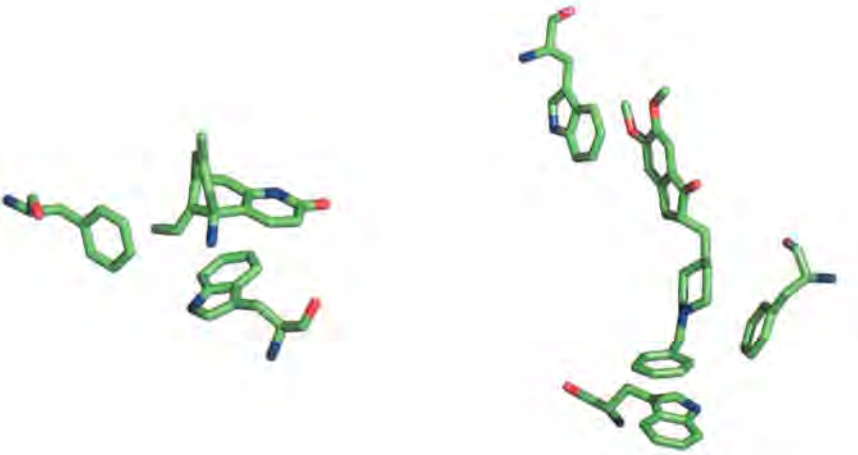

Figura 1. Representación del modo de unión de (-)-huperzina A (izquierda) y E2020 (derecha) al centro catalítico del enzima acetilcolinesterasa.

1.2 El Protein Data Bank

El estudio de las interacciones entre ligando y receptor requiere un conocimiento detallado de la estructura tridimensional del complejo. En este sentido, es obligado reconocer el impacto que han tenido iniciativas como el Protein Data Bank (PDB),[21] que recoge actualmente la información estructural de 47509 estructuras, incluyendo proteínas, ácidos nucleicos y complejos con ligandos o macromoléculas (véase Tabla 1). En los últimos años se ha asistido a un crecimiento gradual del número de estructuras de proteínas depositadas en el PDB (ver figura 1) gracias al desarrollo de técnicas de

cristalografía de rayos X[22,23], espectroscopia RMN[24-26] y microscopía crioelectrónica.[27-30] La estructura 3D proporciona información detallada de las interacciones, pero se deben tener en cuenta factores como la resolución con la que se ha obtenido la estructura o la aparición de contactos intermoleculares a consecuencia del empaquetamiento cristalino para matizar su capacidad real de reproducir la verdadera estructura de la proteína en condiciones fisiológicas.

	Molecule Type				
	Proteins	**Nucleic Acids**	**Protein/NA Complexes**	**Other**	**Total**
Exp. Method **X-ray**	37557	1005	1745	25	40332
Exp. Method **NMR**	5984	797	136	7	6924
Exp. Method **Electron Microscopy**	109	11	40	0	160
Exp. Method **Other**	83	4	4	2	93
Exp. Method **Total**	43733	1817	1925	34	47509

Tabla 1. Información del contenido actual de la naturaleza de las estructuras depositadas en el Protein Data Bank.

La resolución atómica se consigue por debajo de 1.2 Å, pero resoluciones por debajo de 1.5 Å se obtienen en muy pocas ocasiones. Normalmente se obtienen resoluciones entre 2 y 3 Å, que se traduce en una desviación estándar de 0.4 a 2.5 Å de resolución en las coordenadas asignadas a cada átomo.[31-33] Además, por difracción de rayos X es difícil distinguir entre isótopos o entre elementos de similar número atómico debido a que éstos presentan un poder de difracción muy parecido y tampoco es común poder detectar la posición de los hidrógenos. Ello hace necesario llevar a cabo un análisis detallado de las interacciones presentes en la proteica, especialmente en las zonas funcionalmente relevantes. Así, por ejemplo, el anillo de imidazol de una histidina puede adoptar dos conformaciones virtualmente indistinguibles, así como dos posibles estados tautoméricos en su forma neutra o bien un estado correspondiente a la protonación del anillo. Como consecuencia, la asignación de un estado iónico, tautomérico y conformacional debe llevarse a cabo en base a un análisis del entorno en el que se encuentra.

1.3 Difusión de ligandos

La formación de un complejo entre una molécula pequeña y una proteína depende también de la facilidad de difusión del ligando desde el medio hasta el centro de reconocimiento. Generalmente el concepto de difusión se asocia a la facilidad de paso del ligando a través de diversos medios biológicos, caso de la absorción intestinal, el paso de la barrera sangre-cerebro o incluso el acceso al medio intracelular a través de la membrana celular. No obstante, dicho concepto debe generalizarse con objeto de incluir aquellos procesos que suponen la difusión del ligando a través de la matriz proteica del receptor con el fin de alcanzar el centro activo. Con frecuencia éste se encuentra en una zona interna de la estructura de la enzima, a la cual se accede a través de uno o más canales que lo conectan con la superficie. La naturaleza de estos canales modula la difusión del ligando hacia el centro de reconocimiento y regula la actividad de la proteína. A su vez, los canales pueden estar controlados por cambios conformacionales de ciertos aminoácidos[34] o incluso por grupos de residuos que forman bucles (*loops*) con una alta movilidad[35].

La formación del complejo ligando-receptor se puede entender como un proceso de equilibrio dinámico que implica 3 especies: el ligando libre, la proteína libre, y el complejo formado por los dos. Este equilibrio que se puede expresar como:

$$[E] + [L] \underset{k_{off}}{\overset{k_{on}}{\rightleftharpoons}} [EL]$$

e implica dos constantes cinéticas, k_{on} y k_{off} que están relacionadas con los procesos de entrada y salida de ligandos. En particular, la constante k_{off} es inversamente proporcional al tiempo de vida medio del complejo ligando-receptor ([EL]), mientras que k_{on} es bimolecular y es una medida de la probabilidad de que acontezca un encuentro entre el ligando y el receptor que dé lugar a la formación del complejo. El siguiente paso (en el caso de una enzima) sería la reacción química entre ligando y receptor para dar lugar al complejo producto-receptor y la posterior disociación.

$$[E] + [L] \underset{k_{off}}{\overset{k_{on}}{\rightleftharpoons}} [EL] \xrightarrow{k_r} [P]$$

La difusión puede ser la etapa limitante de la reacción en aquellos casos en los que la reacción química ocurre de forma mucho más rápida que la disociación de los reactivos al formarse el complejo, es decir, cuando $k_r >> k_{off}$. En esta clase de proteínas la eficiencia catalítica suele ser muy alta para permitir que toda molécula de sustrato que llegue al centro activo sea transformada en productos.[36] Por ello, conocer el mecanismo por el que la proteína controla la difusión del ligando puede ser de suma importancia en el diseño de potenciales inhibidores.

1.4 Simulación por Dinámica molecular

Además de la información concerniente a las interacciones que se establecen entre el ligando y el receptor, la estructura proteica derivada de datos de difracción de rayos X puede permitir identificar los canales de migración de ligandos por la presencia de cavidades que conectan el centro activo con la superficie de la proteína.[37] No obstante, es mucho más difícil dilucidar la información dinámica sobre la formación tanto de las interacciones como de los canales ya que la geometría cristal corresponde a una conformación representativa resultado de un promedio espacial y temporal. Para poder estudiar los cambios estructurales inducidos en la unión del ligando al receptor o aquéllos que regulan la difusión de ligandos es necesario disponer de una técnica que permita seguir la evolución temporal del sistema.

En los últimos años se ha incrementado de forma notable el uso de la resonancia magnética nuclear (RMN) para la elucidación de estructuras tridimensionales de macromoléculas, así como en el estudio de las interacciones ligando-proteína.[38-40] Las técnicas derivadas de la aplicación de RMN permiten obtener restricciones espaciales de estructuras en solución, que pueden aplicarse al refinado de estructuras cristalográficas. Así, aprovechando el efecto NOE (Nuclear Overhauser Effect) se pueden obtener datos estructurales en forma de restricciones para las distancias entre pares de átomos que permiten resolver en casos favorables la estructura de la proteína. Más recientemente, se ha utilizado el acoplamiento residual dipolar (RCD)[41] para enriquecer el número de restricciones empleadas para resolver la estructura. La espectroscopia de NMR permite también obtener información dinámica de movimientos a gran escala (del orden del

microsegundo hasta el milisegundo) aplicándose por ejemplo al estudio del plegamiento de proteínas. Aún así, las técnicas de NMR presentan una limitación notable en el tamaño del sistema a estudiar y no siempre proporcionan información de alta calidad sobre interacciones específicas ligando-receptor.

La dinámica molecular es una técnica teórica, complementaria a las experimentales, que permite obtener información a nivel atómico de la evolución temporal de sistemas macromoleculares como proteínas, así como de la cinética y la termodinámica de procesos asociados[42]. Proporciona además información detallada del movimiento de cada partícula del sistema y de las posibles interacciones que se establecen entre ellas. Con el análisis de la dinámica de los complejos proteína-ligando se obtiene información detallada de los cambios conformacionales producidos tanto en el ligando como en la proteína, pudiéndose localizar nuevos puntos de interacción o predecir modificaciones del ligando que potencien su afinidad. Además, proporciona información sobre los mecanismos moleculares de difusión de ligandos, permitiendo incluso localizar nuevos canales que no están presentes en la estructura cristalográfica. Su aplicación ha sido de gran ayuda tanto en el diseño racional de medicamentos[42-44] como en la comprensión de los mecanismos de difusión de ligandos[45,46] y se ha convertido en una herramienta habitual en el estudio de sistemas biológicos[47].

Referencias bibliográficas

1 E. Fischer, *Ber. Dtsch. Chem. Ges.*, **1894**, 27, 2985-2993.

2 Stryer, L., Berg, J. M., Tymoczko, J. L., *Biochemistry*, **2002**, W.H.Freeman & Co Ltd.

3 Voet, D., Voet, J. G., *Biochemistry*, **2004**, John Wiley & Sons.

4 Andrew R. Leach, *Molecular Modelling Principles and Applications*, **1996**, Addison Wesley Longman Limited.

5 Gohlke, H., Klebe, G., *Angew. Chem. Int. Ed.*, **2002**, 41, 2644-2676.

6 Hunter, C. A., *Angew. Chem. Int. Ed.*, **2004**, 43, 5310-5324.

7 Murphy, K. P., Gill, S. J., *J. Mol. Biol.*, **1991**, 222, 699-706.

8 Yang, A., Sharp, K. A., Honig, B., *J. Mol. Biol.*, **1992**, 227, 889-900.

9 Fersht, A. R., *Trends Biochem. Sci.*, **1987**, 12, 301-304.

10 Zou, Q., Habermann-Rottinghaus, S. M., Murphy, K. P., *Proteins*, **1998**, 31, 107-115.

11 Wang, Z., Luecke, H., Nanhua, Y., Quiocho, F., *Nat. Struct. Biol.*, **1997**, 4, 519-522.

12 Warshel, A., Papazyan, A., Kollman, P. A., *Science*, **1995**, 269, 102-104.

13 Steiner, T., Saenger, W., *Acta Crystallogr. Sect. B*, **1994**, 50, 348-357.

14 Stahl, M., Böhm, H.-J., *J. Mol. Graphics Model.*, **1998**, 16, 121-132.

15 Beeson, C., Pham, N., Shipps, G., Dix, T. A., *J. Am. Chem. Soc.*, **1993**, 115, 6803-6812.

16 Meyer, E. A., Castellano, R. K., Diederich, F., *Angew. Chem. Int. Ed.*, **2003**, 42, 1210-1250.

17 Barril, X., Alemán, C., Orozco, M., Luque, F. J., *Proteins*, **1998**, 32, 67-79.

18 Raves, M. L., Harel, M., Pang, Y. P., Silman, I., Kozikowski, A. P., Sussman, J. L., *Nat. Struct. Biol.*, **1997**, 4, 57-63.

19 Burley, S. K., Petsko, G. A., *Adv. Protein Chem.*, **1988**, 39, 125-189.

20 Kryger, G., Silman, I., Sussman, J. L., *Structure*, **1999**, 7, 297-307.

21 Berman H. M., Westbrook J., Feng Z., Gilliland G., Bhat T. N., Weissig H., Shindyalov I. N., Bourne P. E., *Nuc. Acids Res.*, **2000**, 28, 235-242

22 Glusker, J. P., Lewis, M., Rossi, M., *Crystal Structure analysis for Chemists and Biologists*, **1994**, VCH, Weinheim.

23 Drenth, J., *Principles of Protein X-ray Crystallography*, **1999**, Springer, New York.

24 Wüthrich, K., *NMR of Proteins and Nucleic Acids*, **1986**, Wiley, New York.

25 Siegal, G., van Duynhoven, J., Baldus, M., *Curr. Opin. Chem. Biol.*, **1999**, 3, 530-536.

26 Clore, M. G., Gronenborn, A. M., *Science*, **1991**, 252, 1390-1399.

27 Kühlbrandt, W., Williams, K. A., *Curr. Opin. Chem. Biol.*, **1999**, 3, 537-543.

28 Stowell, M. H., Miyazawa, A., Unwin, N., *Curr. Opin. Struct. Biol.*, **1998**, 8, 595-600.

29 Chiu, W., McGough, A., Sherman, M. B., Schmid, M. F., *Trends Cell Biol.*, **1999**, 9, 154-159.

30 Baumeister, W., Alasdair, C. S., *Trends Biochem. Sci.*, **2000**, 25, 624-631.

31 Kossiakoff, A. A., Randal, M., Guenot, J., Eigenbrot, C., *Proteins*, **1992**, 14, 65-74.

32 Wlodawer, A., Nachman, J., Gilliland, G. L., Gallagher, W., Woodward, C. G., *J. Mol. Biol.*, **1987**, 198, 469-480.

33 Dauber-Osguthorpe P., Roberts, V. A., Osguthorpe, D. J., Wolff, J., Genest, M., Hagler, A. T., *Proteins*, **1988**, 4, 31-47.

34 Hornak, V., Okur, A., Rizzo, R. C., Simmerling, C., *Proc. Natl. Acad. Sci. USA*, **2006**, 103, 915-920.

35 Trylska, J., Tozzini, V., Chia-en A. Chang, McCammon, J. A., *Biophys. J.*, **2007**, 92, 4179-4187.

36 Stroppolo, M. E., Falconi, M., Caccuri, A. M., Desideri, A., *Cell. Mol. Life Sci.*, **2001**, 58, 1451-1460.

37 Milani, M., Pesce, A., Ouellet, Y., Ascenzi, P., Guertin, M., Bolognesi, M., *EMBO J.*, **2001**, 20, 3902–3909.

38 Lepre, C. A., Moore, J. M., Peng, J. W., *Chem. Rev.*, **2004**, 104, 3641−3675.

39 Lipsitz, R. S., Tjandra, N., *Annu. Rev. Biophys. Biomol. Struct.*, **2004**, 387-413.

40 Carlomagno, T., *Annu. Rev. Biophys. Biomol. Struct.*, **2005**, 245–266.

41 Adcock, S. A., McCammon, J. A., *Chem. Rev.*, **2006**, 106, 1589−1615.

42 Doughty, S., Phillips, R., *Mol. Simul.*, **2000**, 24, 209.

43 Wlodawer, A., Vondrasek, J., *Ann. Rev. Biophys. Biomol. Struct.*, **1998**, 27, 249–84.

44 Carlson, H., Masukawa, K., Rubins, K., Bushman, F., Jorgensen, W., Lins, R., Briggs, J., McCammon, J. A., *J. Med. Chem.*, **2000**, 43 2100–14.

45 Amara, P., Andreoletti, P., Jouve, H. M., Field, M. J., *Prot. Sci.*, **2001**, 10, 1927-1935.

46 Brunori, M., Cutruzzolà, F., Savino, C., Travaglini-Allocatelli, C., Vallone, B., Gibson, Q., H., *Biophys. J.*, **1999**, 76, 1259–1269.

47 Moraitakis, G., Purkiss, A. G., Goodfellow, J. M., *Rep. Prog. Phys.*, **2003**, 66, 383-406.

Objetivos

Objetivos

La eficacia de un ligando en su interacción con una macromolécula biológica depende no sólo de su capacidad para interaccionar de forma complementaria y específica con la constelación de grupos químicos presentes en el centro de unión, sino también de su difusión a través de la matriz proteica para alcanzar dicho centro. Aunque difusión y unión reflejan el balance de fuerzas intermoleculares establecido entre ligando y receptor, los determinantes moleculares que subyacen pueden ser diferentes, lo que plantea un reto en su descripción mediante modelización.

Con el objetivo general de identificar los determinantes moleculares asociados a difusión y unión de ligandos en dos sistemas de relevancia biológica planteamos el análisis de dos sistemas. Por un lado, la acetilcolinesterasa, donde nos interesó la identificación de los factores que determinan la afinidad entre ligando y receptor. Por otro lado la hemoglobina truncada N de *M. tuberculosis* , donde nos interesó estudiar el mecanismo molecular asociado a la difusión de ligandos a través de la matriz proteica.

En cuanto al enzima acetilcolinesterasa, los objetivos específicos del presente trabajo consisten en la identificación de los determinantes moleculares que modulan la afinidad de tres tipos de inhibidores duales:

A.1) derivados tacrina-ftalimida,
A.2) derivados tacrina-indol, y
A.3) derivados tacrina-donepezilo.

Todos ellos tiene como motivo común el anillo de tacrina (o cloro-tacrina), cuya presencia debería permitir la unión al centro catalítico del enzima, mientras que las estructuras consideradas difieren en la unidad química destinada a interaccionar con el centro periférico.

Con respecto a la hemoglobina truncada N de *M. tuberculosis*, los objetivos específicos que se han planteado en este trabajo son:

B.1) identificar el mecanismo molecular de migración de ligandos diatómicos (O_2 y NO) hacia el centro activo, prestando especial atención a las características estructurales de las dos ramas del túnel observado en la matriz proteica, y su implicación funcional en la migración de ligandos, y

B.2) establecer el mecanismo de liberación del anión nitrato, cuya salida a través del túnel observado en la estructura de rayos X no puede explicarse de forma convincente teniendo presente tanto su carga neta como su tamaño, por lo cual cabe especular con la posibilidad de que exista una ruta de eliminación alternativa no observada en la estructura cristalográfica.

Métodos

El elevado número de átomos que contienen los sistemas de interés bioquímico y farmacológico hace inabordable en la actualidad el tratamiento mecanocuántico de los mismos. Por ello, su estudio debe abordarse recurriendo a la mecánica molecular, que supone que las moléculas pueden describirse como un conjunto de masas centradas en los núcleos atómicos unidos mediante muelles. El conjunto de fuerzas a las que se encuentra dichas partículas sigue un tratamiento clásico, con ello la mecánica molecular permite examinar de forma eficiente el espacio configuracional de sistemas con un gran número de átomos, siempre que las propiedades de interés no supongan una redistribución importante en la densidad electrónica de las moléculas, como son los procesos asociados a formación y rotura de enlaces.[1]

Para poder aplicar la mecánica molecular deben asumirse dos principios fundamentales[2]: (1) la descripción de las distintas contribuciones energéticas mediante potenciales efectivos y la *aditividad* de los mismos, y (2) la *transferabilidad* de dichos potenciales.

En base al primer principio, se asume que la energía molecular puede expresarse como una suma de potenciales que representan fuerzas físicas simples. Las contribuciones energéticas se clasifican como *enlazantes*, cuando describen las tensiones de tipo mecánico originadas a consecuencia de desviaciones respecto al valor de equilibrio de las longitudes y ángulos de enlace, así como las torsiones de los diedros, y los términos *no enlazantes*, que generalmente se limitan a las interacciones electrostática y de van der Waals.[1,2] Por consiguiente, la energía puede expresarse como

$$E_{total} = \left(\sum_{\substack{enlaces \\ i}} E_{enlace}(b_i) + \sum_{\substack{ángulos \\ i}} E_{ángulos}(\theta_i) + \sum_{\substack{diedros \\ i}} E_{died.}(\chi_i) \right)_{enlazados} + \left(\sum_{\substack{no\ enlazados \\ (i,j),i<j}} E_r(r_{ij}) \right) \quad (3.1)$$

En base al segundo principio, se asume que los parámetros derivados de datos experimentales o cálculos mecánico-cuánticos de estructuras representativas pueden utilizarse para ajustar los potenciales efectivos que describirán las macromoléculas compuestas a partir de dichas estructuras.[1,2]

3.1 Campos de fuerzas

El conjunto de parámetros y ecuaciones utilizados para describir la energía potencial de un sistema mediante la mecánica molecular se conoce con el nombre de *campo de fuerzas*.[1-4] Existen en la actualidad varios tipos de campos de fuerzas que se diferencian básicamente por el número de términos utilizados para calcular la energía del sistema, así como la manera en que se han obtenido los parámetros individuales presentes en cada una de dichas contribuciones. Aun así, todos ellos comparten en mayor o menor medida la manera de calcular cada término en particular. Se utilizan potenciales armónicos para describir los enlaces y ángulos, series de Fourier para las torsiones, y las interacciones entre pares no enlazados se describen mediante una función del tipo Lennard-Jones (van der Waals) y una función coulómbica (electostático).

Los campos de fuerza actuales se pueden subdividir en tres clases diferentes:

Clase I: aquellos campos que no contienen términos cruzados y en que los términos de flexión y torsión se aproximan mediante funciones armónicas; ejemplos de estos campos serían AMBER[5] y CHARMM[6].

Clase II: desarrollados para reproducir las propiedades de moléculas pequeñas aisladas, para lo cual es necesario incluir términos cruzados y donde los términos de flexión y torsión se describen mediante polinomios de orden superior o series de fourier; esta clase incluye los campos de fuerza MM3[7] y CFF93[8].

Clase III: del mismo tipo que el anterior, pero con términos adicionales para describir fenómenos de hiperconjugación y electronegatividad, como por ejemplo el campo de fuerzas MM4[9].

En lo siguiente explicaremos brevemente las características de los force-fields mas sencillos (clase I; concretamente el formalismo que sigue AMBER) que han sido los empleados en esta tesis.

3.1.1 Términos asociados a enlace

La ley de Hooke para un oscilador armónico es el modelo más simple que puede utilizarse para describir las deformaciones de los enlaces covalentes. Representado el enlace entre dos átomos como un muelle que los mantiene unidos permitiendo cierto desplazamiento mutuo en forma de elongación del mismo, la energía potencial vendrá descrita por:

$$E_{vib} = \sum_{enl} K_{vib}\left(r - r_{eq}\right)^2 \tag{3.2}$$

donde r es la distancia de enlace, r_{eq} la distancia de referencia (normalmente la de equilibrio) y K_{vib} es la constante de fuerza asociada.

El potencial más sencillo que se puede utilizar para describir las deformaciones en los ángulos de enlace es el que se deriva de la aplicación de la ley de Hooke para un oscilador armónico.

$$E_{ang} = \sum_{enl} K_{ang}\left(\theta - \theta_{eq}\right)^2 \tag{3.3}$$

siendo K_{ang} la constante de fuerza asociada y θ_{eq} el valor de referencia para el ángulo entre tres átomos unidos por enlaces covalentes.

Para describir las torsiones es preciso utilizar una expresión más compleja que en los dos casos anteriores. La rotación alrededor de un enlace implica el movimiento de los grupos adyacentes a los átomos que se encuentran formando dicho enlace, que podrán adoptar conformaciones eclipsadas o alternadas confiriendo periodicidad al término de torsión. Para expresar la periodicidad del perfil de energía se utilizan expresiones periódicas en serie de Fourier, que pueden depender solo de los dos átomos centrales implicados en el diedro o bien ser específico de todos los diedros que definen la torsión.

$$E_{tor} = \sum_{tor}\sum_{n}\frac{V_n}{2}\left(1+\cos\left(n\phi - \phi_0\right)\right) \tag{3.4}$$

donde V_n representa la barrera de torsión asociada a cada término de la función, n la periodicidad del término, ϕ el ángulo diedro y ϕ_0 el ángulo de fase.

Para llegar a describir bien las energías y geometrías, es necesario en la mayoría de casos añadir una función para describir las torsiones impropias, a fin de mantener la planaridad o la quiralidad de ciertos grupos. Este término suele describirse mediante una expresión similar a la torsión convencional (Eq. 3.5).

$$E_{tor} = \sum_{tor}\sum_{n}\frac{V_n}{2}\left(1+\cos\left(2\xi_n - 180\right)\right) \tag{3.5}$$

donde V_n representa la constante de fuerza de cada término de la función, n la periodicidad del término y ξ el ángulo diedro.

3.1.2 Términos no-enlazantes

La forma más sencilla de describir la distribución de carga en una molécula es utilizar cargas puntuales fraccionales centradas en los núcleos de los átomos.[1] La interacción entre cargas queda representada entonces por la ley de Coulomb y la energía viene dada por la ecuación:

$$E_{ele} = \sum_{i}\sum_{j>i}\frac{q_i q_j}{4\pi\varepsilon_0 r_{ij}} \tag{3.6}$$

siendo q_i y q_j las cargas puntuales de cada átomo, r_{ij} la distancia entre átomos y ε la constante dieléctrica del medio.

En la mayoría de los campos de fuerza, las cargas puntuales fraccionales se obtienen mediante ajuste al potencial electrostático molecular calculado a partir de la función de onda Hartree-Fock obtenida utilizando una base 6-31G(d). Existen varios métodos para la obtención de dichas cargas, que difieren en la selección de los puntos escogidas para ajustar el potencial y el método de ajuste. Cox y Williams[10] propusieron derivar las cargas puntuales fraccionales ajustando el valor de potencial electrostático calculado en

los puntos de una malla regular situada en la región comprendida desde el radio de van der Waals incrementado 1.2 Å y 1 Å más allá. Chirlian y Francl[11] optaron ajustar los potenciales calculados en capas que siguen la forma de la molécula hasta llegar a una distancia de 3 Å respecto a la superficie de van der Waals. Dicho método, denominado CHELP, tiene una variante, el método CHELPG[12], que aprovecha el mismo algoritmo de ajuste aunque garantiza una distribución simétrica de puntos que garantiza la invarianza rotacional de las cargas ajustadas. En el campo de fuerzas de AMBER, las cargas se derivan con el método RESP[13] (Restrained Electrostatic Potential) muy similar a CHELPG, pero donde se introducen restricciones hiperbólicas sobre la carga de los átomos pesados, a fin de evitar que el ajuste no restringido al potencial conduzca a soluciones en las que las cargas de los átomos internos adopten valores sin sentido químico.

Para describir el potencial generado por las fuerzas de dispersión-repulsión se utiliza una función del tipo Lennard-Jones 12-6.[1-4] Dicha expresión está formada por la suma de dos términos, uno repulsivo para las distancias cortas entre átomos y otro atractivo para distancias mayores, pudiéndose representar las interacciones atractivas a corta distancia fruto de las fuerzas dispersivas y evitar la fusión de átomos no unidos de carga opuesta.

$$E_{vdw} = \sum_{i} \sum_{j>i} \left(\frac{A_{ij}}{r_{ij}^{12}} - \frac{B_{ij}}{r_{ij}^{6}} \right) \tag{3.7}$$

donde A_{ij} y B_{ij} son constantes para cada par de átomos relacionados con sus radios de van der Waals y durezas, y r_{ij} es la distancia entre ellos.

3.1.3 Parametrización de los campos de fuerzas

Uno de los puntos clave para que un campo de fuerzas sea eficaz en su aplicación es sin duda la calidad de los parámetros que se utilizan. Para obtener los términos de enlace se pueden emplear tanto técnicas experimentales como la espectroscopia infrarroja o Raman para los enlaces y ángulos y la de RMN para las torsiones. También es posible ajustar los términos de enlace a cálculos cuánticos de alto nivel. Respecto a

los términos no enlazantes el ajuste es más complejo, en algunos force-fields se ajustan las funciones de van der Waals y electrostáticas simultáneamente a fin de garantizar que el force-field resultante sea capaz de reproducir propiedades físicas macroscópicamente de sistemas (p.ej densidad, calor de vaporización, compresibilidad,... de líquidos). La mayoría de los force-fields, no obstante, optan por una parametrización separada donde primero se ajustan las cargas atómicas a partir de datos mecanocuánticos y luego se refinan los parámetros de van der Waals sea a partir de datos de empaquetamiento cristalino, sea a partir del ajuste a energías de interacción experimentales o mecanocuánticas.

Una vez obtenidos los parámetros que conforman el campo de fuerzas, su utilización para describir nuevas moléculas precisa en la mayoría de los casos de la obtención de nuevos parámetros específicos que reproduzcan las cargas, distancias de enlace, ángulos y torsiones de éstas. En el esquema 1 se detallan los pasos a seguir para la obtención de dichos parámetros en el caso del campo de fuerzas AMBER[14].

I. Términos de enlace:

A. R_0- Distancia de equilibrio

1. utilizar los parámetros del propio campo de fuerzas
2. utilizar los de Allen et al. (J. Chem. Soc. Perkin Trans. II, 1982, S1-16)
3. hacer una optimización a nivel 6-31G* de un modelo simple que contenga el enlace

B. Kr- constantes de fuerza de enlace

1. utilizar parámetros análogos del propio campo de fuerzas
2. llevar a cabo un análisis de modos normales en un modelo simple y variar Kr hasta reproducir los datos experimentales.
3. hacer un análisis de modos normales a nivel 6-31G* y escalar las frecuencias por 0.89 y a continuación realizar un análisis de modos normales para ajustar la constante de fuerza de enlace.

II. Términos de ángulos de enlace:

A. θ_0- Ángulo de equilibrio

1. utilizar parámetros análogos del propio campo de fuerzas
2. tomar 109.5° para sp^3 y 120.0° para sp^2
3. optimizar a nivel 6-31G* un modelo más pequeño del compuesto que contenga dicho ángulo

K_0- constante de fuerza asociada al ángulo

1. utilizar los parámetros del campo de fuerzas
2. utilizar 70 kcal/mol rad^2 para X-sp^2-X y 50 kcal/mol rad^2 para X-sp^3-X

III. Parámetros de Van der Waals:

1. utilizar los propios del campo de fuerzas
2. realizar una simulación por Monte Carlo o Dinámica Molecular de un prototipo más pequeño de la molécula para reproducir el calor experimental de vaporización y la densidad

IV. Cargas electrostáticas parciales:

A. realizar un ajuste RESP en la estructura optimizada. A continuación, utilizar las cargas obtenidas para comprobar que tienen un efecto menor sobre la estructura

B. en caso de ser necesario, realizar un ajuste RESP multiconformacional

V. Términos asociados a la torsión:

A. tomar los parámetros del propio campo de fuerzas

B. Cuando existan efectos torsionales específicos, optimizar a nivel 6-31G* seguida de cálculos puntuales a nivel MP2 para caracterizar las conformaciones de baja energía de la molécula. Si el modelo con torsiones generales y cargas RESP no representa adecuadamente las energías, añadir más términos específicos.

En último término, no podemos olvidar que la parametrización se realiza siempre sobre un sistema modelo y que la transferabilidad de los parámetros no está siempre garantizada. Es por ello que al haber parametrizado una nueva molécula o parte de un sistema se deba verificar la calidad de los parámetros por comparación con observables experimentales.

3.2 Mecánica y dinámica molecular

Dos técnicas de especial utilidad en biología en las cuales se aplican los campos de fuerza son la mecánica molecular y la dinámica molecular. Las dos técnicas comparten muchas características, su principal diferencia estriba en la inclusión del tiempo como variable en la dinámica molecular.

3.2.1 Mecánica Molecular

La energía potencial que describe los estados conformacionales de una molécula es función de las coordenadas cartesianas asociadas a la posición de cada átomo en el espacio. Así, se puede asociar cada estructura a un punto en una hipersuperficie de energía potencial. En dicha hipersuperficie pueden existir muchos puntos de mínima energía que se corresponden con estados configuracionales estables del sistema llamados mínimos locales. El punto que tiene la energía más baja se conoce con el nombre de mínimo global.[1-3]

Existen diversas clases de métodos para identificar los puntos correspondientes a mínimos en la superficie de energía potencial, que difieren en la utilización de la información contenida en el gradiente y/o la hessiana de cara a trazar el camino hacia el mínimo de energía.

Métodos como Simplex o Secuencial son métodos no derivativos. En el primero se localiza el mínimo mediante la exploración de la superficie de energía potencial con desplazamientos geométricos de los vértices de una figura formada por n+1 variables de la función a minimizar. Para la exploración de la superficie se utilizan tres tipos de movimientos: reflexión, expansión y contracción. En el método Secuencial se explora la superficie de energía potencial de forma rotatoria para todas las variables de la función. Tomando como partida una variable, se calcula el valor de la función en dos puntos situados a $x+\delta x$ *i* $x+2\delta x$. A continuación se ajusta una parábola a los tres puntos y se calcula el mínimo de ésta a partir del cual se cambia de variable y así sucesivamente hasta llegar al mínimo.[2]

Los métodos derivativos se clasifican por el orden de las derivadas que se utiliza. Normalmente es preferible usar combinaciones, empezando por un método que utilice primeras derivadas para acercarse al mínimo y refinando la estructura por algún método que calcule o aproxime las segundas derivadas. Dentro de los métodos que utilizan primeras derivadas se encuentran los métodos *steepest-descent* y *conjugate gradient*.[1,2] En el primero la dirección de búsqueda es paralela al gradiente, y la progresión hacia el mínimo se realiza con un ancho de paso variable según que el valor de la función sea menor o mayor que para el punto anterior. En el segundo método, los gradientes en cada punto del camino a seguir para llegar al mínimo son ortogonales, mientras que las direcciones a seguir para pasar de un punto a otro son conjugadas a las direcciones de los pasos previos, simulando de alguna manera la introducción del Hessiano. De esta manera se consigue mayor eficacia cuando se está cerca del mínimo, aunque la convergencia es mas lenta en regiones apartadas. La estrategia más común es combinar pues los dos métodos SD al principio de la optimización y CG en las etapas finales.

Para sistemas pequeños es posible aplicar los métodos que calculan explícitamente segundas derivadas. Entre ellos se encuentra el método Newton-Raphson y sus variantes, los métodos quasi-newtonianos.[2] Todos ellos son eficaces cuando la función de energía potencial depende de un número relativamente pequeño de variables, ya que se debe calcular la hessiana del sistema a cada paso, por lo que los requisitos computacionales son mucho más grandes.

3.2.2 Dinámica molecular

Las simulaciones por dinámica molecular se empezaron a gestar en la década de 1950. En 1957, Alder y Wainwright utilizaron esta técnica por primera vez para simular la evolución de un sistema formado por esferas rígidas que interaccionaban por colisiones perfectas[15]. A lo largo de las décadas siguientes y con el aumento del poder de cálculo, las simulaciones por dinámica molecular han pasado a ser una herramienta esencial en el modelado molecular. Mediante la aplicación de esta técnica es posible obtener información estructural, termodinámica o cinética de procesos biomoleculares, como cambios conformacionales asociados a unión de ligandos, plegamiento de proteínas, transporte de iones o formación de agregados proteicos, entre muchos otros.[16]

Para aplicar la dinámica molecular es necesario tener información espacial de la estructura de la molécula que quiere estudiarse. Dicha información debe contener la situación en el espacio en forma de coordenadas de cada átomo. Aplicando las leyes de Newton al sistema se obtiene una trayectoria que contiene las distintas conformaciones que adopta la molécula a lo largo del tiempo de simulación.

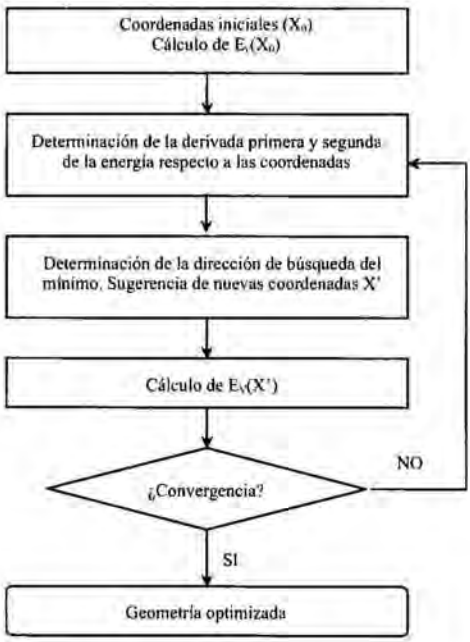

Figura 3.1 Algoritmo básico de los métodos de mecánica molecular

La segunda ecuación de Newton para una partícula i, con masa m_i, y cuya posición en el espacio viene dada por el vector $\boldsymbol{r}$ de tres dimensiones es

$$\frac{dp_i}{dt} = F_i \tag{3.8}$$

donde F_i es la fuerza que actúa sobre el átomo i, y la cantidad de movimiento p_i viene dada por

$$m_i \frac{dr_i}{dt} = p_i \tag{3.9}$$

$$F_i = -\frac{dV}{dr_i} \tag{3.10}$$

donde r_i indica el vector posición del átomo i, t representa el tiempo, y V es el potencial total, que se evalúa a partir del campo de fuerzas.

Si se conoce la posición de la partícula a un tiempo dado t, entonces su posición después de un incremento pequeño y finito Δt vendrá dada por una expansión en serie de Taylor alrededor del punto de origen. Tomando sólo la componente del vector $\boldsymbol{r}$ en una dimensión (x en este caso), la expansión en serie resulta de la forma:

$$x(t+\Delta t) = x(t) + \frac{dx(t)}{dt}\Delta t + \frac{d^2x(t)}{dt^2}\frac{\Delta t^2}{2} + \ldots \tag{3.11}$$

donde aparecen la posición de la partícula a un tiempo dado $x(t)$, su velocidad $\frac{dx(t)}{dt}$ y su aceleración $\frac{d^2x(t)}{dt^2}$.

Si se trunca la serie de Taylor en el segundo orden y se desprecian los términos de orden superior, la integración de las ecuaciones del movimiento se puede llevar a cabo de forma numérica con estas tres variables.

3.2.2.1 Algoritmos de integración

En sistemas formados por múltiples partículas bajo la influencia un potencial continuo, la fuerza que actúa sobre una partícula será función de las posiciones de todas las otras partículas del sistema y cambiará al variar su posición así como la de cualquier otra partícula del sistema. Éste fenómeno, conocido como *problema de muchos cuerpos*, es debido a que el movimiento de las partículas está acoplado entre ellas.[1] En consecuencia, la integración de las ecuaciones del movimiento debe realizarse de forma

diferencial por métodos de diferencias finitas donde la etapa de integración debe ser siempre menor que el movimiento más rápido del sistema (en la escala del femtosegundo en sistema biológicos); véase Tabla 3.1.

A nivel práctico hay desarrollados diferentes métodos. En el algoritmo de Verlet[17], por ejemplo, se utilizan las posiciones y aceleraciones a un tiempo dado t y las posiciones a un tiempo t-δt para calcular las posiciones en el siguiente paso, $t+\delta t$. Eso implica que las velocidades no tienen porqué calcularse y por lo tanto los requisitos de almacenaje y cálculo no son demasiado elevados. El problema de este algoritmo recae en la precisión con que se obtienen las coordenadas para las nuevas posiciones, ya que éstas se obtienen por la ecuación 3.12, donde se suma un valor muy pequeño a la diferencia entre dos valores mucho mayores.

$$\mathbf{r}(t+\delta t) = 2\mathbf{r}(t) - \mathbf{r}(t-\delta t) + \delta t^2 \mathbf{a}(t) \tag{3.12}$$

Existen distintas variantes del método de Verlet que difieren principalmente en la forma con que se obtienen las nuevas posiciones, como por ejemplo el algoritmo de velocidades de Verlet[18] o el de Beeman[19], pero la variante del algoritmo de Verlet más extendida es el método *leap-frog*[20]. En éste, las posiciones a $t+\delta t$ se obtienen a partir de las velocidades a $t+\frac{1}{2}\delta t$ mediante las ecuaciones 3.13 y 3.14.

$$\mathbf{r}(t+\delta t) = \mathbf{r}(t) + \delta t \mathbf{v}\left(t+\tfrac{1}{2}\delta t\right) \tag{3.13}$$

$$\mathbf{v}\left(t+\tfrac{1}{2}\delta t\right) = \mathbf{v}\left(t-\tfrac{1}{2}\delta t\right) + \delta t \mathbf{a}(t) \tag{3.14}$$

De este modo, se evitan los problemas de precisión del algoritmo de Verlet y además pueden obtenerse las velocidades, aunque desfasadas respecto de las posiciones $\frac{1}{2}\delta t$. Las velocidades a un tiempo dado t se obtienen por la ecuación 3.15.

$$\mathbf{v}(t) = \frac{1}{2}\left[\mathbf{v}\left(t+\tfrac{1}{2}\delta t\right) + \mathbf{v}\left(t-\tfrac{1}{2}\delta t\right)\right] \tag{3.15}$$

Finalmente cabe destacar otros métodos de integración, como los de predicción-corrección, donde las posiciones, velocidades y aceleraciones se obtienen por expansión en serie de Taylor. El valor de las aceleraciones se compara con el obtenido a partir de las fuerzas para corregirlas y obtener las nuevas posiciones. Esto hace que los requerimientos de almacenamiento y cálculo sean mayores que en el algoritmo de Verlet y sus variantes antes mencionadas.

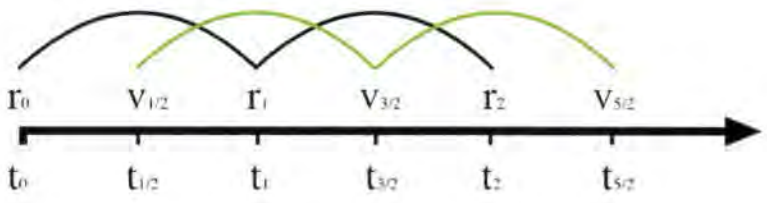

Figura 3.2 Representación esquemática del algoritmo *leap-frog*.

evento	extensión espacial (nm)	amplitud (nm)	tiempo (s)	simulación apropiada
vibración de la distancia de enlace	0.2-0.5	0.001-0.01	10^{-14}-10^{-13}	Métdos QM
vibración elástica de un dominio globular	1.0-2.0	0.005-0.05	10^{-12}-10^{-11}	DM convencional
rotación de cadenas expuestas a solvente	0.5-1.0	0.5-1.0	10^{-12}-10^{-10}	DM convencional
oscilación torsional de grupos internos	0.5-1.0	0.05	10^{-12}-10^{-10}	DM convencional
hinge bending (movimiento relativo de dominios globulares)	1.0-2.0	0.1-0.5	10^{-11}-10^{-7}	Dinámica de Langevin, métodos de amplio muestreo?
rotación de cadenas laterales internas	0.5	0.5	10^{-8}-1	métodos de amplio muestreo?
transiciones alostéricas	0.5-0.4	0.1-0.5	10^{-5}-1	métodos de amplio muestreo?
desnaturalización local	0.5-1.0	0.5-1.0	10^{-5}-10^{3}	métodos de amplio muestreo?
movimientos de loops	1.0-5.0	1.0-5.0	10^{-9}-10^{-4}	Dinámica Browniana
movimientos de cuerpo rígido (hélices)		1.0-5.0	10^{-8}-10^{+}	métodos de amplio muestreo?
transiciones hélice-enrollado		>5.0	10^{-7}-10^{4}	métodos de amplio muestreo?
asociación de proteínas	>>1.0			Dinámica Browniana

Tabla 3.1 Relación entre los intervalos de tiempo de fenómenos característicos de moléculas y sistemas biomoleculares y los métodos teóricos existentes.

3.2.2.2 Tiempo de integración

Como se ha comentado más arriba el tiempo de integración debería ser del orden del femtosegundo. Esto representa que para poder tener un nanosegundo de trayectoria es

necesario realizar 10^6 pasos con todo el coste computacional y temporal que ello requiere. Una de las opciones más utilizadas para aumentar el paso de integración es aplicar al sistema restricciones. El algoritmo más extendido para aplicar restricciones al sistema es SHAKE[21]. Con este método se pueden fijar las distancias de enlace entre átomos quedando como únicas posibilidades de movimiento las torsiones y ángulos que tienen una frecuencia de vibración menor ($2x10^{-14}$ para los átomos ligeros), lo cual permite duplicar el paso de integración.

3.3 Condiciones de simulación

El punto inicial de cualquier simulación es siempre una configuración inicial. Dicha estructura podrá provenir de datos experimentales de Rayos-X, Resonancia Magnética Nuclear o de un modelo teórico. Asimismo, precisa un conjunto de velocidades iniciales, que se asignarán al azar siguiendo una distribución de tipo Maxwell-Boltzmann, tal que la energía cinética asociada se corresponda a la energía térmica diana para la temperatura de trabajo. Finalmente, requiere fijar las condiciones de simulación: el número de partículas (N), el volumen (V), la temperatura (T), la presión (P) o la energía total del sistema (E). En función de la combinación de los mismos se distingue entre varios colectivos:

-microcanónico (NVE)
-isotérmico-isobárico (NPT)
-canónico (NVT)

siendo NPT y NVT los más usados en dinámica molecular de proteínas.

Al trabajar bajo condiciones isotérmicas-isobáricas se tendrá que controlar tanto la temperatura como la presión. En el caso de la temperatura existen diferentes opciones. La primera de ellas sería el re-escalado de las velocidades mediante la aplicación de un factor. Otra alternativa sería mantener la temperatura acoplada a un baño térmico externo fijado a la temperatura deseada. Dichos baños actúan como fuente de energía térmica, añadiendo o eliminando calor del sistema en función de las necesidades. Las velocidades son también re-escaladas periódicamente, en función de la diferencia de

temperatura entre el baño y el sistema. Los métodos más conocidos son el de Berendsen[22] y el de Nosé-Hoover[23]. Métodos similares son empleados para mantener la presión. Típicamente se cálcula el virial para determinar la presión interna y esta se acopla a un pistón que garantiza equilibrio con la presión externa, aumentando o disminuyendo para ello el volumen de sistema simulado.

La imposibilidad de simular sistemas infinitos junto con el uso de potenciales continuos plantea diferentes problemas al llevar a cabo una simulación. Los sistemas están necesariamente confinados en un espacio finito, por lo que las partículas ubicadas en los límites del sistema interaccionan con las paredes de éste. Para sistemas pequeños esto significa que la mayor parte de las partículas del sistema se encuentran bajo la influencia de las paredes. Si se quieren obtener propiedades macroscópicas a partir de sistemas modelo, necesariamente debe eliminarse de alguna manera el efecto de las paredes.[1,2] Por otro lado, dado que cada partícula interacciona con todas las otras, sería necesario calcular N(N-1) pares de interacciones no enlazantes a cada paso, aumentado de forma desmedida el tiempo de cálculo necesario.

El primer problema puede minimizarse si se utilizan condiciones periódicas de contorno, por las cuales se confina las partículas del sistema en una caja que se replica en todas las direcciones del espacio. Durante la simulación, si una partícula abandona la caja central, su imagen en otra caja entrará en la caja central por el lado opuesto, manteniéndose por lo tanto constante el número de partículas en dicha caja.

Para el segundo problema basta con tener en cuenta la forma del potencial que se esté utilizando. El término de van der Waals (eq. 3.7) decae rápidamente con la distancia de tal modo que a una distancia interatómica de 2.5σ (siendo σ la distancia entre átomos para la cual el potencial toma valor nulo) su valor es el 1% del que toma a la distancia de equilibrio, por lo que a distancias suficientemente grandes puede despreciarse. Así, puede restringirse el cálculo de las interacciones no enlazantes cortando a una distancia dada el potencial (*cut-off*) y usando el método de la mínima imagen. De esta manera las interacciones de esta clase se calculan entre una partícula y todas aquéllas que se encuentren en un radio arbitrario a su alrededor escogiendo las imágenes de las partículas que están más cercanas.

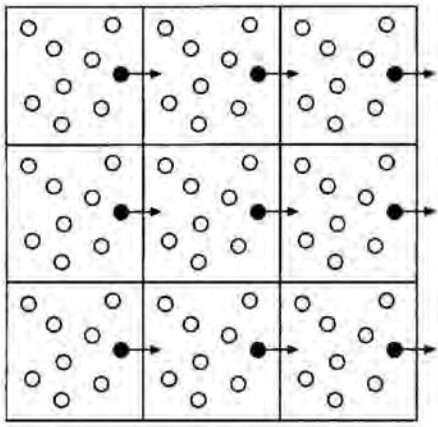

Figura 3.3 Representación esquemática de las condiciones periódicas de contorno

Por otro lado, el potencial electrostático decae con la distancia a *1/r*, por lo que no puede negligirse a distancias grandes si se quieren evitar artefactos en sistemas cargados como proteínas y ácidos nucleicos.[1,2] El método más utilizado para resolver este tipo de problemas es el método de sumas de Ewald[25]. En él se transforma el cálculo de la sumatoria de todas las interacciones electrostáticas posibles en otros dos términos de convergencia mucho más rápida: uno que engloba las interacciones a corta distancia (espacio directo), que son calculadas mediante un potencial coulómbico modificado, y otro en el que se incluyen el resto (espacio recíproco), que se calcula por sumas vectoriales. Una variante más eficaz de este método es Particle Mesh Ewald[26], en la que se optimiza el cálculo del espacio recíproco mediante interpolación *B-spline* de las cargas puntuales a mallas tridimensionales. Dichas mallas son posteriormente tratadas mediante transformadas de Fourier, las cuales reducen notablemente el costo computacional.

3.4 Perfiles de energía libre obtenidos mediante dinámica molecular

Un sistema concreto puede encontrarse en diferentes estados estables que corresponden a mínimos de energía, pero el camino de un mínimo a otro puede estar impedido por una barrera energética alta que dificulta el paso de un estado a otro a lo largo de la dinámica sino se aplica una perturbación externa que guíe el cambio. Por

ello, se han desarrollado diversas técnicas para poder evaluar el perfil de energía libre asociado a diversos procesos.

De las técnicas más habituales para obtener energías libres, destacar la conocida como *Umbrella Sampling* que se utiliza comúnmente par obtener perfiles de energía asociados a cambios conformacionales de residuos o cadenas aminoacídicas. Por otro lado, la técnica de *Jarzynski*[27] que resulta especialmente útil cuando no está clara la coordenada geométrica a seguir y que por lo tanto se utiliza a menudo para el cálculo de perfiles de difusión de moléculas pequeñas a través de membranas o canales.

Umbrella Sampling: La exploración de estados de baja probabilidad mediante este método se consigue introduciendo en la función de energía potencial (V) un potencial perturbativo (V_b), que guiará al sistema para que permanezca en estados concretos durante un tiempo suficiente para explorar el espacio conformacional asociado a ese estado.

$$V' = V + V_b \tag{3.16}$$

Para un proceso concreto, el camino a seguir se divide en pequeñas ventanas y se fuerza el muestreo en cada una de las ventanas mediante una función de "umbrella" como la que se muestra en la eq. 3.17. La división y la selección del potencial perturbativo debe ser tal que permita el solapamiento entre las ventanas, para garantizar que el trabajo calculado al final del proceso (véase más adelante) tiene propiedades de energía libre.

$$V_b(\chi) = \frac{1}{2}k(\chi - \chi_i)^2 \tag{3.17}$$

Dado que se aplica una perturbación al sistema, la distribución obtenida no representa una distribución de Boltzmann y deberá corregirse. Torrie y Valleau[28] introdujeron la siguiente expresión para corregir las distribuciones obtenidas,

$$\langle A \rangle = \frac{\left\langle A \exp\left(V_b / k_b T \right) \right\rangle_{V_b}}{\left\langle \exp\left(V_b / k_b T \right) \right\rangle_{V_b}} \tag{3.18}$$

donde A representa la magnitud termodinámica que se quiere calcular, V_b es el potencial perturbativo aplicado, k_b la constante de Boltzmann y T la temperatura.

Una vez obtenidas las distribuciones corregidas es posible obtener el potencial de fuerza media (PMF) asociado mediante la combinación de los valores que toma en cada ventana:

$$\omega(\chi)_i'' = \omega(\chi^*) - k_B T \ln\left[\frac{\langle \rho_b(\chi) \rangle_i}{\langle \rho(\chi^*) \rangle} \right] - V_b(\chi)_i + F_i \tag{3.19}$$

donde los índices *n* y *b* indican *normal* y *perturbado* respectivamente. F_i representa la energía libre asociada a la introducción del potencial perturbativo, y queda descrita por:

$$e^{-F_i / k_b T} = \left\langle e^{-V_b(\chi)_i / k_b T} \right\rangle \tag{3.20}$$

Los valores de F_i se pueden obtener por ajuste manual del PMF de cada ventana o mediante un ajuste de mínimos cuadrados en las regiones de solapamiento entre ventanas.

Método de Jarzinsky: La técnica de umbrella sampling, igual que otras semejantes se basan en la existencia de una ruta de equilibrio que conecta estados. El método propuesto por Jarzinsky y colaboradores no requiere (en principio) de ese requisito. El método consiste en aplicar al sistema una fuerza que guíe el proceso siguiendo caminos fuera del equilibrio, se calcula entonces el trabajo asociado y la ecuación de Jarzynski permite transformarlo en la energía libre[27] (ec. 3.22).

En un sistema descrito por un parámetro λ y un proceso que cambia el valor del parámetro desde λ_0 a tiempo 0 hasta λ_t a tiempo t, el trabajo promedio realizado en el sistema no puede ser inferior a la diferencia de energía libre de los estados correspondientes a λ_0 y λ_t (eq. 3.21). Por lo tanto, un proceso de no equilibrio proporciona una cota superior a la diferencia de energía libre. Jarzinsky demostró que la los trabajos obtenidos mediante procesos de no equilibrio se relacionan con la energía libre del proceso según la ecuación 3.22.

$$\Delta F = F(\lambda_0) - F(\lambda_t) \leq \langle w \rangle \tag{3.21}$$

$$\exp\left[-\Delta A(\lambda)/k_B T\right] = \left\langle \exp\left[-W(\lambda)/k_B T\right] \right\rangle \tag{3.22}$$

donde $A(\lambda)$ representa la energía libre, $W(\lambda)$ es el trabajo externo realizado sobre el sistema para ir desde λ_0 a λ_t, y k_B es la constante de Boltzmann.

En este caso la perturbación añadida al potencial original es dependiente del tiempo y mueve el sistema a lo largo de la coordenada de reacción variando el potencial de la forma

$$V'(r) = V(r) + k\left[r - (\lambda_0 + v\Delta t)\right]^2 \tag{3.23}$$

donde k es la constante de fuerza con la que forzamos la posición del sistema (por ejemplo la partícula en un canal), λ_0 la distancia inicial, v la velocidad con la que (por ejemplo se mueve la partícula) y Δt el incremento de tiempo entre cada paso.

El problema de éste método es el coste computacional que implica, dado que en el término exponencial de la ecuación de Jarzinsky los trabajos pequeños son los que tendrán mayor contribución al hacer el promedio y éstos son difíciles de obtener en las condiciones de simulación. Por lo tanto, es necesario realizar un número elevado de simulaciones independientes para poder obtener un promedio convergido.[29] En la

práctica pues, la selección del método de Jarzinsky o de umbrella sampling obedecerá a menudo a aspectos prácticos de definición del proceso.

3.5 Dinámica esencial

Dado que la flexibilidad estructural es una de las claves que determina la función de las proteínas[30-37], el estudio de la deformabilidad estructural de las proteinas puede aportar información relevante de los procesos en que participa.

Existen dos técnicas computacionales para extraer las deformaciones esenciales a partir de estructuras de equilibrio: el análisis de Modos Normales (NMA)[38-40] y la Dinámica Esencial (ED)[41]. En el método ED, la matriz de covarianza se diagonaliza obteniéndose vectores propios, que reflejan la naturaleza de los diferentes modos de deformación estructural, y valores propios, que dan una medida de la contribución de cada vector propio a la varianza global.

Los valores propios representan el desplazamiento a lo largo de un modo a una determinada temperatura. Por tanto, multiplicándolos se puede obtener un estimado del volumen configuracional accesible (ecuación 3.24). Desafortunadamente, el uso directo de este valor es ambiguo ya que depende del número de valores propios utilizados, tendiendo a cero al aproximarse a $3N$ (siendo N el número de átomos). Es por ello que es posible referirse al espacio conformacional haciendo uso del *volumen configuracional generalizado* y la *dimensionalidad.* El primero es obtenido como una modificación *ad hoc* del volumen configuracional que tiene propiedades de límite (ecuación 3.25). La dimensionalidad es una medida conformacional que se refiere al número de modos esenciales que se necesitan para describir el espacio de flexibilidad importante de una molécula[44] y se obtiene como el índice del primer modo que contribuye en menos de 1 $Å^2$ al volumen.

$$Vol = \prod_{i=1}^{m} (\lambda_i) \tag{3.24}$$

$$Vol_{gen} = \prod_{i=1}^{m}(1+\lambda_i)^{1/2} \tag{3.25}$$

donde m es el número de valores propios utilizados.

Los vectores propios dan información sobre el tipo de movimiento de la biomolécula. Una primera aproximación al estudio de dichos movimientos sería calcular los desplazamientos de unas coordenadas promedio a lo largo de los vectores más representativos en términos de varianza, pudiendo generar así una nueva trayectoria. Esta *pseudo*-trayectoria puede ser analizada numéricamente o simplemente visualizada.

Cuando se dispone de diferentes sistemas sobre los cuales se requiere un estudio comparativo de la deformabilidad, la obtención de los modos esenciales posibilita una forma directa de comparación a través un índice de similitud[42,43] que se obtiene por multiplicación escalar de los vectores (ec. 3.26).

$$\gamma_{AB} = \frac{1}{n}\sum_{j=1}^{n}\sum_{i=1}^{n}(v_i^A \bullet v_j^B)^2 \tag{3.26}$$

donde n es el número mínimo de vectores propios necesarios para explicar un determinado valor (por ejemplo el 80% o 90%) de la varianza estructural.

El valor del índice se sitúa próximo a 0 cuando los movimientos son ortogonales y próximo a 1 cuando existe un grado elevado de semejanza.

Si bien el índice de similitud señalado es una medida robusta para el estudio de las similitudes entre espacios conformacionales, presenta limitaciones. Por ejemplo, asume que todos los modos contribuyen de igual manera al producto escalar, con lo que es imposible detectar permutaciones de los mismos. El uso de índices más complejos que tienen en cuenta los valores propios asociados a cada movimiento puede ser útil en estos casos (ec. 3.27).[44]

$$\xi_{AB} = \frac{2\sum_{i=1}^{i=z}\sum_{j=1}^{j=z}\left[\left(v_i^A \circ v_j^B\right)\frac{\exp\left\{-\frac{(\Delta x)^2}{\lambda_i^A}-\frac{(\Delta x)^2}{\lambda_j^B}\right\}}{\sum_{i=1}^{i=z}\exp\left\{-\frac{(\Delta x)^2}{\lambda_i^A}\right\}\sum_{j=1}^{j=z}\exp\left\{-\frac{(\Delta x)^2}{\lambda_j^B}\right\}}\right]^2}{\sum_{i=1}^{i=z}\left(\frac{\exp\left\{-2\frac{(\Delta x)^2}{\lambda_i^A}\right\}}{\left(\sum_{i=1}^{i=z}\exp\left\{-\frac{(\Delta x)^2}{\lambda_i^A}\right\}\right)^2}\right)^2+\sum_{j=1}^{j=z}\left(\frac{\exp\left\{-2\frac{(\Delta x)^2}{\lambda_j^B}\right\}}{\left(\sum_{j=1}^{j=z}\exp\left\{-\frac{(\Delta x)^2}{\lambda_j^B}\right\}\right)^2}\right)^2} \qquad (3.27)$$

donde λ_i es el valor propio (en $Å^2$) asociado al vector propio, con vector unitario v_i, y la suma puede ser extendida a todos (z=m) o a un número importante de vectores propios (z=n).

Referencias bibliográficas

1 Leach, A. R., *Molecular Modelling: Principles and applications,* 2nd edition, **2001**, Pearson Education (Prentice Hall), Essex.

2 Schlick, T., *Molecular Modeling and Simulation. An interdisciplinary Guide*, **2002**, Springer-Verlag New York, Inc. New York.

3 Frenkel, D. & Smit, B., *Understanding Molecular Simulation*, **2002**, Academic Press.

4 McCammon, J. A. & Harvey, S. C., *Dynamics of Proteins and Nucleic Acids*, **1987**, Cambridge University Press, Cambridge.

5 Weiner, P. K., Kollman, P. A., *J. Comp. Chem.*, **1981**, 2, 287-303.

6 Brooks, B.R., Bruccoleri, R.E., Olafson, B.D., States, D.J., Swaminathan, S., Karplus, M., *J. Comp. Chem*, **1983**, 4, 187-217.

7 Allinger, N. L., Yuh, Y. H., Lii, J-H., *J. Am. Chem. Soc.*, **1989**, 111, 8551-8565.

8 Hwang, M.-J., Stockfisch, T. P., Hagler, A. T., *J. Am. Chem. Soc.*, **1994**, 116, 2515-2525.

9 Allinger, N. L., Chen, K., Lii, J-H, *J. Comp. Chem.*, **1996**, 17, 642-668.

10 Cox, S. R., Williams, D. E., *J. Comp. Chem.*, **1981**, 2, 304-323.

11 Chirlian, L. E., Francl, M. M., *J. Comp. Chem.*, **1987**, 8, 894-905.

12 Breneman, C. M., Wiberg, K. B., *J. Comp. Chem.*, **1990**, 11, 361-373.

13 Bayly, C. I., Cieplak, P., Cornell, D. W., Kollman, P. A., *J. Phys. Chem.*, **1993**, 97, 10269-10280.

14 Fox, T., Kollman, P. A., *J. Chem. Phys. B*, **1998**, 102, 8070-8079.

15 Alder, B. J., Wainwright, T. E., *J. Chem. Phys.*, **1957**, 27, 1208-1209.

16 Adcock, S. A., McCammon, J. A., *Chem. Rev.*, **2006**, 106, 1589−1615.

17 Verlet, L., *Phys. Rev.*, **1967**, 159, 98-103.

18 Swope, W. C., Anderson, H. C., Berens, P. H., Wilson, K. R., *J. Chem. Phys.*, **1982**, 76, 3271-3276.

19 Beeman, D., *J. Chomp. Phys.*, **1976**, 20, 130-139.

20 Hockney, R. W., *Meth. Comp. Phys.*, **1970**, 9, 136-211.

21 Ryckaert, J. P., Cicotti, G., Berendsen, H. J. C., *J. Chomp. Phys.*, **1977**, 23, 327-341.

22 Berendsen, H. J. C., Postma, J. P. M., vzn Gunsteren, W. F., Di Nola, A., Haak, J. R., *J. Chem. Phys.*, **1984**, 81, 3684-3690.

23 Hoover, W. G., *Phys Rev A*, 1985, 31, 1695-1697.

24 Nosé, S., *Mol. Phys.*, **1984**, 53, 255-268.

25 Ewald, P. P., Ann. Phys., **1921**, 64, 253-287.

26 Darden, T. L., York, D., Pedersen, L., *J. Chem. Phys.*, **1993**, 98, 10089-10092.

27 Jarzynski, C., *Phys. Rev. Lett.*, **1997**, 78, 2690-2693.

28 Torrie, G. M., Valleau, J. P., *J. Comp. Phys.*, **1977**, 23, 187-199.

29 Xong, H., Crespo, A., Martí, M., Estrin, D., Roitberg, A. E., *Theor. Chem. Acc.*, **2006**, 116, 338-346.

30 Daniel, R. M., Dunn, R. V., Finney, J. L., Smith, J. C., *Annu. Rev. Biophys. Biomol. Struct.*, **2002**, 32, 69–92.

31 Eisenmesser, E. Z., Bosco, D. A., Akke, M., Kern, D., *Science*, **2002**, 295, 1520-1523.

32 Hinsen, K., Thomas, A., Field, J., *Proteins*, **1999**, 34, 369-382.

33 Luo, J., Bruice, T.C., *Proc. Natl. Acad. Sci. USA*, **2004**, 101, 13152-13156.

34 Ma, J., Karplus, M., *Proc. Natl. Acad. Sci. USA*, **1998**, 95, 8502-8507.

35 Remy, Y., Wilson, I. A., Michnik, S. W., *Science*, **1999**, 283, 990-993.

36 Sacquin-Mora, S., Lavery, R., *Biophys. J.*, **2006**, 90, 2706-2717.

37 Yang, L-W., Bahar, I., *Structure*, **2005**, 893-904.

38 Go, N., Noguti, T., Nishikawa, T., *Proc. Natl. Acad. Sci. USA*, **1983**, 80, 3696-3700.

39 Levitt, M., Sander, C., Stern, P.S., *J. Mol. Biol.*, **1985**, 181, 423-447.

40 Cui, Q., Bahar, I., eds., *Normal Mode Analysis. Theory and applications to biological and chemical systems*, Chapman & Hall/CRC, London.

41 Amadei, A., Linssen, A. B., Berendsen, H. J., *Proteins*, **1993**, 17, 412-425.

42 Hess, B., *Phys. Rev. E Stat. Nonlin. Soft. Matter. Phys.*, **2000**, 8438-8448.

43 Hess, B., Phys. Rev. E Stat. Nonlin. Soft. Matter. Phys., 2002, 65, 031910.

44 Perez, A., Blas, J. R., Rueda, M., López-Bes, J. M., de La Cruz, X., Luque, F. J., Orozco, M., *J. Chem. Theor. Comp.*, **2005**, 1, 790-800.

Resultados y discusión

Inhibidores duales del enzima acetilcolinesterasa

Introducción

La enfermedad de Alzheimer (AD) es la cuarta causa de muerte entre la gente mayor de 65 años en los países occidentales industrializados[1]. La patología es el resultado de un proceso multifactorial[2] que provoca un desorden neurodegenerativo progresivo cuya patogénesis no está bien establecida. Su tratamiento en la actualidad es de tipo sintomático y esencialmente persigue atenuar la progresión de la neurodegeneración y mejorar la calidad de vida del paciente en los primeros estadios de la enfermedad.

La forma más eficaz de combatir la enfermedad hasta el momento está basada en la llamada hipótesis colinérgica, según la cual como mínimo una parte de la pérdida de la capacidad cognitiva que se produce en los enfermos de Alzheimer está causada por una falta del neurotransmisor acetilcolina (ACh) en el sistema nervioso central. La acetilcolinesterasa (AChE) es la enzima encargada de degradar ACh y es la única diana terapéutica aceptada en la actualidad para esta enfermedad. Los medicamentos que se encuentran en el mercado actualmente (tacrina[3], donepezilo[4], rivastigmina[5] o galantamina[6]) son inhibidores de AChE, que actúan evitando la hidrólisis de ACh para bloquear la disminución de la neurotransmisión colinérgica.

Un fenómeno aún no explicado en el desarrollo de la AD es la mutación de un número de genes, que incluyen el alelo ε4 de la apolipoproteína E, presenilina-1 y presenilina-2 y los genes de las proteínas precursoras del β-amiloide. Estas mutaciones producen un incremento de los niveles de péptido β-amiloide secretado[7], que se deposita en el cerebro siendo la formación de estos depósitos un indicador claro de la aparición de la enfermedad y su posible causa. Ello ha hecho que la formación y agregación del péptido β-amiloide se haya convertido en una diana terapéutica alternativa para el desarrollo de terapias eficientes, como la inhibición de β- y γ-secretasas para suprimir la producción de péptido, inhibidores de la agregación del β-amiloide, agentes disolventes de los agregados y la inmunización con péptido β-amiloide.

Estudios realizados por Alvarez *et. al.*[8] mostraron que la AChE se colocalizaba en los depósitos de β-amiloide, y estudios más recientes han identificado la AChE como un agente promotor de la agregación, así como también que la cantidad de AChE unida a β-amiloide modula la neurotoxicidad de los agregados[9]. La unión de β-amiloide y AChE implica una zona periférica al centro catalítico[10-13], lo que ha motivado nuevas estrategias de inhibición de AChE que abarquen a la vez los dos centros activos a fin de conseguir mejora sintomática relacionada con el aumento de ACh y a la vez posible efecto curativo ligado al péptido β-amiloide.

3.1 Acetilcolinesterasa

La AChE es una proteína de la familia de las colinesterasas cuya función principal es la hidrólisis del neurotransmisor ACh. La reacción ocurre mediante un ataque nucleofílico al carbono carbonílico, que produce la acilación del enzima y la liberación de colina; véase Esquema 3.1. En un segundo paso, la enzima se hidroliza liberando ácido acético y queda de nuevo disponible para llevar a cabo la reacción.

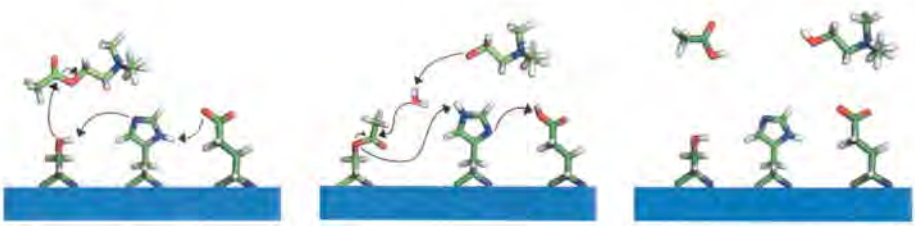

Esquema 3.1. Representación del mecanismo de reacción que tiene lugar en el centro catalítico de la proteína Acetilcolinesterasa.

La enzima es un proteína α/β formada por 537 aminoácidos que se estructuran en 12 hojas β rodeadas por 14 hélices α. En la estructura cristalográfica obtenida por rayos-X (de la proteína[14] de *Torpedo californica*) se diferencia de forma clara un canal, conocido como garganta catalítica, de unos 20 Å de largo, que conecta la superficie de la proteína en la zona donde se encuentra el centro periférico con el centro catalítico de hidrólisis de acetilcolina situado en el fondo del mismo (Figura 3.1).

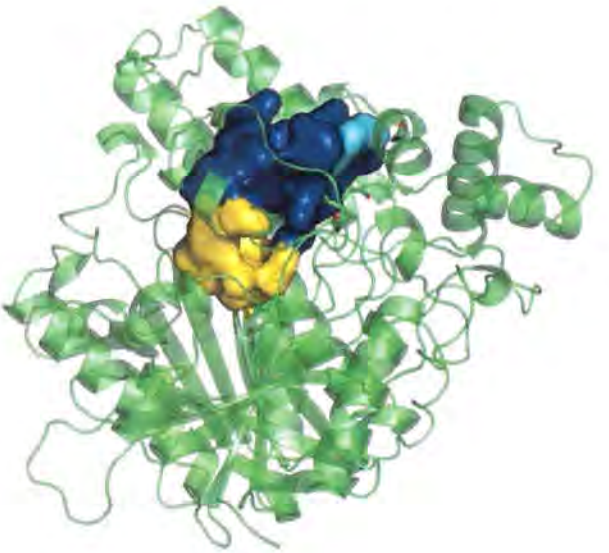

Figura 3.1 Estructura tridimensional de la proteína Acetilcolinesterasa. Los residuos que conforman la garganta catalítica están representados por la superficie accesible a solvente (SASA) en color azul, amarillo para los residuos del centro catalítico y cyan para el centro periférico.

El centro catalítico de AChE está formado por los residuos Ser200-His440-Glu327. El residuo Trp84, situado en el fondo del canal, contribuye a estabilizar la unión del ligando mediante la formación de una interacción π-catión con la amina cuaternaria de ACh y se cree que el residuo Glu199 es clave para orientar correctamente la His440 cuando el ligando se une a la Ser200[15-18]. El segundo centro, denominado periférico o aniónico, está definido por el Trp279 y se encuentra situado en la entrada del canal. Se considera que constituye un primer punto de unión del sustrato, que permite acelerar el proceso de hidrólisis a concentraciones bajas de ACh[19].

La longitud del canal, así como su poca amplitud, no parecen concordar con la eficacia catalítica de la enzima. El valor de la relación k_{cat}/K_m ($\sim 10^9$ $M^{-1}s^{-1}$) es muy elevado si se tiene en cuenta el camino que debe seguir el sustrato para llegar al centro catalítico. Sin embargo, estudios computacionales mostraron la presencia de un campo electrostático muy fuerte, que debería dirigir los ligandos catiónicos a través del canal[20-24]. Este campo electrostático atrapa los ligandos y los atrae hasta el centro catalítico, impidiendo además su salida[25].

3.2 Inhibidores duales reversibles de acetilcolinesterasa

La aceptación de la hipótesis colinérgica desembocó en el desarrollo de inhibidores para impedir la reacción de hidrólisis de ACh. Esta estrategia proporcionó un elevado número de compuestos capaces de inhibir la proteína (ver Fig 3.2) con mayor o menor eficacia, dando como resultado final la aparición de diversos medicamentos (véase más adelante). El problema de esta clase de compuestos es su incapacidad para actuar sobre la agregación del βA y por lo tanto la imposibilidad de tener supuestamente un mayor efecto sobre el avance de la enfermedad.

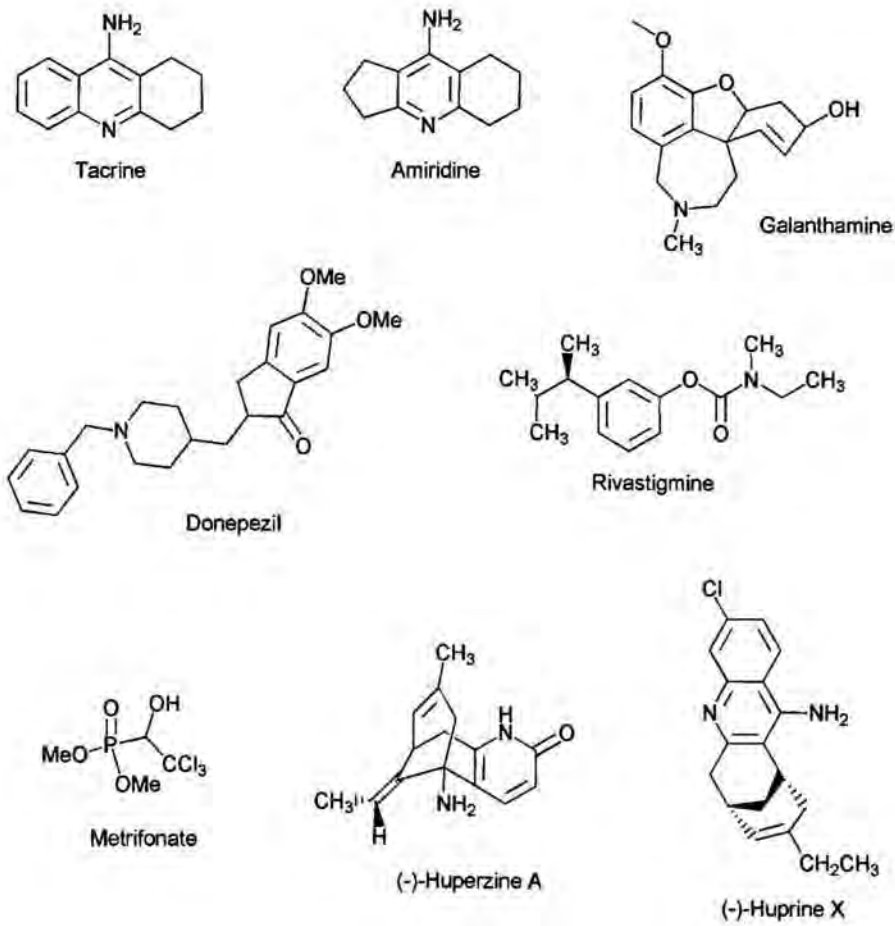

Figura 3.2. Representación esquemática de inhibidores de acetilcolinesterasa.

La relación entre AChE y el péptido βA señalada anteriormente propulsó una nueva vía de investigación basada en el diseño de inhibidores duales (Véase Figura 3.3). Esta nueva clase de compuestos presentan como característica clave la capacidad de inhibir de forma simultánea los dos centros activos de la AChE, evitando así tanto la hidrólisis de ACh como la agregación de βA.

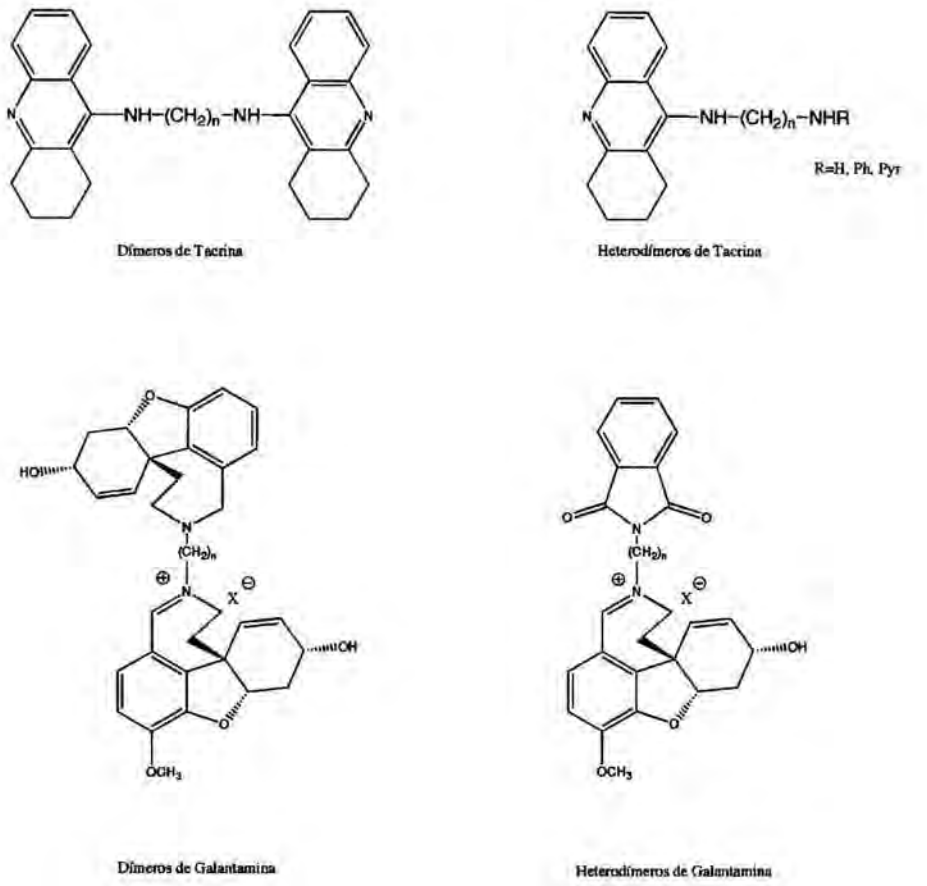

Figura 3.3. Representación esquemática de inhibidores duales de acetilcolinesterasa.

La primera serie de compuestos obtenidos siguiendo esta estrategia fueron derivados bis-tetrahidroaminoacridínicos[26]. En ellos, dos unidades de tacrina se unían mediante una cadena hidrocarbonada de longitud suficiente para acomodar los anillos aromáticos, uno en cada centro. El compuesto más potente contenía una cadena formada por 7 unidades metilénicas y era 149 veces más potente que tacrina. Siguiendo la misma línea,

se sintetizaron compuestos formados por un solo anillo de tacrina unido a una cadena que finalizaba con un aminoderivado (–NHR siendo R=H, Ph, Pyr), que sirvieron para determinar la importancia de la hidrofobicidad en la formación de interacciones π-catión en el centro periférico[26]. También se obtuvieron compuestos potentes derivados de la galantamina[27-29] con buenos resultados en los ensayos de afinidad.

En el diseño de nuevos inhibidores duales de AChE se debe tener en cuenta la capacidad del compuesto para formar interacciones π-catión o π-π con el Trp279, por ser éste el residuo clave del centro periférico. En el caso de donepezilo, su forma le proporciona la capacidad de interaccionar con ambos centros aunque la interacción con el segundo es débil, pues existe un ligero recubrimiento entre el anillo de indol de Trp279 y la unidad indanona de donepezilo. Aprovechando esta capacidad, distintos derivados que contenían como motivo común la N-benzilpiperidina de donepezilo fueron analizados por técnicas de modelado molecular, obteniéndose en todos los casos interacciones favorables con el Trp279 del centro periférico. Ejemplo de estos compuestos son los compuestos híbridos huperzina-A-E2020[30], 1,2,4-thidiazolidinona[31], aminoácidos[32], o derivados de benzazepina[33].

3.3 Derivados de tacrina y donepezilo

Tacrina y donepezilo tienen estructuras completamente distintas que les confieren modos de unión igualmente diferentes (ver Figura 3.4). La tacrina, formada por un anillo de acridina unida a un grupo amino, se une al centro catalítico de AChE quedando confinada entre dos residuos aromáticos, el Trp84 y la Phe330, con los que interacciona por apilamiento π-π. Asimismo, interacciona por puente de hidrógeno con el carbonilo del esqueleto peptídico de la His440 y por dos puentes de hidrógeno mediados por agua con el Asp72 y el carbonilo del Trp84. Por su lado, donepezilo es un derivado de N-benzilpiperidina a la que se le ha adicionado un grupo 5,6-dimetoxi-1-indanona. Por su disposición en el centro activo interacciona por apilamiento π-π con el Trp84, mediante una interacción catión-π con Phe330 y forma dos puentes de hidrógeno mediados por agua, uno con el hidroxilo de Tyr121 y otro con el nitrógeno del grupo amida de Phe288. La particularidad del donepezilo respecto a la tacrina es que tal disposición sitúa el anillo de indanona parcialmente encima del anillo de indol de

Trp279, posibilitando por lo tanto su efecto sobre la agregación del βA. Por tanto, la síntesis de compuestos mixtos tacrina-donepezilo proporciona un camino directo para obtener moléculas potentes capaces de inhibir los dos centros en AChE, incrementando así las posibilidades del tratamiento de la enfermedad. Esta posibilidad es la que se ha explorado preferencialmente a lo largo de la presente tesis.

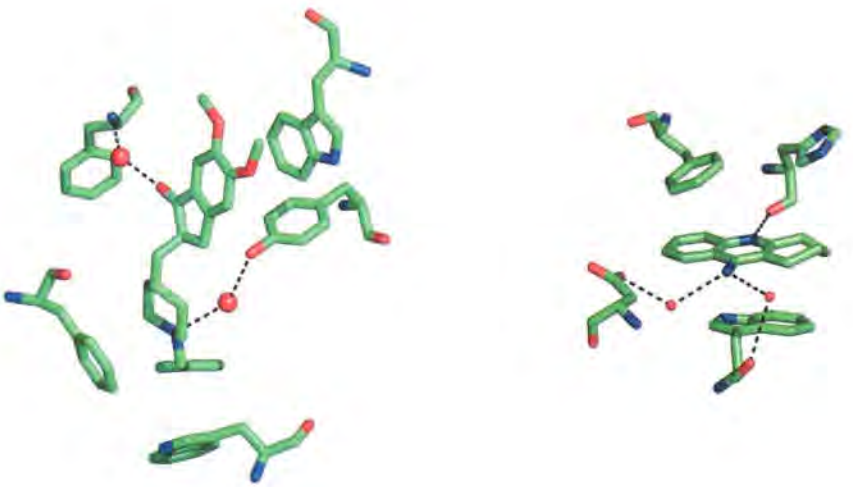

Figura 3.4 Posición ocupada por los inhibidores donepezilo (izquierda) y tacrina (derecha) en el centro activo de AChE. No se muestran los hidrógenos y las moléculas de agua presentes en la estructura cristalográfica se representan como esferas localizadas sobre el átomo de oxígeno. Las interacciones clave por puente de hidrógeno se indican por líneas entrecortadas.

Objetivos

En el marco planteado por esta estrategia, se elaboraron tres conjuntos distintos de moléculas como prototipos de inhibidores duales. Todos ellos tienen como motivo común el anillo de tacrina (o cloro-tacrina), mientras que difieren en la unidad química destinada a interaccionar con el centro periférico. En particular, los inhibidores considerados corresponden a derivados tacrina-ftalimida, tacrina-indol, y tacrina-donepezilo.

Resultados

3.4 Compuestos Tacrina-ftalimida

La estructura química explorada en el caso de los derivados tacrina-ftalimida se muestra en la Figura 3.5. De la serie de 22 compuestos obtenidos por unión de los anillos de tacrina y ftalamida, dos (ver Tabla 3.1) muestran una actividad superior al resto, siendo 8 y 70 veces más potentes que donepezilo o tacrina respectivamente. Los dos contienen un anillo de ftalamida en el extremo que presumiblemente se sitúa en el centro periférico, pero en un caso **(compuesto A)** el otro extremo contiene un anillo de tetrahidroacridina que se une al de ftalamida por una cadena hidrocarbonada con un grupo amida y un grupo metilamonio, mientras que en el otro **(compuesto B)** la unión entre los dos anillos está mediada por una cadena alifática. En el compuesto A (12 en la tabla 3.1 y la figura 3.5) la cadena tiene una longitud de 10 átomos, mientras que en el compuesto B (22 12 en la tabla 3.1 y la figura 3.5) su longitud es de nueve átomos.

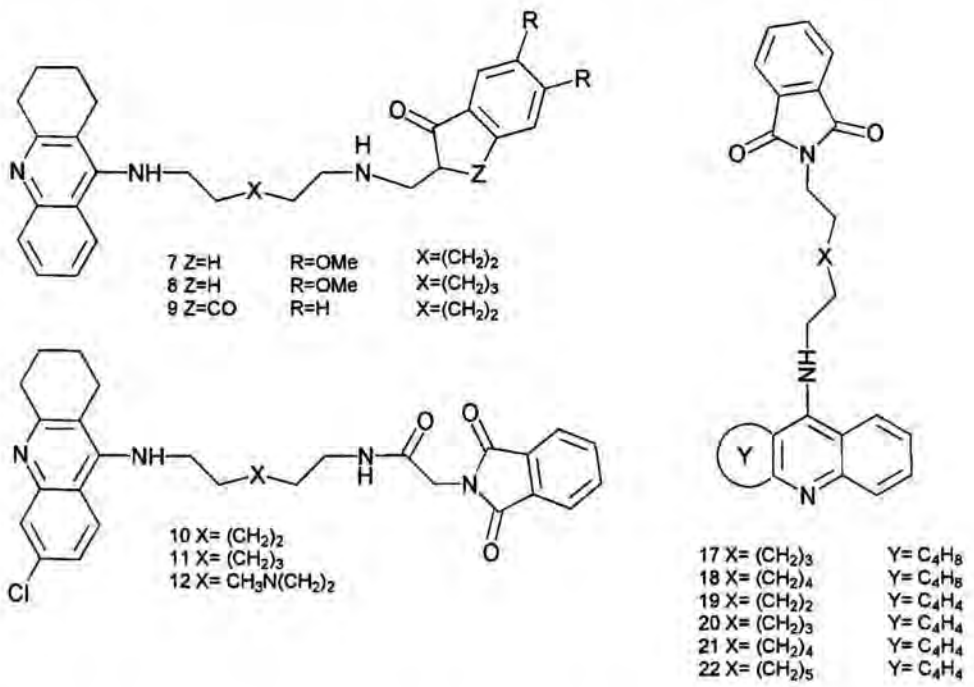

Figura 3.5. Representación esquemática de los derivados tacrina-ftalimida. El compuesto **A** corresponde al compuesto **12** y el compuesto **B** se corresponde con el compuesto **22**.

Comp.	IC50 AChE (nM)	IC50 BChE (nM)	Selectividad (AChE/BChE)	Competencia Propidium (lM)
7	100	50	2	>1000
8	25	0.6	41.6	>1000
9	504	98	5.1	>1000
10	10	220	0.04	10
11	20	660	0.03	100
12 (A)	2.8	75	0.04	10
17	3009	10	300	10
18	93	29	3.2	>1000
19	870	7.8	111.5	10
20	1550	711	2.2	100
21	1140	1010	1.1	>1000
22 (B)	2.4	90	0.02	1
Tacrine	167	24	6.9	1000
Donepezil	19	930	0.02	1

Tabla 3.1. Actividad inhibitoria de los inhibidores mixtos tacrina-ftalimida.

Las diferencias estructurales de los dos compuestos no tienen un efecto significativo en cuanto a su actividad como inhibidores de AChE. El compuesto A presenta una IC_{50}=2.8 nM, que en el caso del compuesto B pasa a ser 2.4 nM. Ello puede explicarse por el hecho de que en ambos compuestos el anillo de acridina/tetrahidroacridina se posiciona entre los residuos Trp84 y Tyr330, el mismo centro de unión que tacrina, manteniéndose a distancias promedio de 3.6 (A) y 4.0 (B) Å del Trp84, y de 4.3 (A) y 4.9 (B) Å de la Tyr330 (Figura 3.6). El nitrógeno aromático del anillo de acridina/tetrahidroacridina forma un puente de hidrógeno con el oxígeno del grupo carbonilo de la His440 (distancia promedio de 3.0 Å en A), que en el compuesto B se transforma en un puente mediado por agua durante el último nanosegundo de la dinámica (distancia promedio de 4.6 Å). La presencia del átomo de cloro en el anillo de tetrahidroacridina del compuesto A le disminuye la movilidad al quedar atrapado en un el bolsillo hidrofóbico formado por los residuos Trp432, Met436 y Ile439, aumentando la estabilidad del puente de hidrógeno entre al nitrógeno aromático del anillo y la His440.

La diferencia principal entre los dos compuestos está en la cadena que une los anillos terminales. En A, la presencia del grupo metilamino cargado positivamente provoca un cambio conformacional en la cadena lateral del Asp72 para formar un

puente salino (distancia promedio N···O de 3.0 Å) y reorienta la cadena a través del canal respecto al compuesto B que no puede formar este tipo de interacción (Figura 3.6). De todos modos, la ganancia de esta interacción en A se ve descompensada por la desolvatación que debe tener lugar para establecerse, pues cálculos en sistemas modelo con el método continuo MST indican que la energía de desolvatación ~90 kcal/mol más desfavorable en A que en B. Por otro lado, la presencia del grupo amido en la cadena de A no da lugar a la aparición de ninguna interacción extra con la proteína. Ello, pues, ofrece una explicación cualitativa acerca de la poca diferencia de actividad entre ambos compuestos a pesar de las diferencias estructurales que presentan en la cadena.

Finalmente, en ambos casos el anillo de ftalamida queda situado sobre el Trp279 con la posibilidad de formar una interacción π-π por apilamiento y los carbonilos del anillo forman un puente de hidrógeno con el grupo amino de la Phe288 y un puente de hidrógeno mediado por agua con el grupo amino de la Gln74 (Figura 3.6). La posición ocupada por este anillo explica la alta competitividad respecto a propidium que muestran ambos compuestos (10 μM A y 1 μM B).

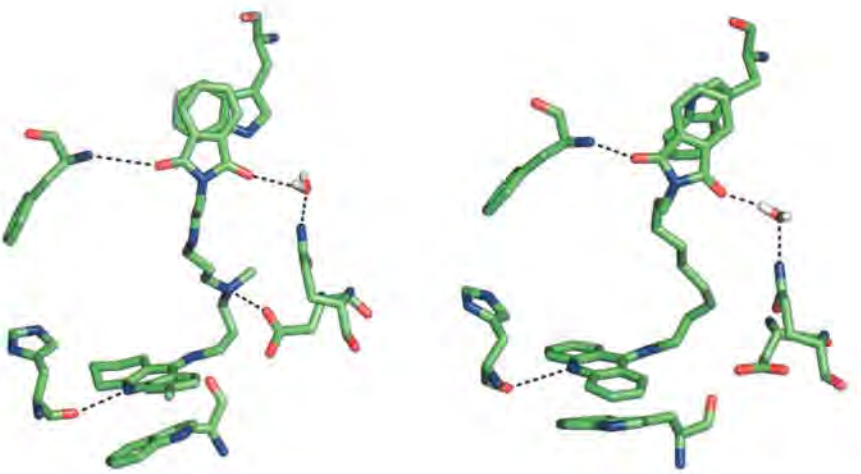

Figura 3.6. Modelos propuestos para la unión de los compuestos A y B al enzima acetilcolinesterasa.

3.5 Compuestos Tacrina-Indol

En este nuevo conjunto de compuestos se escogió como grupo periférico un anillo de indol unido al anillo de clorotacrina mediante una cadena carbonada que en la parte central contenía un grupo amida (Figura 3.7) En total se determinó experimentalmente la actividad en acetilcolinesterasa, selectividad respecto a butirilcolinesterasa y inhibición de la agregación del Aβ para 27 compuestos. El compuesto C (5) fue el que mostró mayor actividad inhibitoria con una IC_{50}=0.02 nM, más de 1 orden de magnitud por debajo del resto (Tabla 3.2). Esto motivó que se estudiara su forma de unión a AChE mediante dinámica molecular para esclarecer los puntos clave de interacción que se establecían entre ambos.

compuesto	R1	R2	R3	X	Y	Z	IC50(AChE) (nM)	IC50(BChE) (nM)	Selectividad AChE/BChE
tacrina							167 (119-233)	24 (12-45)	6.9
3	H	H	H	(CH2)5	(CH2)2	CH	70 (54-95)	1 (0.8-1.5)	70
4	Cl	H	H	(CH2)5	(CH2)2	CH	4 (3-6)	16 (8-31)	0.25
5	Cl	H	H	(CH2)6	(CH2)2	CH	0.02 (0.01-0.03)	2.9 (1.1-7.5)	0.007
6	Cl	H	H	(CH2)7	(CH2)2	CH	0.06 (0.04-0.10)	0.1 (0.06-0.13)	0.6
7	Cl	H	H	(CH2)8	(CH2)2	CH	0.5 (0.3-1.0)	5.7 (3.7-8.7)	0.09
8	Cl	H	H	(CH2)9	(CH2)2	CH	4.4 (2.7-6.8)	9.6 (3-25)	0.4
9	Cl	H	H	(CH2)10	(CH2)2	CH	21.9 (16-29)	54 (30-97)	0.4
10	H	H	H	(CH2)3NMe(CH2)3	(CH2)2	CH	147 (100-202)	0.03 (0.01-0.06)	4900
11	Cl	H	H	(CH2)3NMe(CH2)3	(CH2)2	CH	2.9 (2.2-3.8)	21.4 (12-37)	0.13
12	Cl	CN	H	(CH2)6	(CH2)2	CH	0.7 (0.3-1.4)	11.7 (5-23)	0.06
13	Cl	H	H	(CH2)6	(CHdCH)	CH	18 (12-26)	77 (50-120)	0.2
14	Cl	H	H	(CH2)5		CH	180 (95-350)	9.5 (7-12)	18.9
15	Cl	H	H	(CH2)6		CH	33 (20-53)	1.7 (0.9-3)	19
16	Cl	H	H	(CH2)7		CH	36 (18-70)	19 (12-28)	1.9
17	Cl	H	H	(CH2)8		CH	46 (23-83)	22.4 (13-37)	2.1
18	Cl	H	H	(CH2)7	CH2	CH	0.2 (0.11-0.29)	11.7 (6.4-21)	0.02
19	Cl	Br	H	(CH2)7	CH2	CH	0.6 (0.4-1.0)	1.7 (1.0-2.7)	0.3
20	Cl	H	H	(CH2)5	(CH2)3	CH	0.3 (0.2-0.5)	3.2 (1.7-6.1)	0.09
21	Cl	H	H	(CH2)6	(CH2)3	CH	0.5 (0.2-0.9)	5.6 (3.5-8.8)	0.09
22	Cl	H	Me	(CH2)7		CH	10.9 (6.6-17)	206 (145-292)	0.05
23	Cl	H	H	(CH2)7		N	95 (53-170)	79 (63-97)	1.2
27	Cl	H	H	(CH2)5	(CH2)2O	CH	1.5 (1.0-2.3)	136 (87-212)	0.1
28	Cl	H	H	(CH2)6	(CH2)2O	CH	0.7 (0.4-1.0)	60 (41-86)	0.2
29	Cl	H	H	(CH2)7	(CH2)2O	CH	3.0 (2.0-4.4)	59 (43-81)	0.05

Tabla 3.2. Actividad inhibitoria de los inhibidores mixtos tacrina-indol.

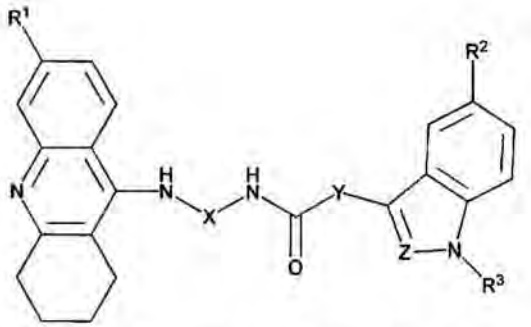

Figura 3.7. Representación esquemática de los derivados tacrina-indol.

Como en los casos anteriores el anillo de clorotacrina queda atrapado entre el Trp84 y la Tyr330 (distancias promedio de 3.52 y 3.56 Å respectivamente; Figura 3.8). El nitrógeno del anillo aromático forma un puente de hidrógeno con el carbonilo del esqueleto peptídico de la His440 (distancia promedio N···O de 2.84 Å) y el átomo de cloro queda confinado en el bolsillo hidrofóbico formado por los residuos Trp432, Met436 y Ile439.

La diferencia principal entre los compuestos estudiados es la posición del grupo amido en la cadena que une los dos anillos. En este caso, el grupo amido forma dos interacciones estables con la proteína, un puente de hidrógeno con el oxígeno del grupo hidroxilo de la Tyr330 a través del nitrógeno (distancia promedio de 3.01 Å) y un puente de hidrógeno entre el hidroxilo de la Tyr121 y el oxígeno carbonílico (distancia promedio de 2.75 Å). Cuando se alarga o se acorta la cadena, dicho conjunto de interacciones queda impedido y en consecuencia se produce la pérdida de afinidad.

Por lo que respecta al centro periférico, los anillos indol del compuesto y del triptófano quedan parcialmente apilados, a diferencia del anillo de ftalimida del caso anterior que quedaba prácticamente paralelo en conjunto. El nitrógeno del anillo forma un puente de hidrógeno mediado por agua con el hidroxilo de la Tyr70, que lo sitúa a una distancia de 3.7 Å y 4.4 Å de los residuos Gly335 y Ile287 respecto al carbono que ocupa la posición 4 del indol. Por esta razón, en algunos compuestos de la serie la presencia de un sustituyente en esta posición, como bromo o ciano, disminuye la actividad notablemente.

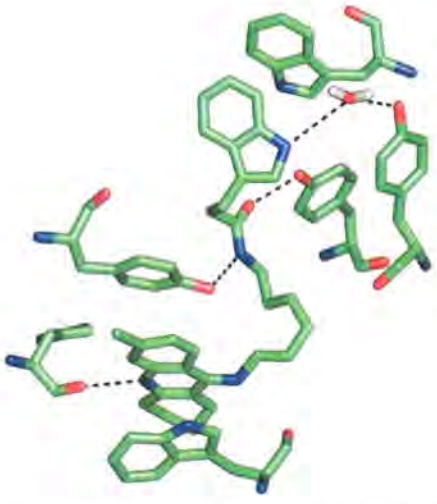

Figura 3.8. Modelo propuesto para la unión del compuesto C al enzima acetilcolinesterasa.

La posición ocupada por Trp279 es muy parecida a la que se encuentra en la estructura cristal del complejo de AChE con el compuesto *syn1*-TZ2PA6[34]. Este compuesto es un inhibidor dual de AChE formado por unión de tacrina y fenilfenantridio mediante un anillo de triazol. La posición del anillo de fenilfenantridio en el centro periférico provoca el cambio conformacional del anillo del triptófano, que rota 85 grados alrededor del enlace C_{α}-C_{β} y 50 grados alrededor del enlace C_{β}-C_{γ}. Debido a este cambio conformacional la cadena lateral del Trp279 queda expuesta al solvente por una de las caras del anillo y la entrada del canal pasa a ser el doble en cuanto a su tamaño[34]. Senapati *et. al.*[35] también estudiaron el mecanismo de unión de la forma *syn1* de TZ2PA6 mediante dinámica molecular a partir del complejo entre la forma *apo* de la enzima y el inhibidor. La estructura final obtenida de la simulación fue prácticamente idéntica a la estructura cristal en la zona de unión del ligando, observando el mismo cambio conformacional del Trp279 para acomodar el anillo de fenilfenantridio.

En el caso del compuesto aquí estudiado, el cambio conformacional del anillo de triptófano no es debido al tamaño del anillo de indol que se une al centro periférico, sino más bien a la presencia del grupo amida en la cadena que le une al anillo de tacrina. La formación de los puentes de hidrógeno entre la Tyr121 y el grupo amido, y de la Tyr70

con el nitrógeno del indol hace que las cadenas laterales de estos dos residuos queden desplazadas respecto a la estructura inicial provocando el movimiento del Trp279, que de esta manera pasa a adoptar una conformación parecida a la encontrada por Bourne *et. al.*[34]y Senapati *et. al.*[35]

3.6 Compuestos Tacrina-donepezilo

En la última serie de inhibidores duales la estrategia sintética a seguir fue la unión del anillo de tacrina/clorotacrina con la cola de donepezilo formada por los anillos de piperidina y indanona mediante una cadena hidrocarbonada con dos o tres unidades metilénicas (Figura 3.9). Se pretendía así aprovechar por un lado, como en los casos anteriores, la potencia de tacrina/clorotacrina para unirse al centro catalítico y por otro aumentar la capacidad de inhibición del centro periférico apreciada en donepezilo.

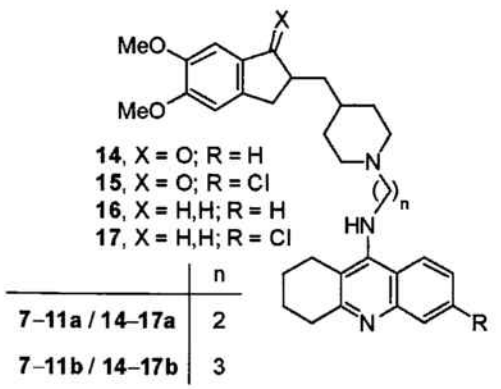

14, X = O; R = H
15, X = O; R = Cl
16, X = H,H; R = H
17, X = H,H; R = Cl

	n
7–11a / 14–17a	2
7–11b / 14–17b	3

Figura 3.9. Representación esquemática de los derivados tacrina-donepezilo.

Los compuestos obtenidos más activos presentaron (ver Tabla 3.3) una IC_{50} de 0.67 nM para el compuesto D (15a) y 0.27 nM para el compuesto E (15b). Ambos compuestos presentan como única diferencia la longitud de la cadena que une las dos subunidades, que se traduce en una mayor potencia del compuesto con dos eslavones (D) en la reducción de la fluorescencia de tioflavina (reducción de 79.4% y 57.0% para los compuestos D y E, respectivamente, lo cual indica una mayor capacidad de unión al centro periférico.

compuesto	IC50 AChE bovina (nM)	IC50 AChE humana (nM)	IC50 BChE humana (nM)
14a·2HCl	1.74 ± 0.02	4.04 ± 0.06	12.4 ± 0.6
14b·2HCl	0.29 ± 0.03	0.88 ± 0.04	12.4 ± 0.6
15a·2HCl	0.57 ± 0.05	0.67 ± 0.06	136 ± 9
15b·2HCl	0.09 ± 0.01	0.27 ± 0.03	66.3 ± 4.0
16a·2HCl	2.28 ± 0.06	5.13 ± 0.52	8.06 ± 0.32
16b·2HCl	0.82 ± 0.06	2.16 ± 0.21	7.25 ± 0.33
17a·2HCl	1.86 ± 0.07	2.60 ± 0.23	88.7 ± 0.2
17b·2HCl	0.82 ± 0.08	1.06 ± 0.05	72.7 ± 4.2
Tacrine·HCl	130 ± 10	205 ± 18	43.9 ± 17
6-Chlorotacrine·HCl	5.73 ± 0.44	8.32 ± 0.75	916 ± 19
Donepezil·HCl	8.12 ± 0.26	11.6 ± 1.6	7273 ± 621

Tabla 3.3. Actividad inhibitoria de los inhibidores mixtos tacrina-donepezilo.

Tanto el compuesto D como el compuesto E mantienen el grupo de interacciones clave del anillo de clorotacrina en el centro catalítico situándose el anillo entre el Trp84 y la Tyr330 (distancias promedio de 3.73 y 4.35 Å en I y de 3.63 y 4.44 Å en II; Figura 3.10). El nitrógeno aromático forma un puente de hidrógeno con el oxígeno del grupo carbonilo de la His440 manteniendo un distancia promedio N···O de 2.81 Å en I y 2.82 en II. Finalmente el átomo de cloro queda confinado en el bolsillo hidrofóbico en ambos casos.

La diferencia en la longitud de la cadena hidrocarbonada es lo que les confiere distintos modos de unión en el canal y la zona periférica (Figura 3.10). En el compuesto I el nitrógeno protonado del anillo de piperidina queda apuntando hacia el oxígeno del grupo hidroxilo de la Tyr330 formando un puente de hidrógeno cuya distancia promedio es de 3.20 Å. La carga positiva del nitrógeno queda compensada por la carga negativa del grupo carboxilato del Asp72 que se mantiene a una distancia promedio de 4.74 Å. La inclusión de un metileno más en la cadena del compuesto E hace que el anillo de piperidina gire, quedando en este caso el nitrógeno apuntando hacia el residuo Asp72 y formando una interacción por puente de hidrógeno (distancia promedio N···O de 2.73 Å) reforzada por la interacción carga-carga con el anión carboxilato. Estas diferencias se traducen a su vez en un reordenamiento de los residuos Asp72, Tyr70 y Tyr330 de la proteína, que establecen interacciones nuevas con otros residuos. El Asp72, que en la estructura que contiene el compuesto D se encuentra formando un puente de hidrógeno con la Tyr70, pasa a formar un nuevo puente de hidrógeno con el N-H de la Leu74, mientras que la Tyr330, que formaba un puente de hidrógeno con el

nitrógeno de la piperidina, se encuentra en formando un puente de hidrógeno con la Tyr120.

La segunda diferencia clave entre los dos compuestos se da en el centro periférico, donde el anillo de indanona de cada uno ocupa posiciones distintas. En el compuesto D el anillo se mantiene sobre el Trp279 formando una interacción por apilamiento π-π con una orientación prácticamente equivalente a la del anillo de indanona en donepezilo. A su vez, el oxígeno del grupo carbonilo forma puentes de hidrógeno mediados por agua con el esqueleto peptídico de los residuos Phe288 y Arg289. La orientación del anillo en el compuesto E cambia durante el primer nanosegundo de dinámica pasando de estar apilado sobre el Trp279 a quedar perpendicular a éste al final de la simulación, provocando un cambio conformacional en el triptófano, que queda girado alrededor del enlace Cα–Cβ respecto a la estructura cristal de donepezilo (código PDB:1EVE). Este cambio está motivado por las distintas interacciones que se establecen en los dos compuestos a través del canal debido a la distinta longitud de la cadena en cada uno.

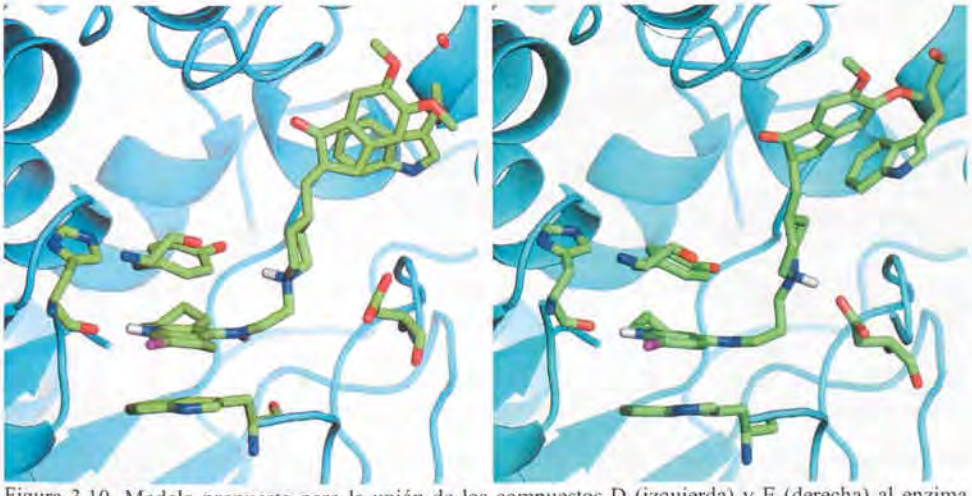

Figura 3.10. Modelo propuesto para la unión de los compuestos D (izquierda) y E (derecha) al enzima acetilcolinesterasa.

3.7 Análisis de los resultados

Los distintos compuestos evaluados presentan como motivo común un anillo de tacrina (o 6-clorotacrina), que en todos los casos se encuentra unido al centro catalítico de la AChE. La unión de dicha unidad al centro catalítico es muy parecida en todos los casos, con pequeñas variaciones en las distancias de puente de hidrógeno características de la formación del complejo AChE-Tacrina (véase Tabla 3.4). La distancia promedio de puente de hidrógeno entre la His440 y el nitrógeno acridínico es de aproximadamente 2.8 Å en todos los casos excepto en el compuesto B, en donde dicho puente de hidrógeno queda reemplazado por un puente mediado por agua al final de la dinámica. La diferencia entre este compuesto y el resto estriba en la falta del átomo de cloro unido al anillo de acridina. La presencia del cloro ayuda a posicionar la tacrina en el centro catalítico al quedar atrapado en el bolsillo hidrofóbico formado por los residuos Trp432, Met436 y Ile439, como puede comprobarse si se comparan las actividades de tacrina (IC_{50}=33.5 nM) y 6-clorotacrina (IC_{50}=1.8 nM).

	Compuesto					
	A	B	C	D	E	tacrina
d(His440-acridina)	3.0	4.6	2.8	2.8	2.8	3.24
d(Trp84-acridina)	3.6	4.0	3.52	3.73	3.63	3.5
d(Tyr330-acridina)	4.3	4.9	3.55	4.35	4.44	3.4

Tabla 3.4. Parámetros geométricos de la interacción de la unidad de tacrina en el centro catalítico.

Las diferencias encontradas en la unión al centro periférico son consecuencia en su mayor parte de las distintas formas de unir los anillos en cada compuesto (Tabla 3.5). La prueba más evidente de ello son las diferentes conformaciones adoptadas por el Trp279 y el anillo de indanona en los compuestos D y E o por el Trp279 en los compuestos A y B. La flexibilidad conformacional del Trp279 también ha sido descrita en la unión de otros inhibidores duales.[34-37] Concretamente, en las estructuras cristalográficas de los complejos syn-TZ2PA6-AChE[36] y tacrine-thiotacrine-AChE[37], la posición que ocupa el anillo de indol del Trp279 es completamente distinta, además de

ser en ambos casos diferente a la posición ocupada en la mayoría de estructuras que contienen inhibidores duales o del centro periférico (ver figura 3.11).

	Compuesto				
	A	B	C	D	E
d(Trp279-anillo)	3.9	3.8	4.7	4.1	5.3
% Apilamiento	99	91	28	100	7

Tabla 3.5. Parámetros geométricos de la interacción del anillo heteroaromático en el centro periférico.

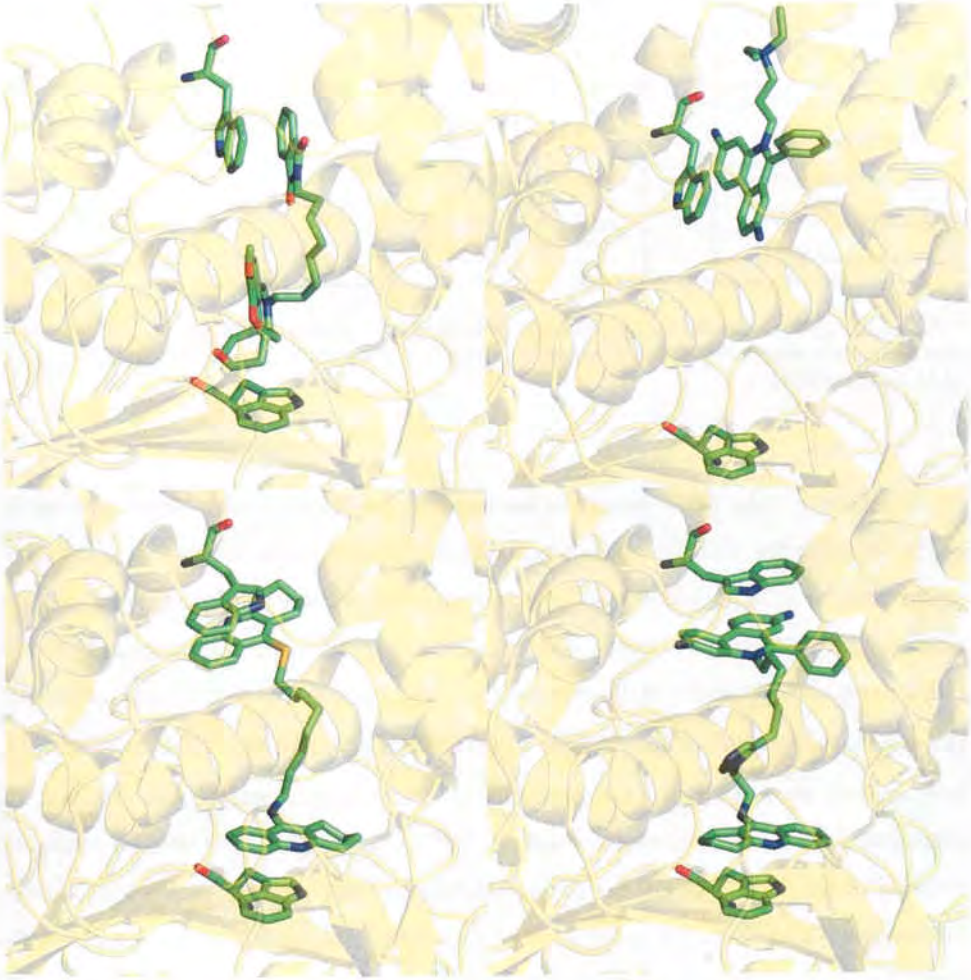

Figura 3.11 Posición ocupada por el Trp279 en distintos complejos lignado-AChE. De izquierda a derecha y de arriba abajo: galanthamine-indole-AChE, propidium-AChE, tacrine-thiotacrine-AChE, y syn-TZ2PA6-AChE.

Cabe pensar que la modificación estructural del centro periférico, y en particular de la accesibilidad del residuo Trp279, está relacionada con la inhibición de la agregación de βA inducida por AChE. En la tabla 3.6 se muestran los resultados obtenidos para los 5 compuestos comparados con los de tres inhibidores conocidos (tacrina, propidium y donepezilo). Es de destacar que los todos compuestos son capaces de actuar sobre el centro periférico y presentan una actividad comparable o incluso superior a la del inhibidor dual donepezilo.

	Compuesto							
	A	B	C	D	E	Propidium	Donepezilo	Tacrina
Competición con propidium (μM)	10	1	-	-	-	-	1	1000
% de inhibición en la agregación de βA inducida por AChE	-	-	98	38	46	82	22	7

Tabla 3.6 Resultados obtenidos para la inhibición de la agregación de βA en presencia de AChE. Medidas directas para los compuestos C, D y E, y indirectas para A y B a partir de la competencia en la unión a AChE con propiduim.

Finalmente, cabe hacer notar que los cambios conformacionales observados en la unión del inhibidor al centro periférico están relacionados por la formación de distintas interacciones a lo largo del canal, cuya plasticidad permite el desplazamiento de algunos residuos para acomodar el ligando a lo largo del centro activo. Dicha plasticidad queda reflejada en el modo de unión del compuesto C, que posee la mayor actividad inhibidora (IC_{50}=0.02 nM) y efecto anti-agregante de βA (98%). Su unión con AChE, mediada por interacciones de puente de hidrógeno con el grupo amida, está relacionada con el desplazamiento coordinado de los residuos Tyr70, Tyr121 y Trp279. Por otro lado, la longitud de la cadena que une las dos subunidades influye también en la formación de interacciones a lo largo del canal y en el posicionamento de los anillos en el centro periférico. Así, en los compuestos D y E, la presencia de un grupo metilénico más en la cadena modifica de forma sustancial las interacciones que se forman con la Tyr330 y el Asp72, y a su vez la posición ocupada por el Trp279 y el anillo de indanona.

En conjunto, los 5 compuestos se presentan como buenos inhibidores duales de la proteína AChE y ponen de manifiesto la plasticidad del centro activo para acomodar ligandos con características muy diferentes. En particular, la posibilidad de formar interacciones con los residuos que conforman la garganta hace que ésta sea un factor más a tener en cuenta en el futuro diseño de inhibidores duales de AChE.

Referencias bibliográficas

1 Boyd, B. *Drug News Perspect.*, **2000**, 13, 425-439.

2 Launer, L. J., Frantiglioni, L., Andersen, K., Breteler, M. M. B., Copeland, R. J. M., Dartigues, J. F., Lobo, A., Martínez-Lage, J., Soininen, H., Hofman, A. In *Alzheimer's Disease and Related Disorders: Etiology, Pathogenesis and Therapeutics.* Iqbal, K., Swaab, D. F., Winblad, B., Wisniewsky, H. M., Eds. Wiley: New York, **1999**, 9-15.

3 Kurz, A. *J. Neural. Transm.*, Suppl. **1998**, 54, 295-299.

4 Sugimoto, H. *Chem. Rec.*, **2001**, 1, 63-73.

5 Jann, M. W. *Pharmaco-therapy*, **2000**, 20, 1-12.

6 Zarotsky, V.; Sramek, J. J.; Cutler, N. R. *Am. J. Health-Syst. Pharm.*, **2003**, 60, 446-452.

7 Haas, C., Selkoe, D. J. *Nature*, **1998**, 391, 339-340.

8 Álvarez, A., Opazo, C., Alarcon, R., Garrido, J., Inestrosa, N. C. *J. Mol. Biol.*, **1997**, 272, 348-361.

9 Muñoz, F. J., Inestrosa, N. C., *FEBS Lett.*, **1999**, 450, 205-209.

10 Inestrosa, N. C.; Alarcón, R. *J. Physiol.* (Paris) **1998**, 92, 341-344.

11 Inestrosa, N. C.; Alvarez, A.; Calderon, F. *Mol. Psychiatry*, **1996**, 1, 359-361.

12 De Ferrari, G. V.; Canales, M. A.; Shin, I.; Weiner, L. M.; Silman, I.; Inestrosa, N. C. *Biochemistry*, **2001**, 40, 10447-10457.

13 Bartolini, M.; Bertucci, C.; Cavrini, V.; Andrisano, V. *Biochem. Pharmacol.*, **2003**, 65, 407-416.

14 Sussman, J. L., Harel, M., Frolow, F., Oefner, C., Goldman, A., Toker, L., Silman, I. *Science*, **1991**, 253, 872-879.

15 Millard, C. B., Koellener, G., Ordentlich, A., Shafferman, A., Silman, I., Sussman, J. L. *J. Am. Chem. Soc.*, **1999**, 121, 9883-9884.

16 Kryger, G., Harel, M., Giles, K., Toker, L., Velan, B., Lazar, A., Kronman, C., Barak, D., Ariel, N., Shafferman, A., Silman, I., Sussman, J. L., *Acta Cryst.*, **2000**, D56, 1385-1394.

17 Radic, Z., Gibney, G., Kawamoto, S., MacPhee-Quigley, K., Bongiorno, C., Taylor, P. *Biochemistry*, **1992**, 31, 9760-9767.

18 Wlodek, S. T., Antosiewicz, J., Briggs, J. M. *J. Am. Chem. Soc.*, **1997**, 119, 8159-8165.

19 Szegletes, T., Mallender, W. D., Thomas, P. J., Rosenberry, T. L. *Biochemistry*, **1999**, 38, 122-133.

20 Ripoll D. R., Faerman, C. H., Axelsen, P. H., Silman, I., Quinn, D. M. *J. Am. Chem. Soc.*, **1992**, 114, 3896-3900.

21 Tan, R. C., Truong, T. N., McCammon, J. A., Sussman, J. L., *Biochemistry*, **1993**, 32, 401-403.

22 Antosiewicz, J., McCammon, J. A., Gislon, M. K. *Biochemistry*, **1996**, 35, 7819-7833.

23 Antosiewicz, J., Briggs, J. M., Elcock, A. H., Gilson, M. K., McCammon, J. A., *J. Comput. Chem.*, **1996**, 17, 1633-1644.

24 Zhou, H. X., Briggs, J. M., McCammon, J. A., *J. Am. Chem. Soc.*, **1996**, 118, 13069-13070.

25 Xu, Y., Shen, J., Luo, X., Silman, I., Sussman, J. L., Chen, K., Jiang, H., *J. Am. Chem. Soc.*, **2003**, 125, 11340-11349.

26 Taylor, P., *Neurology*, **1998**, 51, S30-35.

27 Carlier, P.R., Chow, E.S., Han, Y., Liu, J., Yazal, J., Pang, Y.P., *J. Med. Chem.*, **1999**, 42, 4225-4231.

28 Mary, A., Renko, D.Z., Guillou, C., Thal, C., *Bioorg. Med. Chem.*, **1998**, 6, 1835-1850.

29 Guillou, C., Mary, A., Renko, D.Z., Gras, E., Thal, C., *Bioorg. Med. Chem. Lett.*, **2000**, 10, 637-639.

30 Zeng, F., Jiang, H., Zhai, Y., Zhang, H., Chen, K., Ji, R., *Bioorg. Med. Chem. Lett.*, **1999**, 9, 3279-3284.

31 Martinez, A., Fernandez, E., Castro, A., Conde, S., Rodriguez-Franco, M.I., Baños, J.E., Badia, A., *Eur. J. Med. Chem.*, **2000**, 35, 913-922.

32 Martinez, A., Lanot, C., Perez, C., Castro, A., Lopez- Serrano, P., Conde S., *Bioorg. Med. Chem.*, **2000**, 8, 731- 738.

33 Ishihara, Y., Hirai, K., Miyamoto, M., Goto, G., *J. Med. Chem.*, **1994**, 37, 2292-2299.

34 Bourne, Y., Radic, Z., Kolb, H. C., Sharpless, K. B., Taylor, P., Marchot, P., *Chem.-Biol. Interactions*, **2005**, 157-158, 159-165.

35 Senapati, S., Bui, J. M., McCammon, J. A., , *J. Med. Chem.*, **2005**, 48, 8155-8162.

36 Rosini, M., Andrisano, V., Bartolini, M., Bolognesi, M. L., Hrelia, P., Minarini, A., Tarozzi, A., Melchiorre, C., *J. Med. Chem.*, **2005**, 48, 360–363.

37 Colletier, J. Ph., Sanson, B., Nachon, F., Gabellieri, E., Fattorusso, C., Campiani, G., Weik, M., *J. Am. Chem. Soc.*, **2006**, 128, 4526-4527.

4.1.1 Donepezil-Tacrine hybrid related derivatives as new dual binding site inhibitors of AChE

Alonso, D., Dorronsoro, I., Rubio, L., Muñoz, P., García-Palomero, E., Del Monte, M., **Bidon-Chanal, A.**, Ororzco, M., Luque, F. J., Castro, A., Medina, M. and Martínez, A.

Biorg. Med. Chem., 13, **2005**, 6588-6597

Available online at www.sciencedirect.com
SCIENCE DIRECT®
Bioorganic & Medicinal Chemistry
ELSEVIER
Bioorganic & Medicinal Chemistry 13 (2005) 6588–6597

Donepezil–tacrine hybrid related derivatives as new dual binding site inhibitors of AChE

D. Alonso,[a] I. Dorronsoro,[a] L. Rubio,[a] P. Muñoz,[a] E. García-Palomero,[a] M. Del Monte,[a] A. Bidon-Chanal,[b] M. Orozco,[c] F. J. Luque,[b] A. Castro,[a] M. Medina[a] and A. Martínez[a,*]

[a]*Neuropharma, S.A., Avda. de La Industria 52, 28760 Tres Cantos (Madrid), Spain*
[b]*Departamento de Fisicoquímica, Facultad de Farmacia, Universidad de Barcelona, Avda. Diagonal 643, 08028 Barcelona, Spain*
[c]*Departamento de Bioquímica y Biología Molecular, Facultad de Química, Universidad de Barcelona, Martí i Franqués 1, 08028 Barcelona, Spain*

Received 18 March 2005; revised 18 April 2005; accepted 23 May 2005
Available online 17 October 2005

Abstract—A new series of donepezil–tacrine hybrid related derivatives have been synthesised as dual acetylcholinesterase inhibitors that could bind simultaneously to the peripheral and catalytic sites of the enzyme. These new hybrids combined a tacrine, 6-chlorotacrine or acridine unit as catalytic binding site and indanone (the heterocycle present in donepezil) or phthalimide moiety as peripheral binding site of the enzyme, connected through a different linker tether length. One of the synthesised compounds emerged as a potent and selective AChE inhibitor, which is able to displace propidium in a competition assay. These results seem to confirm the ability of this inhibitor to bind simultaneously to both sites of the enzyme and make it a promising lead for developing disease-modifying drugs for the future treatment of Alzheimer's disease. To gain insight into the molecular determinants that modulate the inhibitory activity of these compounds, a molecular modelling study was performed to explore their binding to the enzyme.

1. Introduction

Alzheimer's disease (AD) is the most common form of dementia accounting for about 50–60% of the overall cases of dementia among persons over 65 years of age.[1] It is a progressive, degenerative disorder of the brain characterised by loss of memory and cognition. Brain regions that are associated with higher mental functions, particularly the neocortex and hippocampus, are those most affected by the characteristic pathology of AD.[2] This includes the extracellular deposits of β-amyloid (derived from amyloid precursor protein, APP) in senile plaques,[3,4] intracellular formation of neurofibrillary tangles (containing an abnormally phosphorylated form of a microtubule associated protein, *tau*)[5,6] and the loss of neuronal synapsis and pyramidal neurons.[7] Nevertheless, current treatment approaches in this disease continue being primarily symptomatic, with the major therapeutic strategy based on the cholinergic hypothesis and specifically on acetylcholinesterase (AChE) inhibition.[8] Accordingly, during the last decade, several cholinergic drugs have been launched on the market, primarily AChE inhibitors indicated for the treatment of mild to moderate AD such as tacrine,[9] donepezil,[10] rivastigmine,[11] or galantamine.[12] More recently, memantine,[13] a moderate affinity NMDA-receptor antagonists, has been approved for the treatment of moderate to severe AD (Fig. 1).

The three-dimensional structure of AChE, as determined by X-ray crystallography, revealed that its active site can apparently be reached only through a deep and narrow 'catalytic gorge'.[14] Inhibitors directed to the active site prevent the binding of the substrate molecule (acetylcholine), or its hydrolysis, either by occupying the site with a high affinity molecule (tacrine)[15] or by reacting irreversibly with the catalytic serine (organophosphates and carbamates).[16] The peripheral site consists of a less well-defined area, located at the entrance of the catalytic gorge. Inhibitors that bind to that site include small molecules, such as propidium,[17,18] and peptide toxins such as fasciculin.[19] Parallel to the development of antidementia drugs, research efforts have been focused, among others, on the therapeutic potential of AChE inhibitors to slow the

Keywords: Acetylcholinesterase inhibitors; Tacrine; Donepezil; Alzheimer's disease.
* Corresponding author. Tel.: +34 91 8061130; fax: +34 91 8034660; e-mail: amartinez@neuropharma.es

0968-0896/$ - see front matter © 2005 Elsevier Ltd. All rights reserved.
doi:10.1016/j.bmc.2005.09.029

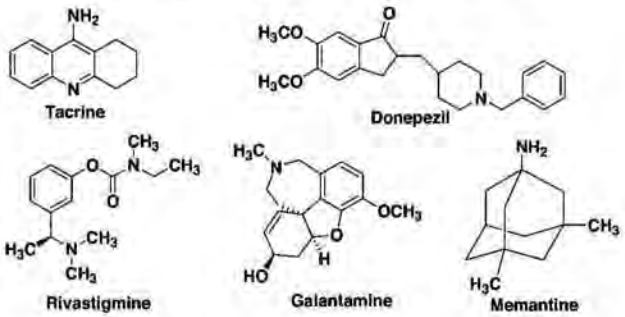

Figure 1. Commercial available drugs for AD treatment.

disorder progression. This fact was based on a range of evidences, which showed that AChE has secondary non-cholinergic functions.[20,21] On the basis of these evidences, it was postulated that AChE binds through its peripheral site to the β-amyloid non-amyloidogenic form acting as a pathological chaperone and inducing a conformational transition to the amyloidogenic conformation with the subsequent amyloid fibril formation.[22] In fact, AChE directly promotes in vitro the assembly of β-amyloid peptide into amyloid fibrils forming stable AChE–β-amyloid complexes.[23] Considering the non-cholinergic aspects of the cholinergic enzyme AChE, their relationship to Alzheimer's hallmarks and the role of the peripheral site of AChE in all these functions, an attractive target for the design of new antidementia drugs emerged.[24] Recent experimental results[25–28] following this approach lead to the synthesis of several chemically diverse structures with potent AChE inhibition and interesting biological profile (Fig. 2). These data corroborate the initial dual site AChE hypothesis[29] and provided a new way to delay the neurodegenerative process.

Continuing our research on catalytic and peripheral binding site inhibitors, that include *N*-benzylpiperidine derivatives of 1,2,4-thiadiazolidinone[30] and tacrine thiadiazolidinone compounds,[31] we present here the synthesis, biological activity and propidium competition assay of novel dual binding site AChE inhibitors. These new dimeric compounds contain the tacrine heterocycle ring, which is recognised as a catalytic AChE inhibitor and indanone or related heterocycles as responsible for the binding to the peripheral site of the enzyme. These new family of inhibitors could be considered as donepezil–tacrine hybrid related derivatives. To study further the biological profile of these compounds, their butyrylcholinesterase (BChE) inhibitory activity was also evaluated. Finally, to explore the ability to bind the peripheral site of AChE, assays were also performed to explore the capacity to displace propidium binding.

2. Results and discussion

2.1. Chemistry

The synthesis of compounds **7–12** was achieved following a convergent pathway strategy summarized in (Scheme 1). Reaction of tetrahydroacridines **1** or **2** with diaminoalkyl derivatives at reflux afforded the intermediates 9-alkylaminotetrahydroacridines **3a–e** in good yields (60–70%), following a procedure previously known.[32] Compounds **7** and **8** can be prepared through a Mannich-type reaction by treatment of commercially available indanone **4** with paraformaldehyde, and amines **3a** and **3b**. The same reaction using the indadione **5** afforded compound **9** in moderate yield. Coupling reaction of the

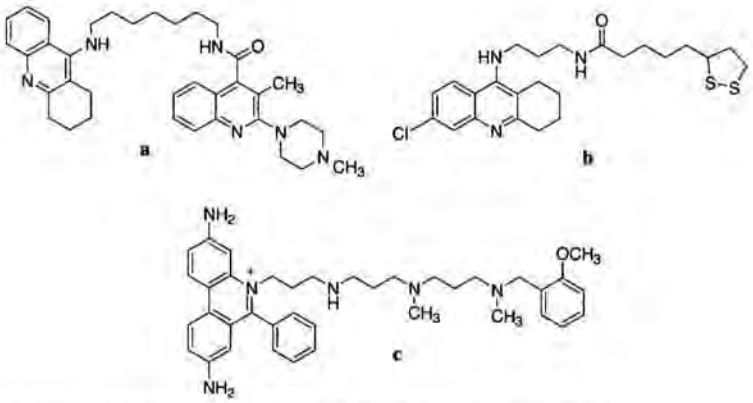

Figure 2. Representative dual binding site hybrid AChE inhibitors. **a**, Ref. 26; **b**, Ref. 27 and **c**, Ref. 28.

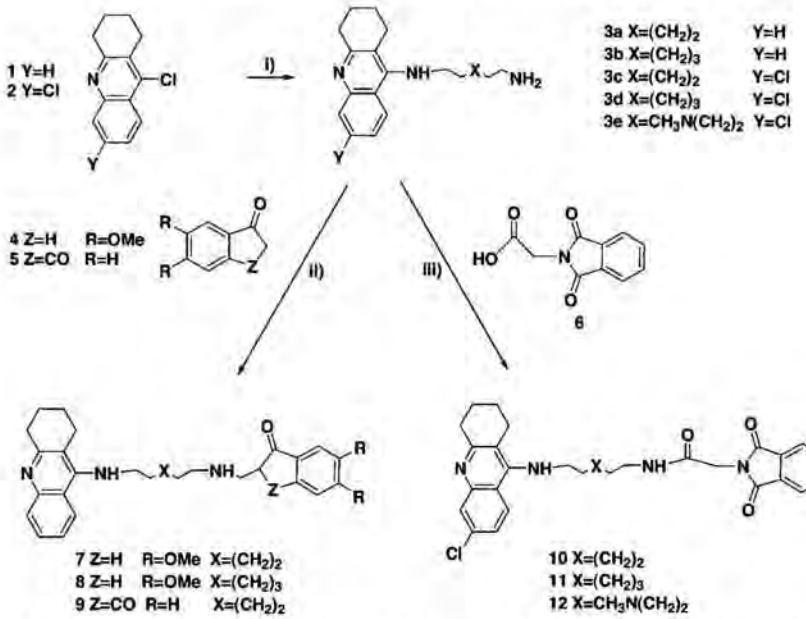

Scheme 1. Convergent pathway leading to the synthesis of compounds **7–12**. Reagents and conditions: (i) $NH_2(CH_2)_2X(CH_2)_2NH_2$, pentanol, Δ; (ii) HCOH, EtOH/H_2O, HCl, Δ; (iii) CDI, THF, rt.

intermediates **3a–e** with *N*-phthalimide acetic acid **6** in the presence of carbonyldiimidazole (CDI) afforded compounds **10–12** in good yields (Scheme 1). These derivatives **9–12** lack any quiral centre in their chemical structures, which is a great advantage for further pharmaceutical development regarding hybrids **7–8**.

The alkylation of phthalimide with different dibromoalkyl derivatives **13a–d** led to intermediates **15a–d**. Subsequent alkylation of **15a–d** with 9-aminoacridine and 9-aminotetrahydroacridine afforded compounds **17–22** in good yields (Scheme 2).

Unequivocal assignment of ^1H and ^{13}C chemical shifts was performed for two representative compounds (**12** and **22**), using bidimensional experiments following HMQC and HMBC sequences. Data are collected in Table 1.

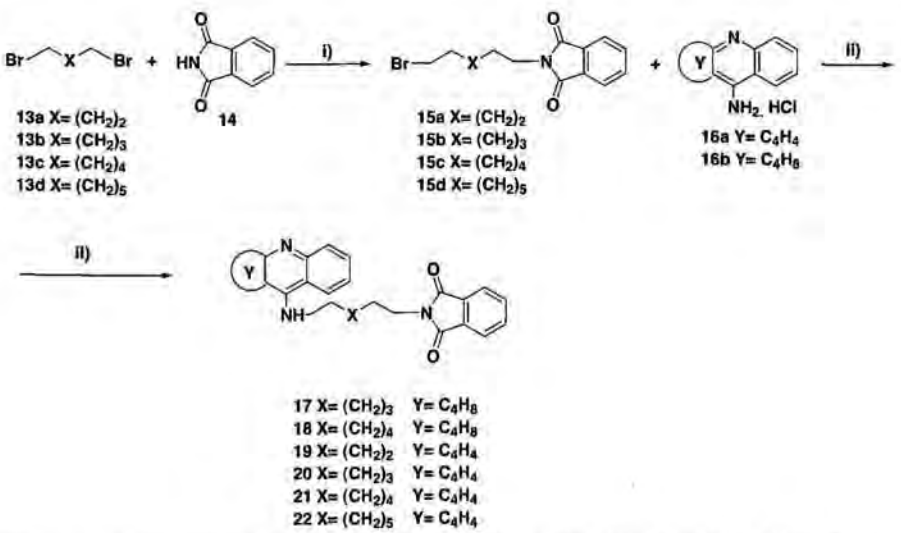

Scheme 2. Synthetic route leading to compounds **17–22**. Reagents and conditions: (i) NaH, DMF, rt; (ii) KOH, DMSO, Δ.

Table 1. Chemical shifts of **12** and **22**

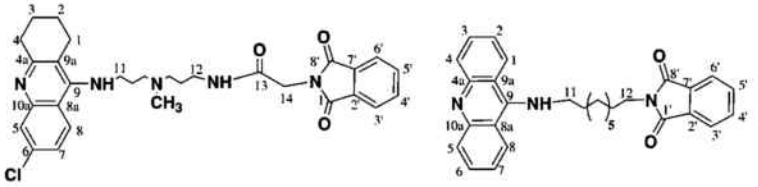

Atom number	Compound **12**		Compound **22**	
	^{1}H (δ ppm) $CDCl_3$, 400 MHz	^{13}C (δ ppm) $CDCl_3$, 100 MHz	^{1}H (δ ppm) $CDCl_3$, 400 MHz	^{13}C (δ ppm) $CDCl_3$, 100 MHz
1	2.58	32.3	8.02	122.5
2	1.80	22.0	7.33	121.3
3	1.80	22.5	7.62	132.7
4	2.90	38.8	8.06	133.6
4a	—	157.3	—	155.4
5	7.90	124.8	8.06	133.6
6	—	135.1	7.62	132.7
7	7.93	124.6	7.33	121.3
8	7.16	124.4	8.02	122.5
8a	—	114.3	—	113.0
9	—	151.8	—	155.4
9a	—	117.0	—	113.0
10a	—	145.4	—	155.4
11	3.22	48.8	3.82	37.6
12	3.48	56.1	3.65	48.6
13	—	167.4	—	—
14	4.21	56.2	—	—
1′	-	166.0	—	168.3
2′		131.6	—	132.0
3′	7.82	123.2	7.80	124.2
4′	7.68	134.0	7.68	134.2
5′	7.68	134.0	7.68	134.2
6′	7.82	123.2	7.80	123.5
7′	—	131.6	—	132.0
8′	—	166.0	—	168.3
N-CH_3	2.12	42.3	—	—

2.2. Biological activity and molecular modelling

To evaluate the biological profiles of these heterodimeric compounds for AD, AChE (bovine erythrocytes) and BChE (human plasma) inhibition was assayed in comparison with tacrine and donepezil as reference compounds. The inhibitory potency against AChE and BChE was evaluated by the method of Ellman et al.[33] Compounds **12** and **22** (see Table 2) exhibit an optimum AChE inhibitory activity, as noted in the fact that they are 8-fold and 70-fold more potent than donepezil and tacrine, respectively. Moreover, compounds **12** and **22** showed more than 20-fold selectivity in AChE versus BChE assays (see Table 2). The proper tether length for the linker between the two anchoring groups, 9-aminoacridine and indanone/phthalimide, seemed to be nine (compound **22**) or 10 (compound **12**).

To gain insight into the molecular determinants that modulate the inhibitory activity of these compounds, a molecular modelling study was performed to explore their binding to the enzyme. The position of compounds **12** and **22** with respect to the key residues in the binding site is shown in Figure 3. The tetrahydroacridine/acridine moiety is firmly bound to the catalytic site of AChE, it being stacked against the aromatic rings of Trp84 (average distance between rings of 3.6 and 4.0 Å for compounds **12** and **22**, respectively) and Tyr330 (average distances of 4.3 and 4.9 Å). The aromatic nitrogen of tetrahydroacridine/acridine is hydrogen-bonded to the main-chain carbonyl oxygen of His440 (average N···O distance: 3.0 Å) in **12**. For compound **22** such an interaction was replaced along the simulation by a water-mediated contact (average N···O distance of 4.6 Å along the last ns). Finally, the chlorine atom in **12** occupies a small hydrophobic pocket formed by Trp432, Met436 and Ile439, a feature that has been identified in both modelled[34] and experimental[35] structures of the AChE–huprine Y complex.

With regard to the linker, the most relevant difference between compounds **12** and **22** comes from the presence of the tertiary amine group in the former. Thus, this group forces the tether to reorient along the gorge to form a coulombic interaction with the carboxylate group of Asp72 (average N···O distance: 3.0 Å). Noteworthy, a relevant difference was found in the orientation of the side chain of Asp72 in the AChE complexes with **12** and **22** (see Fig. 3). Finally, the amido

Table 2. Biological activity of donepezil–tacrine hybrids: inhibitory activity on AChE (bovine erythrocyte) and BChE (human serum) and propidium competition assay results

Compound	IC_{50} AChE (nM)	IC_{50} BChE (nM)	Selectivity (AChE/BChE)	Propidium competition (μM)
7	100	50	2	>1000
8	25	0.6	41.6	>1000
9	504	98	5.1	>1000
10	10	220	0.04	10
11	20	660	0.03	100
12	2.8	75	0.04	10
17	3009	10	300	10
18	93	29	3.2	>1000
19	870	7.8	111.5	10
20	1550	711	2.2	100
21	1140	1010	1.1	>1000
22	2.4	90	0.02	1
Tacrine	167	24	6.9	1000
Donepezil	19	930	0.02	1

Each assay was repeated, at least, three independent times.

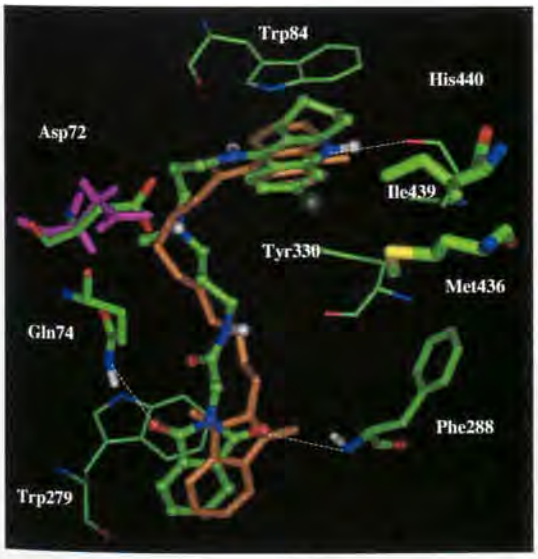

Figure 3. Representation of compounds **12** and **22** docked into the binding site of AChE highlighting the protein residues that form the main interactions with the different structural units of the inhibitor. Compound **22** is shown in orange. For the sake of clarity the enzyme residues in the AChE complex with **22** are not shown, but the side chain of Asp72 is shown in magenta. The dotted (white) lines denote hydrogen-bond contacts between the ligand and enzyme residues.

group of compound **12**, which is buried inside the protein gorge, does not, however, make favourable contact with suitable residues of the enzyme.

Finally, the phthalimide ring occupies a similar position in heterodimers **12** and **22** at the peripheral site and remains stacked onto the aromatic ring of Trp279. Moreover, the carbonyl groups of the phthalimide ring form a direct hydrogen-bond contact with the backbone NH group of Phe288 (average O···N distance of 3.1 Å) and a water-mediated interaction with the amide unit of Gln74 (average O···N distance of 4.2 Å).

The preceding findings suggest that the similar AChE inhibitory activity of compounds **12** and **22** (see Table 2) stems not from the existence of a common pattern of interactions, but from a subtle balance of different forces. Compared to the tetrahydroacridine derivative, the larger delocalization of the positive charge in the acridine ring should weaken the stabilizing cation–π interaction at the catalytic site of the enzyme. Binding of compound **12** at the catalytic site should also be favoured by the presence of the chlorine atom, since it is well known that attachment of a chlorine atom at position 6 of tacrine and related compounds leads to largely enhancing the binding affinity.[36] The favourable electrostatic interaction between the tertiary amine in **12** with the side chain of Asp72 should a priori also contribute to the binding of compound **12**. However, this effect must be largely counterbalanced by the desolvation of the protonated amine. In fact, the desolvation cost for compound **12** is estimated to be around 90 kcal/mol larger than for compound **22** according to AM1 semiempirical calculations (determined for the ligand in the bonded conformation) performed with the MST continuum model.[37] Moreover, the formation of the salt bridge between the tertiary amine and Asp72 likely induces steric strain into the linker, thus explaining the need to include an additional methylene group into the tether compared to compound **22**. At this point, it is worth noting that increasing the length of the tether from nine to 10 methylene units decreases the inhibitory potency, as noted in the results determined for compounds **10** and **11** (see Table 2). Finally, the lack of favourable interactions between the amido group in **12** and the enzyme residues should also contribute to decrease the inhibitory potency compared to **22**.

A propidium competition assay was performed to confirm the interaction of the compounds at the peripheral binding site of AChE, since it is known that propidium is a selective ligand for the peripheral site of the enzyme. Moreover, this is an indirect method to predict the potential effect of the inhibitors on β-amyloid aggregation.[38] The fact that the more potent inhibitors **12** and **22** were able to displace propidium in the competition

assay, showing IC_{50} values of 10 and 1 μM, respectively is relevant. The finding that both compounds possess the phthalimide moiety suggests that this chemical unit acts as an efficient ligand for the peripheral site of the enzyme. As it was found for the AChE inhibition, the best binding to the peripheral site of AChE was found for a tether length between the two anchoring groups (9-aminoacridine and phthalimide) of nine units.

In conclusion, the interesting dual binding site AChE profile of compound **22** makes this inhibitor a promising lead for developing disease-modifying drugs for the future treatment of AD.

3. Experimental

3.1. Chemistry

Reagents and solvents were purchased from common commercial suppliers and were used without further purification. Chromatographic separations were performed on silica gel, using either flash chromatography (CC, using Kieselgel 60 Merck of 230–400 mesh) or preparative centrifugal thin layer chromatography (CTLC, on a circular plate coated with a 1 mm layer of Kieselgel 60 PF_{254} gipshaltig, Merck, using a Chromatotron®). Compounds were detected with UV light (254 nm), iodine chamber, or ninhydrin.

Nuclear magnetic resonance spectra were recorded in $CDCl_3$ solutions, using Varian Unity-500, Varian Mercury 400 MHz or Varian 300 MHz spectrometers. Typical spectral parameters for ^1H NMR were: spectral width 10 ppm, pulse width 9 μs (57°) and data size 32 K. The acquisition parameters in decoupled ^{13}C NMR spectra were: spectral width 16 kHz, acquisition time 0.99 s, pulse width 9 μs (57°) and data size 32 K. Chemical shifts are reported in δ values (ppm) relative to internal Me_4Si and J values are reported in hertz. Other experiments, such as heteronuclear single-quantum coherence (HSQC) and heteronuclear multiple bond correlation (HMBC), were obtained in standard conditions. Mass spectra (MS) were obtained by electronic impact (EI) at 70 eV in a Hewlett-Packard 5973 spectrometer (with direct insertion probe) or by electrospray (ES) in a Waters ZQ2000 spectrometer.

3.1.1. General method for the synthesis of compounds 7–9. To a stirred solution of diamine in a mixture of ethanol/water (3:1), the paraformaldehyde and indanone were added at room temperature. Afterwards the pH was adjusted to 3 with 35% hydrochloric acid and the mixture was refluxed for 24 h. Then, the reaction mixture was cooled to 25 °C and the solvent was removed under vacuum pressure. The resulting residue was treated with K_2CO_3 saturated solution and extracted with methylene chloride. The combined organic extracts were washed with water and dried with anhydrous Na_2SO_4. The solvent was removed under vacuum and the residue was purified by preparative centrifugal thin layer chromatography.

3.1.1.1. 5,6-Dimethoxy-2-{[6-(1,2,3,4-tetrahydro-acridin-9-ylamino)-hexylamino]-methyl}-indan-1-one (7). *Reagents.* (1,2,3,4-Tetrahydro-acridin-9-yl)-hexane-1,6-diamine (96 mg, 0.32 mmol), ethanol/water 3:1 (3.5 ml), paraformaldehyde (19.2 mg, 0.64 mmol) and indanone (62 mg, 0.32 mmol).

Purification. Silica gel column chromatography using AcOEt/MeOH (10:1)–(3:1) and 0.1% NH_3 saturated. Yellow syrup, yield: 5 mg (1%). ^1H NMR ($CDCl_3$, 300 MHz, δ ppm): 7.99 (d, 2H, $J = 7.0$ Hz), 7.57 (t, 1H, $J = 7$ Hz), 7.54 (t, 1H, $J = 7$ Hz), 7.12 (s, 1H), 6.85 (s, 1H), 3.94 (s, 3H), 3.87 (s, 3H), 3.54 (t, 2H, $J = 7.0$), 3.19 (dd, 1H, $J = 6.83$ Hz, $J = 16.90$ Hz), 3.05 (m, 2H), 2.92 (m, 1H), 2.87 (m, 2H), 2.83 (dd, 1H, $J = 3.40$ Hz, $J = 17.10$ Hz), 2.66 (m, 2H), 2.59 (m, 2H), 1.84 (m, 4H), 1.79 (m, 2H), 1.39 (m, 2H), 1.36 (m, 4H). ^{13}C NMR ($CDCl_3$, 75 MHz, δ ppm): 200.8, 155.30, 151.20, 149.20, 149.04, 129.10, 128.79, 128.30, 123.90, 123.00, 120.10, 119.00, 107.00, 107.38, 105.36, 104.18, 56.25, 56.08, 51.27, 49.73, 49.36, 47.29, 31.64, 31.31, 29.72, 26.98, 26.78, 24.61, 22.89, 22.52. ESI-MS $[M+H^+]^+$ 502.

3.1.1.2. 5,6-Dimethoxy-2-{[7-(1,2,3,4-tetrahydro-acridin-9-ylamino)-heptylamino]-methyl}-indan-1-one (8). *Reagents.* (1,2,3,4-Tetrahydro-acridin-9-yl)-hexane-1,7-diamine (134 mg, 0.43 mmol), ethanol/water 3:1 (3.5 ml), paraformaldehyde (26 mg, 0.86 mmol) and indanone (83 mg, 0.43 mmol).

Purification. Silica gel column chromatography using AcOEt/MeOH (10:1)–(3:1) and 0.1% NH_3 saturated. Yellow syrup, yield: 7 mg (6.8%). ^1H NMR ($CDCl_3$, 500 MHz, δ ppm): 7.96 (dd, 1H, $J = 6.80$, $J = 1.06$ Hz), 7.94 (dd, 1H, $J = 6.81$, $J = 1.08$ Hz), 7.55 (dt, 1H, $J = 6.82$, $J = 1.07$ Hz), 7.36 (dt, 1H, $J = 6.82$, $J = 1.07$ Hz), 7.14 (s, 1H), 6.86 (s, 1H), 3.95 (s, 3H), 3.89 (s, 3H), 3.50 (t, 2H, $J = 7.25$ Hz), 3.23 (dd, 1H, $J = 6.61$, $J = 16.85$ Hz), 3.08 (m, 2H), 2.89 (t, 2H, $J = 5.97$ Hz), 2.92 (m, 1H), 2.88 (m, 2H), 2.81 (dd, 1H, $J = 3.20$, $J = 17.06$ Hz), 2.69 (m, 2H), 1.91 (m, 4H), 1.67 (m, 2H), 1.48 (m, 2H), 1.33 (m, 4H). ^{13}C NMR ($CDCl_3$, 125 MHz, δ ppm): 200.0, 155.86, 151.35, 149.69, 149.64, 129.60, 128.79, 128.42, 123.92, 123.18, 120.11, 119.06, 107.63, 107.44, 105.36, 104.43, 56.49, 56.328, 51.534, 50.114, 49.70, 47.60, 33.85, 31.92, 31.57, 30.01, 29.47, 27.13, 27.08, 24.92, 23.20, 22.80. ESI-MS $[M+H^+]^+$ 516.

3.1.1.3. 2-[6-(1,2,3,4-Tetrahydro-acridin-9-ylamino)-hexylamino]-indan-1,3-dione (9). *Reagents.* (1,2,3,4-Tetrahydro-acridin-9-yl)-hexane-1,6-diamine oxalate (339 mg, 0.87 mmol), ethanol/water 3:1 (3.5 ml), paraformaldehyde (26.4 mg, 0.88 mmol) and indan-1,3-dione (129 mg, 0.88 mmol).

Purification. Silica gel column chromatography using AcOEt/MeOH (10:1)–(3:1) and 0.1% NH_3 saturated. Yellow syrup, yield: 17 mg (4.4%). ^1H NMR ($CDCl_3$, 400 MHz, δ ppm): 7.92 (m, 4H), 7.84 (dd, 2H, $J = 6$, $J = 2.8$ Hz), 7.54 (m, 1H), 7.32 (m, 1H), 3.70 (t, 2H, $J = 6.4$), 3.60 (m, 1H), 3.50 (t, 2H, $J = 6.4$ Hz), 3.08 (m, 2H), 2.65 (m, 2H), 31.8–2.0 (m, 4H), 1.80 (m, 2H), 1.70 (m, 2H), 1.45 (m, 4H). ^{13}C NMR ($CDCl_3$, 100 MHz, δ

ppm): 200.0, 159.0, 151.3, 147.1, 140.6, 136.8, 136.1, 130.5, 129.9, 123.6, 123.0, 120.8, 120.4, 53.1, 52.9, 49.3, 48.9, 31.4, 29.8, 26.7, 26.4, 24.7, 22.6, 22.0. ESI-MS $[M+H^+]^+$ 457.

3.1.2. General method for the synthesis of compounds 10–12. Compounds **10–12** have been synthesized following the procedure previously reported in bibliography.[39] 1,1′-Carbonyldiimidazole was added to a solution of isoindol in THF anhydrous was added under N_2, and the mixture was stirred for 4 h at room temperature. Then the amine was added and the resulting amber solution was stirred for 20 h. The solvent was evaporated under reduced pressure, water was added and the resulted mixture was extracted with dichloromethane. The combined organic extracts were washed with saturated aqueous NaCl solution and then were dried with anhydrous Na_2SO_4. The solvent was evaporated under reduced pressure and the residue was purified by silica gel column chromatography using as eluent mixtures of solvents in the proportions indicated for each case.

3.1.2.1. *N*-[6-(6-Chloro-1,2,3,4-tetrahydro-acridin-9-ylamino)-hexyl]-2-(1,3-dioxo-1,3-dihydroisoindol-2-yl)acetamide (10). *Reagents.* Isoindole acid (160.0 mg, 0.78 mmol), THF anhydrous (10 ml), 1,1′-carbonyldiimidazole (126.47 mg, 0.78 mmol) and 6-chloro-9-(6-aminohexylamino)-1,2,3,4-tetrahydroacridine (260 mg, 0.78 mmol).

Purification. Silica gel column chromatography using DCM/MeOH (30:1) and 0.5% NH_3 saturated. Yellow solid, yield: 150 mg (37%). ^1H NMR ($CDCl_3$, 400 MHz, δ ppm): 7.93 (d, 1H, $J = 8.9$ Hz), 7.90 (d, 1H, $J = 1.9$ Hz), 7.82 (dd, 2H, $J = 5.0$ Hz, $J = 2.7$ Hz), 7.68 (dd, 2H, $J = 5.0$ Hz, $J = 2.7$ Hz), 7.16 (dd, 1H, $J = 8.9$ Hz, $J = 1.9$ Hz), 6.64 (m, 1H), 4.30 (s, 2H), 4.21 (m, 1H) 3.50 (m, 2H), 3.30 (c, 2H, $J = 7$ Hz), 3.05 (m, 2H), 2.65 (m, 2H), 1.80 (m, 4H), 1.68 (q, 2H, $J = 7$ Hz), 1.55 (q, 2H, $J = 7$ Hz), 1.40 (m, 4H). ^{13}C NMR ($CDCl_3$, 100 MHz, δ ppm): 167.59, 166.08, 157.63, 151.56, 146.02, 134.88, 134.03, 131.73, 125.44, 124.83, 124.35, 123.32, 117.31, 114.62, 48.90, 40.81, 39.43, 32.80, 31.42, 29.39, 26.23, 24.52, 22.78, 22.28. ESI-MS $[M+H^+]^+$ 519.

3.1.2.2. *N*-[7-(6-Chloro-1,2,3,4-tetrahydro-acridin-9-ylamino)-heptyl]-2-(1,3-dioxo-1,3-dihydroisoindol-2-yl)acetamide (11). *Reagents.* Isoindole acid (100 mg, 0.48 mmol), THF anhydrous (10 ml), 1,1′-carbonyldiimidazole (83.0 mg, 0.51 mmol) and 6-chloro-9-(7-aminoheptylamino)-1,2,3,4-tetrahydroacridine (165.5 mg, 0.48 mmol).

Purification. Silica gel column chromatography using DCM/MeOH (30:1) and 0.1% NH_3 saturated. Yellow solid, yield: 80 mg (30.8%). ^1H NMR ($CDCl_3$, 400 MHz, δ ppm): 7.93 (d, 1H, $J = 8.9$ Hz), 7.90 (d, 1H, $J = 1.9$ Hz), 7.82 (dd, 2H, $J = 5.0$ Hz, $J = 2.7$ Hz), 7.68 (dd, 2H, $J = 5.0$ Hz, $J = 2.7$ Hz), 7.16 (dd, 1H, $J = 8.9$ Hz, $J = 1.9$ Hz), 6.64 (m, 1H), 4.30 (s, 2H), 4.21 (m, 1H) 3.48 (m, 2H), 3.26 (c, 2H, $J = 7$ Hz), 2.90 (m, 2H), 2.65 (m, 2H), 1.80 (m, 4H), 1.68 (q, 2H, $J = 7$ Hz), 1.50 (q, 2H, $J = 7$ Hz), 1.30 (m, 6H). ^{13}C NMR ($CDCl_3$, 100 MHz, δ ppm): 167.75, 166.30, 157.24, 152.04, 145.46, 135.11, 134.03, 131.69, 124.86, 124.62, 124.41, 123.27, 117.00, 114.36, 40.50, 39.62, 32.184, 31.27, 29.12, 28.66, 26.56, 26.42, 24.305, 22.56, 22.04. ESI-MS $[M+H^+]^+$ 533.

3.1.2.3. *N*-(3-{[3-(6-Chloro-1,2,3,4-tetrahydro-acridin-9-ylamino)-propyl]-methyl-amino}-propyl)-2-(1,3-dioxo-1,3-dihydroisoindol-2-yl)acetamide (12). *Reagents.* Isoindole acid (71.1 mg, 0.34 mmol), THF anhydrous (10 ml), 1,1′-carbonyldiimidazole (55.1 mg, 0.34 mmol) and N^1-[3-(6-chloro-1,2,3,4-tetrahydro-acridin-9-ylamino)-propyl]-N^1-methyl-propane-1,3-diamine (200 mg, 0.34 mmol).

Purification. Silica gel column chromatography using DCM/MeOH (30:1) and 0.1% NH_3 saturated. Yellow solid, yield: 60 mg (31.5%). ^1H NMR ($CDCl_3$, 400 MHz, δ ppm): 7.93 (d, 1H, $J = 8.9$ Hz), 7.90 (d, 1H, $J = 1.9$ Hz), 7.82 (dd, 2H, $J = 5.0$ Hz, $J = 2.7$ Hz), 7.68 (dd, 2H, $J = 5.0$ Hz, $J = 2.7$ Hz), 7.16 (dd, 1H, $J = 8.9$ Hz, $J = 1.9$ Hz), 6.04 (m, 1H), 4.21 (s, 2H), 4.12 (m, 1H) 3.48 (m, 2H), 3.22 (c, 2H, $J = 7$ Hz), 2.90 (m, 2H), 2.58 (m, 2H), 2.35 (t, 4H, $J = 7$ Hz), 2.10 (s, 3H), 1.80 (m, 4H), 1.71 (q, 2H, $J = 7$ Hz), 1.60 (q, 2H, $J = 7$ Hz). ^{13}C NMR ($CDCl_3$, 100 MHz, δ ppm): 167.55, 166.02, 157.37, 151.85, 133.99, 131.77, 124.95, 124.16, 123.19, 117,01, 114.41, 56.29, 56.13, 48.88, 42.34, 40.89, 38.89, 32.37, 27.79, 26.15, 24.68, 22.71, 22.15. ESI-MS $[M+H^+]^+$ 548.

3.1.3. General method for the synthesis of compounds 17–22. The bromophthalimide derivates **15a–d** were synthesised following the procedure previously reported in bibliography.[40] 9-Amino-1,2,3,4-tetrahydroacridine was added to a solution of KOH in DMSO under N_2, and the mixture was stirred for 4 h at room temperature. Then the brominated derivative was added and the resulting orange solution was stirred for 12 h at room temperature. The DMSO was eliminated by washing with water and extracted with ethyl acetate. The combined organic extracts were washed with saturated aqueous NaCl solution and dried with anhydrous Na_2SO_4. The solvent was evaporated under reduced pressure and the residue was purified by silica gel column chromatography using as eluent mixtures of solvents in the proportions indicated for each case.

3.1.3.1. 2-[7-(1,2,3,4-Tetrahydro-acridin-9-ylamino)-heptyl]-isoindole-1,3-dione (17). *Reagents.* 9-Amino-1,2,3,4-tetrahydroacridine (100 mg, 0.42 mmol), DMSO (5 ml), KOH (47 mg, 0.8 mmol) and 2-(7-bromo-heptyl)-isoindole-1,3-dione (278 mg, 0.8 mmol).

Purification. Silica gel column chromatography using DCM/MeOH (10:1) and 0.5% NH_3 saturated. Yellow syrup, yield: 17 mg (5%). ^1H NMR ($CDCl_3$, 400 MHz, δ ppm): 8.41 (br s, 1H), 8.12 (d, 1H, $J = 8.6$ Hz), 7.82 (dd, 2H, $J = 5.0$ Hz, $J = 2.7$ Hz), 7.68 (dd, 3H, $J = 5.0$ Hz, $J = 2.7$ Hz), 7.43 (t, 1H, $J = 8.6$ Hz), 3.83 (br s, 2H), 3.65 (t, 2H, $J = 7$ Hz), 3.25 (br s, 2H), 2.61 (t, 2H, $J = 5.8$ Hz), 1.97–1.92 (m, 4H), 1.84–1.80 (m, 2H), 1.78–1.72 (m, 2H), 1.47–1.43 (m, 6H). ^{13}C NMR ($CDCl_3$, 100 MHz, δ ppm): 168.5, 166.5, 154.0, 133.8, 132.5, 132.0, 131.2, 128.9, 125.3, 124.1, 123.3, 119.3,

54.6, 49.1, 38.5, 29.7, 29.2, 28.4, 28.2, 26.5, 25.2, 23.4, 22.9, 22.5, 22.1, 21.1, 14.4. ESI-MS $[M+H^+]^+$ 443.

3.1.3.2. 2-[8-(1,2,3,4-Tetrahydro-acridin-9-ylamino)-octyl]-isoindole-1,3-dione (18). *Reagents.* 9-Amino-1,2,3,4-tetrahydroacridine (100 mg, 0.42 mmol), DMSO (5 ml), KOH (47 mg, 0.8 mmol) and 2-(8-bromo-octyl)-isoindole-1,3-dione (240 mg, 0.8 mmol).

Purification. Silica gel column chromatography using DCM/MeOH (10:1) and 0.5% NH_3 saturated. Yellow syrup, yield: 30 mg (15%). ^1H NMR ($CDCl_3$, 400 MHz, δ ppm): 8.43 (br s, 1H), 8.12 (d, 1H, $J = 8.6$ Hz), 7.82 (dd, 2H, $J = 5.0$ Hz, $J = 2.7$ Hz), 7.68 (dd, 3H, $J = 5.0$ Hz, $J = 2.7$ Hz), 7.43 (t, 1H, $J = 8.6$ Hz), 3.83 (br s, 2H), 3.65 (t, 2H, $J = 7$ Hz), 3.25 (br s, 2H), 2.61 (t, 2H, $J = 5.8$ Hz), 1.97–1.92 (m, 4H), 1.84–1.80 (m, 2H), 1.78–1.72 (m, 2H), 1.47–1.43 (m, 8H). ^{13}C NMR ($CDCl_3$, 100 MHz, δ ppm): 168.6, 166.2, 154.2, 134.1, 132.6, 132.3, 131.0, 129.0, 125.4, 124.0, 123.3, 119.3, 54.5, 49.0, 38.0, 29.8, 29.2, 28.9, 28.6, 26.7, 25.0, 23.6, 23.0, 22.8, 22.1, 21.0, 14.2. ESI-MS $[M+H^+]^+$ 455.

3.1.3.3. 2-[6-(Acridin-9-ylamino)-hexyl]-isoindole-1,3-dione (19). *Reagents.* 9-Amino-acridine (100 mg, 0.42 mmol), DMSO (5 ml), KOH (47 mg, 0.8 mmol) and 2-(6-bromo-hexyl)-isoindole-1,3-dione (240 mg, 0.8 mmol).

Purification. Silica gel column chromatography using DCM/MeOH (10:1) and 0.5% NH_3 saturated. Yellow syrup, yield: 30 mg (15%). ^1H NMR ($CDCl_3$, 400 MHz, δ ppm): 8.08 (d, 2H, $J = 8.6$ Hz), 8.02 (d, 2H, $J = 8.6$ Hz), 7.81 (dd, 2H, $J = 5.4$ Hz, $J = 3.1$ Hz), 7.68 (dd, 3H, $J = 5.4$ Hz, $J = 3.1$ Hz), 7.59 (t, 2H, $J = 6.6$ Hz), 7.30 (t, 2H, $J = 6.6$ Hz) 3.85 (t, 2H, $J = 7$ Hz), 3.67 (t, 2H, $J = 7$ Hz), 1.83 (q, 2H, $J = 7$ Hz), 1.67 (q, 2H, $J = 7$ Hz), 1.45–1.34 (m, 6H). ^{13}C NMR ($CDCl_3$, 100 MHz, δ ppm): 168.2, 156.3, 133.8, 133.6, 131.9, 128.7, 128.5, 124.7, 123.0, 122.8, 119.3, 111.9, 48.4, 37.68, 29.81, 26.37, 22.81. ESI-MS $[M+H^+]^+$ 424.

3.1.3.4. 2-[7-(Acridin-9-ylamino)-heptyl]-isoindole-1,3-dione (20). *Reagents.* 9-Amino-acridine (60 mg, 0.24 mmol), DMSO (5 ml), KOH (27 mg, 0.48 mmol) and 2-(7-bromo-heptyl)-isoindole-1,3-dione (80 mg, 0.24 mmol).

Purification. Silica gel column chromatography using DCM/MeOH (10:1) and 0.1% NH_3 saturated. Yellow syrup, yield: 80 mg (74%). ^1H NMR ($CDCl_3$, 400 MHz, δ ppm): 8.08 (d, 2H, $J = 8.6$ Hz), 8.02 (d, 2H, $J = 8.6$ Hz), 7.81 (dd, 2H, $J = 5.4$ Hz, $J = 3.1$ Hz), 7.68 (dd, 3H, $J = 5.4$ Hz, $J = 3.1$ Hz), 7.59 (t, 2H, $J = 6.6$ Hz), 7.30 (t, 2H, $J = 6.6$ Hz), 3.85 (t, 2H, $J = 7$ Hz), 3.67 (t, 2H, $J = 7$ Hz), 1.83 (q, 2H, $J = 7$ Hz), 1.67 (q, 2H, $J = 7$ Hz), 1.45–1.34 (m, 6H). ^{13}C NMR ($CDCl_3$, 100 MHz, δ ppm): 168.3, 155.3, 133.8, 133.7, 132.7, 132.0, 124.5, 123.0, 122.9, 121.7, 113.2, 49.0, 37.7, 30.4, 28.6, 28.3, 26.6, 26.5. ESI-MS $[M+H^+]^+$ 438.

3.1.3.5. 2-[8-(Acridin-9-ylamino)-octyl]-isoindole-1,3-dione (21). *Reagents.* 9-Amino-acridine (60 mg, 0.24 mmol), DMSO (5 ml), KOH (27 mg, 0.48 mmol) and 2-(7-bromo-heptyl)-isoindole-1,3-dione (68.64 mg, 0.24 mmol).

Purification. Silica gel column chromatography using DCM/MeOH (10:1) and 0.1% NH_3 saturated. Yellow syrup, yield: 20 mg (18.5%). ^1H NMR ($CDCl_3$, 400 MHz, δ ppm): 8.06 (d, 2H, $J = 8.6$ Hz), 8.02 (d, 2H, $J = 8.6$ Hz), 7.80 (dd, 2H, $J = 5.4$ Hz, $J = 3.1$ Hz), 7.68 (dd, 3H, $J = 5.4$ Hz, $J = 3.1$ Hz), 7.59 (t, 2H, $J = 6.6$ Hz), 7.30 (t, 2H, $J = 6.6$ Hz) 3.82 (t, 2H, $J = 7$ Hz), 3.65 (t, 2H, $J = 7$ Hz), 1.83 (q, 2H, $J = 7$ Hz), 1.68 (q, 2H, $J = 7$ Hz), 1.45–1.34 (m, 8H) ^{13}C NMR ($CDCl_3$, 100 MHz, δ ppm): 168.3, 155.4, 134.1, 133.7, 132.7, 131.9, 124.6, 123.1, 122.8, 121.7, 113.1, 48.7, 37.6, 30.0, 28.5, 28.1, 26.4, 26.0, 23.2. ESI-MS $[M+H^+]^+$ 451.

3.1.3.6. 2-[9-(Acridin-9-ylamino)-nonyl]-isoindole-1,3-dione (22). *Reagents.* 9-Amino-acridine (150 mg, 0.60 mmol), DMSO (10 ml), KOH (67.3 mg, 1.2 mmol) and 2-(9-bromo-nonyl)-isoindole-1,3-dione (68.64 mg, 0.24 mmol).

Purification. Silica gel column chromatography using DCM/MeOH (10:1) and 0.1% NH_3 saturated. Yellow syrup, yield: 60 mg (55.5%). ^1H NMR ($CDCl_3$, 400 MHz, δ ppm): 8.06 (d, 2H, $J = 8.6$ Hz), 8.02(d, 2H, $J = 8.6$ Hz), 7.80 (dd, 2H, $J = 5.4$ Hz, $J = 3.1$ Hz), 7.68 (dd, 3H, $J = 5.4$ Hz, $J = 3.1$ Hz), 7.62 (t, 2H, $J = 6.6$ Hz), 7.33 (t, 2H, $J = 6.6$ Hz), 3.82 (t, 2H, $J = 7$ Hz), 3.65 (t, 2H, $J = 7$ Hz), 1.83 (q, 2H, $J = 7$ Hz), 1.68 (q, 2H, $J = 7$ Hz), 1.45–1.34 (m, 10H). ^{13}C NMR ($CDCl_3$, 100 MHz, δ ppm): 168.3, 155.4, 134.2, 133.6, 132.7, 132.0, 124.2, 123.5, 122.5, 121.3, 113.0, 48.6, 37.6, 30.0, 27.5, 28.1, 26.2, 26.0, 23.2, 22.3. ESI-MS $[M+H^+]^+$ 451.

3.2. Biological activity and molecular modelling

3.2.1. Inhibition studies on AChE. The AChE inhibition assays were performed using colorimetric method reported by Ellman et al.[33] The assay solution consisted of 0.02 U AChE from bovine erythrocytes, 0.1 M sodium phosphate buffer, pH 8, 0.3 mM 5,5′-dithiobis(2-nitrobenzoic acid) (DTNB, Ellman's reagent) and 0.5 mM acetylthiocholine iodide as the substrate of the enzymatic reaction. The tested compounds were preincubated with the enzyme for 10 min at 30 °C. Enzyme activity was determined by measuring the absorbance at 405 nm for 10 min with a Fluostar optima plate reader (BMG). The reaction rates were compared and the percent of inhibition due to the presence of test compounds was calculated. The IC_{50} is defined as the concentration of each compound that reduces by 50% the enzymatic activity with respect to that without inhibitors. Each reaction was repeated, at least, three independent times.

3.2.2. Inhibition studies on BchE. BChE inhibitory activity was evaluated at 30 °C by the colorimetric method reported by Ellman et al.[33] The assay solution consisted of 0.01 U BChE from human serum, 0.1 M sodium phosphate buffer, pH 8, 0.3 mM DTNB and 0.5 mM butyrylthiocholine iodide as the substrate of the enzymatic reaction. Enzyme activity was determined by

measuring the absorbance at 405 nm for 5 min with a microplate reader Digiscan 340 T. The tested compounds were preincubated with the enzyme for 10 min at 30 °C. The reaction rate was calculated with, at least, triplicate measurements. The IC_{50} is defined as the concentration of compounds that reduces by 50% the enzymatic activity with respect to that without inhibitors.

3.2.3. Propidium competition assay. Propidium exhibits an increase in fluorescence on binding to AChE peripheral site, making it a useful probe for competitive ligand binding to the enzyme. Fluorescence was measured in a Fluostar optima plate reader (BMG). Measurements were carried out in 100 μl solution volume, in 96-well plates. The buffer used was 1 mM Tris/HCl, pH 8.0, 5 μM AChE which was incubated, for at least 6 h, with the molecules at different concentrations. Twenty micromolar propidium iodide was added 10 min before fluorescence measurement. The excitation wavelength was 485 nm, and that of emission, 620 nm. Each assay was repeated, at least, three different times.

3.2.4. Molecular modelling of compounds 12 and 22. The simulation system was defined following the protocol used in our previous studies on AChE–ligand complexes,[34,41] which is briefly summarized here. The simulation system was based on the X-ray crystallographic structures of the AChE complexes with tacrine (PDB entry 1ACJ),[42] huprine Y (1E66)[35] and donepezil (1EVE),[43] which were used as templates to position the 9-aminotetrahydroacridine or 9-aminoacridine unit in the catalytic binding site, the linker along the gorge and the phthalimide unit in the peripheral binding site. The enzyme was modelled in its physiologically active form with neutral His440 and deprotonated Glu327, which together with Ser200 form the catalytic triad. The standard ionization state at neutral pH was considered for the rest of ionizable residues with the exception of Asp392 and Glu443, which were neutral, and His471, which was protonated, according to previous numerical titration studies.[15] Finally, Phe330 was replaced by Tyr to reflect the binding site sequence in bovine AChE. The heterodimer was protonated at the tetrahydroacridine or acridine ring, as well as at the tertiary amine in compound **12**. The orientation of the methylene side chain bonded to the tetrahydroacridine or acridine ring was determined by means of geometry optimizations performed at the MP2/6-31G(d) level using Gaussian-03.[44] With regard to the phthalimide moiety, two different starting orientations were initially chosen. In both cases, the phthalimide ring was stacked against Trp279, though they differed by a 180° rotation around the bond linking the indole unit in Trp279. The system was hydrated by centring a sphere of 40 Å of TIP3P[45] water molecules at the inhibitor, paying attention to filling the position of the crystallographic waters inside the binding cavity. The parm98 file of the AMBER force field[46] was used to describe the enzyme. For the inhibitor, the charge distribution of the tetrahydroacridine/acridine ring, linker and phthalimide unit was determined from fitting to the HF/6-31G(d) electrostatic potential using the RESP procedure,[47] and the van der Waals parameters were taken from those defined for related atoms in AMBER force field. The final model system was partitioned into a mobile region and a rigid region. The former included the inhibitor, all the protein residues containing at least one atom within 15 Å from the inhibitor, and all the water molecules, while the rest of atoms defined the rigid part.

Starting from the two models of the inhibitor bound to the enzyme, the system was energy minimized and equilibrated using the AMBER program.[48] First, all hydrogen atoms were minimized for 2000 steps of steepest descent. Next, the position of water molecules was relaxed for 5000 steps steepest descent plus 3000 steps of conjugate gradient. At this point, the rigid part of the system was kept frozen and the thermalization of the mobile part was started by running four 10 ps molecular dynamics (MD) simulations to increase the temperature up to 298 K. Subsequently, a 6 ns MD simulation was carried out. Only one of the two simulations provided a stable trajectory, as noted in a small positional root-mean square deviation (around 0.8 Å for the backbone atoms in the mobile region with regard to the crystallographic structure) and favourable contacts with the enzyme (see text). The characterisation of the structural features that mediate the binding of the heterodimers to the enzyme was determined by averaging the geometrical parameters for the snapshots (saved every ps) sampled along the last 2 ns of the MD simulation.

References and notes

1. Leifer, B. P. *J. Am. Geriatr. Soc.* **2003**, *51*, 281–288.
2. Shinosaki, K.; Nishikawa, T.; Takeda, M. *Psychiatry Clin. Neurosci.* **2000**, *54*, 611–620.
3. Neve, R. L.; McPhie, D. L.; Chen, Y. *Brain Res.* **2000**, *886*, 54–66.
4. Bayer, T. A.; Wirths, O.; Majtenyi, K.; Hartmann, T.; Multhaup, G.; Beyreuther, K.; Czech, C. *Brain Pathol.* **2001**, *11*, 1–11.
5. Crowther, R. A.; Goedert, M. *J. Struct. Biol.* **2000**, *130*, 271–279.
6. Iqbal, K.; Alonso, A. D.; Gondal, J. A.; Gong, C. X.; Haque, N.; Khatoon, S.; Sengupta, A.; Wang, J. Z.; Grundke-Iqbal, I. *J. Neural Transm. Suppl.* **2000**, *59*, 213–222.
7. Terry, R. D. *J. Neuropathol. Exp. Neurol.* **2000**, *59*, 1118–1119.
8. Tariot, P. N.; Federoff, H. J. *Alzheimer Dis. Assoc. Disord.* **2003**, *17*, 105–113.
9. Kurz, A. *J. Neural Transm. Suppl.* **1998**, *54*, 295–299.
10. Sugimoto, H. *Chem. Rec.* **2001**, *1*, 63–73.
11. Jann, M. W. *Pharmacotherapy* **2000**, *20*, 1–12.
12. Zarotsky, V.; Sramek, J. J.; Cutler, N. R. *Am. J. Health Syst. Pharm.* **2003**, *60*, 446–452.
13. Reisberg, B.; Doody, R.; Stöffler, A.; Schmitt, F.; Ferris, S.; Möbius, H. J. *N. Engl. J. Med.* **2003**, *348*, 1333–1341.
14. Sussman, J. L.; Harel, M.; Silman, I. *Chem. Biol. Interact.* **1993**, *87*, 187–197.
15. Wlodek, S. T.; Antosiewicz, J.; McCammon, J. A.; Stratsma, T. P.; Gilson, M. K.; Briggs, J. M.; Humblet, C.; Sussman, J. L. *Biopolymers* **1996**, *38*, 109–117.
16. Bartolucci, C.; Perola, E.; Cellai, L.; Brufani, M.; Lamba, D. *Biochemistry* **1999**, *38*, 5714–5719.
17. Szegletes, T.; Mallender, W. D.; Thomas, P. J.; Rosenberry, T. L. *Biochemistry* **1999**, *38*, 122–133.

18. Rosenberry, T. L.; Mallender, W. D.; Thomas, P. J.; Szegletes, T. *Chem. Biol. Interact.* **1999**, *119 120*, 85 97.
19. Harel, M.; Kleywegt, G. J.; Ravelli, R. B.; Silman, I.; Sussman, J. L. *Structure* **1995**, *3*, 1355 1366.
20. Soreq, H.; Seidman, S. *Nat. Rev. Neurosci.* **2001**, *2*, 8 17.
21. Blasina, M. F.; Faria, A. C.; Gardino, P. F.; Hokoc, J. N.; Almeida, O. M.; Mello, F. G.; Arruti, C.; Dajas, F. *Cell Tissue Res.* **2000**, *299*, 173 184.
22. Campos, E. O.; Alvarez, A.; Inestrosa, N. C. *Neurochem. Res.* **1998**, *23*, 135 140.
23. Inestrosa, N. C.; Alvarez, A.; Calderon, F. *Mol. Psychiatry* **1996**, *1*, 359 361.
24. Castro, A.; Martinez, A. *Mini-Rev. Med. Chem.* **2001**, *1*, 267 272.
25. Tumiatti, V.; Andrisano, V.; Banzi, R.; Bartolini, M.; Rosini, M.; Melchiorre, C. *J. Med. Chem.* **2004**, *47*, 6490 6498.
26. Cappelli, A.; Gallelli, A.; Manini, M.; Anzini, M.; Mennuni, L.; Makovec, F.; Menziani, C.; Alcaro, S.; Ortuso, F.; Vomero, S. *J. Med. Chem.* **2005**, *48*, 3564 3575.
27. Rosini, M.; Andrisano, V.; Bartolini, M.; Bolognesi, M.; Hrelia, P.; Minarini, A.; Tarozzi, A.; Melchiorre, C. *J. Med. Chem.* **2005**, *48*, 360 363.
28. Bolognesi, M.; Andrisano, V.; Bartolini, M.; Banzi, R.; Melchiorre, C. *J. Med. Chem.* **2005**, *48*, 24 27.
29. Dorronsoro, I.; Castro, A.; Martinez, A. *Expert Opin. Ther. Patents* **2003**, *13*, 1725 1732.
30. Martinez, A.; Fernandez, E.; Castro, A.; Conde, S.; Rodriguez-Franco, I.; Baños, J. B.; Badia, A. *Eur. J. Med. Chem.* **2000**, *35*, 913 922.
31. Dorronsoro, I.; Alonso, D.; Castro, A.; Del Monte, M.; Garcia-Palomero, E.; Martinez, A. *Arch. Pharm. Pharm. Med. Res.* **2005**, *338*, 18 23.
32. Carlier, P. R.; Chow, E. S.-H.; Han, Y.; Liu, J.; El Yazal, J.; Pang, Y.-P. *J. Med. Chem.* **1999**, *42*, 4225 4231.
33. Ellman, G. L.; Courtney, K. D.; Andres, B.; Featherstone, R. M. *Biochem. Pharmacol.* **1961**, *7*, 88 95.
34. Camps, P.; El Achab, R.; Morral, J.; Muñoz-Torrero, D.; Badia, A.; Baños, J. E.; Vivas, N. M.; Barril, X.; Orozco, M.; Luque, F. J. *J. Med. Chem.* **2000**, *43*, 4657 4666.
35. Dvir, H.; Wong, D. M.; Harel, M.; Barril, X.; Orozco, M.; Luque, F. J.; Muñoz-Torrero, D.; Camps, P.; Rosenberry, T. L.; Silman, I.; Sussman, J. L. *Biochemistry* **2002**, *41*, 2970 2981.
36. Barril, X.; Kalko, S. G.; Orozco, M.; Luque, F. J. *Mini-Rev. Med. Chem.* **2002**, *2*, 27 36.
37. Curutchet, C.; Salichs, A.; Barril, X.; Orozco, M.; Luque, F. J. *J. Comput. Chem.* **2002**, *24*, 32 45.
38. Taylor, P.; Lappi, S. *Biochemistry* **1975**, *14*, 1989 1997.
39. Padwa, A.; Harring, S. R.; Hertzog, D. L.; Nadler, W. R. *Synthesis* **1994**, *9*, 993 1004.
40. Donahoe, H.; Seiwald, R.; Newman, M.; Kimura, K. *J. Org. Chem.* **1957**, *22*, 68 70.
41. Barril, X.; Orozco, M.; Luque, F. J. *J. Med. Chem.* **1999**, *42*, 5110 5119.
42. Sussman, J. L.; Harel, M.; Frolow, F.; Oefner, C.; Goldman, A.; Toker, L.; Silman, I. *Science* **1991**, *253*, 872 879.
43. Kryger, G.; Silman, I.; Sussman, J. L. *Structure* **1999**, *7*, 297 307.
44. Frisch, M. J.; Trucks, G. W.; Schlegel, H. B.; Scuseria, G. E.; Robb, M. A.; Cheeseman, J. R.; Montgomery, J. A., Jr.; Vreven, T.; Kudin, K. N.; Burant, J. C.; Millam, J. M.; Iyengar, S. S.; Tomasi, J.; Barone, V.; Mennucci, B.; Cossi, M.; Scalmani, G.; Rega, N.; Petersson, G. A.; Nakatsuji, H.; Hada, M.; Ehara, M.; Toyota, K.; Fukuda, R.; Hasegawa, J.; Ishida, M.; Nakajima, T.; Honda, Y.; Kitao, O.; Nakai, H.; Klene, M.; Li, X.; Knox, J. E.; Hratchian, H. P.; Cross, J. B.; Adamo, C.; Jaramillo, J.; Gomperts, R.; Stratmann, R. E.; Yazyev, O.; Austin, A. J.; Cammi, R.; Pomelli, C.; Ochterski, J. W.; Ayala, P. Y.; Morokuma, K.; Voth, G. A.; Salvador, P.; Dannenberg, J. J.; Zakrzewski, V. G.; Dapprich, S.; Daniels, A. D.; Strain, M. C.; Farkas, O.; Malick, D. K.; Rabuck, A. D.; Raghavachari, K.; Foresman, J. B.; Ortiz, J. V.; Cui, Q.; Baboul, A. G.; Clifford, S.; Cioslowski, J.; Stefanov, B. B.; Liu, G.; Liashenko, A.; Piskorz, P.; Komaromi, I.; Martin, R. L.; Fox, D. J.; Keith, T.; Al-Laham, M. A.; Peng, C. Y.; Nanayakkara, A.; Hallacombe, M.; Gill, P. M. W.; Johnson, B.; Chen, W.; Wong, M. W.; Gonzalez, C.; Pople, J. A. Gaussian 03, Revision B.04, Gaussian, Inc., Pittsburgh, PA, 2003.
45. Jorgensen, W. L.; Chandrasekhar, J.; Madura, J. D.; Impey, R. W.; Klein, M. L. *J. Chem. Phys.* **1983**, *79*, 926 935.
46. Cornell, W. D.; Cieplak, P.; Bayly, C. I.; Gould, I. R.; Merz, K. M.; Ferguson, D. M.; Spellmeyer, D. C.; Fox, T.; Caldwell, J. W.; Kollman, P. A. *J. Am. Chem. Soc.* **1995**, *117*, 5719 5797.
47. Bayly, C. I.; Cieplak, P.; Cornell, W. D.; Kollman, P. A. *J. Phys. Chem.* **1993**, *97*, 10269 10280.
48. Case, D. A.; Darden, T. A.; Cheatham, T. E.; Pearlman, D. A.; Simmerling, C. L.; Wang, J.; Duke, R. E.; Luo, R.; Merz, K. M.; Pearlman, D. A.; Crowley, M.; Brozell, S.; Tsui, V.; Gohlke, H.; Mongan, J.; Hornak, V.; Cui, G.; Beroza, P.; Schafmeister, P.; Caldwell, J. W.; Ross, W. S.; Kollman, P. A. AMBER8. University of California, San Francisco, 2004.

4.1.2 Design Synthesis and Pharmacological Evaluation of Dual Binding Site Acetylcholinesterase Inhibitors: New Disease Modifying Agents for Alzheimer's Disease

Pilar Muñoz-Ruiz, Laura Rubio, Esther García-Palomero, María del Monte-Millán, Paola Usán, Isabel Dorronsoro, Manuela Bartolini, Vincenza Andrisano, **Axel Bidon-Chanal Badia**, Modesto Orozco, F. Javier Luque, Miguel Medina and Ana Martínez.

J. Med. Chem., 48, **2005**, 7223-7233

Design, Synthesis, and Biological Evaluation of Dual Binding Site Acetylcholinesterase Inhibitors: New Disease-Modifying Agents for Alzheimer's Disease

Pilar Muñoz-Ruiz,[§] Laura Rubio,[§] Esther García-Palomero,[§] Isabel Dorronsoro,[§] María del Monte-Millán,[§] Rita Valenzuela,[§] Paola Usán,[§] Celia de Austria,[§] Manuela Bartolini,[‡] Vincenza Andrisano,[‡] Axel Bidon-Chanal,[#] Modesto Orozco,[⊥] F. Javier Luque,[#] Miguel Medina,[§] and Ana Martínez*[,§]

Neuropharma, S.A., Avda. de La Industria 52, 28760 Tres Cantos, Madrid, Spain, Department of Pharmaceutical Sciences, University of Bologna, Via Belmeloro 6, 40126 Bologna, Italy, Departamento de Fisicoquímica, Facultad de Farmacia, Universidad de Barcelona, Avda. Diagonal 643, 08028 Barcelona, Spain, and Departamento de Bioquímica y Biología Molecular, Facultad de Química, Universidad de Barcelona, Martí i Franquès 1, 08028 Barcelona, Spain

Received April 11, 2005

New dual binding site acetylcholinesterase (AChE) inhibitors have been designed and synthesized as new potent drugs that may simultaneously alleviate cognitive deficits and behave as disease-modifying agents by inhibiting the β-amyloid (Aβ) peptide aggregation through binding to both catalytic and peripheral sites of the enzyme. Particularly, compounds **5** and **6** emerged as the most potent heterodimers reported so far, displaying IC_{50} values for AChE inhibition of 20 and 60 pM, respectively. More importantly, these dual AChE inhibitors inhibit the AChE-induced Aβ peptide aggregation with IC_{50} values 1 order of magnitude lower than that of propidium, thus being the most potent derivatives with this activity reported up to date. We therefore conclude that these compounds are very promising disease-modifying agents for the treatment of Alzheimer's disease (AD).

Introduction

Alzheimer's disease (AD), the most common form of neurodegenerative senil dementia, is associated with selective loss of cholinergic neurons and reduced levels of acetylcholine neurotransmitter, and it is characterized by loss of memory and progressive impairment in cognitive functions.[1] Post-mortem brain studies, specially in neurocortex and hypocampus regions, have revealed the presence of several distinct neuropathological hallmarks, including extracellular β-amyloid (Aβ) containing plaques, intracellular neurofibrillary tangles containing abnormally hyperphosphorylated τ protein, and degeneration of cholinergic neurons of the basal forebrain.[2]

In the past 2 decades, enormous research effort has been spent to understand the molecular pathogenesis of AD, thus providing a robust framework to develop effective pharmacological treatments.[3] However, the only therapeutic approach currently approved exploits the enhancement of the central cholinergic function,[4] which increasees the acetylcholine levels in the brain. Thus, over the past decade various cholinergic drugs, primarily inhibitors of the enzyme acetylcholinesterase (AChE) such as tacrine,[5] donepezil,[6] rivastigmine,[7] and more recently galantamine[8] (Figure 1), have been launched on the market for the symptomatic treatment of AD.

The therapeutic potential of AChE inhibitors has been strengthened by evidence showing that, besides their role on the cognitive function, they might contribute to slow the neurodegeneration in AD patients. In fact, it is known that AChE exerts secondary noncholinergic functions,[9] related to its peripheral anionic site,[10,11] in cell adhesion[12,13] and differentiation,[14] and recent findings also support its role in mediating the processing and deposition of Aβ peptide;[15-18] AChE is one of the proteins that colocalizes with Aβ peptide deposits in the brain of AD patients[15] and promotes Aβ fibrillogenesis by forming stable AChE−Aβ complexes.[16] Additionally, it has also been postulated that AChE binds through its peripheral site to the Aβ nonamyloidogenic form and acts as a pathological chaperone inducing a conformational transition to the amyloidogenic form.[17,18] On the basis of this evidence, dual binding site AChE inhibitors appear to be promising for the design of new antidementia drugs, since they might simultaneously alleviate the cognitive deficit in AD patients and act as disease-modifying agents delaying the amyloid plaque formation.[19,20] Following this rationale, new AChE inhibitors

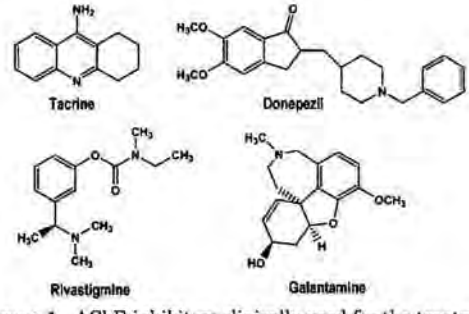

Figure 1. AChE inhibitors clinically used for the treatment of AD.

* To whom correspondence should be addressed. Phone: +34 91 8061130. Fax: +34 91 8034660. E-mail: amartinez@neuropharma.es.
[§] Neuropharma, S.A.
[‡] University of Bologna.
[#] Departamento de Fisicoquímica, Universidad de Barcelona.
[⊥] Departamento de Bioquímica y Biología Molecular, Universidad de Barcelona.

10.1021/jm0503289 CCC: $30.25
Published on Web 00/00/0000 PAGE EST: 10.5

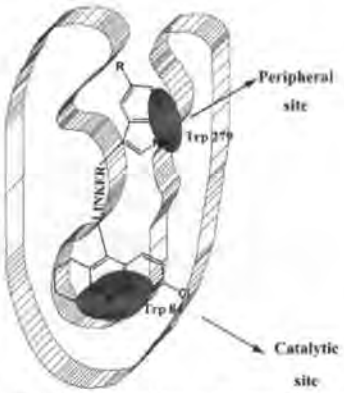

Figure 2. Indole–tacrine heterodimers binding simultaneously to the catalytic and peripheral sites of the AChE.

have been designed to interact simultaneously with both catalytic and peripheral sites.[21-24]

Continuing with our search for new dual-binding site AChE inhibitors,[25-27] we report here the design, synthesis, and pharmacological evaluation of a new series of potent compounds containing in their structures a 1,2,3,4-tetrahydroacridine fused ring (tacrine) as the catalytic anionic site binding unit, and an indole ring as the peripheral site binding unit, connected to each other by a linker of suitable length and nature (Figure 2).[28] The tacrine unit was, in previous studies, incorporated in a series of bis-tacrines, designed by Pang et al.,[19] that showed high potency and selectivity in AChE inhibition, being up to 248-fold more selective and 149-fold more potent than tacrine. Since then, tacrine has been incorporated into several families of AChE dual inhibitors.[29-31] Because the insertion of chlorine into position 6 of tacrine enhances the affinity toward AChE,[32] we have also combined the 6-chlorotacrine unit with the indole ring unit in most of the synthesized heterodimers. The indole ring moiety was chosen on the basis of its pharmacological, structural, and electronic properties. In this view, the indole ring linked to the tacrine moiety by a tether of appropriate length could reach the entrance of the catalytic gorge and interact with the Trp279 by $\pi-\pi$ stacking.[33,34] To our knowledge, the indole unit has been incorporated only once into a dual binding site AChE inhibitor, in the case of tryptamine in combination with tacrine, which resulted in 3-fold less potency than tacrine.[35] Regarding the linker, we first synthesized indole–tacrine inhibitors containing a propionamide moiety linked to position 3 of the indole ring and to an alkylaminotacrine of different methylene tether length. The influence of the linker on the pharmacological activity was explored by different chemical modifications: (i) conformational restriction at the propionamide chain, (ii) inclusion of an additional *N*-Me function in the central part of the methylene chain linked to tacrine, (iii) variation of the relative position of the carbonyl group and the heterocyclic units, and (iv) replacement of the amide group by a carbamate residue, which is present in other AChE inhibitors such as rivastigmine. Finally, derivatives containing other heterocycles such as 5-cyanoindole, 5-bromoindole, *N*-methylindole, and indazole derivatives were also synthesized.

The AChE and BChE inhibitory activity of each compound was evaluated, and their selectivity ratio (AChE/BChE) was also calculated. A molecular modeling study was performed to determine the binding mode of these dual inhibitors to the AChE. Furthermore, for those compounds showing very promising disease-modifying profiles for the treatment of AD, their $A\beta_{1-40}$ peptide aggregation inhibitory activity and their AChE-induced $A\beta_{1-40}$ peptide aggregation inhibitory activity were studied to confirm their dual action. Finally, cytotoxicity studies were performed in human neuroblastoma cells.

Chemistry

The synthetic methodology employed for the preparation of the new dual binding site heterodimers was varied depending on the carbonylic bond type (amide or carbamate) in the linker, which is inserted in the last step of the synthetic pathway, as depicted in Schemes 1 or 2, respectively. Preparation of the new dual heterodimers containing an amide bond, compounds **3**–**23** (Table 1), was carried out by coupling the required 9-alkylaminotetrahydroacridines **1a**–**i** to the corresponding indole carboxylic acid derivatives **2a**–**i**, employing 1,1-carbonyldiimidazol (CDI) as coupling agent (Scheme 1).[36] The 9-alkylaminotetrahydroacridines **1a**–**i** of different tether lengths were readily obtained following the reported methodology.[30] All the indole carboxylic acid derivatives **2** employed for the preparation of the new dual heterodimers **3**–**23** were commercially available except for 5-cyanoindole-3-propionic acid (**2b**), which was synthesized according to a reported methodology.[37] Thus, activation of the indole carboxylic acid derivatives **2** with CDI in THF for about 4 h followed by treatment with the corresponding 9-alkylaminotetrahydroacridines **1a**–**i** generated the desired dual binding site inhibitors **3**–**23** in yields ranging from 8% to 97%. In general, the yield of the reaction decreases dramatically as the number of methylene units of the 9-alkylaminotetrahydroacridines **1** varies from 8 (**7**, 53%) to 10 (**9**, 19%). The presence of an electron-withdrawing group at position 5 of the indole ring, compounds **2b** and **2f**, seemed to decrease the activation of the carboxylic group, since compounds **12** (22%) and **19** (54%) were obtained in much lower yields than their unsubstituted analogues **5** (77%) and **18** (84%). Coupling the indole-3-propenoic acid (**2c**) to the 9-alkylaminotetrahydroacridines **1c** resulted in low formation of the heterodimer **13** (8%), probably because of the conjugation of the double bond with the carboxylic acid group that might reduce the nucleophilicity of the hydroxyl group. Heterodimers **14**–**17**, containing an amide group directly attached to the indole fused-ring, were also obtained in moderate yield as observed when comparing **16** (51%) with **18** (80%) and **6** (79%), where the carbonylic group is separated by one or two methylene groups from the indole ring, respectively. This effect was even more remarkable at synthesizing the heterodimers **22** (8%) and **23** (13%), which also contain an amide directly connected to the *N*-Me indole and indazole rings, respectively.

Regarding the synthesis of the new heterodimers containing a carbamate functionality within the linker (Scheme 2), we designed a synthetic approach in which

Scheme 1[a]

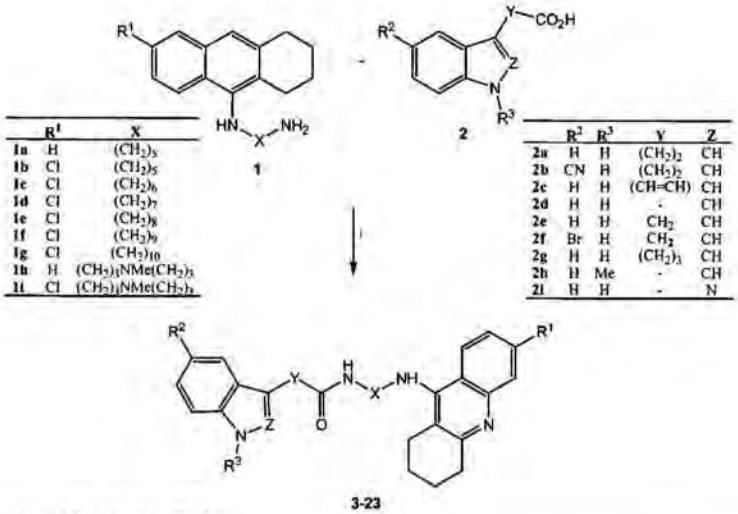

	R^1	X
1a	H	$(CH_2)_5$
1b	Cl	$(CH_2)_5$
1c	Cl	$(CH_2)_6$
1d	Cl	$(CH_2)_7$
1e	Cl	$(CH_2)_8$
1f	Cl	$(CH_2)_9$
1g	Cl	$(CH_2)_{10}$
1h	H	$(CH_2)_3NMe(CH_2)_3$
1i	Cl	$(CH_2)_3NMe(CH_2)_3$

	R^2	R^3	Y	Z
2a	H	H	$(CH_2)_2$	CH
2b	CN	H	$(CH_2)_2$	CH
2c	H	H	(CH=CH)	CH
2d	H	H	-	CH
2e	H	H	CH_2	CH
2f	Br	H	CH_2	CH
2g	H	H	$(CH_2)_3$	CH
2h	H	Me	-	CH
2i	H	H	-	N

[a] Reagents: (i) 1,1′-carbonyldiimidazole, THF.

Scheme 2[a]

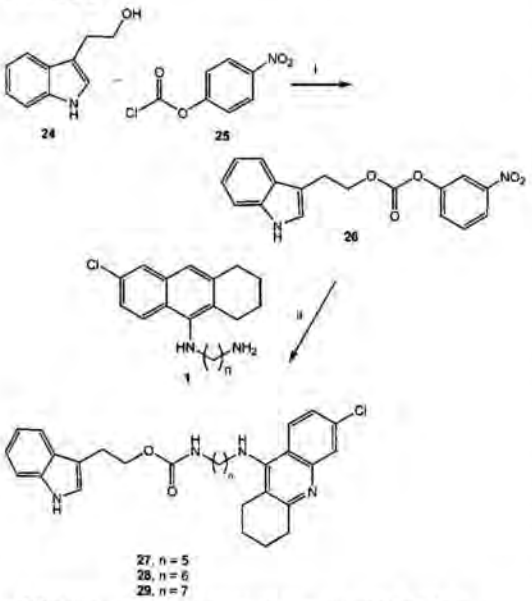

[a] Reagents: (i) *N*-methylmorpholine; (ii) DMAP, DMF.

preparation of the highly reactive intermediate phenyloxycarbonyl derivative **26** was required before coupling to the corresponding 9-alkylaminotetrahydroacridines **1**.[38] Thus, the carbonate intermediate **26** was prepared in 32% yield by treatment of 2-(1*H*-indol-3-yl)ethanol (**24**) with *p*-nitrophenyl chloroformate (**25**) in *N*-methylmorpholine, followed by chromatographic purification. Finally, treatment of the carbonate derivative **26** with the corresponding 9-alkylaminotetrahydroacridines **1b–d** in the presence of DMAP resulted in the formation of the carbamate derivatives **27–29** that were then purified by chromatography.

The chemical structures of all new compounds synthesized herein were fully characterized by analytical and spectroscopic data reported in the Experimental Section. Bidimensional spectroscopic experiments $^1H-^1H$ COSY and $^1H-^{13}C$ HMQC, and $^1H-^{13}C$ HMBC were carried out for unequivocal assignment of the chemical shifts observed in the ^1H and ^{13}C NMR spectra. The molecular weights of all compounds synthesized were confirmed by low-resolution mass spectrometry analysis ESI^+ (electrospray), and their degree of purity was also determined by elemental and HPLC analyses.

Results and Discussion

AChE Inhibitory Activity. To determine the therapeutic potential of this new series of tacrine–indole heterodimers (compounds **3–23** and **27–29**) for the treatment of AD, their AChE inhibitory potency was assayed on AChE from bovine erythrocytes according to Ellman et al.,[39] using tacrine as a reference compound. With only the exception of compound **14**, the tacrine–indole heterodimers were all clearly more active as bovine AChE inhibitors than the parent compound tacrine (see Table 1). In particular, compounds **5** and **6** were >8000- and >2500-fold, respectively, more potent than tacrine. As previously reported in the literature,[40] insertion of a chlorine atom at position 6 of tacrine leads to a large enhancement in the binding affinity, 6-chlorotacrine heterodimers **4** and **11** being 17- and 49-fold more potent than their unsubstituted analogues **3** and **10**, respectively.

With the aim of optimizing the interaction of the heterodimers with both catalytic and peripheral binding sites of AChE, both the length of the tether and the position of the amide group within the linker were varied. Thus, among the heterodimers bearing two methylene groups between the indole ring and the amide functionality, those in which the tether length from the amide to the tacrine unit contains 6 or 7 methylenes (compounds **5** and **6**) displayed the best AChE inhibitory activity (see Table 1). This potency

Table 1. Inhibition of AChE and BChE Activities and Selectivity Ratios Determined for the Indole–Tacrine Heterodimers

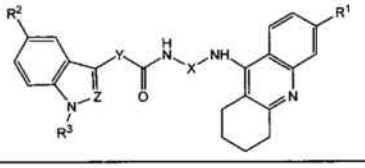

compd	R^1	R^2	R^3	X	Y	Z	IC_{50}(AChE)[a] (nM)	IC_{50}(BChE)[a] (nM)	selectivity AChE/ BChE
tacrine							167 (119–233)	24 (12–45)	6.9
3	H	H	H	$(CH_2)_5$	$(CH_2)_2$	CH	70 (54–95)	1 (0.8–1.5)	70
4	Cl	H	H	$(CH_2)_5$	$(CH_2)_2$	CH	4 (3–6)	16 (8–31)	0.25
5	Cl	H	H	$(CH_2)_6$	$(CH_2)_2$	CH	0.02 (0.01–0.03)	2.9 (1.1–7.5)	0.007
6	Cl	H	H	$(CH_2)_7$	$(CH_2)_2$	CH	0.06 (0.04–0.10)	0.1 (0.06–0.13)	0.6
7	Cl	H	H	$(CH_2)_8$	$(CH_2)_2$	CH	0.5 (0.3–1.0)	5.7 (3.7–8.7)	0.09
8	Cl	H	H	$(CH_2)_9$	$(CH_2)_2$	CH	4.4 (2.7–6.8)	9.6 (3–25)	0.4
9	Cl	H	H	$(CH_2)_{10}$	$(CH_2)_2$	CH	21.9 (16–29)	54 (30–97)	0.4
10	H	H	H	$(CH_2)_3NMe(CH_2)_3$	$(CH_2)_2$	CH	147 (100–202)	0.03 (0.01–0.06)	4900
11	Cl	H	H	$(CH_2)_3NMe(CH_2)_3$	$(CH_2)_2$	CH	2.9 (2.2–3.8)	21.4 (12–37)	0.13
12	Cl	CN	H	$(CH_2)_6$	$(CH_2)_2$	CH	0.7 (0.3–1.4)	11.7 (5–23)	0.06
13	Cl	H	H	$(CH_2)_6$	(CH=CH)	CH	18 (12–26)	77 (50–120)	0.2
14	Cl	H	H	$(CH_2)_5$		CH	180 (95–350)	9.5 (7–12)	18.9
15	Cl	H	H	$(CH_2)_6$		CH	33 (20–53)	1.7 (0.9–3)	19
16	Cl	H	H	$(CH_2)_7$		CH	36 (18–70)	19 (12–28)	1.9
17	Cl	H	H	$(CH_2)_8$		CH	46 (23–83)	22.4 (13–37)	2.1
18	Cl	H	H	$(CH_2)_7$	CH_2	CH	0.2 (0.11–0.29)	11.7 (6.4–21)	0.02
19	Cl	Br	H	$(CH_2)_7$	CH_2	CH	0.6 (0.4–1.0)	1.7 (1.0–2.7)	0.3
20	Cl	H	H	$(CH_2)_5$	$(CH_2)_3$	CH	0.3 (0.2–0.5)	3.2 (1.7–6.1)	0.09
21	Cl	H	H	$(CH_2)_6$	$(CH_2)_3$	CH	0.5 (0.2–0.9)	5.6 (3.5–8.8)	0.09
22	Cl	H	Me	$(CH_2)_7$		CH	10.9 (6.6–17)	206 (145–292)	0.05
23	Cl	H	H	$(CH_2)_7$		N	95 (53–170)	79 (63–97)	1.2
27	Cl	H	H	$(CH_2)_5$	$(CH_2)_2O$	CH	1.5 (1.0–2.3)	136 (87–212)	0.1
28	Cl	H	H	$(CH_2)_6$	$(CH_2)_2O$	CH	0.7 (0.4–1.0)	60 (41–86)	0.2
29	Cl	H	H	$(CH_2)_7$	$(CH_2)_2O$	CH	3.0 (2.0–4.4)	59 (43–81)	0.05

[a] 95% confidence intervals are given in parentheses.

decreases as the number of methylene units is lengthened from 8 to 10 (compounds **7**–**9**) or decreased to 5 (compound **4**). Replacement of the central methylene group of heterodimer **6** by a methylamine group decreases the AChE inhibitory activity of compound **11**, which is nearly 50-fold less potent. Moreover, conformational restriction of heterodimer **5** by introduction of unsaturation at the linker also substantially reduces the AChE binding affinity, as noted by the fact that compound **13** is about 900-fold less potent than **5**. All these findings suggest that along the gorge the tether must satisfy very specific structural requirements to allow the interaction of both tacrine and indole units at both catalytic and peripheral binding sites. Finally, the 5-cyanoindole heterodimer **12** was about 35-fold less potent than the unsubstituted analogue **5**.

Regarding the family of heterodimers where the carbonyl group is directly attached to the indole ring, the AChE inhibitory activity was similar for heterodimers bearing six, seven, and eight methylene units within the linker (compounds **15**–**17**). However, shortening the length of the tether to five methylenes (**14**) leads to a notable decrease in the inhibitory potency. Furthermore, compounds **16** and **17**, which possess the same number of methylene units as **4** and **5** but differ in the position of the amide group within the linker, are clearly less potent, being particularly worse for compound **17**, which is around 2300-fold less potent than **5**. This result strongly suggests that the location of the amide group within the linker is critical. Further support of this conclusion comes from the comparison of the potencies determined for heterodimers **18** and **5**. Though the total length of the linker is identical in the two compounds, compound **18** is around 10-fold less potent than **5**, which must be attributed to the fact that in the former compound the amide group is separated by only one methylene from the indole ring. Likewise, when the amido group is separated by three methylenes from the indole ring (compounds **20** and **21**), the inhibitory activity drops 10-fold with respect to **5** and **6**, though the total length of tether is maintained. Thus, the precise location of the amido group plays a decisive role in modulating the inhibitory potency of the heterodimer.

Replacement of the methylene adjacent to the carbonyl group in heterodimers **20** and **21** by an oxygen (compounds **27** and **28**) did not produce an important variation in the inhibitory activity. Similarly, replacement of the indole ring in **16** by an indazole ring (**23**) or methylation of the indole nitrogen atom (**22**) has modest effects on the inhibitory potency.

On the basis of the preceding results, heterodimers **5**, **6**, and **18**–**20**, which were the most potent inhibitors in bovine erythrocyte AChE, were also assayed in human brain AChE. Within the uncertainty of the experimental measurements, the results confirm the trends mentioned above (see Table 2). Thus, compounds **5** and **6** have similar inhibitory activities, which are close to the values determined for bovine AChE. Moreover, compounds **18**–**20** exhibit similar potencies, being 2- to 10-fold less active than compounds **5** and **6**. These results, therefore, confirm that these tacrine–indole heterodimers possess very potent activities with IC_{50} values at subnanomolar levels.

Table 2. Inhibition of Human AChE by Selected Indole–Tacrine Heterodimers

compd	IC_{50}(AChE)[a] (pM)	K_i(AChE)[a] (pM)	selectivity AChE/BChE
5	70 (0.4–1.0)	14 (3–20)	0.02
6	20 (10–30)	9 (2–17)	0.22
18	120 (80–180)	15 (4–20)	0.01
19	230 (140–370)	20 (8–30)	0.14
20	130 (80–200)	1.7 (−0.7–4)	0.04

[a] 95% confidence intervals are given in parentheses.

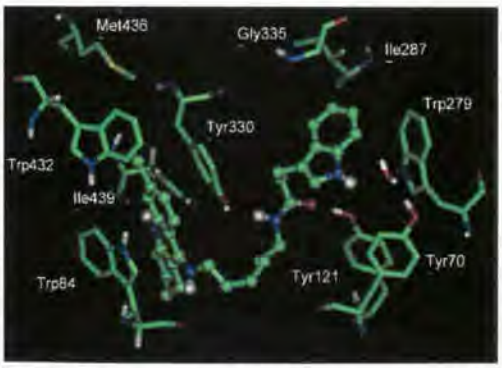

Figure 3. Representation of the heterodimer **5** docked into the binding site of AChE highlighting the protein residues that form the main interactions with the different structural units of the inhibitor.

Molecular Modeling. To gain insight into the molecular determinants that modulate the inhibitory activity, a molecular modeling study was performed to explore the binding of heterodimer **5** to the enzyme (see Experimental Section for details).

The position of heterodimer **5** with respect to the key residues in the binding site is shown in Figure 3. The tacrine moiety is firmly bound to the catalytic site of AChE, it being stacked against the aromatic rings of Trp84 and Tyr330 (average distances between rings: 3.52 (Trp84) and 3.56 (Tyr330) Å). The aromatic nitrogen of tacrine is hydrogen-bonded to the main-chain carbonyl oxygen of His440 (average N···O distance: 2.84 Å). In addition, a hydrogen-bond interaction is also formed along the simulation between the tacrine amino NH group and the main-chain carbonyl oxygen of Trp84 (average N···O distance: 3.27 Å). Finally, the chlorine atom occupies a small hydrophobic pocket formed by Trp432, Met436, and Ile439. This feature, which has been identified in both modeling studies[41] and the X-ray crystallographic structure[42] of the AChE–huprine Y complex, justifies the higher potencies of heterodimers having the 6-chlorotacrine unit compared to the unsubstituted compounds.

With regard to the linker, which is aligned along the gorge, the most relevant feature comes from the interactions formed by the amido group. Thus, the NH group is hydrogen-bonded to the hydroxyl oxygen of Try330 (average N···O distance: 3.01 Å), which in turn remains firmly stacked onto the tacrine unit. Indeed, the carbonyl oxygen is hydrogen-bonded to the hydroxyl oxygen of Tyr121 (average O···O distance: 2.75 Å). Overall, the presence of the amido group in the tether permits us to define a network of interactions that couple several residues of the enzyme gorge and different structural units of the inhibitor, thus explaining the notable dependence of the inhibitory potency on the position of the amido group within the tether (see above and Table 1).

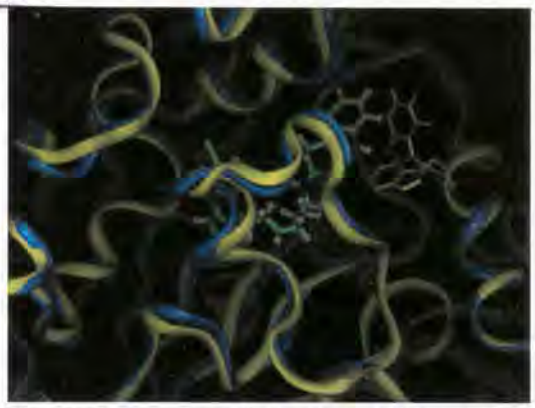

Figure 4. Superposition of the backbone of AChE in the X-ray crystallographic structure complexed with huprine X (PDB entry 1E66; yellow) and in a representative structure of the AChE complex with heterodimer **5** (blue). The inhibitor is represented as a colored ball-and-stick model, and the side chain of Trp279 is displayed using a stick model.

Finally, the indole ring is roughly stacked onto the aromatic ring of Trp279. Moreover, after the first nanosecond of the simulation, the NH group of the indole ring forms a water-mediated interaction with the hydroxyl oxygen of Tyr70 (average N···O distance: 5.18 Å). In this orientation, position 5 of the indole unit lies close to the backbone of Gly335 and to the side chain of Ile287 (average distances from C5 to Cα in Gly335 and Cβ in Ile287 ranging between 3.7 and 4.4 Å), which justifies the decrease in inhibitory activity observed upon inclusion of cyano and bromide substituents (see above and Table 1). Remarkably, there is a notable conformational rearrangement in the side chain of Trp279 (see Figure 4). Since the peripheral site region has been postulated to mediate the interaction of AChE with the Aβ nonamyloidogenic form,[17] it might be hypothesized that binding of compound **5** might have a significant effect in modulating the AChE-induced Aβ peptide fibrillogenesis.

AChE/BChE Selectivity. Recent evidence has shown that in AD patients with severe pathology, AChE is greatly reduced in specific brain regions, while BChE, which catalyzes the hydrolysis of a wide variety of choline esters (butyrylcholine, succinylcholine, and acetylcholine), noncholine esters, acyl amides, and aromatic amines, increases.[43] Therefore, to further characterize the pharmacological profile of the heterodimers, their selectivity to inhibit AChE vs BChE was determined.

The selectivity for BChE is generally small in the case of the 6-chlorotacrine substituted heterodimers **14**–**17** and **23**, it being much less pronounced than the effect due to the detachment of the chlorine atom in compounds **3** and **10**, which reflect and even enhance the larger binding affinity of tacrine for BChE. Particularly, **10** is around 700-fold more selective for BChE than tacrine. Remarkably, the AChE/BChE selectivity of compound **10** is reversed in its 6-chloro derivative

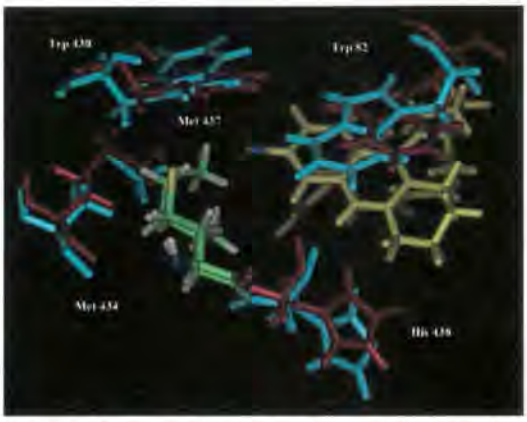

Figure 5. Representation of selected residues in the catalytic binding site of the MD-averaged structure of the complex between AChE (blue) and heterodimer **5** (yellow, but the chlorine atom is shown in magenta), and the superposed structure of BChE (PDB entry 1N5R; red). An atom-based color code is used to distinguish between Met437 in BChE and Ile439 in AChE. The numbering denotes the residues in BChE.

Table 3. Inhibition of $A\beta_{1-40}$ Peptide Aggregation (with and without Human AChE) by Some Heterodimers and Reference Compounds

	with AChE		without AChE
compd	inhibition at 100 μM ± SEM (%)	IC_{50} ± SEM (μM)	inhibition at 100 μM ± SEM (%)
5	98 ± 2	2 ± 1	49 ± 7
6	96 ± 0	6 ± 2	65 ± 5
18	84 ± 1	7 ± 4	63 ± 10
20	99 ± 4	2 ± 0	63 ± 4
19	82 ± 1	15 ± 3	62 ± 14
propidium	82[a]	13 ± 0	46 ± 5
decamethonium	25[a]	nd[b]	0
donepezil	22[a]	nd[b]	0
tacrine	7[a]	nd[b]	0
edrophonium	0[a]	nd[b]	nd[b]
physostigmine	30[a]	nd[b]	nd[b]

[a] SD within 3% (data from ref 43). [b] nd = not determined.

(compound **11**), in agreement with the findings obtained for homodimeric tacrine inhibitors.[44] The influence of the chlorine atom on the AChE/BChE selectivity can be explained by the replacement of Ile439 in AChE by Met437 in BChE, as noted in the superposition (Figure 5) of the MD-averaged structure of the AChE–**5** complex to BChE (PDB entry 1N5R). Such a replacement eliminates the hydrophobic pocket that anchors the chlorine atom in AchE[39,40] and makes the terminal methyl group of Met437 in BChE to be around 1.1 Å closer to the chlorine atom, thus leading to steric hindrance with the 6-chlorotacrine unit.

Effects on the Aβ Aggregation. The heterodimers showing best AChE inhibitory potency (**5**, **6**, and **18**–**20**) were selected to assess their ability to inhibit $A\beta_{1-40}$ peptide aggregation employing the thioflavin T fluorescence method and using propidium, a known inhibitor acting at the AChE peripheral site, as reference compound. Results showed that the heterodimers inhibited the Aβ peptide aggregation at 100 μM in a range varying from 49% to 63% (Table 3), they being at least as potent as propidium, which caused 46% inhibition. To further explore the dual action of these compounds, the capacity of **5**, **6**, and **18**–**20** to inhibit the AChE-induced $A\beta_{1-40}$ peptide fibrillogenesis was examined employing the same thioflavin T-based fluorometric assay. Results are also shown in Table 3, where propidium and some other typical inhibitors of AChE have been used as reference compounds.[45] The most active compounds were **5** and **20**, followed by **6**, **18**, and **19**, the latter being around 2-, 3-, and 10-fold less active than the former compounds, respectively. With only the exception of heterodimer **19**, all of them were more active than the reference compound propidium, which is the most potent AChE-induced $A\beta_{1-40}$ peptide antiaggregating drug reported so far (see Table 3 for comparison with commercially available AChE inhibitors). Clearly, these findings point out a potential disease-modifying action for this new family of dual AChE inhibitors.

Cell Viability. The cytotoxic effect of this new family of heterodimers was assayed in the human neuroblastoma cell line SH-SY5Y. For compounds **6**, **7**, and **11** only, toxicity was found at 10 μM (several orders of magnitude higher than the active concentration). For the rest of compounds we did not found any toxicity at this concentration. Therefore, we state that these new compounds possess a wide therapeutic safety range.

Conclusions

We have synthesized a series of indole–tacrine heterodimers as dual binding site AChE inhibitors. These compounds display high inhibitory potency against AChE (bovine and human) and, in general, are rather selective for AChE regarding BChE. More importantly, compounds **5**, **6**, and **18**–**20** inhibit the AChE-induced Aβ peptide aggregation in vitro, showing lower IC_{50} values than propidium, thus rendering new potent compounds acting as disease-modifying agents for the treatment of AD. In fact, preliminary in vivo studies in a transgenic mice overexpressing human APP (hAPP-(751)) suggest that this class of tacrine–indole heterodimers leads to a net reduction of Aβ peptide plaque load in the animals and an improvement in their cognitive functions.[46] This work is in progress and will be published. Taken together, all the preceding results suggest that the new dual binding AChE inhibitors have potential impact for the future therapeutic treatment of AD.

Experimental Section

Chemistry. All reagents were of commercial quality. All experiments involving water-sensitive compounds were carried out under nitrogen and scrupulously dry conditions, using anhydrous solvents purchased from Aldrich. Analytical thin-layer chromatography (TLC) was performed on aluminum sheets with precoated silica plates, 0.2 mm layer silica gel 60 F_{254} (Merck). Preparative centrifugal circular thin-layer chromatography (CCTLC) was performed on 20 cm diameter circular glass plates coated with a 1 mm layer of Kieselgel 60 PF_{254} (Merk), by using a Chromatotron, with the indicated solvent as eluent. Flash column chromatography was performed at medium pressure on silica gel 60 (particle size 0.040–0.063 mm, 230–240 mesh ASTM, Merck). ^1H NMR and ^{13}C NMR spectra were recorded with Mercury Plus Varian spectrometers operating at 400 and 50 MHz and using tetramethylsilane (TMS) as reference. Chemical shifts are reported in parts per million (ppm) relative to TMS. Elemental analyses were obtained in a LECO CHNS-932 apparatus. Analytical RP HPLC was performed on an Alliance 2605 (Waters) provided with a PDA2996 variable-wavelength detec-

tor and using an Xterra MS C18 column (4.6 mm × 150 mm), a Symmetry C18 column (2.1 mm × 150 mm), or an Atlantis DC18 3 μm (2.1 mm × 100 mm), depending on the case. Mixtures of 0.1% of formic acid in water (solvent A) and 0.1% of formic acid in CH_3CN (solvent B) were used as mobile phases.

General Procedure for the Synthesis of Indole–Tacrine Analogues 3–23. To a solution of the corresponding indole carboxylic acid **2a–i** derivative in anhydrous THF was added 1,1′-carbonyldiimidazol under N_2, and the resulting mixture was stirred for 4 h at room temperature. A solution of the corresponding 9-alkylaminotetrahydroacridine **1a–i** in THF was added, and the stirring was continued for a further 20 h. After evaporation of the solvent under reduced pressure, water was added and the resulting mixture was extracted with dichloromethane. The combined organic extracts were washed with saturated NaCl solution and dried with Na_2SO_4. Evaporation of the solvent under reduced pressure gave a residue that was purified by silica gel flash-column chromatography as indicated below for each case.

3-(1*H*-Indol-3-yl)-*N*-[5-(1,2,3,4-tetrahydroacridin-9-ylamino)pentyl]propionamide (3). Indole-3-propionic acid (**2a**) (63 mg, 0.33 mmol), anhydrous THF (3 mL), 1,1′-carbonyldiimidazol (57 mg, 0.35 mmol), and 9-(5-aminopentylamino)-1,2,3,4-tetrahydroacridine (**1a**) (100 mg, 0.35 mmol) were used to produce **3**. Purification: DCM/MeOH (3:1). Yellow foam (147 mg, 97%). RP HPLC (Atlantis DC18) t_R = 7.83 (8 min gradient from 95:5 to 0:100 A/B). ESI-MS *m/z* 455 [M + H]$^+$. Anal. ($C_{29}H_{34}N_4O\cdot H_2O$) C, H, N.

***N*-[5-(6-Chloro-1,2,3,4-tetrahydroacridin-9-ylamino)pentyl]-3-(1*H*-indol-3-yl)propionamide (4).** Indole-3-propionic acid (**2a**) (57 mg, 0.3 mmol), anhydrous THF (3 mL), 1,1′-carbonyldiimidazol (51 mg, 0.32 mmol), and 6-chloro-9-(5-aminopentylamino)-1,2,3,4-tetrahydroacridine (**1b**) (100 mg, 0.32 mmol) were used to produce **4**. Purification: DCM/MeOH (7:1). Yellow foam (121 mg, 83%). RP HPLC (Symmetry C18) t_R = 5.95 (10 min gradient from 100:0 to 0:100 A/B). ESI-MS *m/z* 489 [M + H]$^+$. Anal. ($C_{29}H_{33}ClN_4O$) C, H, N.

***N*-[5-(6-Chloro-1,2,3,4-tetrahydroacridin-9-ylamino)hexyl]-3-(1*H*-indol-3-yl)propionamide (5).** Indole-3-propionic acid (**2a**) (70 mg, 0.37 mmol), anhydrous THF (3 mL), 1,1′carbonyldiimidazole (63 mg, 0.39 mmol), and 6-chloro-9-(6-aminohexylamino)-1,2,3,4-tetrahydroacridine (**1c**) (131 mg, 0.39 mmol) were used to produce **5**. Purification: DCM/MeOH (50:1, 25:1, 20:1). Yellow foam (143 mg, 77%). RP HPLC (Symmetry C18) t_R = 5.43 (8 min from 95:5 to 0:100 A/B). ESI-MS *m/z* 503 [M + H]$^+$. Anal. ($C_{30}H_{35}ClN_4O\cdot 0.5H_2O$) C, H, N.

***N*-[7-(6-Chloro-1,2,3,4-tetrahydroacridin-9-ylamino)heptyl]-3-(1*H*-indol-3-yl)propionamide (6).** Indole-3-propionic acid (**2a**) (70 mg, 0.37 mmol), anhydrous THF (3 mL), 1,1′-carbonyldiimidazole (63 mg, 0.39 mmol), and 6-chloro-9-(7-aminoheptylamino)-1,2,3,4-tetrahydroacridine (**1d**) (135 mg, 0.39 mmol) were used to produce **6**. Purification: AcOEt/MeOH (50:1). Yellow foam (151 mg, 79%). RP HPLC (Symmetry C18) t_R = 5.60 (8 min from 95:5 to 0:100 A/B). ESI-MS *m/z* 517 [M + H]$^+$. Anal. ($C_{31}H_{37}ClN_4O\cdot 0.5H_2O$) C, H, N.

***N*-[8-(6-Chloro-1,2,3,4-tetrahydroacridin-9-ylamino)octyl]-3-(1*H*-indol-3-yl)propionamide (7).** Indole-3-propionic acid (**2a**) (70 mg, 0.37 mmol), anhydrous THF (3 mL), 1,1′-carbonyldiimidazole (63 mg, 0.39 mmol), and 6-chloro-9-(8-aminooctylamino)-1,2,3,4-tetrahydroacridine (**1e**) (140 mg, 0.39 mmol) were used to produce **7**. Purification: AcOEt/MeOH (50:1). Yellow syrup (104 mg, 53%). RP HPLC (Symmetry C18) t_R = 5.77 (8 min from 95:5 to 0:100 A/B). ESI-MS *m/z* 531 [M + H]$^+$. Anal. ($C_{32}H_{39}ClN_4O\cdot 0.5H_2O$) C, H, N.

***N*-[9-(6-Chloro-1,2,3,4-tetrahydroacridin-9-ylamino)nonyl]-3-(1*H*-indol-3-yl)propionamide (8).** Indole-3-propionic acid (**2a**) (28 mg, 0.15 mmol), anhydrous THF (3 mL), 1,1′-carbonyldiimidazole (25 mg, 0.15 mmol), and 6-chloro-9-(9-aminononylamino)-1,2,3,4-tetrahydroacridine (**1f**) (57 mg, 0.15 mmol) were used to produce **8**. Purification: DCM/MeOH (7:1).Yellow foam (10 mg, 14%). RP HPLC (Atlantis DC18) t_R = 8.90 (8 min gradient from 95:5 to 0:100 A/B and 2 min isocratic at 0:100 A/B). ESI-MS *m/z* 545 [M + H]$^+$. Anal. ($C_{33}H_{41}ClN_4O\cdot H_2O$) C, H, N.

***N*-[10-(6-Chloro-1,2,3,4-tetrahydroacridin-9-ylamino)decyl]-3-(1*H*-indol-3-yl)propionamide (9).** Indole-3-propionic acid (**2a**) (47 mg, 0.25 mmol), anhydrous THF (4 mL), 1,1′-carbonyldiimidazol (44 mg, 0.27 mmol), and 6-chloro-9-(10-aminodecylamino)-1,2,3,4-tetrahydroacridine (**1g**) (105 mg, 0.27 mmol) were used to produce **9**. Purification: DCM/MeOH (10:1). Yellow foam (21 mg, 19%). RP HPLC (Atlantis DC18) t_R = 9.18 (8 min gradient from 95:5 to 0:100 A/B and 2 min isocratic at 0:100 A/B). ESI-MS *m/z* 559 [M + H]$^+$. Anal. ($C_{34}H_{43}ClN_4O\cdot 2H_2O$) C, H, N.

***N*-(3-{[3-(1,2,3,4-Tetrahydroacridin-9-ylamino)propyl]-methylamino}propyl)-3-(1*H*-indol-3-yl)propionamide (10).** Indole-3-propionic acid (**2a**) (56 mg, 0.29 mmol), anhydrous THF (4 mL), 1,1′carbonyldiimidazole (50 mg, 0.31 mmol), and *N*^{1}-[3-(1,2,3,4-tetrahydroacridin-9-ylamino)propyl]-*N*^{1}-methylpropane-1,3-diamine (**1h**) (100 mg, 0.31 mmol) were used to produce **10**. Purification: DCM/MeOH (20:1 + 0.1% NH_3, 10:1 + 0.2% NH_3, 10:1 + 0.4% NH_3). Yellow syrup (70 mg, 46%). RP HPLC (Symmetry C18) t_R = 3.98 (8 min gradient from 95:5 to 0:100 A/B). ESI-MS: *m/z* 498 [M + H]$^+$. Anal. ($C_{31}H_{39}N_5O\cdot H_2O$) C, H, N.

***N*-(3-{[3-(6-Chloro-1,2,3,4-tetrahydroacridin-9-ylamino)propyl]methylamino}propyl)-3-(1*H*-indol-3-yl)propionamide (11).** Indole-3-propionic acid (**2a**) (56 mg, 0.29 mmol), anhydrous THF (4 mL), 1,1′-carbonyldiimidazole (50 mg, 0.3 1 mmol), and *N*^{1}-[3-(6-chloro-1,2,3,4-tetrahydroacridin-9-ylamino)propyl]-*N*^{1}-methylpropane-1,3-diamine (**1i**) (100 mg, 0.31 mmol) were used to produce **11**. Purification: DCM/MeOH (20:1 + 0.1% NH_3, 10:1 + 0.2% NH_3, 10:1 + 0.4% NH_3). Yellow syrup (70 mg, 46%). RP HPLC (Atlantis DC18) t_R = 1.50 (8 min gradient from 95:5 to 0:100 A/B). ESI-MS: *m/z* 532 [M + H]$^+$. Anal. ($C_{31}H_{38}ClN_5O$) C, H, N.

***N*-[6-(6-Chloro-1,2,3,4-tetrahydroacridin-9-ylamino)hexyl]-3-(5-cyano-1*H*-indol-3-yl)propionamide (12).** 5-Cyanoindole-3-propionic acid (**2b**) (111 mg, 0.52 mmol),[35] anhydrous THF (10 mL), 1,1′-carbonyldiimidazol (84 mg, 0.52 mmol), and 6-chloro-9-(6-aminohexylamino)-1,2,3,4-tetrahydroacridine (**1c**) (164 mg, 0.49 mmol) were used to produce **12**. Purification: EtOAc/MeOH 50:1. Yellow syrup (60 mg 22%). RP HPLC (Symmetry C18) t_R = 5.33 (8 min from 95:5 to 0:100 A/B). ESI-MS: *m/z* 528 [M + H]$^+$. Anal. ($C_{31}H_{34}ClN_5O\cdot 1.5H_2O$) C, H, N.

***N*-[6-(6-Chloro-1,2,3,4-tetrahydroacridin-9-ylamino)hexyl]-3-(1*H*-indol-3-yl)acrylamide (13).** Indole-3-acrylic acid (**2c**) (88 mg, 0.47 mmol), anhydrous THF (6 mL), 1,1′-carbonyldiimidazole (76 mg, 0.47 mmol), and 6-chloro-9-(6-aminohexylamino)-1,2,3,4-tetrahydroacridine (**1c**) (150 mg, 0.45 mmol) were used to produce **13**. Purification: EtOAc/MeOH (100:1, 100:1 + 0.1% NH_3). Yellow foam (20 mg, 8%). RP HPLC (Symmetry C18) t_R = 5.46 (8 min from 95:5 to 0:100 A/B). ESI-MS: *m/z* 501 [M]$^+$. Anal. ($C_{30}H_{33}ClN_4O\cdot H_2O$) C, H, N.

1*H*-Indole-3-carboxylic Acid [5-(6-Chloro-1,2,3,4-tetrahydroacridin-9-ylamino)pentyl]amide (14). Indole-3-carboxylic acid (**2d**) (151 mg, 0.94 mmol), anhydrous THF (4 mL), 1,1′-carbonyldiimidazole (153 mg, 0.94 mmol), and 6-chloro-9-(5-aminopentylamino)-1,2,3,4-tetrahydroacridine (**1b**) (276 mg, 0.90 mmol) were used to produce **14**. Purification: EtOAc/MeOH 50:1. Yellow foam (198 mg, 52%). RP HPLC (Symmetry C18) t_R = 5.12 (8 min from 95:5 to 0:100 A/B). ESI-MS: *m/z* 461.07 [M]$^+$. Anal. ($C_{27}H_{29}ClN_4O\cdot H_2O$) C, H, N.

1*H*-Indole-3-carboxylic Acid [6-(6-Chloro-1,2,3,4-tetrahydroacridin-9-ylamino)hexyl]amide (15). Indole-3-carboxylic acid (**2d**) (153 mg, 0.95 mmol), anhydrous THF (10 mL), 1,1′-carbonyldiimidazole (154 mg, 0.95 mmol), and 6-chloro-9-(6-aminohexylamino)-1,2,3,4-tetrahydroacridine (**1c**) (300 mg, 0.90 mmol) were used to produce **15**. Purification: EtOAc/MeOH 50:1. Clear yellow foam (120 mg, 28%). RP HPLC (Symmetry C18) t_R = 5.32 (8 min from 95:5 to 0:100 A/B). ESI-MS: *m/z* 475 [M + H]$^+$. Anal. ($C_{28}H_{31}ClN_4O$) C, H, N.

1*H*-Indole-3-carboxylic Acid [7-(6-Chloro-1,2,3,4-tetrahydroacridin-9-ylamino)heptyl]amide (16). Indole-3-

carboxylic acid (**2d**) (147 mg, 0.91 mmol), anhydrous THF (10 mL), 1,1'-carbonyldiimidazole (147 mg, 0.91 mmol), and 6-chloro-9-(7-aminoheptylamino)-1,2,3,4-tetrahydroacridine (**1d**) (300 mg, 0.87 mmol). Purification: EtOAc/MeOH 50:1. Yellow foam (226 mg, 51%). RP HPLC (Symmetry C18) t_R = 5.49 (8 min from 95:5 to 0:100 A/B). ESI-MS: *m/z* 489 $[M + H]^+$. Anal. ($C_{29}H_{33}ClN_4O \cdot H_2O$) C, H, N.

1*H*-Indole-3-carboxylic Acid [8-(6-Chloro-1,2,3,4-tetrahydroacridin-9-ylamino)octyl]amide (17). Indole-3-carboxylic acid (**2d**) (92 mg, 0.57 mmol), anhydrous THF (3 mL), 1,1'-carbonyldiimidazol (92 mg, 0.57 mmol), and 6-chloro-9-(8-aminooctylamino)-1,2,3,4-tetrahydroacridine (**1e**) (196 mg, 0.54 mmol) were used to produce **17**. Purification: hexane/EtOAc (1:2 + 0.1% NH_3, 1:3 + 0.2% NH_3). Yellow foam (110 mg, 40%). RP HPLC (Symmetry C18) t_R = 5.67 (8 min from 95:5 to 0:100 A/B). ESI-MS: *m/z* 503 $[M + H]^+$. Anal. ($C_{30}H_{35}ClN_4O$) C, H, N.

***N*-[7-(6-Chloro-1,2,3,4-tetrahydroacridin-9-ylamino)heptyl]-2-(1*H*-indol-3-yl)acetamide (18).** Indole-3-acetic acid (**2e**) (1.10 g, 6.3 mmol), anhydrous THF (50 mL), 1,1'-carbonyldiimidazole (1.07 g, 6.6 mmol), and 6-chloro-9-(7-aminoheptylamino)-1,2,3,4-tetrahydroacridine (**1d**) (2.29 g, 6.6 mmol) were used to produce **18**. Purification: EtOAc/MeOH 50:1. Clear yellow foam (2.48 g, 80%). RP HPLC (Symmetry C18) t_R = 5.52 (8 min from 95:5 to 0:100 A/B). ESI-MS: *m/z* 503 $[M + H]^+$. Anal. ($C_{30}H_{35}ClN_4O \cdot H_2O$) C, H, N.

2-(5-Bromo-1*H*-indol-3-yl)-*N*-[7-(6-chloro-1,2,3,4-tetrahydroacridin-9-ylamino)heptyl]acetamide (19). 5-Bromoindole-3-acetic acid (**2f**) (155 mg, 0.61 mmol), anhydrous THF (10 mL), 1,1'-carbonyldiimidazol (99 mg, 0.61 mmol), and 6-chloro-9-(7-aminoheptylamino)-1,2,3,4-tetrahydroacridine (**1d**) (200 mg, 0.58 mmol) were used to produce **19**. Purification: EtOAc/MeOH 50:1. Clear yellow foam (185 mg, 54%). RP HPLC (Symmetry C18) t_R = 5.76 (8 min from 95:5 to 0:100 A/B). ESI-MS: *m/z* 581 $[M + 1, {}^{79}Br]^+$, 583 $[M + 1, {}^{81}Br]^+$. Anal. ($C_{30}H_{35}ClN_4O \cdot H_2O$) C, H, N.

***N*-[5-(6-Chloro-1,2,3,4-tetrahydroacridin-9-ylamino)pentyl]-4-(1*H*-indol-3-yl)butyramide (20).** Indole-3-butyric acid (**2g**) (134 mg, 0.66 mmol), anhydrous THF (10 mL), 1,1'-carbonyldiimidazole (107 mg, 0.66 mmol), and 6-chloro-9-(5-aminopentylamino)-1,2,3,4-tetrahydroacridine (**1b**) (200 mg, 0.63 mmol) were used to produce **20**. Purification: EtOAc/MeOH 100:1. Yellow foam (220 mg, 44%). RP HPLC (Symmetry C18) t_R = 5.43 (8 min from 95:5 to 0:100 A/B). ESI-MS: *m/z* 503 $[M + H]^+$. Anal. ($C_{30}H_{35}ClN_4O \cdot H_2O$) C, H, N.

***N*-[6-(6-Chloro-1,2,3,4-tetrahydroacridin-9-ylamino)hexyl]-4-(1*H*-indol-3-yl)butyramide (21).** Indole-3-butyric acid (**2g**) (134 mg, 0.66 mmol), anhydrous THF (8 mL), 1,1'-carbonyldiimidazol (107 mg, 0.66 mmol), and 6-chloro-9-(6-aminohexylamino)-1,2,3,4-tetrahydroacridine (**1c**) (200 mg, 0.63 mmol) were used to produce **21**. Purification: silica gel column chromatography using DCM/MeOH (20:1, 20:1 + 0.01% NH_3). Yellow syrup (163 mg, 48%). RP HPLC (Symmetry C18) t_R = 5.32 (8 min from 95:5 to 0:100 A/B). ESI-MS: *m/z* $[M + H]^+$ 517. Anal. ($C_{31}H_{37}ClN_4O \cdot H_2O$) C, H, N.

1*H*-Methylindole-3-carboxylic Acid [7-(6-Chloro-1,2,3,4-tetrahydroacridin-9-ylamino)heptyl]amide (22). 1-Methylindole-3-carboxylic acid (**2h**) (214 mg, 1.22 mmol), anhydrous THF (20 mL), 1,1'-carbonyldiimidazole (197 mg, 1.22 mmol), and 6-chloro-9-(7-aminoheptylamino)-1,2,3,4-tetrahydroacridine (**1d**) (400 mg, 1.16 mmol) were used to produce **22**. Purification: EtOAc/MeOH 50:1. Yellow foam (141 mg, 23%). RP HPLC (Symmetry C18) t_R = 5.70 (8 min from 95:5 to 0:100 A/B). ESI-MS: *m/z* 503 $[M + H]^+$. Anal. ($C_{30}H_{35}ClN_4O \cdot H_2O$) C, H, N.

1*H*-Indazole-3-carboxylic Acid [7-(6-Chloro-1,2,3,4-tetrahydroacridin-9-ylamino)heptyl]amide (23). Indazole-3-carboxylic acid (**2h**) (187 mg, 1.15 mmol), anhydrous THF (5 mL), 1,1'-carbonyldiimidazol (162 mg, 1.20 mmol), and 6-chloro-9-(7-aminoheptylamino)-1,2,3,4-tetrahydroacridine (**1d**) (345 mg, 1.15 mmol) were used to produce **23**. Purification: EtOAc/MeOH 50:1. Yellow syrup (79 mg, 13%). RP HPLC (Symmetry C18) t_R = 5.58 (8 min from 95:5 to 0:100 A/B). ESI-MS: *m/z* 490 $[M + H]^+$. Anal. ($C_{28}H_{32}ClN_5O$) C, H, N.

Synthesis of Intermediate Carbonic Acid 2-(1*H*-Indol-3-yl)ethyl Ester 4-Nitrophenyl Ester (26). To a solution of 2-(1*H*-indol-3-yl)ethanol (**24**) (1600 mg, 9.92 mmol) in *N*-methylmorpholine (2000 mg, 19.84 mmol) was added *p*-nitrophenyl chloroformate (**25**) (4000 mg, 19.84 mmol), and the mixture was stirred for 24 h at room temperature. Water was added, and the mixture was extracted with dichloromethane. Evaporation of the solvent gave a residue that was purified by silica gel column chromatography using a mixture of DCM/hexane (3:1) as eluent to produce the title compound **26** (1034 mg, 32%) as a yellow solid. ESI-MS 327 *m/z* $[M + H]^+$.

General Synthesis of Carbamate Derivatives 27–29. To a solution of the carbonic acid 2-(1*H*-indol-3-yl)ethyl ester 4-nitrophenyl ester (**26**) in MeOH was added a solution of the corresponding alkylaminotetrahydroacridine in DMF, in the presence of DMAP, and the resulting mixture was stirred for 24 h at room temperature. After evaporation of the solvent under reduced pressure, water was added and the resulting mixture was extracted with dichloromethane. The combined organic extracts were washed with saturated NaCl solution and filtered, and the solvent was evaporated to give a residue that was purified by silica gel column chromatography as indicated below for each case.

[5-(6-Chloro-1,2,3,4-tetrahydroacridin-9-ylamino)pentyl]carbamic Acid 2-(1*H*-Indol-3-yl)ethyl Ester (27). N^1-(6-Chloro-1,2,3,4-tetrahydroacridin-9-yl)pentane-1,5-diamine (**1b**) (500 mg, 1.58 mmol), carbonic acid 2-(1*H*-indol-3-yl)ethyl ester 4-nitrophenyl ester (**26**) (260 mg, 0.79 mmol), and DMAP (1930 mg, 1.58 mmol) were used to produce **27**. Purification: DCM/MeOH (7:0.5). Yellow syrup (126 mg, 32%). RP HPLC (Atlantis DC18) t_R = 8.60 (8 min gradient from 95:5 to 0:100 A/B and 2 min isocratic at 0:100 A/B). ESI-MS: *m/z* 505.1 $[M + H]^+$. Anal. ($C_{29}H_{33}ClN_4O_2 \cdot H_2O$) C, H, N.

[6-(6-Chloro-1,2,3,4-tetrahydroacridin-9-ylamino)hexyl]carbamic Acid 2-(1*H*-Indol-3-yl)ethyl Ester (28). N^1-(6-Chloro-1,2,3,4-tetrahydroacridin-9-yl)hexane-1,6-diamine (**1c**) (610 mg, 1.84 mmol), carbonic acid 2-(1*H*-indol-3-yl)ethyl ester 4-nitrophenyl ester (**26**) (300 mg, 0.92 mmol), and DMAP (225 mg, 1.84 mmol) were used to produce **28**. Purification: DCM/MeOH (7:0.5). Amber syrup (100 mg, 21%). RP HPLC (Atlantis DC18) t_R = 8.70 (8 min gradient from 95:5 to 0:100 A/B and 2 min isocratic at 0:100 A/B). ESI-MS: *m/z* 519.2 $[M + H]^+$. Anal. ($C_{30}H_{35}ClN_4O_2 \cdot 0.5H_2O$) C, H, N.

[7-(6-Chloro-1,2,3,4-tetrahydroacridin-9-ylamino)heptyl]carbamic Acid 2-(1*H*-Indol-3-yl)ethyl Ester (29). N^1-(6-Chloro-1,2,3,4-tetrahydroacridin-9-yl)heptane-1,7-diamine (**1d**) (344 mg, 1.0 mmol), carbonic acid 2-(1*H*-indol-3-yl)ethyl ester 4-nitrophenyl ester (**26**) (166 mg, 0.5 mmol), and DMAP (122 mg, 1.0 mmol) were used to produce **29**. Purification: DCM/MeOH (7:0.5). Amber syrup (70 mg, 40%). RP HPLC (Atlantis DC18) t_R = 8.90 (8 min gradient from 95:5 to 0:100 A/B and 2 min isocratic at 0:100 A/B). ESI-MS: *m/z* 533.1 $[M + H]^+$. Anal. ($C_{31}H_{37}ClN_4O_2 \cdot 0.5H_2O$) C, H, N.

Biochemical Methods. In Vitro AChE Inhibition Assay. Inhibitory activity against AChE was evaluated at 30 °C by the colorimetric method reported by Ellman et al.[39] The assay solution consisted of 0.1 M phosphate buffer, pH 8, 0.3 mM 5,5'-dithiobis(2-nitrobenzoic acid) (DTNB, Ellman's reagent), 0.02 units of AChE (Sigma Chemical Co. from bovine erythrocytes or human brain), and 0.5 mM acetylthiocholine iodide as the substrate of the enzymatic reaction. Compounds tested were added to the assay solution and preincubated with the enzyme for 10 min at 30 °C. After that period, the substrate was added. The absorbance changes at 405 nm were recorded for 5 min with a microplate reader Digiscan 340T, the reaction rates were compared, and the percent inhibition due to the presence of the test compounds was calculated. The compound concentration producing 50% of AChE inhibition (IC_{50}) was determined for each compound. The sigmoidal dose response curves have been fit by nonlinear regression (GraphPad Prism 4 software). The experimental uncertainties were calculated as 95% confidence interval.

In Vitro BChE Inhibition Assay. BChE inhibitory activity was evaluated at 30 °C by the colorimetric method reported by Ellman et al.[39] The assay solution consisted of 0.01 units of BChE (Sigma Chemical Co. from human serum), 0.1 M sodium phosphate buffer, pH 8, 0.3 mM 5,5'-dithiobis(2-nitrobenzoic acid) (DTNB, Ellman's reagent), and 0.5 mM butyrylthiocholine iodide as the substrate of the enzymatic reaction. Enzyme activity was determined by measuring the absorbance at 405 nm during 5 min with a microplate reader Digiscan 340T. The tested compounds were preincubated with the enzyme for 10 min at 30 °C before starting the reaction by adding the substrate. The reaction rate was calculated with at least triplicate measurements. The IC_{50} is defined as the concentration of compounds that reduces by 50% the enzymatic activity with respect to that without inhibitors. The sigmoidal dose response curves have been fit by nonlinear regression (GraphPad Prism 4 software). The experimental uncertainties were calculated as 95% confidence interval.

Inhibition of β-Amyloid Peptide Aggregation Assay. Thioflavin T-Based Fluorometric Assay. Aβ peptide (1−40), lyophilized from HFIP solution (rPeptide, GA), was dissolved in DMSO to obtain a 2.3 mM solution. Aliquots of Aβ in DMSO were then incubated in constant rotation for 24 h at room temperature in 0.215 M sodium phosphate buffer (pH 8.0) at a final Aβ concentration of 10 μM in the presence or absence of compounds or propidium at 100 μM, used as reference. To quantify amyloid fibril formation, the thioflavin T fluorescence method was used. Analyses were performed with a Fluostar Optima plate reader (BMG). Fluorescence was measured at 450 nm (λ excitation) and 485 nm (λ emission). To determine amyloid fibril formation, after incubation, the solutions containing Aβ or Aβ plus AChE inhibitors were added to 50 mM glycine−NaOH buffer, pH 8.5, containing 3 μM thioflavin T in a final volume of 150 μL. Each assay was run in triplicate. The fluorescence intensities were recorded, and the percent aggregation was calculated by the following expression: $100 - (IF_i/IF_0 \times 100)$ where IF_i and IF_0 are the fluorescence intensities obtained for Aβ in the presence and in the absence of inhibitor, respectively, after subtracting the fluorescence of respective blanks (method adapted from ref 45).

Inhibition of AChE-Induced β-Amyloid Peptide Aggregation Assay. Thioflavin T-Based Fluorometric Assay. Aliquots of 2 μL Aβ(1−40) peptide (Bachem AG, Bubendorf, Switzerland), lyophilized from 2 mg mL^{-1} HFIP solution and dissolved in DMSO, were incubated for 24 h at room temperature in 0.215 M sodium phosphate buffer (pH 8.0) at a final concentration of 230 μM. For co-incubation experiments, aliquots (16 μL) of human recombinant AChE (final concentration of 2.30 μM, Aβ/AChE molar ratio of 100:1) and AChE in the presence of 2 μL of the tested inhibitors were added. Blanks containing Aβ, AChE, and Aβ plus inhibitors at various concentrations in 0.215 M sodium phosphate buffer (pH 8.0) were prepared. The final volume of each vial was 20 μL. Each assay was run in duplicate. Inhibitor stock solutions were prepared ($c = 1.0$ or 0.5 mM) and diluted in methanol. To quantify amyloid fibril formation, the thioflavin T fluorescence method is then applied.[47−49]

Analyses were performed with a Jasco spectrofluorimeter FP-750 using a 3 mL quartz cell. After incubation, the samples containing Aβ, Aβ plus AChE, or Aβ plus AChE in the presence of inhibitors were diluted with 50 mM glycine−NaOH buffer (pH 8.5) containing 1.5 μM thioflavin T to a final volume of 2.0 mL. Fluorescence was monitored with excitation at 446 nm and emission at 490 nm. A time scan of fluorescence is performed, and the intensity values reached at the plateau (around 300 s) are averaged after subtracting the background fluorescence from 1.5 μM thioflavin T and AChE.

The fluorescence intensities were compared, and the percentage of inhibition due to the presence of the tested compounds was calculated. The percent inhibition of the AChE-induced aggregation due to the presence of increasing concentrations of the inhibitor was calculated by the following expression: $100 - (IF_i/IF_0 \times 100)$ where IF_i and IF_0 are the fluorescence intensities obtained for Aβ plus AChE in the presence and in the absence of inhibitor, respectively, after subtracting the fluorescence of respective blanks. Inhibition curves were obtained for each compound by plotting the percent inhibition versus the logarithm of inhibitor concentration in the assay sample. The linear regression parameters were then determined and the IC_{50} was extrapolated, when possible (Microcal Origin, version 3.5, Microcal Software Inc.).

Cytotoxicity. The cytotoxicity effect of the synthesized compounds was studied in the human neuroblastoma cell line SH-SY5Y. These cells were cultured in 96-well plates in minimum essential medium and Ham's F12 medium, supplemented with 10% fetal bovine serum, 1% glutamine, and 1% penicillin/streptomycin, and grown in a 5% CO_2 humidified incubator at 37 °C. Cells were plated at 10^4 cells for each well at least 48 h before the toxicity measurements. Cells were exposed for 24 h to the compound at different concentrations, and quantitative assessment of cell death was made by measurement of the intracellular enzyme lactate dehydrogenase (LDH) (cytotoxicity detection kit, Roche). The quantity of LDH was evaluated in a microplate reader, Anthos 2010, at 492 nm (λ excitation) and 620 nm (λ emission). Controls were taken as having 100% viability.

Molecular modeling methods. Setup of the Model. The simulation system was defined following the protocol used in our previous studies on AChE−ligand complexes,[41,50] which is briefly summarized here. The simulation system was based on the X-ray crystallographic structures of the AChE complexes with tacrine (PDB entry 1ACJ),[51] huprine Y (1E66),[42] and donepezil (1EVE),[52] which were used as templates to position the 6-chlorotacrine unit in the catalytic binding site, the linker along the gorge, and the indole unit in the peripheral binding site. The enzyme was modeled in its physiologically active form with neutral His440 and deprotonated Glu327, which form together with Ser200 the catalytic triad. The standard ionization state at neutral pH was considered for the rest of the ionizable residues with the exception of Asp392 and Glu443, which were neutral, and His471, which was protonated, according to previous numerical titration studies.[53] Finally, Phe330 was replaced by Tyr to reflect the binding site sequence in bovine AChE. According to the basicity of the quinoline ring,[54] the heterodimer was protonated at the tacrine ring. The orientation of the methylene side chain with regard to tacrine was determined by means of geometry optimizations performed at the MP2/6-31G(d) level using Gaussian 03.[55] With regard to the indole moiety, two different starting orientations were initially chosen. In both cases the indole ring was stacked against Trp279, though they differed by a 180° rotation around the bond linking the indole unit to the methylene side chain of the linker. The system was hydrated by centering a sphere of 40 Å of TIP3P[56] water molecules at the inhibitor, paying attention to filling the position of the crystallographic waters inside the binding cavity. The parm98 file of the AMBER force field[57] was used to describe the enzyme. For the inhibitor, the charge distribution of tacrine, linker, and indole units was determined from fitting to the HF/6-31G(d) electrostatic potential using the RESP procedure,[58] and the van der Waals parameters were taken from those defined for related atoms in the AMBER force field. The final model system was partitioned into a mobile region and a rigid region. The former included the inhibitor, all the protein residues containing at least one atom within 15 Å from the inhibitor, and all the water molecules, while the rest of atoms defined the rigid part.

Molecular Dynamics Simulation. Starting from the two models of the inhibitor bound to the enzyme (differing in the orientation of the indole ring), the system was energy-minimized and equilibrated using the AMBER program.[59] First, all hydrogen atoms were minimized for 2000 steps of steepest descent. Next, the positions of water molecules were relaxed for 5000 steps of steepest descent plus 3000 steps of conjugate gradient. At this point, the rigid part of the system was kept frozen and the thermalization of the mobile part was started by running four 10 ps molecular dynamics (MD) simulations to increase the temperature to 298 K. Subse-

quently, a 6 ns MD simulation was carried out. Only one of the two simulations provided a stable trajectory, as noted in a small positional root-mean-square deviation (around 0.7 Å for the backbone atoms in the mobile region with regard to the crystallographic structure) and favorable contacts with the enzyme (see text). The characterization of the structural features that mediate the binding of compound **5** to the enzyme was determined by averaging the geometrical parameters for the snapshots (saved every picosecond) sampled along the last 2 ns of the MD simulation.

Supporting Information Available: Elemental analysis data for **3**–**23** and **27**–**29** and ^{1}H and ^{13}C NMR data for **3**–**23** and **26**–**29**. This material is available free of charge via the Internet at http://pubs.acs.org.

References

(1) Walsh, D. M.; Selkoe D. J. Deciphering the molecular basis of memory failure in Alzheimer's disease. *Neuron* **2004**, *44*, 181–193.

(2) Selkoe, D. J. Alzheimer's disease: genes, proteins and therapy. *Physiol. Rev.* **2001**, *81*, 741–766.

(3) Dekoski, S. T. Pathology and pathways of Alzheimer's disease with an update on new development and treatment. *J. Am. Geriatr. Soc.* **2003**, *51*, 314–320.

(4) Tariot P. N.; Federoff, H. J. Current treatment for Alzheimer's disease and future prospects. *Alzheimer Dis. Assoc. Disord.* **2003**, *17*, 105–113.

(5) Kurz, A. The therapeutical potential of tacrine. *J. Neural. Transm., Suppl.* **1998**, *54*, 295–299.

(6) Sugimoto, H. Donepezil hydrochloride: A treatment drug for Alzheimer's disease. *Chem. Rec.* **2001**, *1*, 63–73.

(7) Jann, M. W. Rivastigmine, a new-generation cholinesterase inhibitor for the treatment of Alzheimer's disease. *Pharmacotherapy* **2000**, *20*, 1–12.

(8) Zarotsky, V.; Sramek, J. J.; Cutler, N. R. Galantamine hydrobromide: an agent for Alzheimer's disease. *Am. J. Health-Syst. Pharm.* **2003**, *60*, 446–452.

(9) Soreq, H.; Seidman, S. Acetylcholinesterase: new roles for an old actor. *Nat. Rev. Neurosci.* **2001**, *2*, 8–17.

(10) Johnson, G.; Moore, S. W. The adhesion function on acetylcholinesterase is located at the peripheral anionic site. *Biochem. Biophys. Res. Commun.* **1999**, *258*, 758–762.

(11) Giacobini, E. Cholinesterases: New roles in brain function and in Alzheimer's disease. *Neurochem. Res.* **2003**, *28*, 515–522.

(12) Muñoz, F. J.; Aldunate, R.; Inestrosa, N. C. Peripheral binding site is involved in the neurotrophic activity of acetylcholinesterase. *NeuroReport* **1999**, *26*, 3621–3625.

(13) Sharma, K. V.; Koenigsberger, C.; Brimijoin, S.; Gigbee, J. W. Direct evidence for an adhesive function in the noncholinergic role of acetylcholinesterase in neurite outgrowth. *J Neurosci. Res.* **2001**, *63*, 165–175.

(14) Blasina, M. F.; Faria, A. C.; Gardino, P. F.; Hokoc, J. N.; Almeida, O. M.; de Mello, F. G.; Arruti, C.; Dajas, F. Evidence of noncholinergic function of acetylcholinesterase during development of chicken retina as shown by fasciculin. *Cell Tissue Res.* **2000**, *299*, 173–184.

(15) Inestrosa, N. C.; Alarcón, R. Molecular interactions of acetylcholinesterase with senile plaques. *J. Physiol. (Paris)* **1998**, *92*, 341–344.

(16) Inestrosa, N. C.; Alvarez, A.; Calderon, F. Acetylcholinesterase is a senile plaque component that promotes assembly of amyloid beta-peptide into Alzheimer's filaments. *Mol. Psychiatry* **1996**, *1*, 359–361.

(17) De Ferrari, G. V.; Canales, M. A.; Shin, I.; Weiner, L. M.; Silman, I.; Inestrosa, N. C. A structural motif of acetylcholinesterase that promotes amyloid β-peptide fibril formation. *Biochemistry* **2001**, *40*, 10447–10457.

(18) Bartolini, M.; Bertucci, C.; Cavrini, V.; Andrisano, V. β-Amyloid aggregation induced by human acetylcholinesterase: inhibition studies. *Biochem. Pharmacol.* **2003**, *65*, 407–416.

(19) Pang, Y. P.; Quiram, P.; Jelacic, T.; Hong, F.; Brimijoin, S. Highly potent, selective, and low cost bis-tetrahydroaminoacrine inhibitors of acetylcholinesterase. *J. Biol. Chem.* **1996**, *271*, 23646–23649.

(20) Castro, A.; Martínez, A. Peripheral and dual binding site acetylcholinesterase inhibitors: Implications in the treatment of Alzheimer's disease. *Mini-Rev. Med. Chem.* **2001**, *1*, 267–272.

(21) Tumiatti, V.; Andrisano, V.; Banzi, R.; Bartolini, M.; Rosini, M.; Melchiorre, C. Structure activity relationships of acetylcholinesterase non-covalent inhibitors based on a polyamine backbone. 3. Effect of replacing the inner polymethylene chain with cyclic moieties. *J. Med. Chem.* **2004**, *47*, 6490–6498.

(22) Pang, Y. P.; Kollmeyer, T. M.; Hong, F.; Lee, J. C.; Hammond, P. I.; Haugabouk, S. P.; Brimijoin, S. Rational design of alkylene-linked bis-pyridiniumaldoxines as improved acetylcholinesterase reactivators. *Chem. Biol.* **2003**, *10*, 491–502.

(23) Piazzi, L.; Rampa, A.; Bisi, A.; Gobbi, S.; Belluti, F.; Cavalli, A.; Bartolini, M.; Andrisano, V.; Valenti, P.; Recanatini, M. 3-[4-[[Benzyl(methyl)amino]methyl]phenyl]-6,7-dimethoxy-2*H*-2-chromenone (AP2238) inhibits both acetylcholinesterase and acetylcholinesterase-induced β-amyloid aggregation: a dual function lead for Alzheimer's disease therapy. *J. Med. Chem.* **2003**, *46*, 2279–2282.

(24) Dorronsoro, I.; Castro, A.; Martínez, A. Peripheral and dual-binding site acetylcholinesterase inhibitors as neurodegenerative disease modifying agents. *Expert Opin. Ther. Pat.* **2003**, *13*, 1725–173.

(25) Martínez, A.; Fernández, E.; Castro, A.; Conde, S.; Rodriguez-Franco, M. I.; Baños, J. E.; Badía, A. *N*-Benzylpiperidine derivatives of 1,2,4-thiadiazolidinone as new acetylcholinesterase inhibitors. *Eur. J. Med. Chem.* **2000**, *35*, 913–919.

(26) Castro, A.; Hernández, L.; Dorronsoro, I.; Sáenz, P.; Pérez, C.; Kalko, S.; Orozco, M.; Luque, F. J.; Martínez, A. Synthesis, biological evaluation and modelling studies of dual binding AChE inhibitors. *Med. Chem. Res.* **2002**, *11*, 219–237.

(27) Dorronsoro, I.; Alonso, D.; Castro, A.; Garcia-Palomero, E.; del Monte, M.; Martínez, A. Synthesis and biological evaluation of tacrine–thiadiazolidinone hybrids as dual acetylcholinesterase inhibitors. *Arch. Pharm. Pharm. Res* **2005**, *338*, 18–23.

(28) Martínez, A.; Dorronsoro, I.; Rubio, L.; Alonso, D.; Fuertes, A.; Morales-Alcelay, S.; Del Monte, M.; Garcia-Palomero, E.; Usán, P.; De Austria, C.; Medina, M.; Muñoz, P. Tacrine derivatives as inhibitors of acetylcholinestererase. WO 2005/005413, 2005.

(29) Savini, L.; Gaeta, A.; Fattorusso, C.; Catalanotti, B.; Campiani, G.; Chiasserini, L.; Pellerano, C.; Novellino, E.; McKissic, D.; Saxena, A. Specific target of acetylcholinesterase and butyrylcholinesterase recognition sites. Rational design of novel, selective, and highly potent cholinesterase inhibitors. *J. Med. Chem.* **2003**, *46* (1), 1–4.

(30) Carlier, P. R.; Chow, E. S. H.; Han, Y.; Liu, J.; El Yazla, J.; Pang, Y. P. Heterodimeric tacrine-based acetylcholinesterase inhibitors: investigating ligand–peripheral site interactiones. *J. Med. Chem.* **1999**, *42*, 4225–4231.

(31) Rosini, M.; Andrisano, V.; Bartolini, M.; Bolognesi, M.; Hrelia, P.; Minarini, A.; Tarozzi, A.; Melchiorre, C. Rational Approach To Discover Multipotent Anti-Alzheimer Drugs. *J. Med. Chem.* **2005**, *48* (2), 360–363.

(32) Recanatini, M.; Cavalli, A.; Belluti, F.; Piazzi, L.; Rampa, A.; Bisi, A.; Gobbi, S.; Valenti, P.; Andrisano, V.; Bartolini, M.; Cavrini, V. SAR of 9-amino-1,2,3,4-tetrahydroacrydine-based acetylcholinesterase inhibitors synthesis, enzyme inhibitory activity, QSAR and structure-based COMFA of tacrine analogues. *J. Med. Chem.* **2000**, *43*, 2007–2018.

(33) Sippl, W.; Holtje, H. D. Structure-based 3D-QSAR—merging the accuracy of structure-based alignments with the computational efficiency of ligand-based methods. *J. Mol. Struct.: THEOCHEM* **2000**, *503*, 31–50.

(34) Morzyc-Ociepa, B.; Michaska, D.; Petraszco, A. Structures and vibrational structures of indole carboxylic acids. Part I. Indole-2-carboxylic acid. *J. Mol. Struct.* **2004**, *688*, 79–86.

(35) Ming-Kuan, H. U.; Jiajiu, S. Tacrine derivatives for treating Alzheimer's disease. WO01/17529, 2001.

(36) Padwa, A.; Harring, S. R.; Hertzog, D. L.; Nadlet, W. R. Cycloaddition chemistry of anhydro-4-hydroxy-1,3-thiazolium hydroxides for the synthesis of heterocycles. *Synthesis* **1994**, *9*, 993–1004.

(37) Agarwal, A.; Jalluri, R. K.; DeWitt Blanton, C.; Will Taylor, E. A new synthesis of the potent 5-HT$_1$ receptor ligand, 5-carboxyamidotryptamine *Synth. Commun.* **1993**, *23* (8), 1101–1110.

(38) Dressman, B. A.; Spangle, L. A.; Kaldor, S. W. Solid phase synthesis of hydantoins using a carbamate linker and a novel cyclization/cleavage step. *Tetrahedron Lett.* **1996**, *7*, 937–940.

(39) Ellman, G. L.; Courtney, K. D.; Andres, B.; Featherstone, R. M. A new and rapid colorimetric determination of acetylcholinesterase activity. *Biochem. Pharmacol.* **1961**, *7*, 88–95.

(40) Barril, X.; Kalko, S. G.; Orozco, M.; Luque, F. J. Rational design of reversible acetylcholinesterase inhibitors. *Mini-Rev. Med. Chem.* **2002**, *2*, 27–36.

(41) Camps, P.; El Achab, R.; Morral, J.; Muñoz-Torrero, D.; Badia, A.; Baños, J. E.; Vivas, N. M.; Barril, X.; Orozco, M.; Luque, F. J. New tacrine–huperzine A hybrids (huprines): highly potent tight-binding acetylcholinesterase inhibitors of interest for the treatment of Alzheimer's disease. *J. Med. Chem.* **2000**, *43*, 4657–4666.

(42) Dvir, H.; Wong, D. M.; Harel, M.; Barril, X.; Orozco, M.; Luque, F. J.; Muñoz-Torrero, D.; Camps, P.; Rosenberry, T. L.; Silman, I.; Sussman, J. L. 3D structure of *Torpedo californica* acetylcholinesterase complexed with huprine X at 2.1 Å resolution: Kinetic and molecular dynamics correlates. *Biochemistry* **2002**, *41*, 2970–2981.

(43) Greig, N. H.; Lahiri, D. K.; Sambamurti, K. Butyrylcholinesterase: an important new target in Alzheimer's disease therapy. *Int. Psychogeriatr.* **2002**, *14* (Suppl. 1), 77–91.
(44) Hu, M.-K.; Wu, L.-J.; Hsiao, G.; Yen, M.-H. Homodimeric tacrine congeners as acetylcholinesterase inhibitors. *J. Med. Chem.* **2002**, *45*, 2277–2282.
(45) Bartolini, M.; Bertucci, C.; Cavrini, V.; Andrisano, V. β-amyloid aggregation induced by human acetylcholinesterase: inhibiton studies *Biochem. Pharmacol.* **2003**, *65*, 407–416.
(46) Outcomes of this study recently presented in the 5th Neurobiology of Aging Conference in San Diego, CA, October 21–27, 2004.
(47) LeVine, H. Thioflavine T interaction with synthetic Alzheimer's disease beta-amyloid peptides: detection of amyloid aggregation in solution. *Protein Sci.* **1993**, *2*, 404–410.
(48) Naiki, H.; Higuchi, K.; Nakakuki, K.; Takeda, T. Kinetic analysis of amyloid fibril polymerization in vitro. *Lab. Invest.* **1991**, *65*, 104–110.
(49) LeVine, H., 3rd; Scholten, J. D. Screening for pharmacologic inhibitors of amyloid fibril formation. *Methods Enzymol.* **1999**, *309*, 467–476.
(50) Barril, X.; Orozco, M.; Luque, F. J. Predicting relative binding free energies of tacrine–huperzine A hybrids as inhibitors of acetylcholinesterase. *J. Med. Chem.* **1999**, *42*, 5110–5119.
(51) Sussman, J. L.; Harel, M.; Frolow, F.; Oefner, C.; Goldman, A.; Toker, L.; Silman, I. Atomic structure of acetylcholinesterase from *Torpedo californica*: a prototypic acetylcholine-binding protein. *Science* **1991**, *253*, 872–879.
(52) Kryger, G.; Silman, I.; Sussman, J. L. Structure of acetylcholinesterase complexed with E2020 (Aricept): Implications for the design of new anti-Alzheimer drugs. *Structure* **1999**, *7*, 297–307.
(53) Wlodek, S. T.; Antosiewicz, J.; McCammon, J. A.; Straatsma, T. P.; Gilson, M. K.; Briggs, M. J.; Humblet, C.; Sussman, J. L. Binding of tacrine and 6-chlorotacrine by acetylcholineterase. *Biopolymers* **1996**, *38*, 109–117.
(54) Foye, W. O.; Lemke, T. L.; Williams, D. A. *Principles of Medicinal Chemistry*, 4th ed.; Williams and Wilkins: Media, PA, 1995; Appendix Table A-1.
(55) Frisch, M. J.; Trucks, G. W.; Schlegel, H. B.; Scuseria, G. E.; Robb, M. A.; Cheeseman, J. R.; Montgomery, J. A., Jr.; Vreven, T.; Kudin, K. N.; Burant, J. C.; Millam, J. M.; Iyengar, S. S.; Tomasi, J.; Barone, V.; Mennucci, B.; Cossi, M.; Scalmani, G.; Rega, N.; Petersson, G. A.; Nakatsuji, H.; Hada, M.; Ehara, M.; Toyota, K.; Fukuda, R.; Hasegawa, J.; Ishida, M.; Nakajima, T.; Honda, Y.; Kitao, O.; Nakai, H.; Klene, M.; Li, X.; Knox, J. E.; Hratchian, H. P.; Cross, J. B.; Adamo, C.; Jaramillo, J.; Gomperts, R.; Stratmann, R. E.; Yazyev, O.; Austin, A. J.; Cammi, R.; Pomelli, C.; Ochterski, J. W.; Ayala, P. Y.; Morokuma, K.; Voth, G. A.; Salvador, P.; Dannenberg, J. J.; Zakrzewski, V. G.; Dapprich, S.; Daniels, A. D.; Strain, M. C.; Farkas, O.; Malick, D. K.; Rabuck, A. D.; Raghavachari, K.; Foresman, J. B.; Ortiz, J. V.; Cui, Q.; Baboul, A. G.; Clifford, S.; Cioslowski, J.; Stefanov, B. B.; Liu, G.; Liashenko, A.; Piskorz, P.; Komaromi, I.; Martin, R. L.; Fox, D. J.; Keith, T.; Al-Laham, M. A.; Peng, C. Y.; Nanayakkara, A.; Challacombe, M.; Gill, P. M. W.; Johnson, B.; Chen, W.; Wong, M. W.; Gonzalez, C.; Pople, J. A. *Gaussian 03*, revision B.04; Gaussian, Inc.: Pittsburgh, PA, 2003.
(56) Jorgensen, W. L.; Chandrasekhar, J.; Madura, J. D.; Impey, R. W.; Klein, M. L. Comparison of simple potential functions for simulating liquid water. *J. Chem. Phys.* **1983**, *79*, 926–935.
(57) Cornell, W. D.; Cieplak, P.; Bayly, C. I.; Gould, I. R.; Merz, K. M.; Ferguson, D. M.; Spellmeyer, D. C.; Fox, T.; Caldwell, J. W.; Kollman, P. A. A second generation force field for the simulation of proteins, nucleic acids, and organic molecules *J. Am. Chem. Soc.* **1995**, *117*, 5719–5197.
(58) Bayly, C. I.; Cieplak, P.; Cornell, W. D.; Kollman, P. A. A well-behaved electrostatic potential based method using charge restraints for deriving atomic charges. *J. Phys. Chem.* **1993**, *97*, 10269–10280.
(59) Case, D. A.; Darden, T. A.; Cheatham, T. E.; Pearlman, D. A.; Simmerling, C. L.; Wang, J.; Duke, R. E.; Luo, R.; Merz, K. M.; Pearlman, D. A.; Crowley, M.; Brozell, S.; Tsui, V.; Gohlke, H.; Mongan, J.; Hornak, V.; Cui, G.; Beroza, P.; Schafmeister, P.; Caldwell, J. W.; Ross, W. S.; Kollman, P. A. *AMBER*, version 8; University of California: San Francisco, CA, 2004.

JM0503289

SUPORTING INFORMATION

Design, synthesis and biological evaluation of dual binding site acetylcholinesterase inhibitors: new disease modifying agents for AD

Pilar Muñoz-Ruiz,[§] Laura Rubio,[§] Esther García-Palomero,[§] Isabel Dorronsoro,[§] María del Monte-Millán,[§] Rita Valenzuela,[§] Paola Usán,[§] Celia de Austria,[§] Manuela Bartolini,[‡] Vincenza Andrisano,[‡] Axel Bidon-Chanal,[#] Modesto Orozco,[&] F. Javier Luque,[#] Miguel Medina[§] and Ana Martínez[§]*.

Contents: Elemental Analysis Data for Evaluated Compounds **3-23** and **27-29**; NMR (^{1}H and ^{13}C) data of compounds **3-23**, intermediate carbonic acid **26** and compounds **27-29**

Elemental Analysis Data for Evaluated Compounds 3-23 and 27-29.

compd	Formula	Calculated (%)			Found (%)		
		C	H	N	C	H	N
3	$C_{29}H_{34}N_4O \cdot H_2O$	74.20	7.68	11.54	74.35	7.54	11.20
4	$C_{29}H_{33}ClN_4O$	71.21	6.80	11.46	71.03	7.11	11.37
5	$C_{30}H_{35}ClN_4O \cdot 0.5\ H_2O$	70.40	7.04	10.95	70.39	7.15	10.90
6	$C_{31}H_{37}ClN_4O \cdot 0.5\ H_2O$	70.86	7.24	10.66	71.02	7.21	10.61
7	$C_{32}H_{39}ClN_4O \cdot 0.5\ H_2O$	71.24	7.40	10.38	71.04	7.47	10.17
8	$C_{33}H_{41}ClN_4O \cdot H_2O$	70.38	7.70	9.95	70.52	7.61	10.18
9	$C_{34}H_{43}ClN_4O \cdot 2\ H_2O$	68.68	7.91	9.40	69.06	7.58	9.74
10	$C_{31}H_{39}N_5O \cdot H_2O$	72.20	8.01	13.58	72.55	7.83	13.41
11	$C_{31}H_{38}ClN_5O$	69.97	7.20	13.16	69.73	7.45	12.98
12	$C_{31}H_{34}ClN_5O \cdot 1.5H_2O$	67.15	6.67	12.63	67.18	6.51	12.92
13	$C_{30}H_{33}ClN_4O \cdot H_2O$	69.42	6.80	10.79	69.27	7.20	10.40
14	$C_{27}H_{29}ClN_4O \cdot H_2O$	67.70	6.52	11.70	67.85	6.40	11.62
15	$C_{28}H_{31}ClN_4O$	70.80	6.58	11.79	70.97	6.50	11.92
16	$C_{29}H_{33}ClN_4O \cdot H_2O$	71.22	6.80	11.46	68.57	7.05	11.35
17	$C_{30}H_{35}ClN_4O$	71.62	7.01	11.14	71.43	7.27	11.03
18	$C_{30}H_{35}ClN_4O \cdot H_2O$	69.15	7.16	10.75	69.44	6.89	11.03
19	$C_{30}H_{35}ClN_4O \cdot H_2O$	61.91	5.89	9.63	61.63	5.93	9.47
20	$C_{30}H_{35}ClN_4O \cdot H_2O$	69.15	7.16	10.75	69.33	6.88	10.77
21	$C_{31}H_{37}ClN_4O \cdot H_2O$	69.58	7.35	10.47	69.87	7.14	10.78
22	$C_{30}H_{35}ClN_4O \cdot H_2O$	69.15	7.16	10.75	69.51	6.98	11.15
23	$C_{28}H_{32}ClN_5O$	68.63	6.58	14.29	68.26	6.71	14.05
27	$C_{29}H_{33}ClN_4O_2 \cdot H_2O$	66.79	6.74	10.71	67.14	6.51	10.72
28	$C_{30}H_{35}ClN_4O_2 \cdot 0.5H_2O$	68.31	6.83	10.60	68.02	6.82	10.79
29	$C_{31}H_{37}ClN_4O_2 \cdot 0.5H_2O$	68.76	7.02	10.35	68.69	6.88	10.15

NMR (^{1}H and ^{13}C) data of compounds 3-23, intermediate carbonic acid 26 and compounds 27-29

3-(1*H*-Indol-3-yl)-*N*-[5-(1,2,3,4-tetrahydro-acridin-9-ylamino)-pentyl]-propionamide (3)

^{1}H NMR ($CDCl_3$): δ 8.53 (br s, 1H, NH [indole]), 7.90 (t, 2H, *J*=8.4 Hz, tacrine), 7.55 (t, 1H, *J*=8.4 Hz, tacrine), 7.52 (dd, 1H, *J*=8.0 Hz, *J*=0.8 Hz, indole), 7.35 (t, 1H, *J*=8.4 Hz, tacrine), 7.30 (dd, 1H, *J*=8.0 Hz, *J*=0.8 Hz, indole), 7.13 (td, 1H, *J*=8 Hz, *J*=1.2 Hz, indole), 7.05 (td, 1H, *J*=8.0 Hz, *J*=0.8 Hz, indol), 6.90 (m, 1H, indole), 5.61 (m, 1H, NHCO), 3.90 (br s, 1H, NH), 3.40 (m, 2H, CH_2NH-tacrine), 3.19 (q, 2H, *J*=6.4 Hz, CH_2NHCO), 3.10 (t, 2H, *J*=7.2 Hz, CH_2CO), 3.01 (m, 2H, 4-H [tacrine]), 2.62 (m, 2H, 1-H [tacrine]), 2.56 (t, 2H, *J*=7.2 Hz, CH_2-indole), 1.80-2.00 (m, 4H, 2-, 3-H [tacrine]), 1.60 (m, 2H, CH_2), 1.38 (m, 2H, CH_2), 1.25 (m, 2H, CH_2).

^{13}C NMR ($CDCl_3$): δ 172.9, 158.6, 150.8, 147.0, 136.5, 128.9, 128.8, 127.0, 123.8, 123.0, 122.1, 122.0, 120.1, 119.4, 118.8, 116.2, 114.8, 111.4, 49.6, 39.5, 37.8, 34.4, 31.7, 29.7, 25.2, 24.5, 23.5, 23.2, 21.8.

***N*-[5-(6-Chloro-1,2,3,4-tetrahydro-acridin-9-ylamino)-pentyl]-3-(1*H*-indol-3-yl)-propionamide (4).**

^{1}H-NMR ($CDCl_3$,): δ8.53 (br s, 1H, NH-indole), 7.88 (d, 1H, *J*=8.8 Hz, 8-H [tacrine]), 7.87 (d, 1H, *J*=2.4 Hz, 5-H [tacrine]), 7.55 (dd, 1H, *J*=8.0 Hz, *J*=1.2 Hz, 4-H [indole]), 7.30 (dd, 1H, *J*=8.0 Hz, *J*=0.8 Hz, 7-H [indole]), 7.21 (dd, 1H, *J*=8.8 Hz, *J*=2.4 Hz, 7-H [tacrine]), 7.13 (td, 1H, *J*=8 Hz, *J*=1.2 Hz, 5-H [indole]), 7.06 (td, 1H, *J*=8.0 Hz, *J*=0.8 Hz, 6-H [indole]), 6.90 (m, 1H, 2-H [indol]) 5.61 (m, 1H, NHCO) 4.24 (br s, 1H, NH-tacrine), 3.43 (t, 2H, *J*= 6.4 Hz, C*H*$_2$NH-tacrine), 3.16 (q, 2H, *J*=6.4 Hz, C*H*$_2$NHCO), 3.10 (t, 2H, *J*=7.2 Hz, CH_2CO), 3.01 (m, 2H, 4-H [tacrine]), 2.62 (m, 2H, 1-H [tacrine]), 2.56 (t, 2H, *J*=7.2 Hz, CH_2-indole), 1.84 (m, 4H, 2-, 3-H [tacrine]), 1.60 (2H, m, CH_2), 1.38 (m, 2H, CH_2), 1.25 (m, 2H, CH_2).

^{13}C NMR ($CDCl_3$): δ 172.9, 159.0, 151.4, 147.9, 136.5, 134.6, 127.2, 126.6, 124.9, 124.5, 122.0, 121.9, 119.4, 118.7, 118.2, 115.4, 114.8, 111.4, 49.5, 39.4, 37.7, 33.6, 31.5, 29.6, 24.9, 24.3, 23.1, 22.7, 21.8.

***N*-[5-(6-Chloro-1,2,3,4-tetrahydro-acridin-9-ylamino)-hexyl]-3-(1*H*-indol-3-yl)-propionamide (5).**

^{1}H NMR ($CDCl_3$): δ 8.40 (br s, 1H, NH-indole), 7.85 (d, 1H, *J*=2.4 Hz, 5-H [tacrine]), 7.84 (d, 1H, *J*=8.8 Hz, 8-H [tacrine]), 7.55 (dd, 1H, *J*=8.0 Hz, *J*=1.2 Hz, 4-H [indole]),

7.29 (dd, 1H, *J*=8.0 Hz, *J*=0.8 Hz, 7-H [indole]), 7.23 (dd, 1H, *J*=8.8 Hz, *J*=2.4 Hz, 7-H [tacrine]), 7.15 (td, 1H, *J*=8.0 Hz, *J*=1.2 Hz, 5-H [indole]), 7.07 (td, 1H, *J*=8.0 Hz, *J*=0.8 Hz, 6-H [indole]), 6.97 (m, 1H, 2-H [indol]), 5.41 (m, 1H, NHCO), 4.42 (br s, 1H, NH-tacrine), 3.41 (t, 2H, *J*=6.4 Hz, C*H*$_2$NH-tacrine), 3.13 (q, 2H, *J*=6.4 Hz, C*H*$_2$NHCO), 3.09 (t, 2H, *J*=7.2 Hz, CH_2CO), 3.01 (m, 2H, 4-H [tacrine]), 2.64 (m, 2H, 1-H [tacrine]), 2.54 (t, 2H, *J*=7.2 Hz, CH_2-indole), 1.91-1.88 (m, 4H, 2-, 3-H [tacrine]), 1.59-1.53 (2H, m, CH_2), 1.36-1.27 (m, 4H, 2 CH_2), 1.22-1.16 (m, 2H, CH_2).

^{13}C NMR ($CDCl_3$): δ172.7, 159.4, 150.7, 148.0, 136.4, 134.0, 127.3, 127.1, 124.6, 124.2, 121.8, 119.1, 118.6, 118.4, 115.7, 114.7, 111.3, 49.5, 39.4, 37.6, 34.1, 31.8, 29.6, 26.6, 26.6, 24.8, 23.1, 22.8, 21.7.

_N_-[7-(6-Chloro-1,2,3,4-tetrahydro-acridin-9-ylamino)-heptyl]-3-(1*H*-indol-3-yl)-propionamide (6).

^{1}H NMR ($CDCl_3$): δ8.10 (br s, 1H, NH-indol), 7.87 (d, 1H, *J*=8.8 Hz, 8-H [tacrine]), 7.85 (d, 1H, *J*=2.4 Hz, 5-H [tacrine]), 7.57 (dd, 1H, *J*=8.0 Hz, *J*=1.2 Hz, 4-H [indole]), 7.32 (dd, 1H, *J*=8.0 Hz, *J*=0.8 Hz, 7-H [indole]), 7.24 (dd, 1H, *J*=8.8 Hz, *J*=2.4 Hz, 7-H [tacrine]), 7.16 (td, 1H, *J*=8 Hz, *J*=1.2 Hz, 5-H [indole]), 7.09 (td, 1H, *J*=8.0 Hz, *J*=0.8 Hz, 6-H [indole]), 6.99 (m, 1H, 2-H [indole]), 5.32 (m, 1H, NHCO), 3.91 (br s, 1H, NH-tacrine), 3.45 (t, 2H, *J*=6.4 Hz, C*H*$_2$NH-tacrine), 3.13 (q, 2H, *J*=6.4 Hz, C*H*$_2$NHCO), 3.11 (t, 2H, *J*=7.2 Hz, C*H*$_2$CO), 3.02 (m, 2H, 4-H [tacrine]), 2.65 (m, 2H, 1-H [tacrine]), 2.55 (t, 2H, *J*=7.2 Hz, CH_2-indole), 1.92-1.88 (m, 4H, 2-, 3-H [tacrine]), 1.64-1.57 (m, 2H, CH_2), 1.36-1.14 (m, 8H, 4 CH_2).

^{13}C NMR ($CDCl_3$): δ172.4, 159.3, 150.6, 147.9, 136.1, 133.8, 127.3, 126.9, 124.4, 124.0, 121.8, 121.6, 119.0, 118.5, 118.2, 115.6, 114.7, 111.0, 49.5, 39.3, 37.5, 34.0, 31.7, 29.4, 28.9, 26.7, 26.6, 24.6, 22.9, 22.7, 21.5.

_N_-[8-(6-Chloro-1,2,3,4-tetrahydro-acridin-9-ylamino)-octyl]-3-(1*H*-indol-3-yl)-propionamide (7).

^{1}H NMR ($CDCl_3$): δ8.21 (br s, 1H, NH-indole), 7.86 (d, 1H, *J*=8.8 Hz, 8-H [tacrine]), 7.85 (d, 1H, *J*=2.4 Hz, 5-H [tacrine]), 7.57 (dd, 1H, *J*=8.0 Hz, *J*=1.2 Hz, 4-H [indole]), 7.34 (dd, 1H, *J*=8.0 Hz, *J*=0.8 Hz, 7-H [indole]), 7.24 (dd, 1H, *J*=8.8 Hz, *J*=2.4 Hz, 7-H [tacrine]), 7.16 (td, 1H, *J*=8.0 Hz, *J*=1.2 Hz, 5-H [indole]), 7.09 (td, 1H, *J*=8.0 Hz, *J*=0.8 Hz, 6-H [indole]), 6.99 (m, 1H, 2-H [indole]), 5.35 (m, 1H, NHCO), 3.91 (br s, 1H, NH-tacrine), 3.46 (t, 2H, *J*=6.4 Hz, C*H*$_2$NH-tacrine), 3.14 (q, 2H, *J*=6.4 Hz, C*H*$_2$NHCO), 3.10 (t, 2H, *J*=7.2 Hz, C*H*$_2$CO), 3.01 (m, 2H, 4-H [tacrine]), 2.65 (m, 2H,

1-H [tacrine]), 2.55 (t, 2H, *J*=7.2 Hz, CH_2-indole), 1.92-1.89 (m, 4H, 2-, 3-H [tacrine]), 1.64-1.58 (m, 2H, CH_2), 1.36-1.31 (m, 4H, 2 CH_2), 1.28-1.14 (m, 6H, 3 CH_2).

^{13}C NMR ($CDCl_3$): δ172.6, 159.4, 150.8, 148.1, 136.4, 133.9, 127.4, 127.1, 124.6, 124.1, 121.9, 121.8, 119.1, 118.6, 118.4, 115.7, 114.8, 111.3, 49.7, 39.6, 37.7, 34.2, 31.9, 29.7, 29.3, 27.0, 26.8, 24.8, 23.1, 22.9, 21.0.

_N_-[9-(6-Chloro-1,2,3,4-tetrahydro-acridin-9-ylamino)-nonyl]-3-(1_H_-indol-3-yl)-propionamide (8).

^{1}H NMR ($CDCl_3$): δ8.53 (br s, 1H, NH-indole), 7.88 (d, 1H, *J*=8.8 Hz, 8-H [tacrine]), 7.87 (d, 1H, *J*=2.4 Hz, 5-H [tacrine]), 7.57 (dd, 1H, *J*=8.0 Hz, *J*=1.2 Hz, 4-H [indole]), 7.30 (dd, 1H, *J*=8.0 Hz, *J*=0.8 Hz, 7-H [indole]), 7.21 (dd, 1H, *J*=8.8 Hz, *J*=2.4 Hz, 7-H [tacrine]), 7.13 (td, 1H, *J*=8.0 Hz, *J*=1.2 Hz, 5-H [indole]), 7.06 (td, 1H, *J*=8.0 Hz, *J*=0.8 Hz, 6-H [indole]), 6.90 (m, 1H, 2-H [indole]), 5.61 (m, 1H, NHCO), 4.24 (br s, 1H, NH-tacrine), 3.50 (m, 2H, CH_2NH-tacrine), 3.19 (q, 2H, *J*=6.4 Hz, CH_2NHCO), 3.10 (t, 2H, *J*=7.2 Hz, CH_2CO), 3.01 (m, 2H, 4-H [tacrine]), 2.62 (m, 2H, 1-H [tacrine]), 2.56 (t, 2H, *J*=7.2 Hz, CH_2-indole), 1.81 (m, 4H, 2-, 3-H [tacrine]), 1.52 (m, 2H, CH_2), 1.01-1.40 (m, 12H, 6 CH_2).

^{13}C-NMR ($CDCl_3$): δ172.7, 159.0, 151.2, 147.8, 136.5, 134.3, 127.3, 127.2, 125.0, 124.4, 122.1, 122.0, 119.3, 118.8, 118.2, 115.3, 115.0, 111.4, 49.8, 39.8, 37.8, 34.0, 32.0, 29.8, 29.7, 29.5, 29.5, 27.2, 27.1, 25.0, 23.4, 23.0, 22.0.

_N_-[10-(6-Chloro-1,2,3,4-tetrahydro-acridin-9-ylamino)-decyl]-3-(1_H_-indol-3-yl)-propionamide (9).

^{1}H NMR ($CDCl_3$): δ8.63 (br s, 1H, NH-indole), 7.89 (d, 1H, *J*=8.8 Hz, 8-H [tacrine]), 7.87 (d, 1H, *J*=2.4 Hz, 5-H [tacrine]), 7.56 (dd, 1H, *J*=8.0 Hz, *J*=1.2 Hz, 4-H [indole]), 7.32 (dd, 1H, *J*=8.0 Hz, *J*=0.8 Hz, 7-H [indole]), 7.21 (dd, 1H, *J*=8.8 Hz, *J*=2.4 Hz, 7-H [tacrine]), 7.14 (td, 1H, *J*=8.0 Hz, *J*=1.2 Hz, 5-H [indole]), 7.08 (td, 1H, *J*=8.0 Hz, *J*=0.8 Hz, 6-H [indole]), 6.97 (m, 1H, 2-H [indole]), 5.61 (m, 1H, NHCO), 4.24 (br s, 1H, NH-tacrine), 3.50 (m, 2H, CH_2NH-tacrine), 3.19 (q, 2H, *J*=6.4 Hz, CH_2NHCO), 3.10 (t, 2H, *J*=7.2 Hz, CH_2CO), 3.01 (m, 2H, 4-H [tacrine]), 2.63 (m, 2H, 1-H [tacrine]), 2.56 (t, 2H, *J*=7.2 Hz, CH_2-indole), 1.80-2.00 (m, 4H, 2-, 3-H [tacrine]), 1.51 (m, 2H, CH_2), 1.01-1.40 (m, 14H, 7 CH_2).

^{13}C NMR ($CDCl_3$): δ172.7, 159.0, 151.2, 147.8, 136.5, 134.3, 127.3, 127.2, 125.0, 124.4, 122.1, 122.0, 119.3, 118.8, 118.2, 115.3, 115.0, 111.4, 49.8, 39.8, 37.8, 34.0, 32.0, 29.8, 29.7, 29.6, 29.5, 29.5, 27.2, 27.1, 25.0, 23.4, 23.0, 22.0.

***N*-(3-{[3-(1,2,3,4-tetrahydro-acridin-9-ylamino)-propyl]-methyl-amino}-propyl)-3-(1*H*-indol-3-yl)-propionamide (10).**

^{1}H NMR ($CDCl_3$): δ8.80 (br s, 1H, NH-indole), 7.86 (t, 2H, *J*=8.4 Hz, tacrine), 7.51 (t, 1H, *J*=8.4 Hz, tacrine), 7.46 (d, 1H, *J*=8.4 Hz, indole), 7.27 (td, 1H, *J*=7.0 Hz, *J*= 2.0 Hz, tacrine), 7.25 (d, 1H, *J*=7.0 Hz, indole), 7.10 (td, 1H, *J*=8.0 Hz, *J*=1.2 Hz, indole), 7.03 (td, 1H, *J*=8.0 Hz, *J*=1.2 Hz, indole), 6.85 (d, 1H, *J*=2.4 Hz, indole), 6.37 (t, 1H, *J*=4.5 Hz, NHCO), 5.00 (br s, 1H, NH-tacrine), 3.46 (m, 2H, C*H*$_2$NH-tacrine), 3.19 (q, 2H, *J*=6.3 Hz, C*H*$_2$NHCO), 3.07-3.01 (m, 4H, CH_2CO, 4-H [tacrine]), 2.63 (m, 2H, 1-H [tacrine]), 2.47 (t, 2H, *J*=7.0 Hz, CH_2-indole), 2.36 (t, 2H, *J*=6.4 Hz, C*H*$_2$NMe), 2.24 (t, 2H, *J*=6.8 Hz, C*H*$_2$NMe), 1.91 (s, 3H, NMe), 1.86-1.84 (m, 4H, 2-, 3-H [tacrine]), 1.70-1.67 (m, 2H, CH_2), 1.54-1.50 (m, 2H, CH_2).

^{13}C NMR ($CDCl_3$): δ172.0, 158.3, 150.8, 147.2, 136.3, 128.4, 128.3, 127.1, 123.6, 122.8, 121.8, 121.8 120.2, 119.0, 118.5, 115.9, 114.7, 111.3, 56.6, 56.1, 48.7, 42.2, 38.5, 37.7, 34.0, 28.5, 26.6, 25.3, 23.2, 22.9, 21.7.

***N*-(3-{[3-(6-chloro-1,2,3,4-tetrahydro-acridin-9-ylamino)-propyl]-methyl-amino}-propyl)-3-(1*H*-indol-3-yl)-propionamide (11).**

^{1}H NMR ($CDCl_3$): δ8.79 (br s, 1H, NH-indole), 7.83 (d, 1H, *J*=8.8 Hz, 8-H [tacrine]), 7.79 (d, 1H, *J*=2.4 Hz, 5-H [tacrine]), 7.30 (dd, 1H, *J*=8.0 Hz, *J*=1.2 Hz, 4-H [indole]), 7.24 (dd, 1H, *J*=8.0 Hz, *J*=0.8 Hz, 7-H [indole]), 7.14 (dd, 1H, *J*=8.8 Hz, *J*=2.4 Hz, 7-H [tacrine]), 7.08 (td, 1H, *J*=8 Hz, *J*=1.2 Hz, 5-H [indol]), 7.01 (td, 1H, *J*=8.0 Hz, *J*=0.8 Hz, 6-H [indole]), 6.86 (m, 1H, 2-H [indole]), 6.30 (m, 1H, NHCO), 4.91 (br s, 1H, NH-tacrine), 3.45 (m, 2H, C*H*$_2$NH-tacrine), 3.17 (q, 2H, *J*=7.2 Hz, C*H*$_2$NHCO), 3.03 (t, 2H, *J*=6.4 Hz, CH_2CO), 2.94 (m, 2H, 4-H [tacrine]), 2.50 (m, 2H, 1-H [tacrine]), 2.46(t, 2H, *J*=7.2 Hz, CH_2-indole), 2.41-2.23 (m, 2H, C*H*$_2$NMe), 2.22-2.18 (m, 2H, C*H*$_2$NMe), 2.10 (s, 3H, NMe), 1.78 (m, 4H, 2-, 3-H [tacrine])), 1.73-1.60 (m, 2H, CH_2), 1.59-1.49 (m, 2H, CH_2).

^{13}C NMR ($CDCl_3$): δ172.7, 159.5, 151.0, 148.0, 136.4, 134.0, 127.3, 127.2, 124.7, 124.1, 122.0, 121.9, 119.2, 118.6, 118.4, 115.7, 114.8, 111.4, 56.7, 56.21, 49.0, 42.3, 38.6, 37.8, 34.2, 28.5, 26.8, 25.2, 23.2, 23.0, 21.8.

***N*-[6-(6-Chloro-1,2,3,4-tetrahydro-acridin-9-ylamino)-hexyl]-3-(5-cyano-1*H*-indol-3-yl)-propionamide (12).**

^{1}H NMR ($CDCl_3$): δ9.48 (br s, 1H, NH-indole), 7.89 (s, 1H, 4-H [indole]), 7.87 (d, 1H, *J*=9.0 Hz, 8-H [tacrine]), 7.82 (d, 1H, *J*=2.1 Hz, 5-H [tacrine]), 7.33 (br s, 2H, 6-, 7-H

[indole]), 7.23 (dd, 1H, *J*=9.0 Hz, *J*=2.1 Hz, 7-H [tacrine]), 7.10 (br s, 1H, 2-H [indole]), 5.70 (t, 1H, *J*=5.6 Hz, NHCO), 4.00 (br s, 1H, NH-tacrine), 3.44 (t, 2H, *J*=7.2 Hz, C*H*$_2$NH-tacrine), 3.18 (q, 2H, *J*=6.6 Hz, C*H*$_2$NHCO), 3.08 (t, 2H, *J*=7.2 Hz, CH_2CO), 2.98 (br s, 2H, 4-H [tacrine]), 2.62 (br s, 2H, 1-H [tacrine]), 2.52 (t, 2H, *J*=7.4 Hz, CH_2-indole), 1.88 (m, 4H, 2-, 3-H [tacrine]), 1.58 (m, 2H, CH_2), 1.42-1.24 (m, 4H, 2 CH_2), 1.23-1.18 (m, 2H, CH_2).

^{13}C NMR ($CDCl_3$): δ172.5, 159.7, 151.2, 148.3, 138.3, 135.3, 134.42, 127.6, 127.4, 125.0, 124.9, 124.7, 124.6, 124.4, 121.1, 118.7, 116.2, 116.1, 112.4, 102.5, 49.6, 39.6, 37.6, 34.2, 31.9, 29.8, 26.7, 24.9, 23.2, 22.9, 21.3.

_N_-[6-(6-Chloro-1,2,3,4-tetrahydro-acridin-9-ylamino)-hexyl]-3-(1*H*-indol-3-yl)-acrylamide (13).

^{1}H NMR ($CDCl_3$): δ8.93 (br s, 1H, NH-indole), 7.79 (d, 1H, *J*=9.0 Hz, 8-H [tacrine]), 7.78 (d, 1H, *J*=2.0 Hz, 5-H [tacrine]), 7.77 (d, 1H, *J*=15.3 Hz, =CH-CO), 7.73 (d, 1H, *J*=7.8 Hz, 4-H [indole]), 7.30 (d, 1H, *J*=7.8 Hz, 7-H [indole]), 7.29 (s, 1H, 2-H [indole]), 7.15 (dd, 1H, *J*=9.0 Hz, *J*=2.0 Hz, 7-H [tacrine]), 7.12 (t, 1H, *J*=7.0 Hz, 5-H [indole], 7.06 (t, 1H, *J*=7.0 Hz, 6-H [indole], 6.35 (d, 1H, *J*=15.3 Hz, Indole-C*H*=), 5.79 (t, 1H, *J*=5.9 Hz, NHCO), 3.92 (br s, 1H, NH-tacrine), 3.38 (t, 2H, *J*=7.0 Hz, C*H*$_2$NH-tacrine), 3.33 (q, 2H, *J*=6.6 Hz, C*H*$_2$NHCO), 2.94 (br s, 2H, 4-H [tacrine]), 2.56 (br s, 2H, 1-H [tacrine]), 1.81 (m, 4H, 2-, 3-H [tacrine]), 1.61-1.36 (m, 4H, 2 CH_2), 1.32 (m, 4H, 2 CH_2).

^{13}C-NMR ($CDCl_3$): δ167.8, 159.4, 151.0, 147.9, 137.5, 134.8, 134.2, 129.0, 127.0, 125.4, 124.9, 124.3, 122.8, 120.9, 120.2, 118.3, 115.6, 113.1, 112.2, 49.4, 39.6, 33.8, 31.7, 29.8, 26.7, 26.6, 24.6, 22.9, 22.6.

1*H*-Indole-3-carboxylic acid [5-(6-chloro-1,2,3,4-tetrahydro-acridin-9-ylamino)-pentyl]-amide (14).

^{1}H NMR (CD_3OD): δ8.07 (d, 1H, *J*=9.0 Hz, 8-H [tacrine]), 8.06 (dt, 1H, *J*=8.0 Hz and *J*=0.8 Hz, 4-H [indole]), 7.80 (s, 1H, 2-H [indole]), 7.69 (d, 1H, *J*=2.0 Hz, 5-H [tacrine]), 7.41 (d, 1H, *J*=8.0 Hz, 7-H [indole]), 7.22 (dd, 1H, *J*=9.0 Hz and *J*=2.0 Hz, 7-H [tacrine]), 7.17 (td, 1H, *J*=8.0 Hz and *J*=1.2 Hz, 5-H [indole]), 7.12 (td, 1H, *J*=8.0 Hz and *J*=1.2 Hz, 6-H [indole]), 3.58 (t, 2H, *J*=7.0 Hz, C*H*$_2$NH-tacrine), 3.37 (t, 2H, *J*=7.0 Hz, C*H*$_2$NHCO), 2.88 (t, 2H, *J*=6.2 Hz, 4-H [tacrine]), 2.65 (t, 2H, *J*=6.2 Hz, 1-H [tacrine]), 1.79 (m, 4H, 2-, 3-H [tacrine]), 1.71 (m, 2H, CH_2), 1.63 (m, 2H, CH_2), 1.45 (m, 2H, CH_2).

^{13}C NMR (CD_3OD): δ168.6, 160.3, 153.4, 148.6, 138.2, 135.6, 128.9, 127.2, 126.7, 126.6, 125.1, 123.5, 122.0, 121.8, 119.5, 116.7, 112.9, 112.0, 40.1, 34.3, 32.0, 30.7, 26.1, 25.4, 24.0, 23.6.

1*H*-Indole-3-carboxylic acid [6-(6-chloro-1,2,3,4-tetrahydro-acridin-9-ylamino)-hexyl]-amide (15).

^{1}H NMR ($CDCl_3$): δ10.24 (br s, 1H, NH-Indole), 7.89 (m, 1H, 4-H [indole]), 7.85 (d, 1H, *J*=9.4 Hz, 8-H [tacrine]), 7.83 (d, 1H, *J*=2.0 Hz, 5-H [tacrine]), 7.71 (d, 1H, *J*=2.8 Hz, 2-H [indol]e), 7.39 (m, 1H, 7-H [indole]), 7.18-7.22 (m, 3H, 7-H [tacrine], 5-, 6-H [indole]), 6.13 (t, 1H, *J*=5.8 Hz, NHCO), 4.0 (br s, 1H, NH-tacrine), 3.46 (m, 4H, CH_2NH-tacrine, CH_2NHCO), 2.97 (m, 2H, 4-H [tacrine]), 2.60 (m, 2H, 1-H [tacrine]), 1.84 (m, 4H, 2-, 3-H [tacrine]), 1.60 (m, 4H, 2 CH_2), 1.39 (m, 4H, 2 CH_2).

^{13}C NMR ($CDCl_3$): δ166.0, 159.6, 151.0, 148.1, 136.7, 134.2, 128.4, 127.2, 124.8, 124.7, 124.3, 122.8, 121.5, 119.7, 118.3, 115.7, 112.4, 112.1, 49.5, 39.4, 33.9, 31.7, 30.0, 26.7, 26.6, 24.6, 22.9, 22.6.

1*H*-Indole-3-carboxylic acid [7-(6-chloro-1,2,3,4-tetrahydro-acridin-9-ylamino)-heptyl]-amide (16).

^{1}H NMR ($CDCl_3$): δ9.88 (br s, 1H, NH-Indole), 7.90 (dd, 1H, *J*=6.3 Hz, *J*=3.0 Hz, 4-H [indole]), 7.87 (d, 1H, *J*=9 Hz, 8-H [tacrine]), 7.84 (d, 1H, *J*=2.0 Hz, 5-H [tacrine]), 7.73 (d, 1H, *J*=2.7 Hz, 2-H [indole]), 7.41 (dd, 1H, *J*=6.3 Hz, *J*=3.0 Hz, 7-H [indole]), 7.23 (d, 1H, *J*=9 Hz, 7-H [tacrine]), 7.23-7.19 (m, 2H, 5-, 6-H [indole]), 6.06 (t, 1H, *J*=5.5 Hz, NHCO), 4.0 (br s, 1H, NH-tacrine), 3.46 (m, 4H, CH_2NH-tacrine, CH_2NHCO), 2.98 (m, 2H, 4-H [tacrine]), 2.61 (m, 2H, 1-H [tacrine]), 1.85 (m, 4H, 2-, 3-H [tacrine]), 1.59 (m, 4H, 2 CH_2), 1.34 (m, 6H, 3 CH_2).

^{13}C NMR ($CDCl_3$): δ165.7, 159.6, 151.1, 148.2, 136.6, 134.2, 128.3, 127.4, 124.8, 124.7, 124.3, 122.8, 121.6, 119.8, 118.4, 115.8, 112.4, 112.3, 49.6, 39.5, 34.0, 31.8, 29.9, 29.1, 27.0, 26.9, 24.7, 22.9, 22.7.

1*H*-Indole-3-carboxylic acid [8-(6-chloro-1,2,3,4-tetrahydro-acridin-9-ylamino)-octyl]-amide (17).

^{1}H NMR ($CDCl_3$): δ10.51 (br s, 1H, NH-Indole), 7.85 (m, 1H, 4-H [indole]), 7.79 (d, 1H, *J*=9.0 Hz, 8-H [tacrine]), 7.76 (d, 1H, *J*=2.0 Hz, 5-H [tacrine]), 7.65 (d, 1H, *J*=1.6 Hz, 2-H [indole]), 7.31 (m, 1H, 7-H [indole]), 7.15 (dd, 1H, *J*=9.0 Hz, *J*=2.0 Hz, 7-H [tacrine]), 7.10 (m, 2H, 5-, 6-H [indole]), 6.09 (t, 1H, *J*=5.5 Hz, NHCO), 3.9 (br s, 1H, NH-tacrine), 3.36 (c, 4H, *J*=7.3 Hz, CH_2NH-tacrine, CH_2NHCO), 2.91 (m, 2H, 4-H

[tacrine]), 2.53 (m, 2H, 1-H [tacrine]), 1.78 (m, 4H, 2-, 3-H [tacrine]), 1.52 (m, 4H, 2 CH_2), 1.26-1.19 (m, 8H, 4 CH_2).

^{13}C NMR ($CDCl_3$): δ165.4, 158.9, 150.4, 147.5, 136.1, 133.5, 127.7, 126.6, 124.2, 123.6, 122.1, 122.0, 120.7, 119.1, 117.7, 115.0, 111.7, 111.4, 48.9, 38.9, 33.2, 31.1, 29.3, 29.1, 28.5, 26.3, 26.1, 23.9, 22.3, 22.0.

_N_-[7-(6-Chloro-1,2,3,4-tetrahydroacridin-9-ylamino)-heptyl]-2-(1_H_-indol-3-yl)-acetamide (18).

^{1}H NMR ($CDCl_3$): δ9.25 (br s, 1H, NH-Indole), 7.79 (d, 1H, J=9 Hz, 8-H [tacrine]), 7.79 (d, 1H, J=2.0 Hz, 5-H [tacrine]), 7.45 (d, 1H, J=8.0 Hz, 4-H [indole]), 7.29 (d, 1H, J=8.0 Hz, 7-H [indole]), 7.26 (dd, 1H, J=9 Hz, J=2.0 Hz, 7-H [tacrine]), 7.11 (t, 1H, J=8.0 Hz, 5-H [indole]), 7.03 (t, 1H, J=8.0 Hz, 6-H [indole]), 7.03 (s, 1H, 2-H [indole]), 5.71 (t, 1H, J=5.5 Hz, NHCO), 3.82 (br s, 1H, NH-tacrine), 3.65 (s, 2H, CH_2CO), 3.34 (t, 2H, J=7.0 Hz, CH_2NH-tacrine), 3.08 (q, 2H, J=6.6 Hz, CH_2NHCO), 2.93 (br s, 2H, 4-H [tacrine]), 2.56 (br s, 2H, 1-H [tacrine]), 1.81 (m, 4H, 2-, 3-H [tacrine]), 1.48 (m, 2H, CH_2), 1.28-1.06 (m, 8H, 4 CH_2).

^{13}C NMR ($CDCl_3$): δ171.4, 159.4, 150.6, 148.0, 136.4, 133.7, 127.2, 126.8, 124.4, 123.9, 123.7, 122.2, 119.6, 118.4, 118.2, 115.5, 111.3, 108.5, 49.3, 39.2, 33.7, 33.3, 31.4, 29.1, 28.6, 26.5, 26.3, 24.3, 22.7, 22.4.

2-(5-Bromo-1_H_-indol-3-yl)-_N_-[7-(6-chloro-1,2,3,4-tetrahydro-acridin-9-ylamino)-heptyl]-acetamide (19).

^{1}H NMR ($CDCl_3$): δ9.36 (br s, 1H, NH-Indole), 7.86 (d, 1H, J=9.0 Hz, 8-H [tacrine]), 7.83 (d, 1H, J=2.3 Hz, 5-H [tacrine]), 7.63 (d, 1H, J=0.8 Hz, 4-H [indole]), 7.24-7.20 (m, 3H, 6-, 7-H [indole], 7-H [tacrine]), 7.09 (d, 1H, J=2.3 Hz, 2-H [indole]), 5.72 (t, 1H, J=5.8 Hz, NHCO), 3.95 (br s, 1H, NH-tacrine), 3.64 (s, 2H, CH_2CO), 3.42 (t, 2H, J=7.2 Hz, CH_2NH-tacrine), 3.15 (q, 2H, J=6.6 Hz, CH_2NHCO), 2.98 (br s, 2H, 4-H [tacrine]), 2.61 (br s, 2H, 1-H [tacrine]), 1.86 (m, 4H, 2-, 3-H [tacrine]), 1.56 (m, 2H, CH_2), 1.34 (m, 2H, CH_2),1.30-1.17 (m, 4H, 2 CH_2), 1.14 (m, 2H, CH_2).

^{13}C NMR ($CDCl_3$): δ171.2, 159.5, 151.1, 148.1, 135.2, 134.2, 128.9, 127.3, 125.4, 125.3, 124.9, 124.3, 121.4, 118.4, 115.7, 113.2, 113.1, 108.6, 49.6, 39.6, 34.0, 33.5, 31.8, 29.5, 29.0, 26.8, 26.7, 24.6, 23.0, 22.7.

_N_-[5-(6-Chloro-1,2,3,4-tetrahydro-acridin-9-ylamino)-pentyl]-4-(1_H_-indol-3-yl)-butyramide (20).

^{1}H NMR ($CDCl_3$):δ8.47 (br s, 1H, NH-Indole), 7.84 (d, 1H, J=1.9 Hz, 5-H [tacrine]), 7.83 (d, 1H, J=10.0 Hz, 8-H [tacrine]), 7.54 (d, 1H, J=7.4 Hz, 4-H [indole]), 7.30 (d, 1H, J=7.4 Hz, 7-H [indole]), 7.21 (dd, 1H, J=9.0 Hz, J=1.9 Hz, 7-H [tacrine]), 7.13 (td, 1H, J=7.4 Hz, J=1.2 Hz, 5-H [indole]), 7.05 (td, 1H, J=7.4 Hz, J=1.2 Hz, 6-H [indole]), 6.90 (d, 1H, J=2.4 Hz, 2-H [indole]), 5.52 (t, 1H, J=5.4 Hz, NHCO), 3.91 (br s, 1H, NH-tacrine), 3.40 (m, 2H, CH_2NH-tacrine), 3.18 (q, 2H, J=6.4 Hz, CH_2NHCO), 2.98 (br s, 2H, 4-H [tacrine]), 2.76 (t, 2H, J=7.0 Hz, CH_2-indole), 2.60 (br s, 2H, 1-H [tacrine]), 2.18 (t, 2H, J=7.0 Hz, CH_2CO), 2.02 (m, 2H, CH_2), 1.85 (m, 4H, 2-, 3-H [tacrine]), 1.61 (m, 2H, CH_2), 1.45 (m, 2H, CH_2), 1.36-1.31 (m, 2H, CH_2).

^{13}C NMR ($CDCl_3$): δ173.3, 159.8, 150.8, 148.3, 136.5, 134.1, 127.6, 127.6, 124.7, 124.4, 122.0, 122.7, 119.2, 118.9, 118.6, 116.0, 115.6, 111.3, 49.5, 39.2, 36.4, 34.2, 31.4, 29.6, 26.3, 24.7, 24.7, 24.3, 23.0, 22.8.

_N_-[6-(6-Chloro-1,2,3,4-tetrahydro-acridin-9-ylamino)-hexyl]-4-(1_H_-indol-3-yl)-butyramide (21).

^{1}H NMR ($CDCl_3$): δ8.93 (br s, 1H, NH-Indole), 7.85 (d, 1H, J=1.9 Hz, 5-H [tacrine]), 7.84 (d, 1H, J=9.0 Hz, 8-H [tacrine]), 7.51 (d, 1H, J=8.0 Hz, 4-H [indole]), 7.29 (d, 1H, J=8.0 Hz, 7-H [indole]), 7.20 (dd, 1H, J=9.0 Hz, J=2.0 Hz, 7-H [tacrine]), 7.10 (t, 1H, J=7.5 Hz, 5-H [indole]), 7.02 (t, 1H, J=7.5 Hz, 6-H [indole]), 6.87 (d, 1H, J=1.4 Hz, 2-H [indole]), 5.80 (br s, 1H, NHCO), 4.12 (br s, 1H, NH-tacrine), 3.41 (t, 2H, J=7.4 Hz, CH_2NH-tacrine), 3.16 (q, 2H, J=6.6 Hz, CH_2NHCO), 2.97 (br s, 2H, 4-H [tacrine]), 2.72 (t, 2H, J=7.4 Hz, CH_2-indole), 2.56 (br s, 2H, 1-H [tacrine]), 2.17 (t, 2H, J=7.4 Hz, CH_2CO), 1.99 (m, 2H, CH_2), 1.83 (m, 4H, 2-, 3-H [tacrine]), 1.56 (m, 2H, CH_2), 1.41 (m, 2H, CH_2), 1.35-1.21 (m, 4H, 2 CH_2).

^{13}C NMR ($CDCl_3$): δ173.6, 159.2, 151.4, 147.7, 136.7, 134.5, 127.6, 126.9, 125.1, 124.5, 122.0, 121.9, 120.0, 118.9, 118.3, 115.6, 115.4, 111.5, 49.5, 39.4, 36.5, 33.7, 31.8, 29.8, 26.7, 26.6, 26.4, 24.8, 24.7, 23.0, 22.7.

1_H_-Methylindole-3-carboxylic acid [7-(6-chloro-1,2,3,4-tetrahydroacridin-9-ylamino)-heptyl]-amide (22).

^{1}H NMR ($CDCl_3$): δ7.88 (d, 1H, J=7.0 Hz, 4-H [indole]), 7.86 (d, 1H, J=9.0 Hz, 8-H [tacrine]), 7.84 (d, 1H, J=2.3 Hz, 5-H [tacrine]), 7.63 (s, 1H, 2-H [indole]), 7.33 (d, 1H, J=7.0 Hz, 7-H [indole]), 7.28-7.20 (m, 3H, 6-, 7-H [indole], 7-H [tacrine]), 5.97 (t, 1H, J=5.5 Hz, NHCO), 3.9 (br s, 1H, NH-tacrine), 3.44 (m, 4H, CH_2NH-tacrine,

CH_2NHCO), 2.99 (m, 2H, 4-H [tacrine]), 2.62 (m, 2H, 1-H [tacrine]), 1.87 (m, 4H, 2-, 3-H [tacrine]), 1.59 (m, 4H, 2 CH_2), 1.36 (m, 6H, 3 CH_2).

^{13}C NMR ($CDCl_3$): δ165.3, 159.7, 150.9, 148.3, 137.3, 134.0, 132.4, 127.7, 125.3, 124.7, 124.3, 122.6, 121.5, 120.0, 118.5, 115.9, 111.1, 110.2, 49.7, 39.5, 34.2, 33.4, 31.8, 30.0, 29.1, 27.0, 26.9, 24.7, 23.0, 22.8.

1*H*-Indazole-3-carboxylic acid [7-(6-chloro-1,2,3,4-tetrahydroacridin-9-ylamino)-heptyl]-amide (23).

^1H NMR ($CDCl_3$): δ11.26 (br s, 1H, NH [indazole]), 8.34 (d, 1H, *J*=8.0 Hz, 4-H [indazole]), 7.84 (d, 1H, *J*=2.0 Hz, 5-H [tacrine]), 7.82 (d, 1H, *J*=9.0 Hz, 8-H [tacrine]), 7.43 (dd, 1H, *J*=8.0 Hz, 7-H [indazole]), 7.5 (t, 1H, *J*=7 Hz, 5-H [indazole]), 7.21 (t, 1H, *J*=7 Hz, 6-H [indazole]), 7.18 (dd, 1H, *J*=9.0 Hz, *J*=2.0 Hz, 7-H [tacrine]), 7.03 (t, 1H, *J*=5.5 Hz, NHCO), 3.9 (br s, 1H, NH-tacrine), 3.42 (m, 4H, CH_2NH-tacrine, CH_2NHCO), 2.96 (br s, 2H, 4-H [tacrine]), 2.58 (br s, 2H, 1-H [tacrine]), 1.82 (m, 4H, 2-, 3-H [tacrine]), 1.57 (m, 4H, 2 CH_2), 1.32 (m, 6H, 3 CH_2).

^{13}C NMR ($CDCl_3$): δ162.9, 159.6, 151.1, 148.2, 141.5, 139.6, 134.2, 127.5, 127.4, 124.8, 124.4, 122.9, 122.8, 122.1, 118.5, 115.8, 109.9, 49.7, 39.0, 34.1, 31.8, 29.8, 29.1, 26.9, 26.8, 24.7, 23.0, 22.7.

Intermediate carbonic acid 2-(1*H*-indol-3-yl)-ethyl ester 4-nitro-phenyl ester (26).

^1H NMR ($CDCl_3$): δ8.18 (d, 2H, *J*=8.8 Hz, Ph), 8,07 (br s, 1H, NH [indole]), 7.63 (d, 1H, *J*=8.0 Hz, 4-H [indole]), 7.33 (d, 1H, *J*=8.0 Hz, 7-H [indole]), 7.24 (d, 2H, *J*=8.8 Hz, Ph), 7.20 (t, 1H, *J*=7 Hz, 5-H [indole]), 7.13 (t, 1H, *J*=7 Hz, 6-H [indole]), 7.04 (d, 1H, *J*=2 Hz, 2-H [indole]), 4.5 (t, 2H, *J*=7.2 Hz, CH_2O), 4.5 (t, 2H, *J*=7.2 Hz, CH_2).

^{13}C NMR ($CDCl_3$): δ155.47, 152.48, 145.24, 136.18, 127.21, 125.14, 122.38, 122.19, 121.7, 119.56, 118.52, 111.24, 110.8, 69.32, 24.91.

[5-(6-Chloro-1,2,3,4-tetrahydro-acridin-9-ylamino)-pentyl]-carbamic acid 2-(1*H*-indol-3-yl)-ethyl ester (27).

^1H NMR ($CDCl_3$): δ8,51 (br s, 1H, NH-Indole), 7.86 (d, 1H, *J*=1.9 Hz, 5-H [tacrine]), 7.86 (d, 1H, *J*=9.0 Hz, 8-H [tacrine]), 7.57 (d, 1H, *J*=8.0 Hz, 4-H [indole]), 7.28 (d, 1H, *J*=8.0 Hz, 7-H [indole]), 7.22 (dd, 1H, *J*=9.0 Hz, *J*=1.9 Hz, 7-H [tacrine]), 7.12 (t, 1H, *J*=7.6 Hz, 5-H [indole]), 7.05 (t, 1H, *J*=7.6 Hz, 6-H [indole]), 6.97 (d, *J*=1.4 Hz, 2-H [indole]), 4.77 (br s, 1H, NHCO), 4.31 (t, 2H, *J*=7.2 Hz, CH_2O), 4.04 (br s, 1H, NH), 3.46-3.42 (m, 2H, CH_2NH-tacrine), 3.14-3.13 (m, 2H, CH_2NHCO), 3.04 (t, 2H, *J*=7.2 Hz, CH_2-indole), 2.98 (br s, 2H, 4-H [tacrine]), 2.59 (br s, 2H, 1-H [tacrine]), 1.87-1.83

(m, 4H, 2-, 3-H [tacrine]), 1.62-1.61 (m, 2H, CH_2), 1.49-1.47 (m, 2H, CH_2), 1.37-1.35 (m, 2H, CH_2).

^{13}C NMR ($CDCl_3$): δ165.7, 159.4, 157.07, 151.3, 147.8, 136.5, 134.6, 127.8, 127.0, 126.6, 124.9, 124.6, 122.3, 122.1, 119.5, 118.9, 118.4, 116.3, 115.8, 112.2, 111.4, 65.4, 49.54, 40.86, 33.70, 31.50, 30.03, 25,46, 24.75, 24.20, 23.02, 22.68.

[6-(6-Chloro-1,2,3,4-tetrahydro-acridin-9-ylamino)-hexyl]-carbamic acid 2-(1*H*-indol-3-yl)-ethyl ester (28)

^{1}H NMR ($CDCl_3$): δ8,25 (br s, 1H, NH-Indole), 7.89 (d, 1H, *J*=1.9 Hz, 5-H [tacrine]), 7.88 (d, 1H, *J*=9.0 Hz, 8-H [tacrine]), 7.62 (d, 1H, *J*=8.0 Hz, 4-H [indol]), 7.34 (d, 1H, *J*=8.0 Hz, 7-H [indole]), 7.27 (dd, 1H, *J*=9.0 Hz, *J*=1.9 Hz, 7-H [tacrine]), 7.18 (t, 1H, *J*=7.6 Hz, 5-H [indole]), 7.11 (t, 1H, *J*=7.6 Hz, 6-H [indoe]), 7.02 (d, *J*=1.4 Hz, 2-H [indole]), 4.67 (br s, 1H, NHCO), 4.34 (t, 2H, *J*=7.2 Hz, CH_2O), 3.96 (br s, 1H, NH), 3.46 (m, 2H, C*H*$_2$NH-tacrine), 3.16 (m, 2H, C*H*$_2$NHCO), 3.08 (t, 2H, *J*=7.2 Hz, CH_2-indole), 3.03 (br s, 2H, 4-H [tacrine]), 2.66 (br s, 2H, 1-H [tacrine]), 1.92-1.89 (m, 4H, 2-, 3-H [tacrine]), 1.66-1.61 (m, 2H, CH_2), 1.50-1.47 (m, 2H, CH_2), 1.40-1.33 (m, 4H, 2 CH_2).

^{13}C NMR ($CDCl_3$): δ159.5, 156.7, 150.8, 148.1, 136.1, 134.0, 127.5, 124.6, 124.2, 122.0, 119.3, 118.7, 118.3, 115.7, 112.1, 111.1, 64.8, 49.4, 40.7, 34.0, 31.6, 30.0, 26.5, 26.3, 25.2, 24.5, 22.9, 22.6.

[7-(6-Chloro-1,2,3,4-tetrahydro-acridin-9-ylamino)-heptyl]-carbamic acid 2-*(1H*-indol-3-yl)-ethyl ester (29).

^{1}H NMR ($CDCl_3$): δ8.25 (br s, 1H, NH-Indole), 7.90 (d, 1H, *J*=1.9 Hz, 5-H [tacrine]), 7.88 (d, 1H, *J*=9.0 Hz, 8-H [tacrine]), 7.62 (d, 1H, *J*=8.0 Hz, 4-H [indole]), 7.34 (d, 1H, *J*=8.0 Hz, 7-H [indol]e), 7.26 (dd, 1H, *J*=9.0 Hz, *J*=1.9 Hz, 7-H [tacrine]), 7.18 (t, 1H, *J*=7.6 Hz, 5-H [indole]), 7.11 (t, 1H, *J*=7.6 Hz, 6-H [indole]), 7.02 (d, *J*=1.4 Hz, 2-H [indole]), 4.71 (br s, 1H, NHCO), 4.34 (t, 2H, *J*=7.2 Hz, CH_2O), 3.98 (br s, 1H, NH), 3.48 (t, 2H, *J*=8.0 Hz, C*H*$_2$NH-tacrine), 3.15 (q, 2H, *J*=6.8 Hz, C*H*$_2$NHCO), 3.09 (t, 2H, *J*=7.2 Hz, CH_2-indole), 3.03 (br s, 2H, 4-H [tacrine]), 2.64 (br s, 2H, 1-H [tacrine]), 1.91-1.88 (m, 4H, 2-, 3-H [tacrine]), 1.64-1.60 (m, 2H, CH_2), 1.47-1.44 (m, 2H, CH_2), 1.31-1.25 (m, 6H, 3 CH_2).

^{13}C NMR ($CDCl_3$): 159.6, 156.9, 151.2, 148.2, 136.4, 134.3, 127.8, 127.6, 124.9, 124.5, 122.3, 122.2, 119.5, 119.0, 118.5, 115.8, 112.3, 111.4, 65.1, 49.8, 41.1, 34.1, 31.9, 30.1, 29.2, 27.0, 26.8, 25.5, 24.7, 23.1, 22.8.

4.1.3 Synthesis, Pharmacological evaluation and molecular modeling of novel Donepezil–Tacrine hybrid inhibitors of Acetylcholinesterase targeting catalytic, peripheral and midgorge binding sites

Pelayo Camps, Xavier Formosa, Diego Muñoz-Torrero, Michele Scarpellini, Albert Badia, M. Victòria Clos, **Axel Bidon-Chanal**, and F. Javier Luque

Synthesis, Pharmacological Evaluation and Molecular Modeling of Novel Donepezil–Tacrine Hybrid Inhibitors of Acetylcholinesterase Targeting Catalytic, Peripheral and Midgorge Binding Sites

Pelayo Camps,[*,†] *Xavier Formosa,*[†] *Diego Muñoz-Torrero,*[*,†] *Michele Scarpellini,*[†]

Albert Badia,[‡] *M. Victòria Clos,*[‡] *Antoni Camins,*[§] *Mercè Pallàs,*[§] *Joan Estelrich,*[∥,⊥] *Mònica Lizondo,*[∥,⊥]

Axel Bidon-Chanal,[∥] *and F. Javier Luque*[∥]

Laboratori de Química Farmacèutica (Unitat Associada al CSIC), Facultat de Farmàcia, Universitat de Barcelona, Av. Diagonal 643, E-08028, Barcelona, Spain; Departament de Farmacologia, de Terapèutica i de Toxicologia, Facultat de Medicina, Universitat Autònoma de Barcelona, E-08193-Bellaterra, Barcelona, Spain; Unitat de Farmacologia i Farmacognòsia, Facultat de Farmàcia, Universitat de Barcelona, Av. Diagonal 643, E-08028, Barcelona, Spain; Departament de Fisicoquímica, Facultat de Farmàcia, Universitat de Barcelona, Av. Diagonal 643, E-08028, Barcelona, Spain; Institut de Nanociència i Nanotecnologia, Universitat de Barcelona

RECEIVED DATE (to be automatically inserted after your manuscript is accepted if required according to the journal that you are submitting your paper to)

* To whom correspondence should be addressed. Phone: int. code + 34 + 934024536 / 934024533. Fax:

int. code + 34 + 934035941. E-mail: camps@ub.edu / dmunoztorrero@ub.edu

[†] Laboratori de Química Farmacèutica, Universitat de Barcelona

[‡] Universitat Autònoma de Barcelona

[§] Unitat de Farmacologia i Farmacognòsia, Universitat de Barcelona

[||] Departament de Fisicoquímica, Universitat de Barcelona

[⊥] Institut de Nanociència i Nanotecnologia, Universitat de Barcelona

ABSTRACT. A novel series of donepezil–tacrine hybrids designed to simultaneously interact with the active, peripheral and midgorge binding sites of acetylcholinesterase (AChE) have been synthesized and tested as AChE and butyrylcholinesterase (BChE) inhibitors. These compounds consist of a unit of tacrine or 6-chlorotacrine, which occupies the same position than tacrine at the AChE active site, and the 5,6-dimethoxy-2-[(4-piperidinyl)methyl]-1-indanone moiety of donepezil (or the indane derivative thereof), whose position along the enzyme gorge and the peripheral site can be modulated by a suitable tether which connects tacrine and donepezil fragments. All of the new compounds are highly potent inhibitors of bovine and human AChE and BChE, exhibiting IC_{50} values in the subnanomolar or low nanomolar range in most cases. Moreover, the most active inhibitors interact more potently than donepezil at the AChE peripheral site in a thioflavin T competition assay, which confers them a potential to inhibit the AChE-induced Aβ aggregation. These findings make the new hybrids promising anti-Alzheimer drug candidates.

Introduction

Since *bis*(7)-tacrine, a heptamethylene-linked dimer of the first marketed anti-Alzheimer drug tacrine (**1**, Chart 1), was developed one decade ago,[1,2] the search for inhibitors of acetylcholinesterase (AChE) able to simultaneously bind to its catalytic and peripheral binding sites has become an area of very active research.[2,3] Several classes of dual binding site AChE inhibitors have been developed by connecting through a suitable linker the two interacting units, which generally derive from known AChE inhibitors either commercialized or under development.[2-15] The success of the dual binding site strategy is evidenced by the large increase in AChE inhibitory potency of these dimers or hybrids relative to the parent compounds from which they have been designed. Further interest comes from the fact that some of these dual binding site AChE inhibitors[11,12,14,16,17] have been shown to inhibit the aggregation of β-amyloid peptide (Aβ), which is a key event in the neurotoxic cascade of Alzheimer's disease (AD).[18] This effect, which has been related to the blockade of the AChE peripheral site[19] by dual binding site AChE inhibitors, makes these compounds very promising disease-modifying anti-Alzheimer drug candidates.[20]

Chart 1. Structures of tacrine, donepezil, and the known donepezil–tacrine hybrids **3** and **4**.

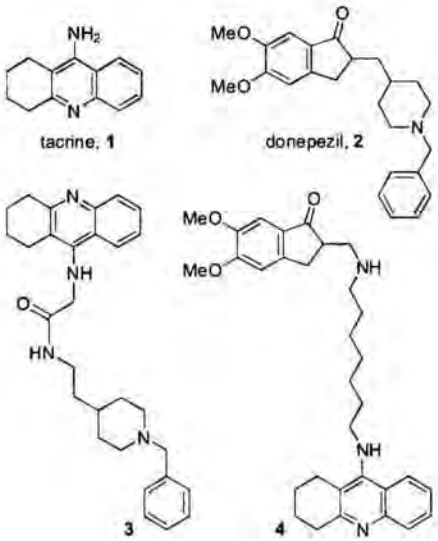

To date, the sole dual binding site AChE inhibitor approved for the treatment of AD is donepezil (**2**, Chart 1), though it was not specifically designed as such.[21] The X-ray crystallographic structure of the complex between *Torpedo californica* AChE (*Tc*AChE) and donepezil (PDB entry 1EVE)[22] shows that the elongated structure of donepezil spans the entire length of the enzyme active-site gorge forming a variety of interactions with specific residues, such as aromatic stacking interactions between its benzyl and indanone moieties with the indole rings of Trp84 and Trp279 (numbering of residues corresponding to *Tc*AChE) at the catalytic and peripheral sites, respectively, and the cation–π interaction between the protonated piperidine nitrogen and the phenyl ring of Phe330. Different *N*-benzylpiperidine derivatives of donepezil have been designed, mainly by bioisosteric replacements of the indanone moiety,[23–26] which are up to 17-fold more potent than donepezil.[24] To the best of our knowledge, only two classes of donepezil-based hybrids have been purposely designed as dual binding site AChE inhibitors by combining tacrine with different fragments of donepezil.[10,13] Among these donepezil–tacrine hybrids, compounds **3** and **4** (Chart 1), which retain the *N*-benzylpiperidine and the 5,6-dimethoxy-1-indanone moieties of donepezil, respectively, are the most potent, they being 37- and 7-fold more potent than

tacrine, but nearly equipotent to donepezil.

Herein we describe the synthesis, pharmacological evaluation and molecular modeling of a novel class of highly potent donepezil–tacrine hybrids. On the basis of the binding modes of donepezil[22] and tacrine[27] within *Tc*AChE, these novel compounds were designed through a conjunctive approach by combining the 5,6-dimethoxy-2-[(4-piperidinyl)methyl]-1-indanone moiety of donepezil with tacrine, which would thus replace the benzyl moiety of donepezil. In contrast to the preceding approaches,[10,13] the strategy adopted here largely preserves the chemical skeleton of donepezil, which should allow the new hybrid compounds to mimic not only the interactions of tacrine at the catalytic site and of the indanone ring at the peripheral one, but also to preserve the contacts of the piperidine moiety with the residues that are lining the wall of the AChE gorge as a third binding site within the enzyme.

Chemistry

The structures of the novel donepezil–tacrine hybrids **14–15a,b**, designed through the conjuctive strategy mentioned above, are shown in Scheme 1. The linker was selected taking into account the sizeable increase in AChE inhibitory potency observed in tacrine-based homo- and heterodimers upon introduction in the tether of a protonatable amino group at a distance equivalent to 3 methylene groups.[8,9] As this protonatable amino group could be the piperidine nitrogen atom of these donepezil–tacrine hybrids, a length of 2–3 methylenes for the linker was considered. Moreover, introduction of a chlorine atom at position 6 of tacrine should lead to additional interactions within the active site of the enzyme.[28–30]

The synthesis of the novel donepezil–tacrine hybrids **14–15a,b** was carried out through a three-step sequence involving amination of the known 9-chloro-1,2,3,4-tetrahydroacridines **5** or **6**[31,32] with an ω-aminoalcohol **7**, followed by mesylation of the resulting alcohols **8** or **9**, and subsequent reaction with

the known piperidine **12** (Scheme 1).[21] As the indane derivative **13** is also readily available,[33] we also carried out the synthesis of a parallel series of hybrids **16–17a,b** through the same methodology but using piperidine **13** in the last step instead of **12** (Scheme 1).

Scheme 1. Synthesis of the donepezil–tacrine hybrids **14–17a,b**.

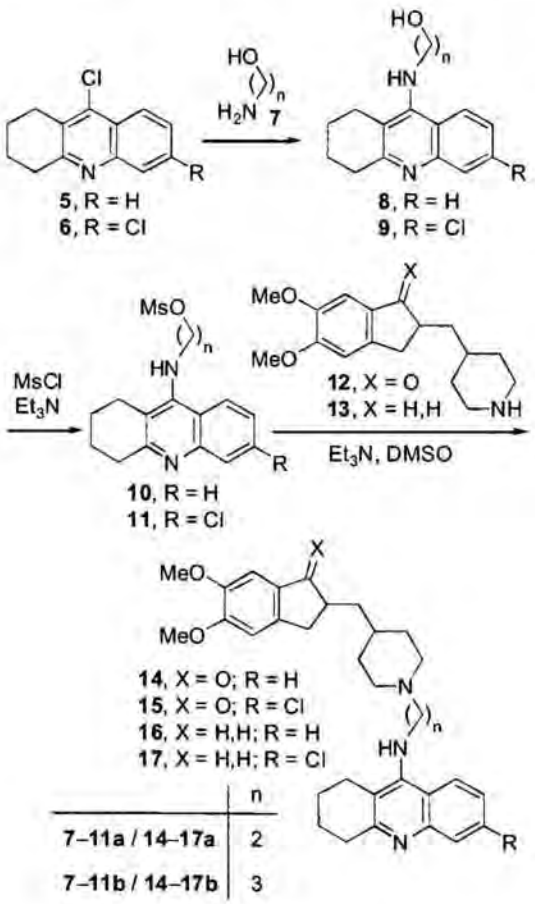

The amination of the chloroquinolines **5** and **6** with 3 equiv. of 2-aminoethanol (**7a**) or 3-amino-1-propanol (**7b**) in refluxing 1-pentanol[34] for 18 h, followed by removal of the solvent and excess of aminoalcohol by distillation under reduced pressure, afforded in excellent yields the new alcohols **8a**

and **9a,b**, which were fully characterized as hydrochlorides, and the known alcohol **8b**.[32] Mesylation of **8–9a,b** proceeded almost quantitatively. Worthy of note, mesylate **11b** was obtained slightly impure and used directly in the third step without further purification, while **10a,b** and **11a** were obtained in pure form and characterized either as base (**10a,b**) or hydrochloride (**11a**). The alkylation of piperidines **12** and **13** with a stoichiometric amount of mesylates **10–11a,b** in the presence of excess of Et_3N in DMSO at 85 °C for 2 days afforded the desired donepezil–tacrine hybrids **14–15a,b** and the indane derivatives thereof **16–17a,b** in low to moderate yields, after a tedious purification of the crude products by silica gel column chromatography. The novel hybrids were fully characterized as dihydrochlorides through their spectroscopic data and elemental analyses (C, H, N, Cl).

Pharmacology

AChE and BChE inhibition. To determine the potential interest of the new donepezil–tacrine hybrids **14–15a,b** and the indane derivatives **16–17a,b** for the treatment of AD, their AChE inhibitory activity was assayed by the method of Ellman et al.[35] on AChE from bovine (bAChE) and human (hAChE) erythrocytes. Recent evidences have shown that in advanced AD patients, AChE activity is greatly reduced in specific brain regions, while butyrylcholinesterase (BChE) activity increases, perhaps partly compensating for AChE action.[36] The increasing importance of BChE in the hydrolysis of acetylcholine as the ratio AChE/BChE gradually decreases in these patients suggests that inhibition of BChE might be valuable in the search for anti-Alzheimer agents. Consequently, the inhibitory activity on human serum BChE (hBChE) was also assayed by the same method.

Table 1. Pharmacological Data of the Hydrochlorides of Tacrine, 6-Chorotacrine, and Donepezil, and the Dihydrochlorides of the Donepezil–Tacrine Hybrids **14–15a,b** and Their Indane Derivatives **16–17a,b**.[a]

compound	IC_{50} (nM)		
	bovine AChE	human AChE	human BChE
14a·2HCl	1.74 ± 0.02	4.04 ± 0.06	12.4 ± 0.6
14b·2HCl	0.29 ± 0.03	0.88 ± 0.04	12.4 ± 0.6
15a·2HCl	0.57 ± 0.05	0.67 ± 0.06	136 ± 9
15b·2HCl	0.09 ± 0.01	0.27 ± 0.03	66.3 ± 4.0
16a·2HCl	2.28 ± 0.06	5.13 ± 0.52	8.06 ± 0.32
16b·2HCl	0.82 ± 0.06	2.16 ± 0.21	7.25 ± 0.33
17a·2HCl	1.86 ± 0.07	2.60 ± 0.23	88.7 ± 0.2
17b·2HCl	0.82 ± 0.08	1.06 ± 0.05	72.7 ± 4.2
Tacrine·HCl	130 ± 10	205 ± 18	43.9 ± 17
6-Chlorotacrine·HCl	5.73 ± 0.44	8.32 ± 0.75	916 ± 19
Donepezil·HCl	8.12 ± 0.26	11.6 ± 1.6	7273 ± 621

[a] Values are expressed as mean ± standard error of the mean of at least four experiments. IC_{50} inhibitory concentration (nM) of AChE (from bovine or human erythrocytes) or BChE (from human serum) activity.

Table 1 summarizes the data for the new compounds, as well as for tacrine·HCl, 6-chlorotacrine·HCl, and donepezil·HCl as reference compounds. All of the new hybrids are highly potent bAChE inhibitors, exhibiting IC_{50} values in the subnanomolar range in most cases, and being clearly more potent than the parent compounds tacrine (57–1444-fold), 6-chlorotacrine (3–64-fold), and donepezil (4–90-fold).

Hybrids **14–15**, which bear the indanone system of donepezil, are more potent bovine inhibitors (1.3–9.1-fold more potent) than their indane analogs **16–17**. The presence of a chlorine atom in the tacrine moiety enhances the inhibitory potency by 3-fold in indanone hybrids, while it has less effect in indane hybrids. Moreover, the tether length of 3 methylenes of hybrids of the **b** series makes them 6- and 3-fold more potent than their indanone and indane counterparts of the **a** series, respectively. Overall, compound **15b** is the most active compound with an IC_{50} of 90 pM.

The new hybrids are less potent inhibitors of human than bovine AChE (1.2–3-fold less potent), as it is the case for the parent compounds from which they were designed (around 1.5-fold less potent). Nevertheless, they are highly potent hAChE inhibitors, being more active than tacrine (40–759-fold), 6-chlorotacrine (2–31-fold), and donepezil (2–43-fold). Again, the best substitution pattern involves the presence of a chlorine atom at position 6 of the tacrine unit, the indanone ring of donepezil, and a tether length of 3 methylenes. As a result, **15b** is also the most active hAChE inhibitor (IC_{50} = 0.27 nM).

The new hybrids are also potent inhibitors of hBChE, though their activity is lower than that shown for hAChE. Thus, these compounds are 1.6–246-fold more potent toward hAChE than hBChE, as it is found for 6-chlorotacrine and donepezil, which are 110- and 627-fold more potent toward AChE, but in contrast with tacrine, which is 4.7-fold more potent toward BChE. When hBChE inhibitory activity is considered, the structure–activity relationships in this novel class of compounds reveal differential trends from those observed for the AChE inhibitory activity. Thus, the indane hybrids **16–17** are 1.5-fold more potent than their analogs **14–15** bearing the indanone system of donepezil (with the only exception of **17b**, which is slightly less potent than **15b**). Moreover, a chlorine atom at position 6 of the tacrine unit is detrimental for the hBChE inhibitory activity, the unsubstituted hybrids **14** and **16** being 10-fold more potent than their 6-chloro-derivatives **15** and **17**, which agrees with the 21-fold increase in potency of tacrine relative to 6-chlorotacrine, and with the results reported for other tacrine-based dual binding site AChE inhibitors.[6,14] The effect of the tether length on the BChE inhibitory activity is much

lower than that observed when the AChE inhibitory activity is considered, the hybrids of the **b** series being equipotent or slightly more potent (up to 2-fold more potent) than their counterparts of the **a** series. Overall, the most active BChE inhibitor is **16b** (IC_{50} = 7.25 nM), which is 6-, 126-, and 1003-fold more potent than tacrine, 6-chlorotacrine, and donepezil, respectively. Although the higher AChE vs BChE inhibitory activity of the first tacrine–based homo- and hetero-dimers was initially ascribed to the lack of a peripheral binding site in BChE,[1,37] recent studies have suggested the presence of a peripheral interaction site also in hBChE, where the aromatic residue Phe278 would be responsible for π–π interactions with aromatic moieties of tacrine–based heterodimers.[8] The higher BChE inhibitory activity of *bis*(7)-tacrine and several tacrine-based heterodimers,[8,9] as well as that of some of the new donepezil–tacrine hybrids herein described, relative to tacrine seems to validate this hypothesis.

The novel compounds reported in this study compare quite favorably with the previously known donepezil–tacrine hybrids.[10,13] Thus, hybrids **14–17a,b** are more potent inhibitors of AChE than compound **3** (IC_{50} = 6.0 nM, using rat cortex AChE; IC_{50} = 223 and 5.7 nM[21] for tacrine and donepezil, respectively, with the same enzyme source) and **4** (IC_{50} = 25 nM, using bovine erythrocyte AChE; IC_{50} = 167 and 19 nM for tacrine and donepezil, respectively, in the same assay). Regarding the BChE inhibitory activity, the most potent donepezil–tacrine hybrids examined here (compounds **14a,b** and **16a,b**) are more potent than compound **3** (IC_{50} = 76 nM, using rat serum BChE; IC_{50} = 92 and 7138 nM[21] for tacrine and donepezil, respectively, with the same enzyme source), though none of them is as potent as compound **4** (IC_{50} = 0.6 nM, using human serum BChE; IC_{50} = 24 and 930 nM for tacrine and donepezil, respectively).

Thioflavin T competition assay. Inestrosa *et al.* reported that AChE binds, through its peripheral site, to Aβ, thereby inducing amyloid fibril formation,[19,38–40] thus making blockade of the AChE peripheral site an interesting pharmacological target to develop disease-modifying anti-Alzheimer drug

candidates. Since propidium, a selective inhibitor of the AChE peripheral site, exhibits an increase in fluorescence upon binding to AChE, it has been used as a probe for competitive ligand binding to the enzyme.[13,41,42] Thioflavin T is another fluorescent probe widely used to detect amyloid structures,[43] though it can also bind to different proteins irrespective of their conformation or aggregation state.[44,45] In particular, thioflavin T binds to the AChE peripheral site, and the fluorescence enhancement reported for thioflavin T upon binding to AChE is much greater than that observed with propidium.[45] Therefore, we chose thioflavin T to study the interaction of selected donepezil–tacrine hybrids (compounds **15a** and **15b**) at the AChE peripheral site.

Table 2. Thioflavin T Competition Assay Results with the Dihydrochlorides of the Donepezil–Tacrine Hybrids **15a** and **15b**, and the Hydrochlorides of Tacrine, 6-Chlorotacrine, and Donepezil.[a]

Compound	Reduction of fluorescence (%)
15a·2HCl	79.4 ± 3.5
15b·2HCl	57.0 ± 2.0
Tacrine·HCl	12.6 ± 3.8
6-Chlorotacrine·HCl	12.4 ± 1.9
Donepezil·HCl	26.0 ± 3.5

[a] Percentage of thioflavin T fluorescence reduction by effect of several AChE inhibitors at 100 μM concentration. Values are expressed as mean ± standard error of the mean of three experiments.

Table 2 shows the reduction of thioflavin T fluorescence arising from the competition with **15a** and **15b**, as well as tacrine, 6-chlorotacrine, and donepezil as reference compounds. Since the excitation wavelength of propidium is very close to the emission wavelength of thioflavin T, this compound was

not included in the assay. The active site inhibitors tacrine and 6-chlorotacrine reduce thioflavin T fluorescence, on average, by 12%, an effect that might be ascribed to changes in the local conformation at the periperal site induced upon binding at the AChE active site.[45] The dual binding site AChE inhibitor donepezil led to a 2-fold greater reduction in fluorescence (26% reduction) relative to the preceding active site inhibitors, as expected from the direct interaction of its indanone moiety with the AChE peripheral site. Finally, the novel donepezil–tacrine hybrids **15a** and **15b** produced the highest reductions in thioflavin T fluorescence among all the tested compounds (79% and 57% reduction, respectively), which could be ascribed to the displacement of the fluorophore at the peripheral site of the enzyme. Moreover, the 3- and 2-fold greater effect obtained for **15a** and **15b** relative to donepezil suggests a larger occupancy of the AChE peripheral site by the indanone unit of the novel hybrids.

Molecular Modeling Studies

To gain insight into the molecular determinants that modulate the inhibitory activity of the novel donepezil–tacrine hybrids, the binding mode of **15a** and **15b** was explored by means of 10 ns molecular dynamics (MD) simulations performed for their complexes to hAChE. In the two cases the potential energy droped smoothly during the first ns, but it remained nearly constant for the rest of the 10 ns trajectory (Figure 1). Indeed, the stability of the trajectories is supported by the small positional root-mean square deviations determined for the backbone and heavy atoms, which amount to around 0.9 and 1.4 Å, respectively (Figure 1).

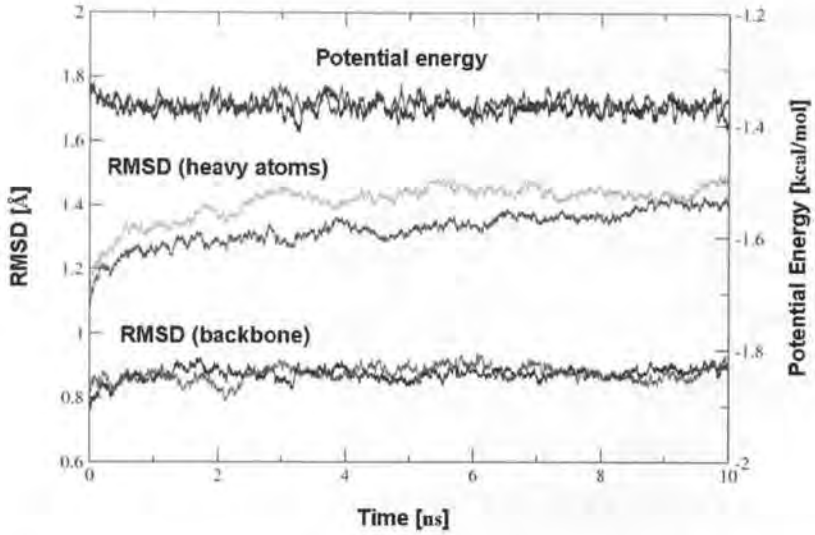

Figure 1. Time dependence of the potential energy ($\times 10^5$; kcal/mol) and the positional root-mean square deviation (RMSD; Å) determined for the backbone and heavy atoms in the mobile part of the simulation system for the hAChE complexes with **15a** (gray) and **15b** (black). The profiles were smoothed in 50 ps windows for the sake of clarity.

The position of **15a** with respect to selected key residues in the binding site is shown in Figure 2. The tacrine moiety is firmly bound to the catalytic site of hAChE, it being stacked against the aromatic rings of Trp86 and Tyr337 (average distances from the central ring of tacrine of 3.73 and 4.35 Å, respectively, numbering of residues corresponding to hAChE). The aromatic nitrogen of tacrine, protonated at physiological pH, is hydrogen-bonded to the main chain carbonyl oxygen of His447 (average N⁺O distance of 2.81 Å). Finally, the chlorine atom occupies a small hydrophobic pocket formed by Trp439, Met443 and Pro446, which parallels the interaction observed between the chlorine atom at position 3 of huprine X, a hybrid compound whose structure contains a 6-chlorotacrine moiety, and *Tc*AChE,[30,46] though in this latter case Pro446 is replaced by Ile439. The occupancy of such hydrophobic pocket by the chlorine atom contributes to the higher potency of heterodimers having the 6-chlorotacrine unit relative to their unsubstituted counterparts. As noted previously,[14] in hBChE

Met437 replaces Pro446 of hAChE and Ile439 of *Tc*AChE, which makes the terminal methyl group of Met437 to be around 1.2 Å closer to the chlorine atom. The larger steric hindrance due to the greater proximity of the chlorine atom to Met437 could account for the detrimental influence of this substituent on the hBChE inhibitory activity.

Regarding the linker, which is aligned along the gorge, the most relevant features come from the interactions formed by the piperidine ring. This unit occupies a position slightly shifted from that found in the X-ray crystallographic structure of the *Tc*AChE–donepezil complex (PDB entry 1EVE), although it still retains the electrostatic interaction with the carboxylate group of Asp74 (average N(piperidine)···O(carboxylate) distance of 4.72 Å). In turn, this latter residue is hydrogen-bonded to the hydroxyl group of Tyr72 (average O···O distance of 2.87 Å). Moreover, the protonated piperidine nitrogen is hydrogen-bonded to the hydroxyl group of Tyr337 (average N(piperidine)···O distance of 3.20 Å). Thus, a network of interactions that couple several residues in the gorge and the catalytic binding site is formed. Finally, the indanone ring is stacked onto the aromatic ring of Trp286 (average distance between the centers of indanone and indole rings of 4.38 Å), whose orientation resembles that found in the *Tc*AChE–donepezil complex. Moreover, the carbonyl group of the indanone unit forms water-mediated contacts with the backbone N–H groups of Phe295 and Arg296 and the C=O groups of Pro290 and Ser293, which should contribute to the higher AChE inhibitory activity of indanone derivatives relative to the indane analogs.

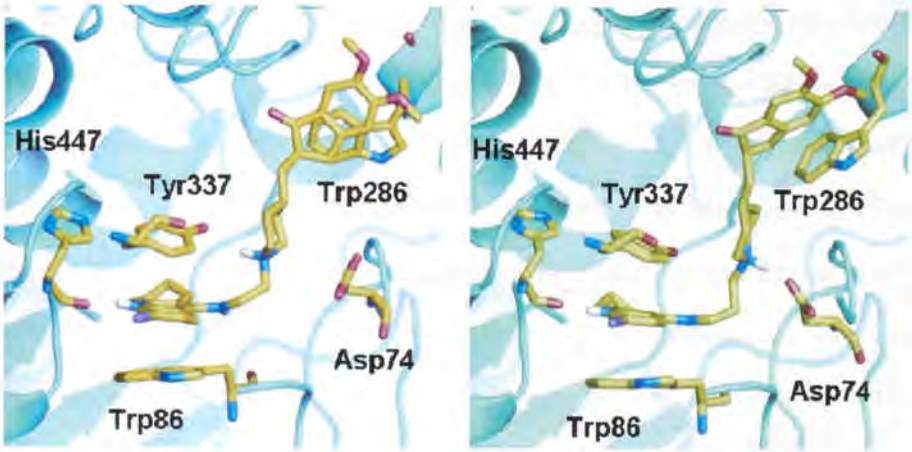

Figure 2. Representation of the heterodimers **15a** (left) and **15b** (right) in the binding site of hAChE highlighting selected residues that form the main interactions with tacrine, piperidine and indanone units of the inhibitors. Most hydrogen atoms are omitted for the sake of clarity.

The binding mode of **15b** at the catalytic site of hAChE closely mimics the interactions noted above for **15a** (Figure 2). Thus, the tacrine ring is stacked against Trp86 and Tyr337 (average distances between rings of 3.63 and 4.44 Å, respectively), the protonated quinoline nitrogen is hydrogen-bonded to the main chain carbonyl oxygen of His447 (average N···O distance of 2.82 Å), and the chlorine atom fills the hydrophobic pocket formed by Trp439, Met443, and Pro446. The enlargement of the tether length, however, leads to differences in the interactions found along the gorge and at the peripheral site. First, the protonated piperidine N–H group points directly to the carboxylate group of Asp74 (average N···O distance of 2.73 Å), which would strengthen the electrostatic interaction. The hydrogen bonds between Asp74 and Tyr72 and between the piperidine N–H unit and Tyr337 observed in the binding of **15a** are lost in the complex with **15b**. Thus, Asp74 forms a hydrogen-bond interaction with the backbone N–H unit of Leu76 and the hydroxyl group of Tyr337 establishes a hydrogen-bond contact with Tyr124. Second, though at the beginning of the simulation the indanone ring was stacked onto the

indole ring of Trp286, its orientation changed along the first ns of MD simulation and adopted an arrangement roughly normal to the indole ring (Figure 3). This change was accompanied by a conformational change in the indole ring of Trp286, whose position differed from that found in the X-ray structure by a rotation around the C_α–C_β–indole C3–indole C3a from –83 (in 1EVE) to +32 degrees. This finding, therefore, supports the conformational plasticity of this residue in the peripheral site of the enzyme already noted by other studies.[12,47–49]

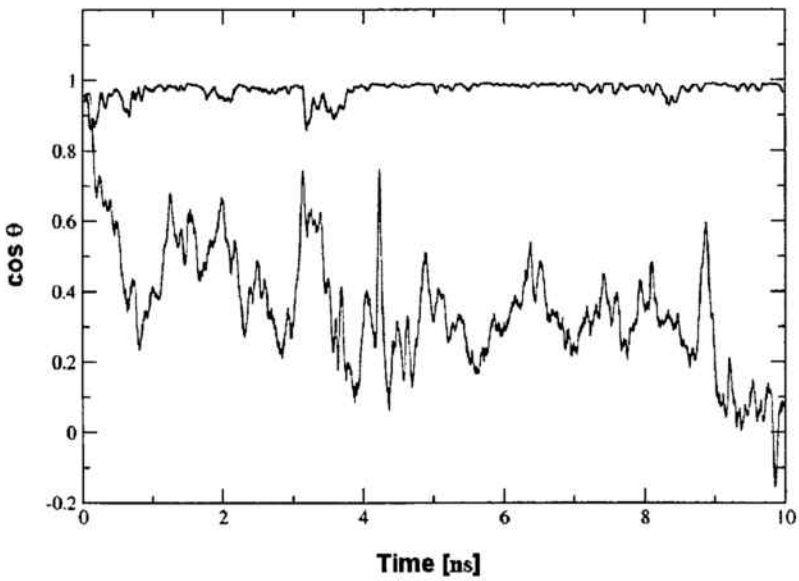

Figure 3. Time dependence of the relative orientation of the indanone ring of heterodimers **15a** (black) and **15b** (gray) and the indole ring of Trp286 at the peripheral site. The relative orientation was measured from the cosine function of the angle formed by the vectors normal to the indanone and indole rings. Accordingly, a perfect stacking would correspond to cos θ = 1, while a perpendicular arrangement is denoted by cos θ = 0.

Comparison of the binding mode of compounds **15a** and **15b** with that of tacrine and donepezil (taken

from X-ray structures 1ACJ and 1EVE, respectively) shows that the tacrine unit in the dual binding site inhibitors closely matches the position occupied by tacrine in the catalytic site (Figure 4). There are, however, notable differences in the relative arrangement of the indanone units of **15a** and **15b**. Thus, in **15a** this unit is shifted compared to the position occupied by the corresponding moiety of donepezil, leading to a more efficient π–π stacking interaction between the indanone ring of **15a** and the indole ring of Trp286 (Figure 4). In **15b** the strong electrostatic interaction formed between the protonated piperidine and Asp74 explains the distinct orientation of the indanone unit relative to donepezil, and the conformational change adopted by the indole ring of Trp286, which impedes the formation of a π–π stacking interaction (Figure 4). These results might help to rationalize the differences observed for **15a** and **15b** in the thioflavin T competition assay.

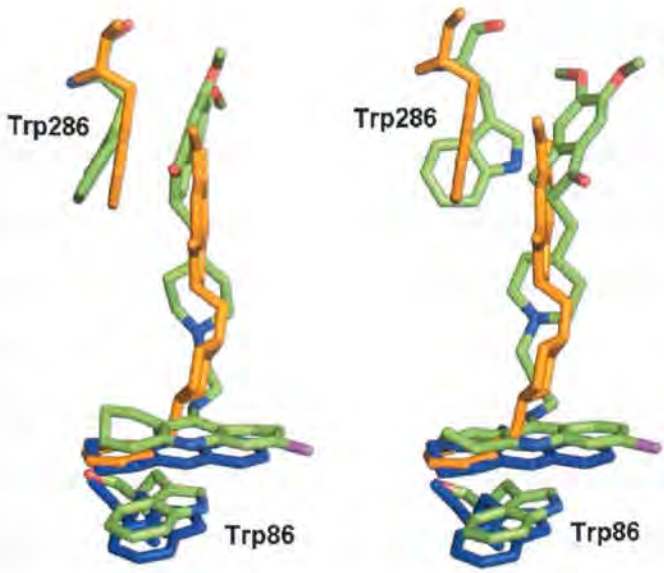

Figure 4. Superposition of the heterodimers **15a** (left) and **15b** (right) with tacrine (taken from the 1ACJ X-ray structure of the *Tc*AChE–tacrine complex; blue) and donepezil (from the 1EVE X-ray structure of the *Tc*AChE–donepezil complex; orange) showing the relative position of Trp86 (Trp84 in 1ACJ) and Trp286 (Trp279 in 1EVE) at the catalytic and peripheral sites, respectively. Compounds **15a**

and **15b** are colored by atom.

Conclusion

We have synthesized a new series of donepezil–tacrine hybrids, designed to simultaneously interact with the active, peripheral and midgorge binding sites of AChE. In contrast to previous approaches to the design of donepezil–tacrine hybrids, the conjunctive strategy adopted here largely preserves the chemical skeleton of donepezil, while its benzyl moiety is replaced by a tacrine unit. The length of the tether that connects the two constituting fragments of the novel hybrids, i.e. the 5,6-dimethoxy-2-[(4-piperidinyl)methyl]-1-indanone moiety of donepezil (or its corresponding indane derivative) and the tacrine (or 6-chlorotacrine) unit, has a relevant effect on the arrangement of the hybrid along the gorge, leading to different orientations of the piperidine ring and the indanone system within the enzyme gorge and at the peripheral site, respectively, while their tacrine unit closely matches the position occupied by tacrine within the AChE active site. Thus, enlargement of the linker from two to three methylenes permits the piperidine ring to form a direct electrostatic interaction with Asp74, though at the expense of a less efficient π–π interaction between the indanone unit and the indole ring of Trp286. In spite of these structural differences, all of the new hybrids are highly potent bovine and human AChE inhibitors, exhibiting IC_{50} values in the subnanomolar range in most cases, and being clearly more potent than the parent compounds from which they were designed and the previously described donepezil–tacrine hybrids. The most potent AChE inhibitors are those bearing an indanone system, a chlorine atom at the tacrine unit and a tether length of three methylenes. Though all of the new hybrids are less potent toward hBChE, the most active compounds, i.e. those bearing an unsubstituted tacrine unit irrespective of the presence of an indanone or indane system and the tether length, are also more potent hBChE inhibitors than the parent compounds from which they were designed. Finally, these compounds interact at the peripheral site of hAChE stronger than donepezil, which suggests that they could interfere with

the AChE-induced Aβ aggregation, and therefore, with the neurotoxic cascade of AD. The preceding results point out that the new donepezil–tacrine hybrids constitute promising anti-Alzheimer drug candidates.

Experimental Section

Chemistry. General Methods. Melting points were determined in open capillary tubes with a MFB 595010M Gallenkamp melting point apparatus. 300 MHz ^{1}H / 75.4 MHz ^{13}C NMR spectra, 400 MHz ^{1}H / 100.6 MHz ^{13}C NMR spectra, and 500 MHz ^{1}H NMR spectra were recorded on Varian Gemini 300, Varian Mercury 400, and Varian Inova 500 spectrometers, respectively. The chemical shifts are reported in ppm (δ scale) relative to internal TMS, and coupling constants are reported in Hertz (Hz). Assignments given for the NMR spectra of the new compounds have been carried out by comparison with the NMR data of **15a**, **16a**, **17b**, and 6-chlorotacrine, as model compounds, which in turn, were assigned on the basis of DEPT, COSY ^{1}H/^{1}H (standard procedures), NOESY ^{1}H/^{1}H, and COSY ^{1}H/^{13}C (gHSQC and gHMBC sequences) experiments. IR spectra were run on a Perkin-Elmer Spectrum RX I spectrophotometer. Absorption values are expressed as wave-numbers (cm^{-1}); only significant absorption bands are given. Column chromatography was performed on silica gel 60 AC.C (35–70 mesh, SDS, ref 2000027). Thin-layer chromatography (TLC) was performed with aluminum-backed sheets with silica gel 60 F_{254} (Merck, ref 1.05554), and spots were visualized with UV light and 1% aqueous solution of $KMnO_4$. Analytical grade solvents were used for crystallization, while pure for synthesis solvents were used in the reactions, extractions and column chromatography. For characterization purposes, the new donepezil–tacrine hybrids were transformed into the corresponding dihydrochlorides, and recrystallized. Worthy of note, as previously reported for some tacrine-related dimeric compounds,[50] the new donepezil–tacrine hybrids have the ability to retain molecules of water, which can not be removed after drying the analytical samples at 80 °C / 30 Torr for 2 days. Thus, the

elemental analyses of these compounds showed the presence of variable amounts of water. NMR spectra of all of the new compounds were performed at the Serveis Científico-Tècnics of the University of Barcelona, while elemental analyses and high resolution mass spectra were carried out at the Mycroanalysis Service of the IIQAB (CSIC, Barcelona, Spain) with a Carlo Erba model 1106 analyzer, and at the Mass Spectrometry Laboratory of the University of Santiago de Compostela (Spain) with a Micromass Autospec spectrometer, respectively.

General procedure for the reaction of 9-chloro-1,2,3,4-tetrahydroacridine, 5, or 6,9-dichloro-1,2,3,4-tetrahydroacridine, 6, with ω-aminoalcohols. A mixture of **5** or **6** (1 mmol) and an excess of the aminoalcohol **7** (3 mmol) in 1-pentanol (1 mL) was heated under reflux with magnetic stirring for 18 h. The resulting mixture was cooled to room temperature, diluted with CH_2Cl_2 (3.5 mL), washed with 10% aqueous NaOH (3.5 mL) and water (2×3 mL). The organic phase was dried with anhydrous Na_2SO_4, filtered and concentrated in vacuo to give an oily residue. The excess of aminoalcohol and solvent was removed from this residue by distillation in a rotary microdistillation equipment at 85 °C / 0.8 Torr to give the substitution product **8** or **9** as a pale brown solid residue.

The analytical samples of the hydrochlorides of **8** and **9** were prepared as follows: the alcohol **8** or **9** (1 mmol) was dissolved in MeOH (10 mL), the solution was filtered through a PTFE 0.45 μm filter, and treated with an excess of a methanolic solution of HCl (3 mmol) and the resulting solution was concentrated in vacuo to dryness. The solid was recrystallized from a mixture MeOH / AcOEt in the ratio of 1:4 (5 mL), and dried at 80 °C / 30 Torr for 48 h, to give the 9-(ω-hydroxyalkylamino)tetrahydroacridine hydrochloride **8**·HCl or **9**·HCl as a light brown solid.

9-[(2-Hydroxyethyl)amino]-1,2,3,4-tetrahydroacridine hydrochloride (8a·HCl). From **5** (3.00 g, 13.8 mmol) and 2-aminoethanol, **7a** (2.49 mL, 2.52 g, 41.3 mmol), alcohol **8a** (3.07 g, 92% yield, free base) was obtained: R_f 0.38 (CH_2Cl_2 / MeOH / 25% aqueous NH_4OH 9:1:0.1). **8a**·HCl: mp 184–185 °C (MeOH / AcOEt 1:4); IR (KBr) ν 3700–2400 (max. at 3358, 3142, 3058, 3016, 2938, 2872, O–H, N–H,

$^{+}$N–H and C–H st), 1633, 1592, 1577 and 1524 (ar–C–C and ar–C–N st) cm^{-1}; ^{1}H NMR (300 MHz, CD_3OD) δ 1.90–2.04 (complex signal, 4H, 2-H_2 and 3-H_2), 2.74 (m, 2H, 1-H_2), 3.01 (m, 2H, 4-H_2), 3.86 (t, J = 5.4 Hz, 2H, 2'-H_2), 4.01 (t, J = 5.4 Hz, 2H, 1'-H_2), 4.87 (s, OH, NH and $^{+}$NH), 7.54 (ddd, J = 8.4 Hz, J' = 6.0 Hz, J'' = 2.4 Hz, 1H, 7-H), 7.76–7.84 (complex signal, 2H, 5-H and 6-H), 8.40 (d, J = 8.4 Hz, 1H, 8-H); ^{13}C NMR (75.4 MHz, CD_3OD) δ 21.1 (CH_2, C3), 23.1 (CH_2, C2), 24.8 (CH_2, C1), 30.1 (CH_2, C4), 51.2 (CH_2, C1'), 61.7 (CH_2, C2'), 113.7 (C, C9a), 117.7 (C, C8a), 121.2 (CH, C5), 126.0 (CH, C8), 126.1 (CH, C7), 133.3 (CH, C6), 140.9 (C, C10a), 152.8 (C, C4a), 157.4 (C, C9). HRMS calcd for ($C_{15}H_{18}N_2O$ + H^+) 243.1497, found 243.1494.

General procedure for the mesylation of alcohols 8 and 9. To a cold solution (–10 °C, ice-salt bath) of the alcohol **8** or **9** (1 mmol) and anhydrous Et_3N (1.7 mmol) in anhydrous CH_2Cl_2 (6 mL), methanesulfonyl chloride (1.5 mmol) was added dropwise and the reaction mixture was stirred for 30 min at this temperature. The mixture was concentrated in vacuo, the residue was taken in CH_2Cl_2 (3 mL) and the resulting organic solution was washed with 10% aqueous NaOH (2×3 mL) until the aqueous phase remained basic (pH > 10), dried with anhydrous Na_2SO_4 and concentrated in vacuo to give the corresponding mesylate **10** or **11** as a brown oily residue. The analytical samples of the mesylates were obtained by extraction of the oily crude product with hot AcOEt, except in the case of **11a**, whose analytical sample was prepared by recrystallization of the corresponding hydrochloride, obtained in a similar way to that described for the hydrochlorides of alcohols **8** and **9**.

9-[(2-Methanesulfonyloxyethyl)amino]-1,2,3,4-tetrahydroacridine (10a). From alcohol **8a** (2.15 g, 8.88 mmol), mesylate **10a** (3.13 g, quantitative yield) was obtained: R_f 0.67 (CH_2Cl_2 / MeOH / 25% aqueous NH_4OH 9:1:0.1); IR (NaCl) ν 3391 and 3339 (N-H st), 1638, 1586 and 1524 (ar–C–C and ar–C–N st), 1352 (SO_2 st as), 1178 (SO_2 st s) cm^{-1}; ^{1}H NMR (300 MHz, $CDCl_3$) δ 1.88–1.98 (complex signal, 4H, 2-H_2 and 3-H_2), 2.76 (m, 2H, 1-H_2), 2.97 (s, 3H, OSO_2CH_3), 3.08 (m, 2H, 4-H_2), 3.81 (m, 2H, 1'-H_2), 4.34 (t, J = 4.9 Hz, 2H, 2'-H_2), 4.54 (broad s, 1H, NH), 7.39 (ddd, J = 8.4 Hz, J' = 6.8 Hz,

J'' = 1.5 Hz, 1H, 7-H), 7.57 (ddd, J = 8.4 Hz, J' = 6.8 Hz, J'' = 1.5 Hz, 1H, 6-H), 7.91–7.95 (complex signal, 2H, 5-H and 8-H); ^{13}C NMR (75.4 MHz, $CDCl_3$) δ 22.4 (CH_2) and 22.7 (CH_2) (C2 and C3), 24.7 (CH_2, C1), 33.3 (CH_2, C4), 37.3 (CH_3, OSO_2CH_3), 47.4 (CH_2, C1'), 69.0 (CH_2, C2'), 117.7 (C, C9a), 120.7 (C, C8a), 122.2 (CH), 124.3 (CH), 127.8 (CH), and 128.7 (CH) (C5, C6, C7, and C8), 146.2 (C, C10a), 149.6 (C, C4a), 158.2 (C, C9). HRMS calcd for ($C_{16}H_{20}N_2O_3S + H^+$) 321.127, found 321.128.

General procedure for the coupling of mesylates 10 and 11 with 5,6-dimethoxy-2-[(4-piperidinyl)methyl]indan-1-one (12) or 5,6-dimethoxy-2-[(4-piperidinyl)methyl]indane (13). A solution of the mesylate **10** or **11** (1 mmol), the piperidine **12** or **13** (1 mmol) and anhydrous Et_3N (2.5 mmol) in DMSO (8 mL) was heated at 85 °C for 48 h. The resulting solution was allowed to cool to room temperature and was concentrated in vacuo. The brown oily residue was treated with aqueous 2 N NaOH (25 mL) and extracted with CH_2Cl_2 (3×35 mL). The combined organic extracts were washed with water (5×40 mL) and brine (2×30 mL), dried with anhydrous Na_2SO_4, filtered, and evaporated under reduced pressure to give an oily residue which was submitted to column chromatography (35–70 μm silica gel, CH_2Cl_2 / MeOH / 25% aqueous NH_4OH mixtures as eluent).

The isolated donepezil–tacrine hybrids **14–17** were transformed into the corresponding dihydrochlorides as follows: A solution of the free base (1 mmol) in MeOH (40 mL) was filtered through a 0.45 μm PTFE filter and treated with excess of a methanolic solution of HCl (5 mmol). The solution was concentrated in vacuo to dryness and the solid residue was recrystallized from MeOH (20 mL), and dried at 80 °C / 30 Torr for 48 h.

9-[(2-{4-[(5,6-Dimethoxy-1-oxoindan-2-yl)methyl]piperidin-1-yl}ethyl)amino]-1,2,3,4-tetrahydroacridine dihydrochloride (14a·2HCl). From mesylate **10a** (276 mg, 0.86 mmol) and piperidine **12** (249 mg, 0.86 mmol), compound **14a** (87 mg, 20% yield) was obtained as a pale brown solid, on elution with a mixture of CH_2Cl_2 / MeOH / 25% aqueous NH_4OH 99.5:0.5:0.4: R_f 0.91 (CH_2Cl_2 / MeOH / 25% aqueous NH_4OH 90:10:0.1). **14a**·2HCl: mp 190–191 °C (MeOH). IR (KBr) ν 3700–2400

(max. at 3401, 2928, 2871, 2718, N–H, $^{+}$N–H and C–H st), 1685, 1672 (C=O st), 1636, 1588, 1523 and 1500 (ar–C–C and ar–C–N st) cm^{-1}; ^{1}H NMR (500 MHz, CD_3OD) δ 1.45 (m, 1H, indanone-2-CH_a), 1.62–1.73 (broad signal, 2H, piperidine 3-H_{ax} and 5-H_{ax}), 1.86 (m, 1H, indanone-2-CH_b), 1.90–2.02 (broad signal, 1H, piperidine 4-H), superimposed 1.99 (complex signal, 4H, acridine 2-H_2 and 3-H_2), 2.02 (broad d, J = 14.5 Hz, 1H) and 2.14 (broad d, J = 14.0 Hz, 1H) (piperidine 3-H_{eq} and 5-H_{eq}), 2.74–2.80 (complex signal, 2H, indanone 2-H and 3-H_a), 2.84 (m, 2H, acridine 1-H_2), 3.08 (m, 2H, acridine 4-H_2), 3.12 (broad signal, 2H, piperidine 2-H_{ax} and 6-H_{ax}), superimposed in part 3.34 (dd, J = 18.0 Hz, J' = 8.5 Hz, 1H, indanone 3-H_b), 3.60 (broad signal, 2H, $NHCH_2CH_2N$), 3.72 (broad signal, 2H, piperidine 2-H_{eq} and 6-H_{eq}), 3.85 (s, 3H, 6-OCH_3), 3.94 (s, 3H, 5-OCH_3), 4.42 (t, J = 7.7 Hz, 2H, $NHCH_2CH_2N$), 4.85 (s, NH and $^{+}$NH), 7.07 (s, 1H, indanone 4-H), 7.15 (s, 1H, indanone 7-H), 7.68 (ddd, J = 8.5 Hz, J' = 7.0 Hz, J'' = 1.0 Hz, 1H, acridine 7-H), 7.83 (dd, J = 8.5 Hz, J' = 1.0 Hz, 1H, acridine 5-H), 7.91 (ddd, J = 8.5 Hz, J' = 7.0 Hz, J'' = 1.0 Hz, 1H, acridine 6-H), 8.43 (d, J = 8.5 Hz, 1H, acridine 8-H); ^{13}C NMR (100.6 MHz, CD_3OD) δ 21.7 (CH_2, acridine C3), 23.0 (CH_2, acridine C2), 25.7 (CH_2, acridine C1), 29.5 (CH_2, acridine C4), 30.3 (CH_2) and 31.1 (CH_2) (piperidine C3 and C5), 33.0 (CH, piperidine C4), 34.2 (CH_2, indanone C3), 39.0 (CH_2, indanone-2-CH_2), 43.1 (CH_2, $NHCH_2CH_2N$), 46.1 (CH, indanone C2), 54.1 (2 CH_2, piperidine C2 and C6), 56.5 (CH_3, 6-OCH_3), 56.7 (CH_3, 5-OCH_3), 57.4 (CH_2, $NHCH_2CH_2N$), 105.3 (CH, indanone C7), 109.0 (CH, indanone C4), 114.4 (C, acridine C9a), 117.6 (C, acridine C8a), 120.3 (CH, acridine C5), 125.9 (CH, acridine C8), 127.2 (CH, acridine C7), 129.8 (C, indanone C7a), 134.3 (CH, acridine C6), 139.4 (C, acridine C10a), 151.1 (C, indanone C6), 151.3 (C, indanone C3a), 153.1 (C, acridine C4a), 157.8 (C) and 158.0 (C) (indanone C5 and acridine C9), 209.7 (C, indanone C1). Anal. ($C_{32}H_{39}N_3O_3 \cdot 2HCl \cdot 1.5H_2O$) C, H, N, Cl.

Biochemical studies. AChE inhibitory activity was evaluated spectrophotometrically at 25 °C by the method of Ellman,[35] using AChE from bovine or human erythrocytes and acetylthiocholine iodide (0.53 mM or 0.13 mM for bovine and human AChE, respectively) as substrate. The reaction took place in a final volume of 3 mL of 0.1 M phosphate-buffered solution pH 8.0, containing 0.025 or 0.04 units of

bovine or human AChE, respectively, and 333 μM 5,5'-dithiobis(2-nitrobenzoic) acid (DTNB) solution used to produce the yellow anion of 5-thio-2-nitrobenzoic acid. Inhibition curves were performed in triplicate by incubating with at least 12 concentrations of inhibitor for 15 min. One triplicate sample without inhibitor was always present to yield 100% of AChE activity. The reaction was stopped by the addition of 100 μL 1 mM eserine, and the color production was measured at 414 nm. BChE inhibitory activity determinations were carried out similarly, using 0.035 unit of human serum BChE and 0.56 mM butyrylthiocholine, instead of AChE and acetylthiocholine, in a final volume of 1 mL.

Data from concentration-inhibition experiments of the inhibitors were calculated by non-linear regression analysis, using the GraphPad Prism program package (GraphPad Software; San Diego, USA), which gave estimates of the IC_{50} (concentration of drug producing 50% of enzyme activity inhibition). Results are expressed as mean ± S.E.M. of at least 4 experiments performed in triplicate. DTNB, acetylthiocholine, butyrylthiocholine, and the enzymes were purchased from Sigma and eserine from Fluka.

Thioflavin T Competition Assay. Fluorescence measurements were carried out at room temperature in a SFM-25 spectrofluorimeter (Biotek, Italy) using a 1 mL quartz cell. Fluorescence was monitored at 448 nm and 488 for excitation and emission, respectively. An aqueous solution of hAChE at 2.3 μM concentration was stirred at room temperature for 24 h. After incubation, 50 μL of the enzyme solution were mixed with 750 μL of 50 mM glycine-NaOH buffer (pH 8.5) containing 15 μM thioflavin T. The resulting solution was stirred for 1 h, and the fluorescence of the sample was recorded (F_1). To check the ability of reducing the fluorescence arising from the interaction of AChE and thioflavin T, the enzyme, at a final concentration of 2.3 μM, was mixed with the inhibitor (final concentration 100 μM), and the solution was stirred for 24 h. After incubation, 50 μL of the protein solution were mixed with 750 μL of fluorophore solution, as indicated above, and the corresponding fluorescence was recorded (F_2). Finally, the fluorescence of a solution formed by 750 μL of the buffer containing the dye and 50 μL of water was recorded (F_0). The percentage of reduction of ThT fluorescence was determined as:

$$\% = 1 - \frac{F_2 - F_0}{F_1 - F_0}$$

Molecular Modeling Methods. The binding mode of compounds **15a** and **15b** was explored by means of 10 ns molecular dynamics simulations performed for their complexes to human acetylcholinesterase (hAChE). To this end, models of the bonded ligands were built up using the X-ray crystallographic structure of the hAChE–fasciculin complex (PDB code 1B41).[51] Fasciculin was removed from the structure, truncated residues were reconstructed and missing residues were modeled using InsightII graphics package.[52] The X-ray crystallographic structures of the *Tc*AChE complexes with tacrine (1ACJ),[27] huprine X (1E66)[30] and donepezil (1EVE)[22] and the final structures of previous heterodimer studies[13,14] were used to position the ligands along the gorge. The system was hydrated by centering a sphere of 50 Å of TIP3P[53] water molecules at the inhibitor, paying attention to filling the position of crystallographic waters inside the binding cavity. Finally, six Na^+ cations were added to neutralize the negative charge of the system with the xleap module of AMBER8.[54]

Molecular dynamics simulations were run using the sander module of AMBER8 and the parm98 parameters for the protein. The charge distribution of the inhibitor was determined from fitting to the HF/6-31G(d) electrostatic potential obtained with Gaussian'03[55] using the RESP procedure,[56] and the van der Waals parameters were taken from those defined for related atoms in AMBER force field. The system was partitioned into a mobile region, which included the ligand, all the protein residues containing at least one atom within 20 Å from the ligand, and all the water molecules and Na^+ cations. The geometry of the system was minimized in four steps. First, the position of hydrogen atoms was optimized using 3000 steps of steepest descent algorithm. Then, water molecules were refined throught 2000 steps of steepest descent followed by 3000 steps of conjugate gradient. Next, ligand, water molecules and counterions were optimized with 2000 steps of steepest descent and 4000 steps of conjugate gradient, and finally the whole system was optimized with 3000 steps of steepest descent and 7000 steps of conjugate gradient. Thermalization of the mobile part of the system was performed in five

steps of 20 ps incrementing the temperature up to 298 K. At this point, a 10 ns molecular dynamics simulation was carried out using a time step of 1 fs. SHAKE was used for those bonds containing hydrogen atoms, and a cut off of 11 Å was used for nonbonded interactions.

The analysis of the structural features that mediate the binding mode to the enzyme was determined by averaging the parameters for the snapshots (saved every picosecond) sampled along the last 5 ns of the molecular dynamics simulations.

Acknowledgment. Financial support from Dirección General de Investigación of Ministerio de Ciencia y Tecnología and FEDER (projects CTQ2005-02192/BQU, SAF2002-00049, CTQ2005-09365, and SAF2005-01604) and Comissionat per a Universitats i Recerca of the Generalitat de Catalunya (projects 2005-SGR00180, 2001-SGR00216, and 2005-SGR00893) are gratefully acknowledged. We also thank the Serveis Científico-Tècnics of the University of Barcelona for NMR facilities, and Ms. P. Domènech from the IIQAB (CSIC, Barcelona, Spain) for carrying out the elemental analyses.

Supporting Information Available: Experimental procedures, spectral and analytical characterization data of all of the new compounds (except for **8a**, **10a** and **14a**, herein described). This material is available free of charge via the Internet at http://pubs.acs.org.

References

(1) Pang, Y. –P.; Quiram, P.; Jelacic, T.; Hong, F.; Brimijoin, S. Highly Potent, Selective, and Low Cost Bis-tetrahydroaminacrine Inhibitors of Acetylcholinesterase. *J. Biol. Chem.* **1996**, *271*, 23646–23649.

(2) For a review see: Du, D. –M.; Carlier, P. R. Development of Bivalent Acetylcholinesterase

Inhibitors as Potential Therapeutic Drugs for Alzheimer's Disease. *Curr. Pharm. Des.* **2004**, *10*, 3141–3156.

(3) For a review see: Recanatini, M.; Valenti, P. Acetylcholinesterase Inhibitors as a Starting Point Towards Improved Alzheimer's Disease Therapeutics. *Curr. Pharm. Des.* **2004**, *10*, 3157–3166.

(4) Carlier, P. R.; Du, D. –M.; Han, Y.; Liu, J.; Pang, Y. –P. Potent, Easily Synthesized Huperzine A-Tacrine Hybrid Acetylcholinesterase Inhibitors. *Bioorg. Med. Chem. Lett.* **1999**, *9*, 2335–2338.

(5) Savini, L.; Campiani, G.; Gaeta, A.; Pellerano, C.; Fattorusso, C.; Chiasserini, L.; Fedorko, J. M.; Saxena, A. Novel and Potent Tacrine-Related Hetero- and Homobivalent Ligands for Acetylcholinesterase and Butyrylcholinesterase. *Bioorg. Med. Chem. Lett.* **2001**, *11*, 1779–1782.

(6) Hu, M. –K.; Wu, L. –J.; Hsiao, G.; Yen, M. –H. Homodimeric Tacrine Congeners as Acetylcholinesterase Inhibitors. *J. Med. Chem.* **2002**, *45*, 2277–2282.

(7) Lewis, W. G.; Green, L. G.; Grynszpan, F.; Radić, Z.; Carlier, P. R.; Taylor, P.; Finn, M. G.; Sharpless, K. B. Click Chemistry In Situ: Acetylcholinesterase as a Reaction Vessel for the Selective Assembly of a Femtomolar Inhibitor from an Array of Building Blocks. *Angew. Chem. Int. Ed.* **2002**, *41*, 1053–1057.

(8) Savini, L.; Gaeta, A.; Fattorusso, C.; Catalanotti, B.; Campiani, G.; Chiasserini, L.; Pellerano, C.; Novellino, E.; McKissic, D.; Saxena, A. Specific Targeting of Acetylcholinesterase and Butyrylcholinesterase Recognition Sites. Rational Design of Novel, Selective, and Highly Potent Cholinesterase Inhibitors. *J. Med. Chem.* **2003**, *46*, 1–4.

(9) Camps, P.; Formosa, X.; Muñoz-Torrero, D.; Petrignet, J.; Badia, A.; Clos, M. V. Synthesis and Pharmacological Evaluation of Huprine–Tacrine Heterodimers: Subnanomolar Dual Binding Site Acetylcholinesterase Inhibitors. *J. Med. Chem.* **2005**, *48*, 1701–1704.

(10) Shao, D.; Zou, C.; Luo, C.; Tang, X.; Li, Y. Synthesis and Evaluation of Tacrine–E2020 Hybrids as Acetylcholinesterase Inhibitors for the Treatment of Alzheimer's Disease. *Bioorg. Med. Chem. Lett.* **2004**, *14*, 4639–4642.

(11) Bolognesi, M. L.; Andrisano, V.; Bartolini, M.; Banzi, R.; Melchiorre, C. Propidium-Based Polyamine Ligands as Potent Inhibitors of Acetylcholinesterase and Acetylcholinesterase-Induced Amyloid-β Aggregation. *J. Med. Chem.* **2005**, *48*, 24–27.

(12) Rosini, M.; Andrisano, V.; Bartolini, M.; Bolognesi, M. L.; Hrelia, P.; Minarini, A.; Tarozzi, A.; Melchiorre, C. Rational Approach to Discover Multipotent Anti-Alzheimer Drugs. *J. Med. Chem.* **2005**, *48*, 360–363.

(13) Alonso, D.; Dorronsoro, I.; Rubio, L.; Muñoz, P.; García-Palomero, E.; Del Monte, M.; Bidon-Chanal, A.; Orozco, M.; Luque, F. J.; Castro, A.; Medina, M.; Martínez, A. Donepezil–Tacrine Hybrid Related Derivatives as New Dual Binding Site Inhibitors of AChE. *Bioorg. Med. Chem.* **2005**, *13*, 6588–6597.

(14) Muñoz-Ruiz, P.; Rubio, L.; García-Palomero, E.; Dorronsoro, I.; del Monte-Millán, M.; Valenzuela, R.; Usán, P.; de Austria, C.; Bartolini, M.; Andrisano, V.; Bidon-Chanal, A.; Orozco, M.; Luque, F. J.; Medina, M.; Martínez, A. Design, Synthesis, and Biological Evaluation of Dual Binding Site Acetylcholinesterase Inhibitors: New Disease-Modifying Agents for Alzheimer's Disease. *J. Med. Chem.* **2005**, *48*, 7223–7233.

(15) Gemma, S.; Gabellieri, E.; Huleatt, P.; Fatorusso, C.; Borriello, M.; Catalanotti, B.; Butini, S.;

De Angelis, M.; Novellino, E.; Nacci, V.; Belinskaya, T.; Saxena, A.; Campiani, G. Discovery of Huperzine A–Tacrine Hybrids as Potent Inhibitors of Human Cholinesterases Targeting Their Midgorge Recognition Sites. *J. Med. Chem.* **2006**, *49*, 3421–3425.

(16) Piazzi, L.; Rampa, A.; Bisi, A.; Gobbi, S.; Belluti, F.; Cavalli, A.; Bartolini, M.; Andrisano, V.; Valenti, P.; Recanatini, M. 3-(4-{[Benzyl(methyl)amino]methyl}phenyl)-6,7-dimethoxy-2*H*-2-chromenone (AP2238) Inhibits Both Acetylcholinesterase and Acetylcholinesterase-Induced β-Amyloid Aggregation: A Dual Function Lead for Alzheimer's Disease Therapy. *J. Med. Chem.* **2003**, *46*, 2279–2282.

(17) Belluti, F.; Rampa, A.; Piazzi, L.; Bisi, A.; Gobbi, S.; Bartolini, M.; Andrisano, V.; Cavalli, A.; Recanatini, M.; Valenti, P. Cholinesterase Inhibitors: Xanthostigmine Derivatives Blocking the Acetylcholinesterase-Induced β-Amyloid Aggregation. *J. Med. Chem.* **2005**, *48*, 4444–4456.

(18) Coughlan, C. M.; Breen, K. C. Factors Influencing the Processing and Function of the Amyloid β Precursor Protein–A Potential Therapeutic Target in Alzheimer's Disease?. *Pharmacol. Ther.* **2000**, *86*, 111–144.

(19) De Ferrari, G. V.; Canales, M. A.; Shin, I.; Weiner, L. M.; Silman, I.; Inestrosa, N. C. A Structural Motif of Acetylcholinesterase That Promotes Amyloid Beta-Peptide Fibril Formation. *Biochemistry* **2001**, *40*, 10447–10457.

(20) For a review see: Muñoz-Torrero, D.; Camps, P. Dimeric and Hybrid Anti-Alzheimer Drug Candidates. *Curr. Med. Chem.* **2006**, *13*, 763–771.

(21) Sugimoto, H.; Iimura, Y.; Yamanishi, Y.; Yamatsu, K. Synthesis and Structure–Activity Relationships of Acetylcholinesterase Inhibitors: 1-Benzyl-4-[(5,6-dimethoxy-1-oxoindan-2-

yl)methyl]piperidine Hydrochloride and Related Compounds. *J. Med. Chem.* **1995**, *38*, 4821–4829.

(22) Kryger, G.; Silman, I.; Sussman, J. L. Structure of Acetylcholinesterase Complexed with E2020 (Aricept®): Implications for the Design of New Anti-Alzheimer Drugs. *Structure* **1999**, *7*, 297–307.

(23) Villalobos, A.; Blake, J. F.; Biggers, C. K.; Butler, T. W.; Chapin, D. S.; Chen, Y. L.; Ives, J. L.; Jones, S. B.; Liston, D. R.; Nagel, A. A.; Nason, D. M.; Nielsen, J. A.; Shalaby, I. A.; White, W. F. Novel Benzisoxazole Derivatives as Potent and Selective Inhibitors of Acetylcholinesterase. *J. Med. Chem.* **1994**, *37*, 2721–2734.

(24) Villalobos, A.; Butler, T. W.; Chapin, D. S.; Chen, Y. L.; DeMattos, S. B.; Ives, J. L.; Jones, S. B.; Liston, D. R.; Nagel, A. A.; Nason, D. M.; Nielsen, J. A.; Ramírez, A. D.; Shalaby, I. A.; White, W. F. 5,7-Dihydro-3-[2-[1-(phenylmethyl)-4-piperidinyl]ethyl]-6*H*-pyrrolo[3,2-*f*]-1,2-benzisoxazol-6-one: A Potent and Centrally-Selective Inhibitor of Acetylcholinesterase with an Improved Margin of Safety. *J. Med. Chem.* **1995**, *38*, 2802–2808.

(25) Martinez, A.; Fernandez, E.; Castro, A.; Conde, S.; Rodriguez-Franco, I.; Baños, J. -E.; Badia, A. *N*-Benzylpiperidine Derivatives of 1,2,4-Thiadiazolidinone as New Acetylcholinesterase Inhibitors. *Eur. J. Med. Chem.* **2000**, *35*, 913–922.

(26) Vidaluc, J. -L.; Calmel, F.; Bigg, D.; Carilla, E.; Stenger, A.; Chopin, P.; Briley, M. Novel [2-(4-Piperidinyl)ethyl](thio)ureas: Synthesis and Antiacetylcholinesterase Activity. *J. Med. Chem.* **1994**, *37*, 689–695.

(27) Harel, M.; Schalk, I.; Ehret-Sabatier, L.; Bouet, F.; Goeldner, M.; Hirth, C.; Axelsen, P.; Silman, I.; Sussman, J. L. Quaternary Ligand Binding to Aromatic Residues in the Active-Site

Gorge of Acetylcholinesterase. *Proc. Natl. Acad. Sci. U.S.A.* **1993**, *90*, 9031–9035.

(28) Wlodek, S. T.; Antosiewicz, J.; McCammon, J. A.; Straatsma, T. P.; Gilson, M. K.; Briggs, J. M.; Humblet, C.; Sussman, J. L. Binding of Tacrine and 6-Chlorotacrine by Acetylcholinesterase. *Biopolymers* **1996**, *38*, 109–117.

(29) Recanatini, M.; Cavalli, A.; Belluti, F.; Piazzi, L.; Rampa, A.; Bisi, A.; Gobbi, S.; Valenti, P.; Andrisano, V.; Bartolini, M., Cavrini, V. SAR of 9-Amino-1,2,3,4-tetrahydroacridine-Based Acetylcholinesterase Inhibitors: Synthesis, Enzyme Inhibitory Activity, QSAR, and Structure-Based CoMFA of Tacrine Analogues. *J. Med. Chem.* **2000**, *43*, 2007–2018.

(30) Dvir, H.; Wong, D. M.; Harel, M.; Barril, X.; Orozco, M.; Luque, F. J.; Muñoz-Torrero, D.; Camps, P.; Rosenberry, T. L.; Silman, I.; Sussman, J. L. 3D Structure of *Torpedo californica* Acetylcholinesterase Complexed with Huprine X at 2.1 Å Resolution: Kinetic and Molecular Dynamic Correlates. *Biochemistry* **2002**, *41*, 2970–2981.

(31) Hu, M. -K.; Lu, C. -F. A Facile Synthesis of Bis-Tacrine Isosteres. *Tetrahedron Lett.* **2000**, *41*, 1815–1818.

(32) Michalson, E.T.; D'Andrea, S.; Freeman, J.P.; Szmuszkovicz, J. The Synthesis of 9-(1-Azetidinyl)-1,2,3,4-tetrahydroacridine. *Heterocycles* **1990**, *30*, 415–425.

(33) Reddy, K. V. S. R. K.; Babu, J. M.; Kumar, P. A.; Chandrashekar, E. R. R.; Mathad, V. T.; Eswaraiah, S.; Reddy, M. S.; Vyas, K. Identification and Characterization of Potential Impurities of Donepezil. *J. Pharm. Biomed. Anal.* **2004**, *35*, 1047–1058.

(34) Galanakis, D.; Davis, C. A.; Ganellin, C. R.; Dunn, P. M. Synthesis and Quantitative Structure-Activity Relationship of a Novel Series of Small Conductance Ca^{2+}-Activated K^+

Channel Blockers Related to Dequalinium. *J. Med. Chem.* **1996**, *39*, 359–370.

(35) Ellman, G. L.; Courtney, K. D.; Andres, B., Jr.; Featherstone, R. M. A New and Rapid Colorimetric Determination of Acetylcholinesterase Activity. *Biochem. Pharmacol.* **1961**, *7*, 88–95.

(36) Giacobini, E. Cholinesterases: New Roles in Brain Function and in Alzheimer's Disease. *Neurochem. Res.* **2003**, *28*, 515–522.

(37) Carlier, P. R.; Chow, E. S. -H.; Han, Y.; Liu, J.; El Yazal, J.; Pang, Y. -P. Heterodimeric Tacrine-Based Acetylcholinesterase Inhibitors: Investigating Ligand–Peripheral Site Interactions. *J. Med. Chem.* **1999**, *42*, 4225–4231.

(38) Alvarez, A.; Bronfman, F.; Pérez, C. A.; Vicente, M.; Garrido, J.; Inestrosa, N. C. Acetylcholinesterase, a Senile Plaque Component, Affects the Fibrillogenesis of Amyloid-β-Peptides. *Neurosci. Lett.* **1995**, *201*, 49–52.

(39) Inestrosa, N.C.; Alvarez, A.; Pérez, C. A.; Moreno, R. D.; Vicente, M.; Linker, C.; Casanueva, O. I.; Soto, C.; Garrido, J. Acetylcholinesterase Accelerates Assembly of Amyloid-β-Peptides into Alzheimer's Fibrils: Possible Role of the Peripheral Site of the Enzyme. *Neuron* **1996**, *16*, 881–891.

(40) Alvarez, A.; Alarcón, R.; Opazo, C.; Campos, E. O.; Muñoz, F. J.; Calderón, F. H.; Dajas, F.; Gentry, M. K.; Doctor, B. P.; De Mello, F. G.; Inestrosa, N. C. Stable Complexes Involving Acetylcholinesterase and Amyloid-β-Peptide Change the Biochemical Properties of the Enzyme and Increase the Neurotoxicity of Alzheimer's Fibrils. *J. Neurosci.* **1998**, *18*, 3213–3223.

(41) Taylor, P.; Lappi, S. Interaction of Fluorescence Probes with Acetylcholinesterase. The Site and Specificity of Propidium Binding. *Biochemistry* **1975**, *14*, 1989–1997.

(42) Camps, P.; Cusack, B.; Mallender, W. D.; El Achab, R.; Morral, J.; Muñoz-Torrero, D.; Rosenberry, T. L. Huprine X Is a Novel High-Affinity Inhibitor of Acetylcholinesterase That Is of Interest for Treatment of Alzheimer's Disease. *Mol. Pharmacol.* **2000**, *57*, 409–417.

(43) LeVine, H., III. Quantification of β-sheet amyloid fibril structures with thioflavin T. *Methods Enzymol.* **1999**, *309*, 274–284.

(44) Eisert, R.; Felau, L.; Brown, L. R. Methods for Enhancing the Accuracy and Reproducibility of Congo Red and Thioflavin T Assays. *Anal. Biochem.* **2006**, *353*, 144–146.

(45) De Ferrari, G. V.; Mallender, W. D.; Inestrosa, N. C.; Rosenberry, T. L. Thioflavin T Is a Fluorescent Probe of the Acetylcholinesterase Peripheral Site That Reveals Conformational Interactions between the Peripheral and Acylation Sites. *J. Biol. Chem.* **2001**, *276*, 23282–23287.

(46) Camps, P.; El Achab, R.; Morral, J.; Muñoz-Torrero, D.; Badia, A.; Baños, J. E.; Vivas, N. M.; Barril, X.; Orozco, M.; Luque, F. J. New Tacrine-Huperzine A Hybrids (Huprines): Highly Potent Tight-Binding Acetylcholinesterase Inhibitors of Interest for the Treatment of Alzheimer's Disease. *J. Med. Chem.* **2000**, *43*, 4657-4666.

(47) Senapati, S.; Bui, J. M.; McCammon, J. A. Induced Fit in Mouse Acetylcholinesterase upon Binding a Femtomolar Inhibitor: A Molecular Dynamics Study. *J. Med. Chem.* **2005**, *48*, 8155-8162.

(48) Bourne, Y.; Radic, Z.; Kolb, H. C.; Sharpless, K. B.; Taylor, P.; Marchot, P. Structural Insights Into Conformational Flexibility at the Peripheral Site and Within the Active Center

Gorge of AChE. *Chem.-Biol. Interactions* **2005**, *157-158*, 159-165.

(49) Colletier, J. Ph.; Sanson, B.; Nachon, F.; Gabellieri, E.; Fattorusso, C.; Campiani, G.; Weik, M. Conformational Flexibility in the Peripheral Site of *Torpedo californica* Acetylcholinesterase Revealed by the Complex Structure with a Bifunctional Inhibitor. *J. Am. Chem. Soc.* **2006**, *128*, 4526-4527.

(50) Aguado, F.; Badía, A.; Baños, J. E.; Bosch, F.; Bozzo, C.; Camps, P.; Contreras, J.; Dierssen, M.; Escolano, C.; Görbig, D. M.; Muñoz-Torrero, D.; Pujol, M. D.; Simón, M.; Vázquez, M. T.; Vivas, N. M. Synthesis and Evaluation of Tacrine-Related Compounds for the Treatment of Alzheimer's Disease. *Eur. J. Med. Chem.* **1994**, *29*, 205–221.

(51) Kryger, G; Harel, M; Giles, K; Toker, L; Velan, B; Lazar, A; Kronman, C; Barak, D; Ariel, N; Shafferman, A; Silman, I; Sussman, J.L. Structures of Recombinant Native and E202Q Mutant Human Acetylcholinesterase Complexed with the Snake-Venom Toxin Fasciculin-II. *Acta Cystallogr. D: Biol. Crystallogr.* **2000**, 56, 1385-1394.

(52) InsightII, Accelrys Inc.: San Diego, CA, 1996.

(53) Jorgensen, W. L.; Chandrasekhar, J.; Madura, J. D.; Impey, R. W.; Klein, M. L. Comparison of Simple Potential Functions for Simulating Liquid Water. *J. Chem. Phys.* **1983**, *79*, 926–935.

(54) Case, D. A.; Darden, T. A.; Cheatham, T. E.; Pearlman, D. A.; Simmerling, C L..; Wang, J.; Duke, R. E.; Luo, R.; Merz, K. M.; Pearlman, D. A.; Crowley, M.; Brozell, S.; Tsui, V.; Gohlke, H.; Mongan, J.; Hornak, V.; Cui, G.; Beroza, P.; Schafmeister, P.; Caldwell, J. W.; Ross, W. S.; Kollman, P. A. AMBER8. University of California. San Francisco. 2004.

(55) Gaussian 03, Revision B.04, M. J. Frisch, G. W. Trucks, H. B. Schlegel, G. E. Scuseria, M. A. Robb, J. R. Cheeseman, J. A. Montgomery, Jr., T. Vreven, K. N. Kudin, J. C. Burant, J. M.

Millam, S. S. Iyengar, J. Tomasi, V. Barone, B. Mennucci, M. Cossi, G. Scalmani, N. Rega, G. A. Petersson, H. Nakatsuji, M. Hada, M. Ehara, K. Toyota, R. Fukuda, J. Hasegawa, M. Ishida, T. Nakajima, Y. Honda, O. Kitao, H. Nakai, M. Klene, X. Li, J. E. Knox, H. P. Hratchian, J. B. Cross, C. Adamo, J. Jaramillo, R. Gomperts, R. E. Stratmann, O. Yazyev, A. J. Austin, R. Cammi, C. Pomelli, J. W. Ochterski, P. Y. Ayala, K. Morokuma, G. A. Voth, P. Salvador, J. J. Dannenberg, V. G. Zakrzewski, S. Dapprich, A. D. Daniels, M. C. Strain, O. Farkas, D. K. Malick, A. D. Rabuck, K. Raghavachari, J. B. Foresman, J. V. Ortiz, Q. Cui, A. G. Baboul, S. Clifford, J. Cioslowski, B. B. Stefanov, G. Liu, A. Liashenko, P. Piskorz, I. Komaromi, R. L. Martin, D. J. Fox, T. Keith, M. A. Al-Laham, C. Y. Peng, A. Nanayakkara, M. Challacombe, P. M. W. Gill, B. Johnson, W. Chen, M. W. Wong, C. Gonzalez, and J. A. Pople, Gaussian, Inc., Pittsburgh PA, 2003.

(56) Bayly, C. I.; Cieplak, P.; Cornell, W. D.; Kollman, P. A. A Well-Behaved Electrostatic Potential Based Method Using Charge Restraints for Deriving Atomic Charges. *J. Phys. Chem.* **1993**, *97*, 10269–10280.

Supporting Information

for

Synthesis, Pharmacological Evaluation and Molecular Modeling of Novel Donepezil–Tacrine Hybrids, Subnanomolar Dual Binding Site Acetylcholinesterase Inhibitors

Pelayo Camps,[a,*] Xavier Formosa,[a] Diego Muñoz-Torrero,[a,*] Michele Scarpellini,[a,b] Albert Badia,[c] Maria Victòria Clos,[c] Axel Bidon-Chanal,[d] and F. Javier Luque[d]

[a] Laboratori de Química Farmacèutica (Unitat Associada al CSIC), Facultat de Farmàcia, Universitat de Barcelona, Av. Diagonal 643, E-08028, Barcelona, Spain

[b] Current address:

[c] Departament de Farmacologia, de Terapèutica i de Toxicologia, Institut de Neurociències, Universitat Autònoma de Barcelona, E-08193-Bellaterra, Barcelona, Spain

Supporting information available: Experimental part (chemistry, pharmacology, and molecular modeling) (Total xx pages).

Chemistry. General Methods. Melting points were determined in open capillary tubes with a MFB 595010M Gallenkamp melting point apparatus. 300 MHz ^{1}H / 75.4 MHz ^{13}C NMR spectra, 400 MHz ^{1}H / 100.6 MHz ^{13}C NMR spectra, and 500 MHz ^{1}H NMR spectra were recorded on Varian Gemini 300, Varian Mercury 400, and Varian Inova 500 spectrometers, respectively. The chemical shifts are reported in ppm (δ scale) relative to internal TMS, and coupling constants are reported in Hertz (Hz). Assignments given for the NMR spectra of the new compounds have been carried out by comparison with the NMR data of **15a**, **16a**, **17b**, and 6-chlorotacrine, as model compounds, which in turn, were assigned on the basis of DEPT, COSY $^{1}H/^{1}H$ (standard procedures), NOESY $^{1}H/^{1}H$, and COSY $^{1}H/^{13}C$ (gHSQC and gHMBC sequences) experiments. IR spectra were run on a Perkin-Elmer Spectrum RX I spectrophotometer. Absorption values are expressed as wave-numbers (cm^{-1}); only significant absorption bands are given. Column chromatography was performed on silica gel 60 AC.C (35–70 mesh, SDS, ref 2000027). Thin-layer chromatography (TLC) was performed with aluminum-backed sheets with silica gel 60 F_{254} (Merck, ref 1.05554), and spots were visualized with UV light and 1% aqueous solution of $KMnO_4$. Analytical grade solvents were used for crystallization, while pure for synthesis solvents were used in the reactions, extractions and column chromatography. For characterization purposes, the new donepezil–tacrine hybrids were transformed into the corresponding dihydrochlorides, and recrystallized,. Worthy of note, as previously reported for some tacrine-related dimeric compounds,[1] the new donepezil–tacrine hybrids have the ability to retain molecules of water, which can not be removed after drying the analytical

samples at 80 °C / 30 Torr for 2 days. Thus, the elemental analyses of these compounds showed the presence of variable amounts of water. NMR spectra of all of the new compounds were performed at the Serveis Científico-Tècnics of the University of Barcelona, while elemental analyses and high resolution mass spectra were carried out at the Mycroanalysis Service of the IIQAB (CSIC, Barcelona, Spain) with a Carlo Erba model 1106 analyzer, and at the Mass Spectrometry Laboratory of the University of Santiago de Compostela (Spain) with Micromass Autospec spectrometer, respectively.

General procedure for the reaction of 9-chloro-1,2,3,4-tetrahydroacridine, 5, or 6,9-dichloro-1,2,3,4-tetrahydroacridine, 6, with ω-aminoalcohols. A mixture of **5** or **6** (1 mmol) and an excess of the aminoalcohol **7** (3 mmol) in 1-pentanol (1 mL) was heated under reflux with magnetic stirring for 18 h. The resulting mixture was cooled to room temperature, diluted with CH_2Cl_2 (3.5 mL), washed with 10% aqueous NaOH (3.5 mL) and water (2×3 mL). The organic phase was dried with anhydrous Na_2SO_4, filtered and concentrated in vacuo to give an oily residue. The excess of aminoalcohol and solvent was removed from this residue by distillation in a rotary microdistillation equipment at 85 °C / 0.8 Torr to give the substitution product **8** or **9** as a pale brown solid residue.

The analytical samples of the hydrochlorides of **8** and **9** were prepared as follows: the alcohol **8** or **9** (1 mmol) was dissolved in MeOH (10 mL), the solution was filtered through a PTFE 0.45 μm filter, and treated with an excess of a methanolic solution of HCl (3 mmol) and the resulting solution was concentrated in vacuo to dryness. The solid was

recrystallized from a mixture MeOH / AcOEt in the ratio of 1:4 (5 mL), and dried at 80 °C / 30 Torr for 48 h, to give the 9-(ω-hydroxyalkylamino)tetrahydroacridine hydrochloride **8**·HCl or **9**·HCl as a light brown solid.

9-[(2-Hydroxyethyl)amino]-1,2,3,4-tetrahydroacridine (8a). From **5** (3.00 g, 13.8 mmol) and 2-aminoethanol, **7a** (2.49 mL, 2.52 g, 41.3 mmol), alcohol **8a** (3.07 g, 92% yield, free base) was obtained: R_f 0.38 (CH_2Cl_2 / MeOH / 25% aqueous NH_4OH 9:1:0.1). **8a**·HCl: mp 184–185 °C (MeOH / AcOEt 1:4); IR (KBr) ν 3700–2400 (max. at 3358, 3142, 3058, 3016, 2938, 2872, O–H, N–H, $^+$N–H and C–H st), 1633, 1592, 1577 and 1524 (ar–C–C and ar–C–N st) cm^{-1}; ^{1}H NMR (300 MHz, CD_3OD) δ 1.90–2.04 (complex signal, 4H, 2-H_2 and 3-H_2), 2.74 (m, 2H, 1-H_2), 3.01 (m, 2H, 4-H_2), 3.86 (t, J = 5.4 Hz, 2H, 2'-H_2), 4.01 (t, J = 5.4 Hz, 2H, 1'-H_2), 4.87 (s, OH, NH and $^+$NH), 7.54 (ddd, J = 8.4 Hz, J' = 6.0 Hz, J'' = 2.4 Hz, 1H, 7-H), 7.76–7.84 (complex signal, 2H, 5-H and 6-H), 8.40 (d, J = 8.4 Hz, 1H, 8-H); ^{13}C NMR (75.4 MHz, CD_3OD) δ 21.1 (CH_2, C3), 23.1 (CH_2, C2), 24.8 (CH_2, C1), 30.1 (CH_2, C4), 51.2 (CH_2, C1'), 61.7 (CH_2, C2'), 113.7 (C, C9a), 117.7 (C, C8a), 121.2 (CH, C5), 126.0 (CH, C8), 126.1 (CH, C7), 133.3 (CH, C6), 140.9 (C, C10a), 152.8 (C, C4a), 157.4 (C, C9). HRMS calcd for ($C_{15}H_{18}N_2O + H^+$): 243.1497. Found: 243.1494.

9-[(3-Hydroxypropyl)amino]-1,2,3,4-tetrahydroacridine (8b). From **5** (1.12 g, 5.15 mmol) and 3-amino-1-propanol, **7b** (1.16 mL, 1.14 g, 15.2 mmol), alcohol **8b** (1.25 g, 95%

yield, free base) was obtained: R_f 0.27 (CH_2Cl_2 / MeOH / 25% aqueous NH_4OH 9:1:0.1). **8b**·HCl: mp 125–126 °C (MeOH / AcOEt 1:4) [described 130–133 °C].[2]

6-Chloro-9-[(2-hydroxyethyl)amino]-1,2,3,4-tetrahydroacridine (9a). From **6** (3.00 g, 11.9 mmol) and 2-aminoethanol, **7a** (2.16 mL, 2.19 g, 35.9 mmol), alcohol **9a** (3.16 g, 96% yield, free base) was obtained: R_f 0.42 (CH_2Cl_2 / MeOH / 25% aqueous NH_4OH 9:1:0.1). **9a**·HCl: mp 221–222 °C (MeOH / AcOEt 1:4); IR (KBr) ν 3600–2400 (max. at 3372, 3291, 3136, 3052, 3009, 2939, 2872, 2784, O–H, N–H, $^+$N–H and C–H st), 1632, 1588, 1573, and 1518 (ar–C–C and ar–C–N st) cm^{-1}; ^1H NMR (500 MHz, CD_3OD) δ 1.93–2.02 (complex signal, 4H, 2-H_2 and 3-H_2), 2.71 (m, 2H, 1-H_2), 3.00 (m, 2H, 4-H_2), 3.89 (t, J = 5.2 Hz, 2H, 2'-H_2), 4.07 (t, J = 5.2 Hz, 2H, 1'-H_2), 4.85 (s, OH, NH and $^+$NH), 7.56 (dd, J = 9.0 Hz, J' = 2.0 Hz, 1H, 7-H), 7.77 (d, J = 2.0 Hz, 1H, 5-H), 8.49 (d, J = 9.0 Hz, 1H, 8-H); ^{13}C NMR (75.4 MHz, CD_3OD) δ 21.8 (CH_2, C3), 22.8 (CH_2, C2), 24.6 (CH_2, C1), 29.3 (CH_2, C4), 51.2 (CH_2, C1'), 61.4 (CH_2, C2'), 113.5 (C, C9a), 115.4 (C, C8a), 119.0 (CH, C5), 126.6 (CH, C7), 128.7 (CH, C8), 139.9 (C, C6), 140.3 (C, C10a), 152.2 (C, C4a), 158.2 (C, C9). Anal. ($C_{15}H_{17}ClN_2O$·HCl·1/4H_2O) C, H, N, Cl.

6-Chloro-9-[(3-hydroxypropyl)amino]-1,2,3,4-tetrahydroacridine (9b). From **6** (2.29 g, 9.09 mmol) and 3-amino-1-propanol, **7b** (2.08 mL, 2.04 g, 27.2 mmol), alcohol **9b** (2.10 g, 80% yield, free base) was obtained: R_f 0.32 (CH_2Cl_2 / MeOH / 25% aqueous NH_4OH 9:1:0.1). **9b**·HCl: mp 164–165 °C (MeOH / AcOEt 1:4); IR (KBr) ν 3500–2400 (max. at

3353, 3314, 3263, 3131, 3051, 3014, 2936, 2907, 2875, 2845, 2803, O–H, N–H, $^{+}$N–H and C–H st), 1630, 1572, and 1526 (ar–C–C and ar–C–N st) cm^{-1}; ^{1}H NMR (500 MHz, CD_3OD) δ 1.92–2.00 (complex signal, 4H, 2-H_2 and 3-H_2), 2.03 (m, 2H, 2'-H_2), 2.64 (m, 2H, 1-H_2), 2.99 (m, 2H, 4-H_2), 3.83 (t, J = 5.5 Hz, 2H, 3'-H_2), 4.14 (t, J = 6.0 Hz, 2H, 1'-H_2), 4.85 (s, OH, NH and $^{+}$NH), 7.54 (dd, J = 9.0 Hz, J' = 2.0 Hz, 1H, 7-H), 7.76 (d, J = 2.0 Hz, 1H, 5-H), 8.46 (d, J = 9.0 Hz, 1H, 8-H); ^{13}C NMR (75.4 MHz, CD_3OD) δ 21.8 (CH_2, C3), 22.8 (CH_2, C2), 24.6 (CH_2, C1), 29.3 (CH_2, C4), 33.0 (CH_2, C2'), 48.6 (CH_2, C1'), 61.5 (CH_2, C3'), 113.1 (C, C9a), 115.1 (C, C8a), 118.9 (CH, C5), 126.1 (CH, C7), 129.0 (CH, C8), 139.9 (C, C6), 140.5 (C, C10a), 151.6 (C, C4a), 157.5 (C, C9). Anal. ($C_{16}H_{19}ClN_2O \cdot HCl \cdot 1/4H_2O$) C, H, N, Cl.

General procedure for the mesylation of alcohols 8 and 9. To a cold solution (–10 °C, ice-salt bath) of the alcohol **8** or **9** (1 mmol) and anhydrous Et_3N (1.7 mmol) in anhydrous CH_2Cl_2 (6 mL), methanesulfonyl chloride (1.5 mmol) was added dropwise and the reaction mixture was stirred for 30 min at this temperature. The mixture was concentrated in vacuo, the residue was taken in CH_2Cl_2 (3 mL) and the resulting organic solution was washed with 10% aqueous NaOH (2×3 mL) until the aqueous phase remained basic (pH > 10), dried with anhydrous Na_2SO_4 and concentrated in vacuo to give the corresponding mesylate **10** or **11** as a brown oily residue. The analytical samples of the mesylates were obtained by washing the oily crude product with AcOEt, except in the case of **11a**, whose analytical

sample was prepared by recrystallization of the corresponding hydrochloride, obtained in a similar way to that described for the hydrochlorides of alcohols **8** and **9**.

9-[(2-Methanesulfonyloxyethyl)amino]-1,2,3,4-tetrahydroacridine (10a). From alcohol **8a** (2.15 g, 8.88 mmol), mesylate **10a** (3.13 g, quantitative yield) was obtained: R_f 0.67 (CH_2Cl_2 / MeOH / 25% aqueous NH_4OH 9:1:0.1); IR (NaCl) ν 3391 and 3339 (N-H st), 1638, 1586 and 1524 (ar–C–C and ar–C–N st), 1352 (SO_2 st as), 1178 (SO_2 st s) cm^{-1}; ^1H NMR (300 MHz, $CDCl_3$) δ 1.88–1.98 (complex signal, 4H, 2-H_2 and 3-H_2), 2.76 (m, 2H, 1-H_2), 2.97 (s, 3H, OSO_2CH_3), 3.08 (m, 2H, 4-H_2), 3.81 (m, 2H, 1'-H_2), 4.34 (t, J = 4.9 Hz, 2H, 2'-H_2), 4.54 (broad s, 1H, NH), 7.39 (ddd, J = 8.4 Hz, J' = 6.8 Hz, J'' = 1.5 Hz, 1H, 7-H), 7.57 (ddd, J = 8.4 Hz, J' = 6.8 Hz, J'' = 1.5 Hz, 1H, 6-H), 7.91–7.95 (complex signal, 2H, 5-H and 8-H); ^{13}C NMR (75.4 MHz, $CDCl_3$) δ 22.4 (CH_2) and 22.7 (CH_2) (C2 and C3), 24.7 (CH_2, C1), 33.3 (CH_2, C4), 37.3 (CH_3, OSO_2CH_3), 47.4 (CH_2, C1'), 69.0 (CH_2, C2'), 117.7 (C, C9a), 120.7 (C, C8a), 122.2 (CH), 124.3 (CH), 127.8 (CH), and 128.7 (CH) (C5, C6, C7, and C8), 146.2 (C, C10a), 149.6 (C, C4a), 158.2 (C, C9). HRMS calcd for ($C_{16}H_{20}N_2O_3S + H^+$): 321.127. Found: 321.128.

9-[(3-Methanesulfonyloxypropyl)amino]-1,2,3,4-tetrahydroacridine (10b). From alcohol **8b** (433 mg, 1.69 mmol), mesylate **10b** (565 mg, quantitative yield) was obtained: R_f 0.95 (CH_2Cl_2 / MeOH / 25% aqueous NH_4OH 9:1:0.1); IR (NaCl) ν 3282 (N-H st), 1639, 1586, 1524 and 1501 (ar–C–C and ar–C–N st), 1352 (SO_2 st as), 1174 (SO_2 st s) cm^{-1}; ^1H

NMR (300 MHz, $CDCl_3$) δ 1.84–1.94 (complex signal, 4H, 2-H_2 and 3-H_2), 2.06 (m, 2H, 2'-H_2), 2.71 (m, 2H, 1-H_2), 2.96 (s, 3H, OSO_2CH_3), 3.04 (m, 2H, 4-H_2), 3.60 (m, 2H, 1'-H_2), 4.33 (t, J = 5.8 Hz, 2H, 3'-H_2), 7.35 (pseudo t, J = 7.6 Hz, 1H, 7-H), 7.54 (pseudo t, J = 7.6 Hz, 1H, 6-H), 7.88–7.92 (complex signal, 2H, 5-H and 8-H) (the signal corresponding to the NH group was not observed); ^{13}C NMR (75.4 MHz, $CDCl_3$) δ 22.5 (CH_2) and 22.8 (CH_2) (C2 and C3), 24.7 (CH_2, C1), 30.6 (CH_2, C2'), 33.5 (CH_2, C4), 37.2 (CH_3, OSO_2CH_3), 44.7 (CH_2, C1'), 67.4 (CH_2, C3'), 116.7 (C, C9a), 120.1 (C, C8a), 122.2 (CH), 124.0 (CH), 128.1 (CH), and 128.4 (CH) (C5, C6, C7, and C8), 146.6 (C, C10a), 150.2 (C, C4a), 158.2 (C, C9). HRMS calcd for ($C_{17}H_{22}N_2O_3S + H^+$): 335.142. Found: 335.141.

6-Chloro-9-[(2-methanesulfonyloxyethyl)amino]-1,2,3,4-tetrahydroacridine (11a). From alcohol **9a** (2.95 g, 10.7 mmol), mesylate **11a** (3.72 g, 98% yield) was obtained: R_f 0.63 (CH_2Cl_2 / MeOH / 25% aqueous NH_4OH 9:1:0.1). **11a**·HCl: mp: 149–150 °C (MeOH); IR (KBr) ν 3700–2500 (max. at 3426, 3234, 3114, 3012, 2925, 2798, N–H, $^+$N–H and C–H st), 1630, 1606, 1582 and 1572 (ar–C–C and ar–C–N st), 1354 (SO_2 st as), 1161 (SO_2 st s) cm^{-1}; ^1H NMR (500 MHz, CD_3OD) δ 1.94–2.00 (complex signal, 4H, 2-H_2 and 3-H_2), 2.76 (m, 2H, 1-H_2), 3.03 (m, 2H, 4-H_2), 3.08 (s, 3H, OSO_2CH_3), 4.31 (t, J = 5.0 Hz, 2H, 1'-H_2), 4.57 (t, J = 5.0 Hz, 2H, 2'-H_2), 4.85 (s, NH and $^+$NH), 7.59 (dd, J = 9.0 Hz, J' = 2.0 Hz, 1H, 7-H), 7.82 (d, J = 2.0 Hz, 1H, 5-H), 8.39 (d, J = 9.0 Hz, 1H, 8-H); ^{13}C NMR (75.4 MHz, CD_3OD) δ 21.7 (CH_2, C3), 22.8 (CH_2, C2), 25.1 (CH_2, C1), 29.5 (CH_2, C4), 37.4 (CH_3, OSO_2CH_3), 48.3 (CH_2, C1'), 69.7 (CH_2, C2'), 114.7 (C, C9a), 116.0 (C, C8a), 119.2

(CH, C5), 127.2 (CH, C7), 128.3 (CH, C8), 140.2 (2 C, C6 and C10a), 153.2 (C, C4a), 158.6 (C, C9). HRMS calcd for ($C_{16}H_{19}ClN_2O_3S + H^+$): 355.0878. Found: 355.0889.

6-Chloro-9-[(3-methanesulfonyloxypropyl)amino]-1,2,3,4-tetrahydroacridine (11b). From alcohol **9b** (1.50 g, 5.16 mmol), impure mesylate **11b** (1.90 g) was obtained, and directly used in the next step without further purification: R_f 0.70 (CH_2Cl_2 / MeOH / 25% aqueous NH_4OH 9:1:0.1).

General procedure for the coupling of mesylates 10 and 11 with 5,6-dimethoxy-2-[(4-piperidyl)methyl]indan-1-one (12) or 5,6-dimethoxy-2-[(4-piperidyl)methyl]indane (13). A solution of the mesylate **10** or **11** (1 mmol), the piperidine **12** or **13** (1 mmol) and anhydrous Et_3N (2.5 mmol) in DMSO (8 mL) was heated at 85 °C for 48 h. The resulting solution was allowed to cool to room temperature and was concentrated in vacuo. The brown oily residue was treated with aqueous 2 N NaOH (25 mL) and extracted with CH_2Cl_2 (3×35 mL). The combined organic extracts were washed with water (5×40 mL) and brine (2×30 mL), dried with anhydrous Na_2SO_4, filtered, and evaporated at reduced pressure to give an oily residue which was submitted to column chromatography (35–70 μm silica gel, CH_2Cl_2 / MeOH / 25% aqueous NH_4OH mixtures as eluent).

The isolated donepezil–tacrine hybrids **14–17** were transformed into the corresponding dihydrochlorides as follows: A solution of the free base (1 mmol) in MeOH (40 mL) was filtered through a 0.45 μm PTFE filter and treated with excess of a methanolic solution of

HCl (5 mmol). The solution was concentrated in vacuo to dryness and the solid residue was recrystallized from MeOH (20 mL), and dried at 80 °C / 30 Torr for 48 h.

9-[(2-{4-[(5,6-Dimethoxy-1-oxoindan-2-yl)methyl]piperidin-1-yl}ethyl)amino]-1,2,3,4-tetrahydroacridine dihydrochloride (14a·2HCl). From mesylate **10a** (276 mg, 0.86 mmol) and piperidine **12** (249 mg, 0.86 mmol), compound **14a** (87 mg, 20% yield) was obtained as a pale brown solid, on elution with a mixture of CH_2Cl_2 / MeOH / 25% aqueous NH_4OH 99.5:0.5:0.4: R_f 0.91 (CH_2Cl_2 / MeOH / 25% aqueous NH_4OH 90:10:0.1). **14a**·2HCl: mp 190–191 °C (MeOH). IR (KBr) ν 3700–2400 (max. at 3401, 2928, 2871, 2718, N–H, $^+$N–H and C–H st), 1685, 1672 (C=O st), 1636, 1588, 1523 and 1500 (ar–C–C and ar–C–N st) cm^{-1}; ^{1}H NMR (500 MHz, CD_3OD) δ 1.45 (m, 1H, indanone-2-CH_a), 1.62–1.73 (broad signal, 2H, piperidine 3-H_{ax} and 5-H_{ax}), 1.86 (m, 1H, indanone-2-CH_b), 1.90–2.02 (broad signal, 1H, piperidine 4-H), superimposed 1.99 (complex signal, 4H, acridine 2-H_2 and 3-H_2), 2.02 (broad d, J = 14.5 Hz, 1H) and 2.14 (broad d, J = 14.0 Hz, 1H) (piperidine 3-H_{eq} and 5-H_{eq}), 2.74–2.80 (complex signal, 2H, indanone 2-H and 3-H_a), 2.84 (m, 2H, acridine 1-H_2), 3.08 (m, 2H, acridine 4-H_2), 3.12 (broad signal, 2H, piperidine 2-H_{ax} and 6-H_{ax}), superimposed in part 3.34 (dd, J = 18.0 Hz, J' = 8.5 Hz, 1H, indanone 3-H_b), 3.60 (broad signal, 2H, $NHCH_2CH_2N$), 3.72 (broad signal, 2H, piperidine 2-H_{eq} and 6-H_{eq}), 3.85 (s, 3H, 6-OCH_3), 3.94 (s, 3H, 5-OCH_3), 4.42 (t, J = 7.7 Hz, 2H, $NHCH_2CH_2N$), 4.85 (s, NH and $^+$NH), 7.07 (s, 1H, indanone 4-H), 7.15 (s, 1H, indanone 7-H), 7.68 (ddd, J = 8.5 Hz, J' = 7.0 Hz, J'' = 1.0 Hz, 1H, acridine 7-H), 7.83 (dd, J = 8.5 Hz, J' = 1.0 Hz, 1H,

acridine 5-H), 7.91 (ddd, J = 8.5 Hz, J' = 7.0 Hz, J'' = 1.0 Hz, 1H, acridine 6-H), 8.43 (d, J = 8.5 Hz, 1H, acridine 8-H); ^{13}C NMR (100.6 MHz, CD_3OD) δ 21.7 (CH_2, acridine C3), 23.0 (CH_2, acridine C2), 25.7 (CH_2, acridine C1), 29.5 (CH_2, acridine C4), 30.3 (CH_2) and 31.1 (CH_2) (piperidine C3 and C5), 33.0 (CH, piperidine C4), 34.2 (CH_2, indanone C3), 39.0 (CH_2, indanone-2-CH_2), 43.1 (CH_2, NH*C*H_2CH_2N), 46.1 (CH, indanone C2), 54.1 (2 CH_2, piperidine C2 and C6), 56.5 (CH_3, 6-OCH_3), 56.7 (CH_3, 5-OCH_3), 57.4 (CH_2, NHCH_2*C*H_2N), 105.3 (CH, indanone C7), 109.0 (CH, indanone C4), 114.4 (C, acridine C9a), 117.6 (C, acridine C8a), 120.3 (CH, acridine C5), 125.9 (CH, acridine C8), 127.2 (CH, acridine C7), 129.8 (C, indanone C7a), 134.3 (CH, acridine C6), 139.4 (C, acridine C10a), 151.1 (C, indanone C6), 151.3 (C, indanone C3a), 153.1 (C, acridine C4a), 157.8 (C) and 158.0 (C) (indanone C5 and acridine C9), 209.7 (C, indanone C1). Anal. ($C_{32}H_{39}N_3O_3 \cdot 2HCl \cdot 1.5H_2O$) C, H, N, Cl.

9-[(3-{4-[(5,6-Dimethoxy-1-oxoindan-2-yl)methyl]piperidin-1-yl}propyl)amino]-1,2,3,4-tetrahydroacridine dihydrochloride (14b·2HCl). From mesylate **10b** (80 mg, 0.24 mmol) and piperidine **12** (82 mg, 0.28 mmol), compound **14b** (87 mg, 69% yield) was obtained as a pale brown solid, on elution with a mixture of CH_2Cl_2 / MeOH / 25% aqueous NH_4OH 98:2:0.5: R_f 0.46 (CH_2Cl_2 / MeOH / 25% aqueous NH_4OH 9:1:0.1). **14b**·2HCl: mp 198–199 °C (MeOH); IR (KBr) ν 3700–2400 (max. at 3435, 2930, 2706, N–H, $^+$N–H and C–H st), 1690 (C=O st), 1636, 1590, 1522 and 1500 (ar–C–C and ar–C–N st) cm^{-1}; ^{1}H NMR (500 MHz, CD_3OD) δ1.44 (m, 1H, indanone-2-CH_a), 1.50–1.62 (broad signal, 2H,

piperidine 3-H_{ax} and 5-H_{ax}), 1.80–1.96 (broad signal, 2H, piperidine 4-H and indanone-2-CH_b), 1.96–2.05 (complex signal, 5H, acridine 2-H_2 and 3-H_2, and piperidine 3-H_{eq} or 5-H_{eq}), 2.10 (broad d, J = 13.0 Hz, piperidine 5-H_{eq} or 3-H_{eq}), 2.31 (complex signal, 2H, $NHCH_2CH_2CH_2N$), 2.72-2.80 (complex signal, 4H, acridine 1-H_2, indanone 2-H and 3-H_a), 2.95–3.03 (broad signal, 2H, piperidine 2-H_{ax} and 6-H_{ax}), 3.05 (m, 2H, acridine 4-H_2), 3.25 (complex signal, 2H, $NHCH_2CH_2CH_2N$), superimposed in part 3.34 (dd, 1H, indanone 3-H_b), 3.56–3.68 (broad signal, 2H, piperidine 2-H_{eq} and 6-H_{eq}), 3.85 (s, 3H, 6-OCH_3), 3.93 (s, 3H, 5-OCH_3), 4.08 (t, J = 7.0 Hz, 2H, $NHCH_2CH_2CH_2N$), 4.85 (s, NH and $^+$NH), 7.06 (s, 1H, indanone 4-H), 7.15 (s, 1H, indanone 7-H), 7.64 (ddd, J = 9.0 Hz, J' = 7.0 Hz, J'' = 1.0 Hz, 1H, acridine 7-H), 7.80 (dd, J = 8.5 Hz, J' = 1.0 Hz, 1H, acridine 5-H), 7.88 (ddd, J = 8.5 Hz, J' = 7.0 Hz, J'' = 1.0 Hz, 1H, acridine 6-H), 8.43 (d, J = 9.0 Hz, 1H, acridine 8-H); ^{13}C NMR (100.6 MHz, CD_3OD) δ 21.7 (CH_2, acridine C3), 23.0 (CH_2, acridine C2), 25.2 (CH_2, acridine C1), 26.3 (CH_2, $NHCH_2CH_2CH_2N$), 29.4 (CH_2, acridine C4), 30.3 (CH_2) and 31.2 (CH_2) (piperidine C3 and C5), 33.1 (CH, piperidine C4), 34.1 (CH_2, indanone C3), 39.0 (CH_2, indanone-2-CH_2), 45.9 (CH_2, $NHCH_2CH_2CH_2N$), 46.1 (CH, indanone C2), 54.1 (CH_2) and 54.2 (CH_2) (piperidine C2 and C6), 55.3 (CH_2, $NHCH_2CH_2CH_2N$), 56.5 (CH_3, 6-OCH_3), 56.8 (CH_3, 5-OCH_3), 105.2 (CH, indanone C7), 109.0 (CH, indanone C4), 113.5 (C, acridine C9a), 117.2 (C, acridine C8a), 120.2 (CH, acridine C5), 126.3 (CH, acridine C8), 126.8 (CH, acridine C7), 129.7 (C, indanone C7a), 134.2 (CH, acridine C6), 139.6 (C, acridine C10a), 151.0 (C, indanone C6), 151.4 (C,

indanone C3a), 152.3 (C, acridine C4a), 157.7 (C) and 157.9 (C) (indanone C5 and acridine C9), 209.9 (C, indanone C1). Anal. ($C_{33}H_{41}N_3O_3 \cdot 2HCl \cdot 2.5H_2O$) C, H, N, Cl.

6-Chloro-9-[(2-{4-[(5,6-dimethoxy-1-oxoindan-2-yl)methyl]piperidin-1-yl}ethyl)amino]-1,2,3,4-tetrahydroacridine dihydrochloride (15a·2HCl). From mesylate **11a** (305 mg, 0.86 mmol) and piperidine **12** (248 mg, 0.86 mmol), compound **15a** (178 mg, 38% yield) was obtained as a pale brown solid, on elution with a mixture of CH_2Cl_2 / MeOH / 25% aqueous NH_4OH 99.2:0.8:0.4: R_f = 0.94 (CH_2Cl_2 / MeOH / 25% aqueous NH_4OH 9:1:0.01). **15a**·2HCl: mp 222–223 °C (MeOH); IR (KBr) ν 3700–2400 (max. at 3375, 3259, 3125, 3051, 2927, 2854, 2792, N–H, $^+$N–H and C–H st), 1687 (C=O st), 1633, 1588 and 1501 (ar–C–C and ar–C–N st) cm^{-1}; ^1H NMR (500 MHz, CD_3OD) δ 1.44 (m, 1H, indanone-2-CH_a), 1.50–1.58 (broad signal, 2H, piperidine 3-H_{ax} and 5-H_{ax}), 1.82–1.92 (broad signal, 2H, piperidine 4-H and indanone-2-CH_b), 1.94–2.04 (complex signal, 5H, acridine 2-H_2 and 3-H_2, and piperidine 3-H_{eq} or 5-H_{eq}), 2.06 (broad d, J = 13.5 Hz, piperidine 5-H_{eq} or 3-H_{eq}), 2.74-2.80 (complex signal, 4H, acridine 1-H_2, indanone 2-H and 3-H_a), 2.8–3.0 (broad signal, 2H, piperidine 2-H_{ax} and 6-H_{ax}), 3.04 (m, 2H, acridine 4-H_2), superimposed in part 3.33 (dd, J = 17.5 Hz, J' = 7.5 Hz, 1H, indanone 3-H_b), 3.3–3.45 (broad signal, 2H, $NHCH_2CH_2N$), 3.45–3.6 (broad signal, 2H, piperidine 2-H_{eq} and 6-H_{eq}), 3.85 (s, 3H, 6-OCH_3), 3.93 (s, 3H, 5-OCH_3), 4.32 (m, 2H, $NHCH_2CH_2N$), 4.85 (s, NH and $^+$NH), 7.06 (s, 1H, indanone 4-H), 7.14 (s, 1H, indanone 7-H), 7.62 (broad d, J = 9.0 Hz, 1H, acridine 7-H), 7.81 (d, J = 1.5 Hz, 1H, acridine 5-H), 8.43 (d, J = 9.0 Hz, 1H, acridine

8-H); ^{13}C NMR (100.6 MHz, CD_3OD) δ 21.7 (CH_2, acridine C3), 22.9 (CH_2, acridine C2), 25.3 (CH_2, acridine C1), 29.6 (CH_2, acridine C4), 30.7 (CH_2) and 31.7 (CH_2) (piperidine C3 and C5), 33.5 (CH, piperidine C4), 34.1 (CH_2, indanone C3), 39.0 (CH_2, indanone-2-CH_2), 43.7 (CH_2, NHCH_2CH_2N), 46.3 (CH, indanone C2), 54.4 (2 CH_2, piperidine C2 and C6), 56.5 (CH_3, 6-OCH_3), 56.7 (CH_3, 5-OCH_3), 57.1 (CH_2, NHCH$_2$$CH_2$N), 105.2 (CH, indanone C7), 109.0 (CH, indanone C4), 114.5 (C, acridine C9a), 115.9 (C, acridine C8a), 119.4 (CH, acridine C5), 127.3 (CH, acridine C7), 128.4 (CH, acridine C8), 129.7 (C, indanone C7a), 140.1 (C, acridine C6), 140.4 (C, acridine C10a), 151.0 (C, indanone C6), 151.3 (C, indanone C3a), 153.3 (C, acridine C4a), 157.6 (C) and 157.7 (C) (indanone C5 and acridine C9), 209.8 (C, indanone C1). Anal. ($C_{32}H_{38}ClN_3O_3 \cdot 1.8HCl \cdot 1.8H_2O$) C, H, N, Cl. HRMS calcd for ($C_{32}H_{38}ClN_3O_3 + H^+$): 548.2680. Found: 548.2661.

6-Chloro-9-[(3-{4-[(5,6-Dimethoxy-1-oxoindan-2-yl)methyl]piperidin-1-yl}propyl)amino]-1,2,3,4-tetrahydroacridine dihydrochloride (15b·2HCl). From crude mesylate **11b** (506 mg, ≈ 1.37 mmol) and piperidine **12** (470 mg, 1.63 mmol), compound **15b** (254 mg, 33% yield) was obtained as a pale brown solid, on elution with a mixture of CH_2Cl_2 / MeOH / 25% aqueous NH_4OH 98:2:0.2: R_f = 0.52 (CH_2Cl_2 / MeOH / 25% aqueous NH_4OH 9:1:0.1). **15b**·2HCl: mp 185–186 °C (MeOH); IR (KBr) ν 3700–2400 (max. at 3402, 3263, 3071, 3039, 2925, 2842, N–H, $^+$N–H and C–H st), 1695 (C=O st), 1631, 1608, 1590, 1556 and 1501 (ar–C–C and ar–C–N st) cm^{-1}; ^{1}H NMR (500 MHz, CD_3OD) δ 1.42 (m, 1H, indanone-2-CH_a), 1.40–1.56 (broad signal, 2H, piperidine 3-H_{ax}

and 5-H_{ax}), 1.78–1.88 (broad signal, 2H, piperidine 4-H and indanone-2-CH_b), 1.90–2.05 (complex signal, 6H, acridine 2-H_2 and 3-H_2, and piperidine 3-H_{eq} and 5-H_{eq}), 2.20 (complex signal, 2H, $NHCH_2CH_2CH_2N$), 2.70–2.78 [complex signal, 6H, acridine 1-H_2, indanone 2-H and 3-H_a, piperidine 2-H_{ax} and 6-H_{ax}), superimposed in part 3.02 (m, 2H, acridine 4-H_2), 2.98–3.10 (broad signal, 2H, $NHCH_2CH_2CH_2N$), superimposed in part 3.33 (dd, J = 17.0 Hz, J' = 8.0 Hz, 1H, indanone 3-H_b), 3.36–3.48 (broad signal, 2H, piperidine 2-H_{eq} and 6-H_{eq}), 3.86 (s, 3H, 6-OCH_3), 3.94 (s, 3H, 5-OCH_3), 4.03 (t, J = 7.0 Hz, 2H, $NHCH_2CH_2CH_2N$), 4.86 (s, NH and $^+$NH), 7.07 (s, 1H, indanone 4-H), 7.15 (s, 1H, indanone 7-H), 7.57 (dd, J = 9.0 Hz, J' = 2.0 Hz, 1H, acridine 7-H), 7.78 (d, J = 2.0 Hz, 1H, acridine 5-H), 8.40 (d, J = 9.0 Hz, 1H, acridine 8-H); ^{13}C NMR (100.6 MHz, CD_3OD) δ 22.5 (CH_2, acridine C3), 23.2 (CH_2, acridine C2), 25.8 (CH_2, acridine C1), 27.1 (CH_2, acridine C4), 31.4 (CH_2), 31.5 (CH_2) and 32.7 (CH_2) ($NHCH_2CH_2CH_2N$ and piperidine C3 and C5), 34.1 (CH_2, indanone C3), 34.4 (CH, piperidine C4), 39.5 (CH_2, indanone-2-CH_2), 46.4 (CH, indanone C2), 48.2 (CH_2, $NHCH_2CH_2CH_2N$), 54.7 (2 CH_2, piperidine C2 and C6), 56.4 (CH_3, 6-OCH_3), 56.7 (CH_3, 5-OCH_3), 57.1 (CH_2, $NHCH_2CH_2CH_2N$), 105.2 (CH, indanone C7), 108.9 (CH, indanone C4), 115.0 (C, acridine C9a), 117.1 (C, acridine C8a), 122.2 (CH, acridine C5), 126.1 (CH, acridine C7), 127.9 (CH, acridine C8), 129.7 (C, indanone C7a), 138.1 (C) and 143.8 (C) (acridine C6 and C10a), 151.0 (C, indanone C6), 151.2 (C, indanone C3a), 155.4 (C), 155.6 (C) and 157.6 (C) (acridine C4a and C9, and indanone C5), 209.9 (C, indanone C1). Anal. ($C_{33}H_{40}ClN_3O_3 \cdot 2.1HCl \cdot 3H_2O$) C, H, N, Cl.

9-[(2-{4-[(5,6-Dimethoxyindan-2-yl)methyl]piperidin-1-yl}ethyl)amino]-1,2,3,4-tetrahydroacridine dihydrochloride (16a·2HCl). From mesylate **10a** (365 mg, 1.14 mmol) and piperidine **13** (306 mg, 1.11 mmol), compound **16a** (191 mg, 34% yield) was obtained as a pale brown solid, on elution with a mixture of CH_2Cl_2 / MeOH / 25% aqueous NH_4OH 99:1:0.1: R_f 0.68 (CH_2Cl_2 / MeOH / 25% aqueous NH_4OH 90:10:0.1). **16a**·2HCl: mp 254–255 °C (MeOH); IR (KBr) ν 3700–2400 (max. at 3399, 3245, 2928, 2834, N–H, $^+$N–H and C–H st), 1635, 1613, 1584, 1524 and 1504 (ar–C–C and ar–C–N st) cm^{-1}; ^1H NMR (500 MHz, CD_3OD) δ 1.52 (t, J = 6.7 Hz, 2H, indane-2-CH_2), 1.65 [broad pseudo q, J = 11.7 Hz, 2H, piperidine 3(5)-H_{ax}], 1.76 (m, 1H, piperidine 4-H), 1.96–2.00 (complex signal, 4H, acridine 2-H_2 and 3-H_2), 2.03 [broad d, J = 11.7 Hz, piperidine 3(5)-H_{eq}], 2.48-2.58 [complex signal, 3H, indane 2-H and 1(3)-H_{cis}], 2.84 [m, 2H, indane 1(3)-H_{trans}], 2.99 (m, 2H, acridine 1-H_2), 3.04–3.16 [complex signal, 4H, acridine 4-H_2 and piperidine 2(6)-H_{ax}], 3.56 (m, 2H, $NHCH_2CH_2N$), 3.65 [broad signal, 2H, piperidine 2(6)-H_{eq}], 3.77 [s, 6H, 5(6)-OCH_3], 4.41 (t, J = 6.7 Hz, 2H, $NHCH_2CH_2N$), 4.85 (s, NH and $^+$NH), 6.78 [s, 2H, indane 4(7)-H], 7.67 (dd, J = 8.0 Hz, J' = 7.5 Hz, 1H, acridine 7-H), 7.83 (d, J = 8.0 Hz, 1H, acridine 5-H), 7.89 (dd, J = 8.0 Hz, J' = 7.5 Hz, 1H, acridine 6-H), 8.44 (d, J = 8.0 Hz, 1H, acridine 8-H); ^{13}C NMR (100.6 MHz, CD_3OD) δ 21.7 (CH_2, acridine C3), 23.0 (CH_2, acridine C2), 25.6 (CH_2, acridine C1), 29.5 (CH_2, acridine C4), 31.0 [broad CH_2, piperidine C3(5)], 33.5 (broad CH, piperidine C4), 38.9 (CH, indane C2), 40.3 [CH_2, indane C1(3)], 43.0 (broad CH_2, $NHCH_2CH_2N$), 43.2 (CH_2, indane-2-CH_2), 54.7 [broad CH_2, piperidine C2(6)], 56.7 [CH_3, 5(6)-OCH_3], 57.4 (broad CH_2, $NHCH_2CH_2N$), 109.7 [CH, indane

C4(7)], 114.3 (C, acridine C9a), 117.6 (C, acridine C8a), 120.3 (CH, acridine C5), 126.0 (CH, acridine C8), 127.2 (CH, acridine C7), 134.3 (CH, acridine C6), 136.3 [C, indane C3a(7a)], 139.5 (C, acridine C10a), 149.4 [C, indane C5(6)], 153.0 (C, acridine C4a), 158.0 (C, acridine C9). Anal. ($C_{32}H_{41}N_3O_2 \cdot 2HCl \cdot H_2O$) C, H, N, Cl.

9-[(3-{4-[(5,6-dimethoxyindan-2-yl)methyl]piperidin-1-yl}propyl)amino]-1,2,3,4-tetrahydroacridine dihydrochloride (16b·2HCl). From mesylate **10b** (294 mg, 0.88 mmol) and piperidine **13** (242 mg, 0.88 mmol), compound **16b** (81 mg, 18% yield) was obtained as a pale brown solid, on elution with a mixture of CH_2Cl_2 / MeOH / 25% aqueous NH_4OH 99:1:0.2: R_f 0.66 (CH_2Cl_2 / MeOH / 25% aqueous NH_4OH 9:1:0.01). **16b**·2HCl: mp 184–185 °C (MeOH); IR (KBr) ν 3660–2200 (max. at 3370, 2924, 2854, 2706, N–H, $^+$N–H and C–H st), 1634, 1588, 1522 and 1503 (ar–C–C and ar–C–N st) cm^{-1}; ^1H NMR (500 MHz, CD_3OD) δ 1.50–1.58 [complex signal, 4H, indane-2-CH_2 and piperidine 3(5)-H_{ax}], 1.74 (broad signal, 1H, piperidine 4-H), 1.99 (complex signal, 4H, acridine 2-H_2 and 3-H_2), 2.04 [broad d, J = 14.5 Hz, piperidine 3(5)-H_{eq}], 2.33 (m, 2H, $NHCH_2CH_2CH_2N$), 2.49–2.59 [complex signal, 3H, indane 2-H and 1(3)-H_{cis}], 2.78 (m, 2H, acridine 1-H_2), 2.97–3.06 [complex signal, 6H, indane 1(3)-H_{trans}, acridine 4-H_2 and piperidine 2(6)-H_{ax}], 3.25 (m, 2H, $NHCH_2CH_2CH_2N$), 3.62 [broad d, J = 12.5 Hz, 2H, piperidine 2(6)-H_{eq}], 3.78 [s, 6H, 5(6)-OCH_3], 4.08 (t, J = 7.2 Hz, 2H, $NHCH_2CH_2CH_2N$), 4.85 (s, NH and $^+$NH), 6.78 [s, 2H, indane 4(7)-H], 7.64 (ddd, J = 8.5 Hz, J' = 7.0 Hz, J'' = 1.5 Hz, 1H, acridine 7-H), 7.79 (broad d, J = 8.5 Hz, 1H, acridine 5-H), 7.88 (ddd, J = 8.5 Hz, J' = 7.0 Hz, J'' =

1.0 Hz, 1H, acridine 6-H), 8.43 (d, J = 8.5 Hz, 1H, acridine 8-H); ^{13}C NMR (100.6 MHz, CD_3OD) δ 21.8 (CH_2, acridine C3), 23.0 (CH_2, acridine C2), 25.3 (CH_2, acridine C1), 26.3 (CH_2, $NHCH_2CH_2CH_2N$), 29.4 (CH_2, acridine C4), 30.9 [CH_2, piperidine C3(5)], 33.6 (CH, piperidine C4), 38.8 (CH, indane C2), 40.3 [CH_2, indane C1(3)], 43.1 (CH_2, indane-2-CH_2), 45.9 (CH_2, $NHCH_2CH_2CH_2N$), 54.3 [CH_2, piperidine C2(6)], 55.3 (CH_2, $NHCH_2CH_2CH_2N$), 56.7 [CH_3, 5(6)-OCH_3], 109.7 [CH, indane C4(7)], 113.5 (C, acridine C9a), 117.3 (C, acridine C8a), 120.2 (CH, acridine C5), 126.3 (CH, acridine C8), 126.8 (CH, acridine C7), 134.2 (C, acridine C6), 136.3 [C, indane C3a(7a)], 139.6 (C, acridine C10a), 149.4 [C, indane C5(6)], 152.3 (C, acridine C4a), 157.9 (C, acridine C9). Anal. ($C_{33}H_{43}N_3O_2 \cdot 2HCl \cdot 3{,}25H_2O$) C, H, Cl. N: calcd, 6.51; found, 5.94.

6-Chloro-9-[(2-{4-[(5,6-dimethoxyindan-2-yl)methyl]piperidin-1-yl}ethyl)amino]-1,2,3,4-tetrahydroacridine dihydrochloride (17a·2HCl). From mesylate **11a** (386 mg, 1.09 mmol) and piperidine **13** (300 mg, 1.09 mmol), compound **17a** (165 mg, 28% yield) was obtained as a pale brown solid, on elution with a mixture of CH_2Cl_2 / MeOH / 25% aqueous NH_4OH 99:1:0.1: R_f 0.68 (CH_2Cl_2 / MeOH / 25% aqueous NH_4OH 9:1:0.01). **17a**·2HCl: mp 159–160 °C (MeOH); IR (KBr) ν 3700–2400 (max. at 3414, 3259, 3047, 2932, 2835, N–H, $^+$N–H and C–H st), 1631, 1585 and 1504 (ar–C–C and ar–C–N st) cm^{-1}; ^{1}H NMR (500 MHz, CD_3OD) δ 1.53 (t, J = 7.0 Hz, 2H, indane-2-CH_2), 1.62 [pseudo q, J = 13.0 Hz, 2H, piperidine 3(5)-H_{ax}], 1.70–1.80 (broad signal, 1H, piperidine 4-H), 1.94–2.03 (complex signal, 4H, acridine 2-H_2 and 3-H_2), 2.06 [broad d, J = 14.5 Hz, piperidine 3(5)-

H_{eq}], 2.50-2.59 [complex signal, 3H, indane 2-H and 1(3)-H_{cis}], 2.81 (m, 2H, acridine 1-H_2), 2.98–3.14 [complex signal, 6H, acridine 4-H_2, indane 1(3)-H_{trans}, and piperidine 2(6)-H_{ax}], 3.52–3.62 (broad signal, 2H, $NHCH_2CH_2N$), 3.65–3.75 [broad signal, 2H, piperidine 2(6)-H_{eq}], 3.78 [s, 6H, 5(6)-OCH_3], 4.40 (t, J = 6.5 Hz, 2H, $NHCH_2CH_2N$), 4.85 (s, NH and $^+$NH), 6.79 [s, 2H, indane 4(7)-H], 7.65 (dd, J = 9.0 Hz, J' = 2.0 Hz, 1H, acridine 7-H), 7.83 (d, J = 2.0 Hz, 1H, acridine 5-H), 8.42 (d, J = 9.0 Hz, 1H, acridine 8-H); ^{13}C NMR (100.6 MHz, CD_3OD) δ 21.6 (CH_2, acridine C3), 22.9 (CH_2, acridine C2), 25.6 (CH_2, acridine C1), 29.6 (CH_2, acridine C4), 30.9 [CH_2, piperidine C3(5)], 33.4 (CH, piperidine C4), 38.8 (CH, indane C2), 40.3 [CH_2, indane C1(3)], 43.1 (2 CH_2, indane-2-CH_2 and $NHCH_2CH_2N$), 54.9 [broad CH_2, piperidine C2(6)], 56.7 [CH_3, 5(6)-OCH_3], 57.3 (broad CH_2, $NHCH_2CH_2N$), 109.6 [CH, indane C4(7)], 114.6 (C, acridine C9a), 115.8 (C, acridine C8a), 119.2 (CH, acridine C5), 127.5 (CH, acridine C7), 128.2 (CH, acridine C8), 136.2 [C, indane C3a(7a)], 140.0 (C, acridine C6), 140.1 (C, acridine C10a), 149.3 [C, indane C5(6)], 153.5 (C, acridine C4a), 157.7 (C, acridine C9). Anal. ($C_{32}H_{40}ClN_3O_2 \cdot 2HCl \cdot 2{,}25H_2O$) C, H, N, Cl.

6-Chloro-9-[(3-{4-[(5,6-dimethoxyindan-2-yl)methyl]piperidin-1-yl}propyl)amino]-1,2,3,4-tetrahydroacridine dihydrochloride (17b·2HCl). From crude mesylate **11b** (368 mg, ≈ 1.0 mmol) and piperidine **13** (271 mg, 0.99 mmol), compound **17b** (210 mg, 39% yield) was obtained as a pale brown solid, on elution with a mixture of CH_2Cl_2 / MeOH / 25% aqueous NH_4OH 97:3:0.2: R_f 0.49 (CH_2Cl_2 / MeOH / 25% aqueous NH_4OH 9:1:0.01).

17b·2HCl: mp 173–174 °C (MeOH); IR (KBr) ν 3700–2450 (max. at 3401, 2928, N–H, $^{+}$N–H and C–H st), 1630, 1581 and 1503 (ar–C–C and ar–C–N st) cm^{-1}; ^{1}H NMR (500 MHz, CD_3OD) δ 1.50 (t, J = 6.7 Hz, 2H, indane-2-CH_2), 1.57 [broad pseudo q, J = 13.0 Hz, 2H, piperidine 3(5)-H_{ax}], 1.74 (m, 1H, piperidine 4-H), 1.92–2.00 (complex signal, 4H, acridine 2-H_2 and 3-H_2), 2.03 [broad d, J = 14.0 Hz, piperidine 3(5)-H_{eq}], 2.35 (m, 2H, $NHCH_2CH_2CH_2N$), 2.48-2.58 [complex signal, 3H, indane 2-H and 1(3)-H_{cis}], 2.75 (m, 2H, acridine 1-H_2), 2.99–3.04 [complex signal, 6H, acridine 4-H_2, indane 1(3)-H_{trans}, and piperidine 2(6)-H_{ax}], 3.26 (m, 2H, $NHCH_2CH_2CH_2N$), 3.62 [broad d, J = 12.0 Hz, 2H, piperidine 2(6)-H_{eq}], 3.77 [s, 6H, 5(6)-OCH_3], 4.07 (t, J = 7.5 Hz, 2H, $NHCH_2CH_2CH_2N$), 4.85 (s, NH and $^{+}$NH), 6.77 [s, 2H, indane 4(7)-H], 7.60 (dd, J = 9.0 Hz, J' = 2.0 Hz, 1H, acridine 7-H), 7.80 (d, J = 2.0 Hz, 1H, acridine 5-H), 8.44 (d, J = 9.0 Hz, 1H, acridine 8-H); ^{13}C NMR (100.6 MHz, CD_3OD) δ 21.7 (CH_2, acridine C3), 22.8 (CH_2, acridine C2), 25.1 (CH_2, acridine C1), 26.2 (CH_2, $NHCH_2CH_2CH_2N$), 29.4 (CH_2, acridine C4), 30.9 [CH_2, piperidine C3(5)], 33.6 (CH, piperidine C4), 38.8 (CH, indane C2), 40.3 [CH_2, indane C1(3)], 43.1 (CH_2, indane-2-CH_2), 46.0 (CH_2, $NHCH_2CH_2CH_2N$), 54.3 [CH_2, piperidine C2(6)], 55.3 (CH_2, $NHCH_2CH_2CH_2N$), 56.7 [CH_3, 5(6)-OCH_3], 109.7 [CH, indane C4(7)], 114.0 (C, acridine C9a), 115.7 (C, acridine C8a), 119.2 (CH, acridine C5), 127.7 (CH, acridine C7), 128.6 (CH, acridine C8), 136.3 [C, indane C3a(7a)], 140.2 (C, acridine C6), 140.4 (C, acridine C10a), 149.4 [C, indane C5(6)], 152.7 (C, acridine C4a), 157.9 (C, acridine C9). Anal. ($C_{33}H_{42}ClN_3O_2$·1.9HCl·3H_2O) C, H, N, Cl.

Biochemical studies. AChE inhibitory activity was evaluated spectrophotometrically at 25 °C by the method of Ellman,[3] using AChE from bovine or human erythrocytes and acetylthiocholine iodide (0.53 mM or 0.27 mM for bovine and human AChE, respectively) as substrate. The reaction took place in a final volume of 3 mL of 0.1 M phosphate-buffered solution pH 8.0, containing 0.025 units of AChE and 333 μM 5,5'-dithiobis(2-nitrobenzoic) acid (DTNB) solution used to produce the yellow anion of 5-thio-2-nitrobenzoic acid. Inhibition curves were performed in triplicate by incubating with at least 12 concentrations of inhibitor for 15 min. One triplicate sample without inhibitor was always present to yield 100% of AChE activity. The reaction was stopped by the addition of 100 μL 1 mM eserine, and the color production was measured at 414 nm. BChE inhibitory activity determinations were carried out similarly, using 0.035 unit of human serum BChE and 0.56 mM butyrylthiocholine, instead of AChE and acetylthiocholine, in a final volume of 1 mL.

Data from concentration-inhibition experiments of the inhibitors were calculated by non-linear regression analysis, using the GraphPad Prism program package (GraphPad Software; San Diego, USA), which gave estimates of the IC_{50} (concentration of drug producing 50% of enzyme activity inhibition). Results are expressed as mean ± S.E.M. of at least 4 experiments performed in triplicate. DTNB, acetylthiocholine, butyrylthiocholine, and the enzymes were purchased from Sigma and eserine from Fluka.

Molecular Modeling: Methods. The binding mode of compounds **15a** and **15b** was explored by means of 10 ns molecular dynamics simulations performed for their complexes

to the human acetylcholinesterase (hAChE). In the two cases a stable trajectory was obtained, as noted in a small positional root-mean square deviation (about 0.7 for thr backbone atoms in the mobile region determined relative to the X-ray crystallographic structure)

To this end, fascicullin was removed, truncated residues (Glu268, Gln291, Gln369 and Arg522) were reconstructed and missing residues (Pro259, Gly260, Gly261, Thr262, Gly263, Arg439, Asp494) were added using InsightII graphics package.[5] The enzyme was modeled in its physiologically active form with neutral His447 and deprotonated Glu334, which from together with Ser203 the catalytic triad. The standard ionization state at neutral pH was considered for the rest of ionizable residues with the exception of Asp392 and Glu450, which were neutral, and His478, which was protonated, according to previous numerical titration studies.[6] The X-ray crystallographic structures of the *AChE* complexes with tacrine (1ACJ),[7] huprine Y (1E66)[8] and donepezil (1EVE)[9] and the final structures of previous heterodimer studies[10,11] were used to position the ligands along the gorge. The system was hydrated by centering a sphere of 50 Å of TIP3P[12] water molecules centered at the inhibitor, paying attention to filling the position of crystallographic waters inside the binding cavity. Finally, six Na^+ cations were added to neutralize the negative charge of the system with the xleap module of AMBER8.[13]

Molecular dynamics simulations were run using the sander module of AMBER8 and the parm98 parameters for the protein. The charge distribution of the inhibitor was determined from fitting to the HF/6-31G(d) electrostatic potential obtained with

Gaussian'03[14] using the RESP procedure,[15] and the van der Waals parameters were taken from those defined for related atoms in AMBER force field. The system was partitionated into a mobile region, which included the ligand, all the protein residues containing at least one atom within 20 Å from the ligand, and all the water molecules and Na^+ cations. The geometry of the system was minimized in four steps. First, the position of hyrdrogen atoms was optimized using 3000 steps of steepest descent algorithm. Then, water molecules were refined throught 2000 steps of steepest descent followed by 3000 steps of conjugate gradient. Next, ligand, water molecules and counterions were optimized with 2000 steps of steepest descent and 4000 steps of conjugate gradient, and finally the whole system was optimized with 3000 steps of steepest descent and 7000 steps of conjugate gradient. Thermalization of the mobile part of the system was performed in five steps of 20 ps incrementing the temperature up to 298 K. At this point, a 10 ns molecular dynamics simulation was carried out using a time step of 1 fs. SHAKE was used for those bonds containing hydrogen atoms, and a cut off of 11 Å was used for nonbonded interactions.

The analysis of the structural features that mediate the binding mode to the enzyme was determined by averaging the parameters for the snapshots (saved every picosecond) sampled along the last 5 ns of the molecular dynamics simulations.

References

(1) Aguado, F.; Badía, A.; Baños, J. E.; Bosch, F.; Bozzo, C.; Camps, P.; Contreras, J.; Dierssen, M.; Escolano, C.; Görbig, D. M.; Muñoz-Torrero, D.; Pujol, M. D.; Simón, M.; Vázquez, M. T.; Vivas, N. M. Synthesis and Evaluation of Tacrine-Related Compounds for the Treatment of Alzheimer's Disease. *Eur. J. Med. Chem.* **1994**, *29*, 205–221.

(2) Michalson, E. T.; D'Andrea, S.; Freeman, J. P.; Szmuszkovicz, J. The Synthesis of 9-(1-Azetidinyl)-1,2,3,4-tetrahydroacridine. *Heterocycles* **1990**, *30*, 415–425.

(3) Ellman, G. L.; Courtney, K. D.; Andres, B., Jr.; Featherstone, R. M. A New and Rapid Colorimetric Determination of Acetylcholinesterase Activity. *Biochem. Pharmacol.* **1961**, *7*, 88–95.

(4) Kryger, G; Harel, M; Giles, K; Toker, L; Velan, B; Lazar, A; Kronman, C; Barak, D; Ariel, N; Shafferman, A; Silman, I; Sussman, J.L. *Acta Cystallogr. D: Biol. Crystallogr.* **2000**, 56, 1385-1394.

(5) InsightII, Accelrys Inc.: San Diego, CA, 1996.

(6) Wlodek, S. T.; Antosiewicz, J.; McCammon, J. A.; Straatsma, T. P.; Gilson, M. K.; Briggs, M. J.; Humblet, C.; Sussman, J. L. Binding of Tacrine and 6-Chlorotacrine by Acetylcholineterase. *Biopolymers* **1996**, *38*, 109–117.

(7) Sussman, J. L.; Harel, M.; Frolow, F.; Oefner, C.; Goldman, A.; Toker, L.; Silman, I. *Science* **1991**, 253, 872-879.

(8) Dvir, H.; Wong, D. M.; Harel, M.; Barril, X.; Orozco, M.; Luque, F. J.; Muñoz-Torrero, D.; Camps, P.; Rosenberry, T. L.; Silman, I.; Sussman, J. L. *Biochemistry* **2002**, *41*, 2970-2981.

(9) Kryger, G.; Silman, I.; Sussman, J. L. *Structure* **1999**, *7*, 297-307.

(10) Alonso,D.; Dorronsoro, I.; Rubio, L.; Muñoz, P.; García-Palomero E.; Del Monte, M.; Bidon-Chanal, A.; Orozco,M.; Luque, F. J.; Castro, A.; Medina, M.; Martínez, A.; *Bioorg. Med Chem.* **2005**,

(11) Pilar Muñoz-Ruiz, Laura Rubio, Esther García-Palomero, María del Monte-Millán, Paola Usán, Isabel Dorronsoro, Manuela Bartolini, Vincenza Andrisano, Axel Bidon-Chanal Badia, Modesto Orozco, F. Javier Luque, Miguel Medina and Ana Martínez, Design Synthesis and Pharmacological Evaluation of Dual Binding Site Acetylcholinesterase Inhibitors: New Disease Modifying Agents for Alzheimer's Disease, J. Med. Chem., 2005,

(12) Jorgensen, W. L.; Chandrasekhar, J.; Madura, J. D.; Impey, R. W.; Klein, M. L. Comparison of Simple Potential Functions for Simulating Liquid Water. *J. Chem. Phys.* **1983**, *79*, 926–935.

(13) Case, D. A.; Darden, T. A.; Cheatham, T. E.; Pearlman, D. A.; Simmerling, C L..; Wang, J.; Duke, R. E.; Luo, R.; Merz, K. M.; Pearlman, D. A.; Crowley, M.; Brozell, S.; Tsui, V.; Gohlke, H.; Mongan, J.; Hornak, V.; Cui, G.; Beroza, P.; Schafmeister, P.; Caldwell, J. W.; Ross, W. S.; Kollman, P. A. AMBER8. University of California. San Francisco. 2004.

(14) Gaussian 03, Revision B.04, M. J. Frisch, G. W. Trucks, H. B. Schlegel, G. E. Scuseria, M. A. Robb, J. R. Cheeseman, J. A. Montgomery, Jr., T. Vreven, K. N. Kudin, J. C. Burant, J. M. Millam, S. S. Iyengar, J. Tomasi, V. Barone, B. Mennucci, M. Cossi, G. Scalmani, N. Rega, G. A. Petersson, H. Nakatsuji, M. Hada, M. Ehara, K. Toyota, R. Fukuda, J. Hasegawa, M. Ishida, T. Nakajima, Y. Honda, O. Kitao, H. Nakai, M. Klene, X. Li, J. E. Knox, H. P. Hratchian, J. B. Cross, C. Adamo, J. Jaramillo, R. Gomperts, R. E. Stratmann, O. Yazyev, A. J. Austin, R. Cammi, C. Pomelli, J. W. Ochterski, P. Y. Ayala, K. Morokuma, G. A. Voth, P. Salvador, J. J. Dannenberg, V. G. Zakrzewski, S. Dapprich, A. D. Daniels, M. C. Strain, O. Farkas, D. K. Malick, A. D. Rabuck, K. Raghavachari, J. B. Foresman, J. V. Ortiz, Q. Cui, A. G. Baboul, S. Clifford, J. Cioslowski, B. B. Stefanov, G. Liu, A. Liashenko, P. Piskorz, I. Komaromi, R. L. Martin, D. J. Fox, T. Keith, M. A. Al-Laham, C. Y. Peng, A. Nanayakkara, M. Challacombe, P. M. W. Gill, B. Johnson, W. Chen, M. W. Wong, C. Gonzalez, and J. A. Pople, Gaussian, Inc., Pittsburgh PA, 2003.

(15) Bayly, C. I.; Cieplak, P.; Cornell, W. D.; Kollman, P. A. A Well-Behaved Electrostatic Potential Based Method Using Charge Restraints for Deriving Atomic Charges. *J. Phys. Chem.* **1993**, *97*, 10269–10280.

Appendix

Compd	Molecular Formula	Calculated				Found			
		C	H	N	Cl	C	H	N	Cl
9a·HCl·1/4H_2O	$C_{15}H_{17}ClN_2O$·HCl·1/4H_2O	56.70	5.87	8.82	22.32	56.58	5.85	8.85	22.09
9b·HCl·1/4H_2O	$C_{16}H_{19}ClN_2O$·HCl·1/4H_2O	57.93	6.23	8.44	21.37	58.03	6.31	8.41	21.23
14a·2HCl·1.5H_2O	$C_{32}H_{39}N_3O_3$·2HCl·1.5H_2O	62.64	7.23	6.85	11.56	62.64	7.05	6.59	11.59
14b·2HCl·2.5H_2O	$C_{33}H_{41}N_3O_3$·2HCl·2.5H_2O	61.39	7.49	6.51	10.98	61.60	7.24	6.31	11.16
15a·1.8HCl·1.8H_2O	$C_{32}H_{38}ClN_3O_3$·1.8HCl·1.8H_2O	59.48	6.77	6.50	15.36	59.57	6.61	6.36	15.37
15b·2.1HCl·3H_2O	$C_{33}H_{40}ClN_3O_3$·2.1HCl·3H_2O	57.21	7.00	6.07	15.86	57.22	6.62	6.09	15.94
16a·2HCl·H_2O	$C_{32}H_{41}N_3O_2$·2HCl·H_2O	65.07	7.68	7.11	12.01	65.11	7.70	7.02	11.72
16b·2HCl·3.25H_2O	$C_{33}H_{43}N_3O_2$·2HCl·3.25H_2O	61.43	8.05	6.51	10.99	61.67	8.00	5.94	10.79
17a·2HCl·2.25H_2O	$C_{32}H_{40}ClN_3O_2$·2HCl·2.25H_2O	59.35	7.24	6.49	16.42	59.12	6.83	6.64	16.57
17b·1.9HCl·3H_2O	$C_{33}H_{42}ClN_3O_2$·1.9HCl·3H_2O	59.03	7.49	6.26	15.31	59.04	7.39	5.82	15.24

Mecanismo de regulación de la proteína trHbN
de *Mycobacterium tuberculosis*

Introducción

Mycobacterium tuberculosis, el agente causante de la enfermedad de tuberculosis en humanos[1], es capaz de sobrevivir en estado latente dentro del organismo infectado durante décadas pudiendo reactivarse cuando las defensas del organismo se ven mermadas por algún motivo. Durante los primeros estadios de la infección la bacteria es atacada por los macrófagos, que generan grandes cantidades de óxido nítrico (NO)[2]. Éste presenta una elevada toxicidad gracias a su capacidad de dañar el ADN[3], actuar sobre los centros hierro-sulfuro de enzimas como la aconitasa[4] y la inhibición de las oxidasas terminales del proceso respiratorio[5]. Así, el óxido nítrico impide el desarrollo de parásitos como *Trypanosoma*, *Leishmania*, *Plasmodium* y *Toxoplasma*[6,7] probablemente inactivando cisteín proteasas del parásito y/o otros enzimas clave del mismo.

En algunos invertebrados y en microorganismos se ha demostrado que la presencia de ciertas hemoglobinas les confiere la capacidad de detoxificar óxido nítrico. Asimismo, en organismos microbianos algunas flavohemoglobinas poseen esa capacidad[8,9]. Los mecanismos de defensa estarían ligados en ambos casos a la presencia de proteínas que contienen oxígeno ligado a un grupo hemo, pudiéndose llevar a cabo la conversión de óxido nítrico a anión nitrato mediante la reacción $Fe(II)\text{-}O_2 + NO \rightarrow Fe(III) + NO_3^-$. En el caso de *Mycobacterium tuberculosis*, se han detectado dos pequeñas hemoproteínas llamadas Hemoglobina truncada O (trHbO)[10] y Hemoglobina truncada N (trHbN)[11], que son capaces de llevar a cabo dicha reacción. La primera se expresa durante la fase de crecimiento, mientras que la segunda se expresa principalmente durante la fase estacionaria y muestra una mucho mayor capacidad catalítica [11,12]. Las hemoglobinas truncadas forman una familia distinta dentro de la superfamilia de las hemoglobinas, caracterizadas estructuralmente por tener un plegamiento de dos α-hélices dispuestas sobre dos α-hélices en vez del clásico plegamiento de las hemoglobinas formado por tres α-hélices sobre tres α-hélices[13]. Al igual que en el resto de hemoglobinas, el residuo de histidina H8 que se encuentra ligado al hierro se conserva en todas las hemoglobinas truncadas secuenciadas hasta el momento, y en la mayoría se conserva el residuo de tirosina B10 del centro activo. La característica más interesante de esta clase de hemoglobinas es la existencia en gran

parte de ellas de un túnel apolar que conecta la superficie de la proteína con el centro activo formando un canal que se postula sirve para la entrada de ligandos[13-16]. En la hemoglobina truncada N de *Mycobacterium tuberculosis* el túnel está formado por dos canales perpendiculares de distinto tamaño. El más pequeño tiene una longitud aproximada de 8 Å y está situado entre las hélices G y H, mientras que el canal más largo tiene una longitud de 20 Å y se sitúa entre las hélices B y E (ver Figura 4.1).

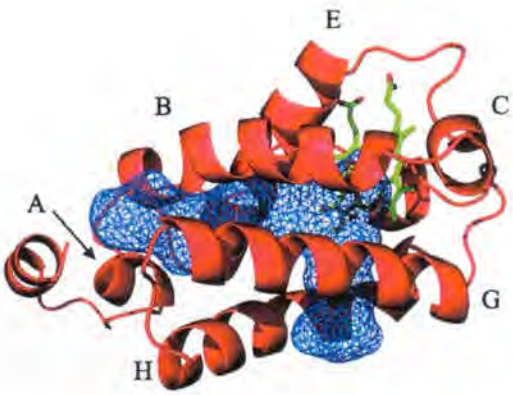

Figura 4.1. Representación del túnel hidrofóbico en la proteína trHbN de *Mycobacterium tuberculosis*.

La proteína muestra una gran afinidad por la molécula de oxígeno, encontrándose en estado oxigenado incluso a concentraciones muy bajas de O_2.. La entrada de oxígeno se produce de forma rápida (Tabla 4.1) en comparación con los valores obtenidos para otras hemoproteínas como mioglobina, y a su vez la constante de disociación tiene un valor muy pequeño (k_{off}=0.2 s^{-1} en trHbN y k_{off}=12 s^{-1} en mioglobina) [11]. La clave de esta alta afinidad es la presencia del residuo de tirosina B10, que forma un puente de hidrógeno con la molécula de O_2 ligada al hierro a través del hidrógeno del grupo hidroxilo. La sustitución del residuo de tirosina por una fenilalanina tiene como consecuencia una pérdida de afinidad de aproximadamente 150 veces (ver Tabla 4.1)[17], lo que refleja la imposibilidad de la fenilanalina para formar dicho puente de hidrógeno.

Ouellet et. al.[17] estudiaron la capacidad de la proteína para detoxificar NO siguiendo la cinética del consumo de óxido nítrico en suspensiones de células mutantes de *Mycobacterium bovis* en las que se había inactivado la expresión de trHbN. Como

puede verse en la Figura 4.2, las células inactivadas que no expresan dicha proteína (ΔHbN) presentan un consumo de óxido nítrico prácticamente idéntico al del medio de disolución. Cuando se reactiva la expresión de trHbN (ΔHbN:HbN) la actividad deoxigenasa queda restablecida y es incluso superior al de las células normales (WT) debido a la sobreexpresión de la proteína. Del mismo modo, estudiaron la capacidad detoxificadora de la proteína mutante en la que una fenilalanina reemplazaba el residuo de TyrB10. En la misma Figura 4.2 puede comprobarse que el comportamiento de las células con el gen mutado (ΔHbN:YB10F) es idéntico al de las células que no expresan la proteína, perdiéndose de igual manera la capacidad de oxidar NO. También Pathania *et. al.*[18] comprobaron la capacidad de trHbN para detoxificar NO al insertar en células de E. Coli un plásmido para expresar la proteína y registrar un aumento en el consumo de óxido nítrico 250 veces superior.

El efecto de mutación del residuo de tirosina B10 a fenilalanina fue estudiado a su vez mediante técnicas computacionales QM/MM para determinar la capacidad del mutante para llevar a cabo la reacción[19]. Los resultados obtenidos por Crespo *et. al.* mostraron que la capacidad del enzima nativo y la del modificado para completar la reacción química catalizada por el enzima era prácticamente idéntica (ΔE_{tyr}=-18.0 y ΔE_{phe}=-19.3 kcal/mol). La contradicción que supone este resultado con los obtenidos por Ouellet *et. al.* no puede entenderse sin tener en cuenta los procesos de difusión de los ligandos al centro activo.

	k_{on} (O_2) [$\mu M^{-1}s^{-1}$]	k_{off} (O_2) [$\mu M^{-1}s^{-1}$]	P_{50} [mmHg]	k_{obs} [$\mu M^{-1}s^{-1}$]
trHbN	25	0.199	0.013	745
trHbN(YB10F)	—	30	—	—
Mb	14	12	0.51	30-45

Tabla 4.1. Constantes cinéticas del proceso global de entrada y salida de O_2, presión parcial de oxígeno al 50% de saturación y constante cinética de la reacción de oxidación[11,18].

En la estructura cristal de la proteína oxigenada (código PDB 1IDR)[13] se observa la presencia de un residuo, la fenilalanina E15, en una doble conformación diferenciadas entre ellas por una rotación ~63° una con respecto a la otra alrededor del enlace C_α-C_β . El residuo en cuestión está situado en la parte central de la cadena E de la proteína justo

en la mitad del canal largo. En un caso el anillo de benzeno de la cadena lateral está situado paralelo al eje del canal, conformación denominada abierta, mientras que en el otro el plano del anillo yace perpendicular al eje del canal (ver figura 4.2), denominada conformación cerrada. Milani *et. al.* asociaron estas dos conformaciones a la posibilidad de que el residuo de fenilalanina E15 actuara como puerta de entrada al centro activo y regulara así la difusión de ligandos. El mecanismo de difusión implicaría por lo tanto un cambio conformacional de este residuo que permitiría la entrada de ligandos.

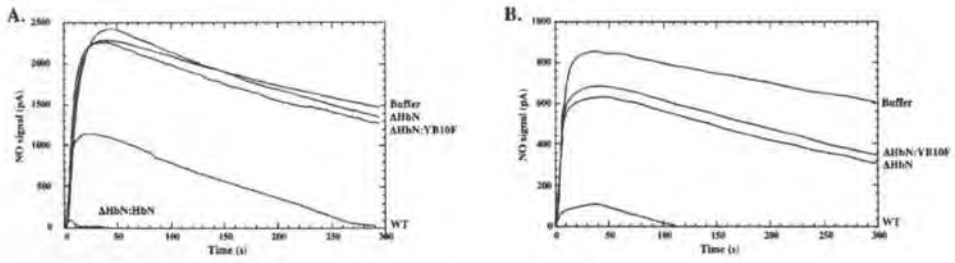

Figura 4.2. Seguimiento del consumo de NO en diferentes suspensiones celulares de *M. bovis* en donde se ha activado la transcripción de trHbN (ΔHbN:HbN), se ha activado la transcripción de la proteína mutada (ΔHbN:YB10F) o se ha desactivado la transcripción de dicha proteína (ΔHbN), así como de células normales (WT). Reproducido de Ouellet, H. *et al.*, Proc. Natl. Acad. Sci. U.S.A., 2002, 99, 5902-5907.

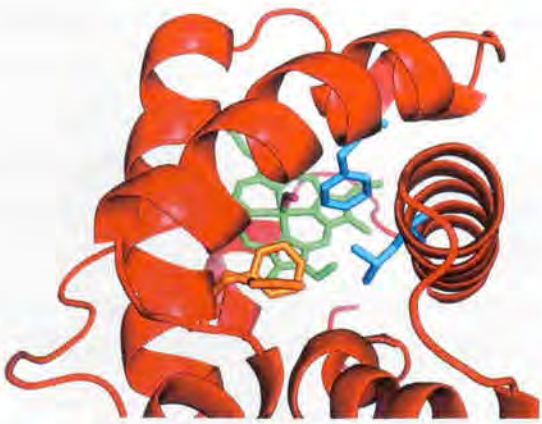

Figura 4.3. Detalle del canal largo en el que se muestra el residuo PheE15 (naranja), en sus dos conformaciones, y los residuos que hacen de "cuello de botella" en la conformación cerrada, PheB9 y LeuG12 (azul). En verde se encuentra representado el grupo hemo unido a oxígeno molecular.

Objetivos

Los estudios realizados para esta proteína estaban dirigidos a elucidar el mecanismo molecular de entrada de ligandos (O_2 y NO), a la determinación del proceso implicado en el cambio conformacional de la fenilalanina E15 y finalmente a elucidar el mecanismo de salida del producto (NO_3^-).

Resultados

4.1 Captación de los ligandos

Para determinar el mecanismo de migración de los ligandos O_2 y NO al centro activo de la proteína, se llevaron a cabo dos simulaciones de dinámica molecular de 0.1 μs cada una. En un caso el punto de partida consistió en la subunidad A de la estructura cristal con oxígeno coordinado al hierro del grupo hemo, y en el otro la misma estructura pero eliminando la molécula de oxígeno (dado que no existe ninguna estructura cristal de la proteina en estado deoxigenado).

En la trayectoria obtenida para la forma oxigenada se observan varias transiciones entre los estados abierto y cerrado del residuo de fenilalanina E15. Entre estas transiciones se producen tiempos suficientemente largos de permanencia en el estado abierto como para permitir el paso de NO al centro activo. Las conformaciones adoptadas por la fenilalanina están caracterizadas por el ángulo diedro H_α-C_α-C_β-C_γ, con valores promedio de +40° y -50° para los estados abierto y cerrado. De la misma manera que en la estructura cristal, en la conformación cerrada el anillo de benzeno ocupa el canal largo impidiendo el paso de ligandos, mientras que en la conformación abierta se encuentra paralelo al eje del canal y permitiendo el acceso de dichos ligandos. Prueba de ello son los perfiles de Potencial Clásico de Interacción Molecular obtenidos a lo largo del canal para los dos casos en un conjunto representativo de estructuras. Cuando la fenilalanina se encuentra en la conformación abierta se observa un contorno de energía contínuo desde el exterior hasta el interior del centro activo, mientras que cuando el residuo se encuentra en la conformación cerrada aparece una discontinuidad en el contorno que coincide con la posición del residuo en el canal (Figura 4.3).

Para certificar este hecho y esclarecer la posibilidad o no de entrada de un ligando a través del canal principal en la forma oxigenada de trHbN, se realizaron simulaciones de dinámica molecular guiada (*Steered Molecular Dynamics*) aplicando el método de Jarzynski para obtener los perfiles de energía del paso de NO a través del canal para las conformaciones abierta y cerrada (Figura 4.4). Cuando la fenilalanina no se encuentra ocupando el canal, el paso de una molécula de NO se produce prácticamente sin barrera

(< 2 kcal/mol) y está favorecido por entre 3 y 4 kcal/mol. Por el contrario, cuando el anillo de benzeno ocupa el canal el acceso al centro activo se ve claramente impedido, tal como refleja la aparición de una barrera energética de ~5 kcal/mol.

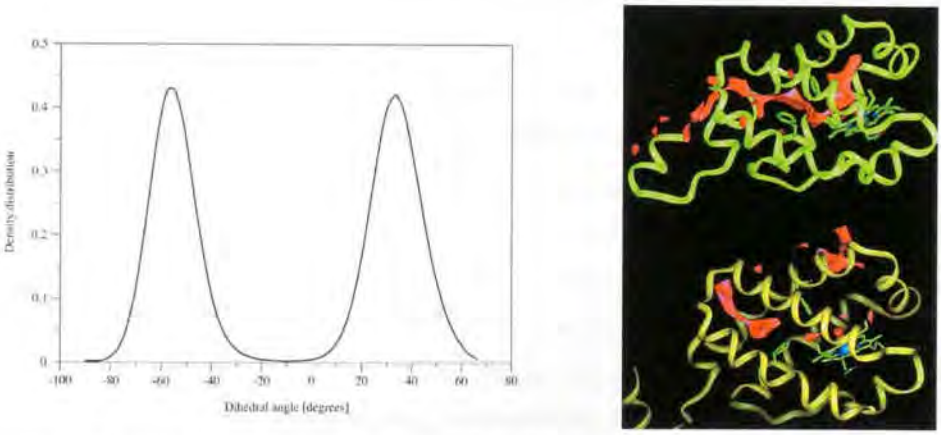

Figura 4.3. Densidad de probabilidad normalizada de la distribución del ángulo diedro C_o-C_β (H_o-C_α-C_β-C_γ) de la PheE15 a lo largo de la trayectoria (izquierda). Isocontornos del Potencial Clásico de interacción molecular obtenidos para el paso de una molécula de NO a través del canal principal en los estados abierto (superior) y cerrado (inferior) para la proteína oxigenada (derecha).

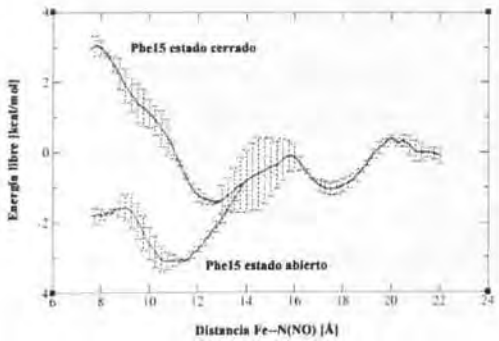

Figura 4.4. Perfil de energía libre del paso de una molécula de NO a través del canal largo en los estados abierto y cerrado de la PheE15.

Dado que existe un segundo canal, esto es, el canal corto, el mismo tipo de simulaciones de dinámica molecular guiada se realizaron para evaluar la posibilidad de entrada de óxido nítrico a través de este segundo camino. Los resultados muestran un camino desfavorable para la entrada de NO con una barrera energética del orden de ~7 kcal/mol. Esto significa que la entrada de NO cuando la proteína está oxigenada se

producirá a través del canal principal cuyo estado, abierto o cerrado, depende de la conformación adoptada por el residuo de fenilalanina E15.

Para que tenga lugar la reacción la proteína debe contener oxigeno unido al grupo hemo previo a la captación de óxido nítrico, es decir, la proteína debe ser capaz de captar O_2 cuando se encuentra libre de ligandos. A partir de la trayectoria obtenida por dinámica molecular de la forma deoxigenada se realizaron los mismos estudios que en el caso anterior para determinar la capacidad de entrada del oxígeno. En este caso la fenilalanina E15 se encuentra poblando únicamente una de las dos conformaciones, la que se corresponde con el estado cerrado del canal largo, y por lo tanto impide el tránsito de ligandos a través del mismo. La barrera torsional que debe superar el residuo para realizar el cambio conformacional calculada mediante simulaciones con *umbrella sampling* es de más de 6 kcal/mol, mientras que en el caso de la proteína oxigenada la misma barrera es de sólo 3 kcal/mol (Figura 4.5). Esto sugiere la posibilidad de que la entrada de oxígeno pueda ocurrir a través del canal secundario y de hecho los perfiles de energía obtenidos para este caso muestran una clara preferencia por la entrada a través del canal corto en la forma deoxigenada con una barrera de ~4 kcal/mol, que pasa a ser de ~7 kcal/mol cuando la proteína ya contiene oxigeno (Figura 4.5).

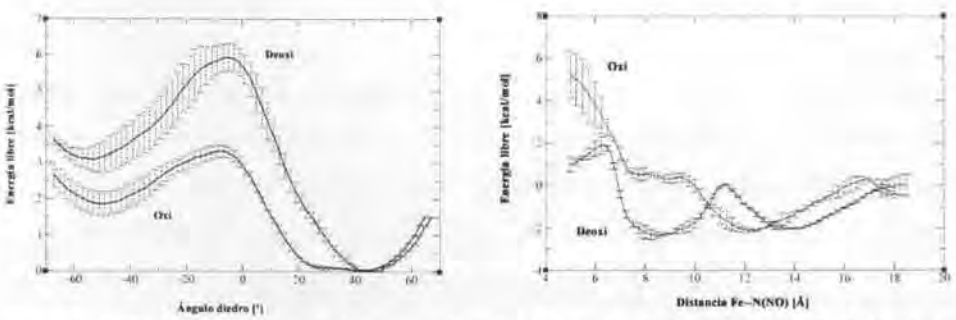

Figura 4.5. Perfil de energía libre de la torsión alrededor del ángulo diedro C_α-C_β (H_α-C_α-C_β-C_γ) de la PheE15 en las formas oxigenada i deoxigenada de trHbN (izquierda). Perfiles de energía libre para el paso de una molécula de O_2 (en la forma deoxigenada) o NO (en la forma oxigenada) a través del canal corto (derecha).

Estos resultados indican que la proteína tiene un mecanismo que habilita la captación independiente de ligandos y que le permite llevar a cabo la reacción de forma eficiente. Dado que el oxígeno se encuentra en mayor abundancia que el NO en el

medio, la entrada por el canal secundario se producirá de forma rápida (como indican los valores de las constantes cinéticas), activando el canal largo para la entrada de NO. Este último canal es altamente hidrofóbico, ya que está formado por los residuos IleA15, AlaB1, IleB2, ValB5, ValB6, PheB9, PheE15, AlaE16, LeuE19, LeuG12, LeuG16 y AlaG19, lo cual debe facilitar la presencia de una molécula de NO en la entrada del canal largo y evitar su ocupación por moléculas de agua. Así, una vez formado el complejo trHbN·O_2, sólo es necesario que ocurra el cambio conformacional de la fenilalanina E15 para que entre NO y la reacción tenga lugar.

4.2 Cambios estructurales inducidos por ligando en el centro activo

La unión de oxígeno al grupo hemo genera un conjunto de cambios estructurales en el centro activo de la proteína debidos a la formación del puente de hidrógeno entre la tirosina B10 y la molécula de O_2 polarizada. En la proteína libre, los residuos de glutamina E11 y tirosina B10 interaccionan mediante el intercambio de puentes de hidrógeno entre el grupo amida de la glutamina y el grupo hidroxilo de la tirosina en un pseudo-equilibrio de dos estructuras. En una de ellas la glutamina actúa como dador y el oxígeno de la tirosina como aceptor, mientras que en la otra el oxígeno del grupo carbonilo de la amida actúa como aceptor y el hidroxilo de la tirosina como dador. Para formar esta interacción doble la cadena lateral de la glutamina se despliega totalmente adoptando una conformación extendida (*all-trans.*). Cuando el oxígeno se une al hierro el aspecto del centro activo cambia radicalmente. La tirosina B10 pasa a formar un puente de hidrógeno con el oxígeno y fuerza la recolocación de la glutamina E11, que adopta entonces una conformación plegada para formar un puente de hidrógeno con el hidroxilo de la tirosina a través del grupo amino (ver Figura 4.6).

Este reajuste parece ser clave en el cambio de comportamiento de la fenilalanina E15. La situación cercana en la cadena E de los residuos glutamina E11 y fenilalanina E15 podría ser determinante para el cambio conformacional que abre el canal principal, ya que en la forma oxigenada la distancia entre ambos se acorta en ~1.5 Å quedando la cadena lateral de la glutamina a una distancia promedio de 3.9 Å de la cadena lateral de la fenilalanina. De hecho, durante la dinámica molecular, aproximadamente el 45% de las estructuras tiene una distancia entre las cadenas laterales inferior a dicha distancia

promedio. Si se tiene en cuenta que la distancia de contacto de van der Waals entre los grupos $-CH_2-$ y >CH (adoptando los radios de Pauling) es igual a la distancia promedio hallada durante la dinámica, la conclusión es que la cadena lateral de la glutamina ejerce presión sobre el anillo de benzeno de la fenilalanina, y es por ello responsable en parte del cambio conformacional de este residuo y de la apertura del canal.

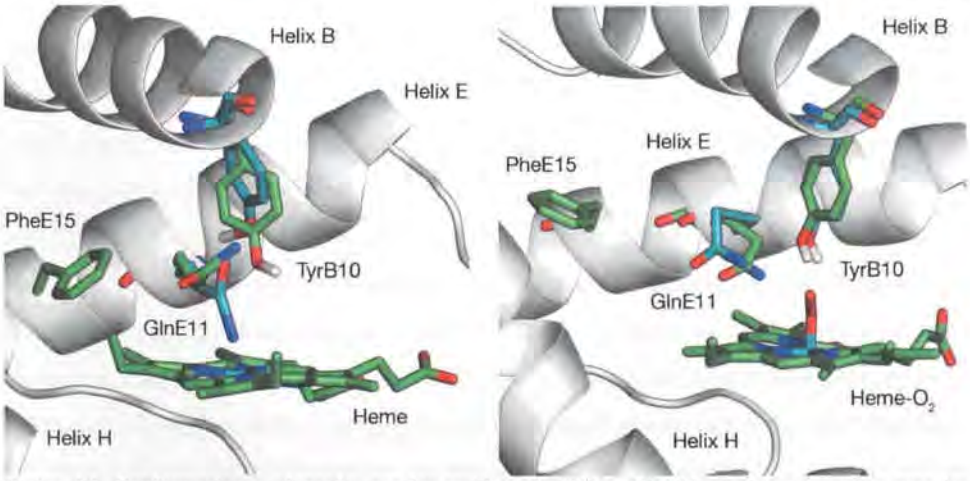

Figura 4.6. Conformaciones adoptadas por los residuos TyrB10 y GlnE11 en el centro activo para las formas deoxigenada (izquierda) y oxigenada(derecha) de trHbN. Se muestra también el residuo de PheE15 en sus conformaciones cerrada (izquierda) y abierta (derecha).

Para corroborar el efecto de la glutamina sobre la fenilalanina, se realizaron dos dinámicas moleculares de 0.1 μs cada una en las que los residuos glutamina E11 y tirosina B10 fueron mutados a alanina y fenilalanina respectivamente. Dichas mutaciones fueron seleccionadas para romper la cadena de puentes de hidrógeno del centro activo y permitir el movimiento independiente de ambos residuos. En ambos casos el análisis de las conformaciones adoptadas por la fenilalanina E15 muestra el mismo resultado manteniéndose el canal largo cerrado durante toda la trayectoria. Por lo tanto, la entrada de NO no puede ocurrir y la proteína queda inactiva. En el caso de la mutante de tirosina B10 a fenilalanina, este hecho proporciona una explicación a los resultados cinéticos experimentales obtenidos por Ouellet *et. al.*[17] y teóricos de Crespo *et. al.*[18].

Aunque teóricamente la reacción podría tener lugar, experimentalmente no sucede porque el NO no puede llegar al centro activo por encontrarse cerrado el paso a través del canal largo. Cabe hacer notar que para el mutante TyrB10→Phe existe un incremento notable en la distancia que separa los residuos glutamina E11 y fenilalanina E15, lo cual indica una disminución en la presión mecánica ejercida por el primero sobre el segundo (Figura 4.7). Ello es debido a que el residuo de glutamina adopta de una conformación extendida durante toda la trayectoria, dado que forma un puente de hidrógeno directamente con la molécula de oxígeno. Del mismo modo puede concluirse que para el caso de la mutación de glutamina E11 por alanina la proteína queda igualmente inactivada, aunque en este caso la ausencia de dicha presión mecánica obedece claramente a la reducción del tamaño de la cadena lateral.

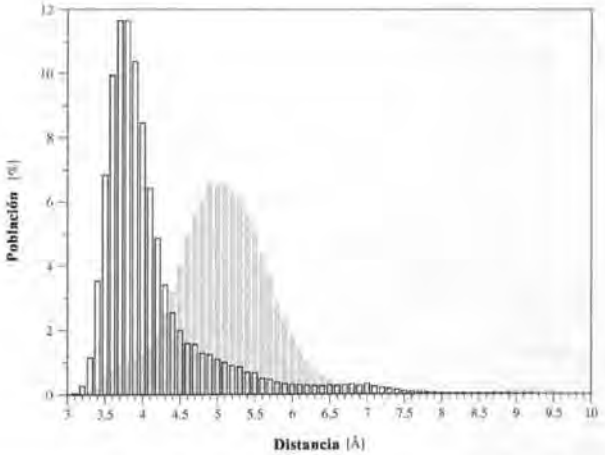

Figura 4.7. Distribución de las distancias entre los residuos GlnE11 y PheE15 en la forma oxigenada de la proteína natural (barras en blanco) y de la mutante TyrB10→Phe (barras color gris).

4.3 Cambios conformacionales inducidos por ligando

La unión de oxígeno no solo modifica la morfología del centro activo, sino que altera de forma apreciable la dinámica esencial del esqueleto peptídico de la proteína. La inspección de los 10 primeros modos esenciales para cada una de las simulaciones realizadas muestra claras diferencias en cada una de ellas respecto a los que se obtienen para la proteína oxigenada en su estado natural (Figura 4.8). El primer modo en la forma

oxigenada conlleva el movimiento casi exclusivo de las hélices B y E, cuya fricción ayudaría al desplazamiento de la fenialanina E15 y a la consecuente apertura del canal. Por el contrario, en la forma deoxigenada, así como en las formas mutantes TyrB10→Phe y GlnE11→Ala el primer modo no implica el movimiento de dichas hélices. En el caso de la forma deoxigenada, la contribución al primer modo está compuesta por el movimiento de las hélices C, G, H y el *loop* F, en la mutante TyrB10→Phe por las hélices G, H y el *loop* F, y por último, en el mutante GlnE11→Ala por las hélices C, G y H.

a) b)

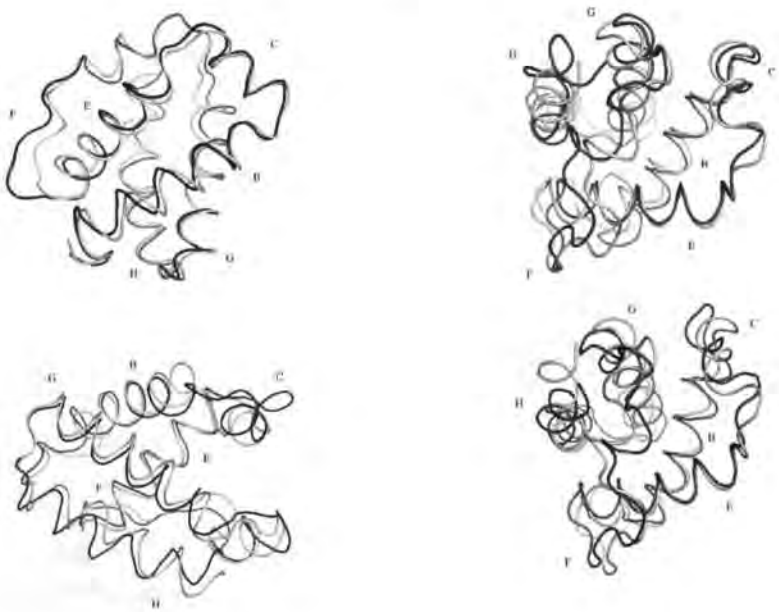

c) d)

Figura 4.8. Primer modo esencial representado por el máximo desplazamiento del esqueleto peptídico en la porteína trHbN oxigenada (a), deoxigenada (b), y las mutantes oxigenadas, YB10F (c) y QE11A (d)

La posibilidad de comparar los modos esenciales de cada proteína de forma numérica proporciona una medida más objetiva y a su vez cuantitativa para establecer la similitud entre los movimientos esenciales que más contribuyen a la varianza estructural global. En la Tabla 4.2 se muestra el valor del índice de similitud obtenido al comparar los 10 primeros modos entre las dos mutantes y la proteína natural. Tomando como referencia las medidas de autosimilitud para cada trayectoria de dinámica molecular

(0.74 para trHbN·O_2, 0.86 para TyrB10→Phe trHbN·O_2 y 0.89 en GlnE11→Ala trHbN·O_2), es posible constatar que la similitud que existe entre cada una de las mutantes y la proteína natural es notablemente inferior, con un valor para el índice de similitud no superior a 0.48.

ξ	trHbN	trHbN(YB10F)	trHbN(QE11A)
trHbN	0.74	0.48	0.37
trHbN(YB10F)		0.86	0.42
trHbN(QE11A)			0.89

Tabla 4.2. Valores obtenidos para el índice de similitud teniendo en cuenta los 10 primeros modos asociados al esqueleto peptídico de la proteína.

Estos resultados indican que la unión de O_2 al centro activo no sólo induce el reordenamiento de los residuos TyrB10 y GlnE11, sino que a su vez provoca una alteración en la naturaleza de las fluctuaciones dinámicas del esqueleto peptídico de la proteína que conduce a un incremento de la movilidad de las hélices B y E, favoreciendo así la apertura del canal principal y por lo tanto el acceso de NO a la cavidad del grupo hemo.

4.4 Mecanismo de salida del anión nitrato

Para que el mecanismo de detoxificación sea efectivo, el producto de la reacción (NO_3^-) debe ser expulsado del centro activo con rapidez para permtitir de nuevo la entrada de oxígeno. Los canales presentes en la estructura cristal son altamente hidrofóbicos dada la naturaleza de los residuos que los conforman. Por ello, el paso de una especie con carga negativa a través de ellos no estaría favorecido en modo alguno. Cabe pensar entonces que la salida del anión se producirá a través de un nuevo canal, cuya formación estará sujeta a la presencia del producto en el centro activo.

Para evaluar el impacto que tiene el anión nitrato en la conformación del centro activo se realizó una dinámica molecular de 30 ns manteniendo el anión NO_3^- unido al

átomo de hierro mediante una restricción armónica. El análisis de la trayectoria revela una tendencia del centro activo a ensancharse para acomodar el anión, dado que éste tiene un tamaño superior a la molécula de oxígeno y está cargado negativamente. Este ensanchamiento aumenta el volumen de la cavidad promedio durante la trayectoria, duplicando aproximadamente el volumen (según mediciones de Voidoo[20,21] para 50 estructuras extraídas de forma aleatoria de las trayectorias de trHbN·O_2 y trHbN·NO_3^-) que tiene cuando sólo el oxígeno está presente. La mayor parte de residuos que conforman la cavidad del centro activo son de carácter hidrofóbico y carecen de buenos grupos dadores de puente de hidrógeno y/o de cargas positivas para estabilizar al anión unido al hierro. Los residuos ValB13, LeuB14, LeuC4, PheC7, PheC8, ValG8, MetE4 y LeuE7 cambian su posición respecto a la estructura oxigenada y se alejan entre 0.5 y 1.5 Å del átomo de hierro del grupo hemo (ver Figura 4.9).

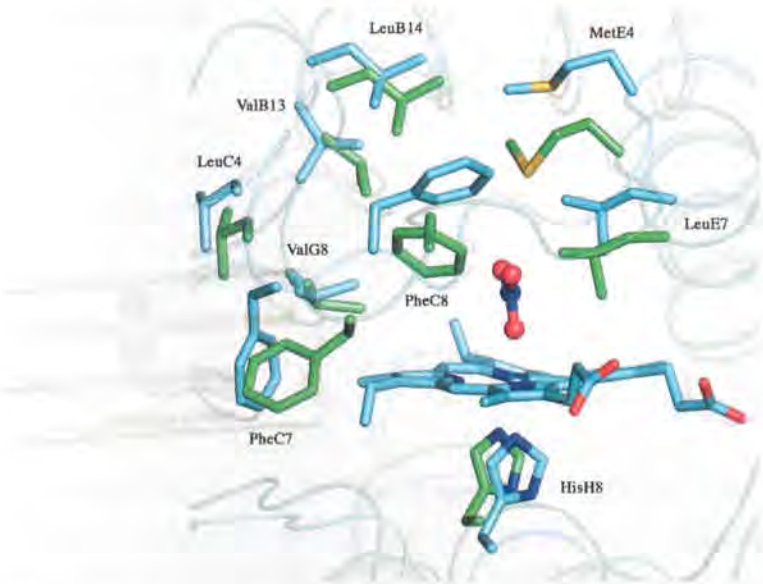

Figura 4.9. La presencia del anión nitrato en el centro activo provoca el reordenamiento estructural de los residuos del centro activo LeuB14, ValB13, LeuC4, ValG8, PheC7, PheC8, LeuE7 y MetE4. En verde se representa la estructura de trHbN·O_2 y en azul la estructura final de la trayectoria de dinámica molecular de trHbN·NO_3^-.

Cálculos QM/MM realizados para el sistema muestran que la solvatación del anión conlleva un aumento del ~8% en la distancia del enlace Fe–$ONOO^-$ (desde 2.07 Å para un modelo sin aguas a 2.32 Å cuando se tienen en cuenta aguas de solvatación),

describiendo cuánticamente las aguas y los residuos TyrB10, GlnE11, HisH8 y el grupo hemo). La entrada de moléculas de agua en el centro activo contribuye por lo tanto a debilitar el enlace, facilitando así la rotura para que el nitrato pueda escapar de la cavidad. El valor de la barrera de energía para la rotura del enlace obtenida para éste sistema es inferior a 4 kcal/mol. El reordenamiento de estos residuos posibilita la aparición no simultánea de dos canales independientes a través de los cuales se produce la entrada de moléculas de agua al centro activo, que se disponen alrededor del anión NO_3^-. Durante los primeros 7 nanosegundos de la trayectoria se forma un primer canal entre los residuos TyrB10, LeuB14, MetE4 y LysE8, que posteriormente queda cerrado al formarse un nuevo canal entre el esqueleto de la hélice C y el grupo hemo fruto del cambio conformacional de los residuos Phe45 y Phe46, que en la estructura oxigenada ocupan esa zona.

Una vez que el nitrato solvatado queda libre en la cavidad, la salida se produce casi sin barrera. Mediante cálculos de dinámica molecular y de dinámica molecular guiada se analizaron los caminos que seguía el anión libre para salir de la cavidad. El proceso de salida tiene lugar en dos etapas (Figura 4.10). En un primer paso el anión libre se aleja del hierro hasta aproximadamente 9 Å y forma un puente de hidrógeno con el grupo hidroxilo de ThrE2. Este primer paso ocurre con una barrera inferior a 1 kcal/mol y conlleva una estabilización de 2 kcal/mol. En este punto la salida se puede producir por dos caminos: (i) por la parte superior de la hélice C o (ii) por la parte inferior. Ambas salidas son igualmente probables desde un punto de vista estrictamente energético y con un bajo impedimento, proporcionando por lo tanto un camino rápido de expulsión del anión nitrato, que es esencial para que la proteína recupere su estado pre-reactivo.

De acuerdo con los resultados obtenidos, el proceso de salida del anión nitrato se produce de forma rápida una vez roto el enlace Fe–O, como indica el valor de la barrera de energía en buena concordancia con los datos experimentales. La salida no tiene lugar a través de un único camino bien definido como en el caso de la entrada de ligandos. Los caminos de salida que sigue el anión se forman como consecuencia de la distorsión que provoca la presencia de la carga negativa del anión nitrato, distorsión que a su vez facilita la entrada de aguas que solvatan al ión. La entrada de aguas es clave para debilitar el enlace entre el hierro del grupo hemo y el anión, cuya distancia de enlace

aumenta en 0.35 Å al quedar éste solvatado. A diferencia de las trayectorias obtenidas para las formas oxigenada y deoxigenada de trHbN, las moléculas de agua que entran en la cavidad permanecen en la cavidad o son reemplazadas por otras, quedando el anión nitrato solvatado durante el resto de la trayectoria. La rotura del enlace en este estado es térmicamente accesible, lo que concuerda con la dificultad de observar experimentalmente complejos hemo-NO_3.

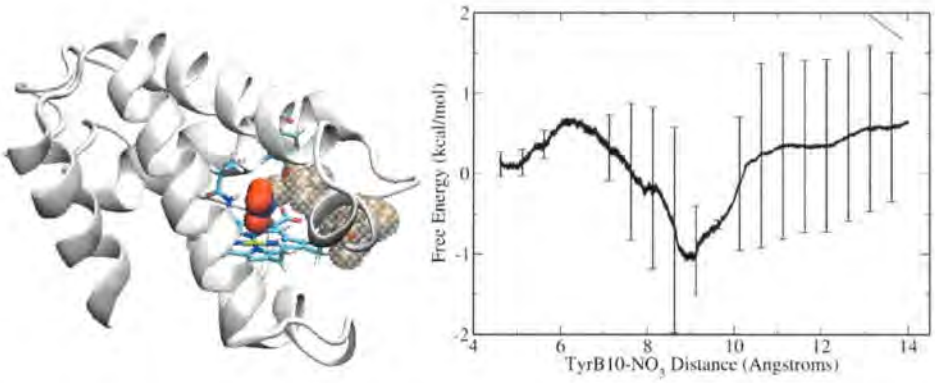

Figura 4.10 Representación del camino de salida del anión nitrato solvatado (izquierda) y del perfil de energía libre para el proceso (derecha).

Referencias bibliográficas

1 Bloom BR. Tuberculosis: pathogenesis, protection and control. Washington, DC: ASM Press, **1994**, 22.

2 MacMicking JD, North RJ, LaCourse R, Mudgett JS, Shah SK, Nathan CF. *Proc. Natl. Acad. Sci. USA*, **1997**, 94, 5243–5248.

3 Gardner, P.R., Constantino, G., Szabo, C., and Salzman, A.L. *J. Biol. Chem.*, **1997**, 272, 25071–25076.

4 Gardner, P.R., Constantino, G., and Salzman, A.L. *J. Biol. Chem.*, **1998**, 273, 26528–26533.

5 Stevanin, T.M., Ionnidis, M., Mills, C.E., Kim, S.O., Hughes, M.M., and Poole, R.K. *J. Biol. Chem.*, **2000**, 275, 35865–35875.

6 Clark, I. A.; Rocket, K. A. *Adv. Parasitol.*, **1996**, 37, 1-56.

7 Colasanti, M., Gradoni, L., Mattu, M., Persichini, T., Salvati, L., Venturini, G., Ascenzi, P. *Int. J. Mol. Med.*, **2002**, 9, 131-134.

8 Gardner, P. R., Gardner, A. M., Martin, A. M., Dou, Y., Li, T., Olson, J. S., Zhu, H., Riggs, A. F. *J. Biol. Chem.*, **2000**, 275, 12581-12589.

9 Liu, L.; Zeng, M.; Hausladen, A.; Heitman, J.; Stamler, J. S. *Proc. Natl. Acad. Sci. U.S.A.*, **2000**, 97, 4672-4676.

10 Cole, S. T., Brosch, R., Parkhill, J., Garnier, T., Churcher, C., Harris, D., Gordon, S. V., Eiglmeier, K., Gas, S., Barr y, C. E., III, et al . *Nature*, **1998**, 393, 537-544.

11 Couture, M., Yeh, S., Wittenberg, B. A., Wittenberg, J. B., Ouellet, Y., Rousseau, D. L., Guertin, M. *Proc. Natl. Acad. Sci. U.S.A.*, **1999**, 96, 11223-11228.

12 Ouellet H., Juszczak L., Dantsker D., Samuni U., Ouellet Y. H., Savard P. Y., Wittenberg J. B., Wittenberg B. A., Friedman J. M., Guertin M. *Biochem.*, **2003**, 42, 5764-5774.

13 Pesce A, Couture M, Dewilde S, Guertin M, Yamauchi K, Ascenzi P., Moens L. *EMBO J.*, **2000**, 19, 2424-2434.

14 Milani M, Pesce A, Nardini M, Ouellet H, Ouellet Y, Dewilde S, Bocedi A, Ascenzi P, Guertin M, Moens L, Friedman JM, Wittenberg JB, Bolognesi M. *J. Inorg. Biochem.*, **2005**, 99, 97–109.

15 Milani M, Pesce A, Ouellet Y, Ascenzi P, Guertin M, Bolognesi M. *EMBO J.*, **2001**, 20, 3902–3909.

16 Milani M, Pesce A, Ouellet Y, Dewilde S, Friedman JM, Ascenzi P, Guertin M, Bolognesi M. *J. Biol. Chem.*, **2004**, 279, 21520–21525.

17 Ouellet, H., Ouellet, Y., Richard, C., Labarre, M., Wittenberg, B., Wittenberg, J., Guertin, M. *Proc. Natl. Acad. Sci. U.S.A.*, **2002**, 99, 5902-5907.

18 Pathania, R., Navani, N. K., Gardner, A. M., Gardner, P. R., Dikshit, K. L., *Molecular Microbiology*, **2002**, 45, 1303-1314.

19 Crespo A., Martí M. A-, Kalko S. G., Morreale A., Orozco M., Gelpi J. L., Luque F. J., Estrin D. A., *J. Am. Chem. Soc.*, **2005**, 127, 4433–4444.

20 Kleywegt, J. G., Zou, J. Y., Kjeldgaard, M., Jones, T. A., *International Tables for Crystallography*, **2001**, Volumen F, capítulo 17.1, 353-356.

21 Kleywegt, G. J., Jones, T. A., *Acta Cryst.*, **1994**, D50, 178-185.

4.2.1 Ligand-induced dynamical regulation in Mycobacterium tuberculosis truncated-hemoglobin-N

A. Bidon-Chanal, Marcelo A. Martí, Alejandro Crespo, Mario Milani, Modesto Orozco, Martino Bolognesi, F. Javier Luque, and Dario Estrín.

Proteins, 64, **2006**, 457-464.

PROTEINS: Structure, Function, and Bioinformatics 64:457–464 (2006)

Ligand-Induced Dynamical Regulation of NO Conversion in *Mycobacterium tuberculosis* Truncated Hemoglobin-N

Axel Bidon-Chanal,[1] Marcelo A. Martí,[2] Alejandro Crespo,[2] Mario Milani,[3] Modesto Orozco,[4] Martino Bolognesi,[3] F. Javier Luque,[1]* and Darío A. Estrin[2]*

[1]*Departament de Fisicoquímica, Facultat de Farmacia, Universitat de Barcelona, Av. Diagonal 643, 08028, Barcelona, Spain*
[2]*Departamento de Química Inorgánica,Analítica y Química Física/INQUIMAE-CONICET, Facultad de Ciencias Exactas y Naturales, Universidad de Buenos Aires, Ciudad Universitaria, Pabellón 2, Buenos Aires, C1428EHA, Argentina*
[3]*Department of Biomolecular Sciences and Biotechnology, and CNR-INFM, University of Milano, Milano, Italy*
[4]*Departament de Bioquímica i Biologia Molecular, Facultat de Química, Universitat de Barcelona, Martí i Franqués 1, 08028 Barcelona, Spain; Unidad de Modelización Molecular y Bioinformática, Parc Científic de Barcelona, Josep Samitier 1-6, 08028 Barcelona; Span and Computacional Biology Program. Barcelona Supercomputing Center, Edificio Nexus II, Barcelona 08028, Spain*

ABSTRACT ***Mycobacterium tuberculosis*, the causative agent of human tuberculosis, is forced into latency by nitric oxide produced by macrophages during infection. In response to nitrosative stress *M. tuberculosis* has evolved a defense mechanism that relies on the oxygenated form of "truncated hemoglobin" N (trHbN), formally acting as NO-dioxygenase, yielding the harmless nitrate ion. X-ray crystal structures have shown that trHbN hosts a two-branched protein matrix tunnel system, proposed to control diatomic ligand migration to the heme, as the rate-limiting step in NO conversion to nitrate. Extended molecular dynamics simulations (0.1 μs), employed here to characterize the factors controlling diatomic ligand diffusion through the apolar tunnel system, suggest that O_2 migration in deoxy-trHbN is restricted to a short branch of the tunnel, and that O_2 binding to the heme drives conformational and dynamical fluctuations promoting NO migration through the long tunnel branch. The simulation results suggest that trHbN has evolved a dual-path mechanism for migration of O_2 and NO to the heme, to achieve the most efficient NO detoxification. Proteins 2006;64:457–464.**

Key words: molecular dynamics; *M. tuberculosis*; ligand migration; nitric oxide

INTRODUCTION

Mycobacterium tuberculosis is the causative agent of human tuberculosis,[1] a disease that infects about one-third of the human population, causing more than a million deaths per year. It has been reported that nitric oxide is produced in the macrophages during the initial growth infection stage, and that it may be involved in restricting the bacteria into latency.[2] The reaction of nitric oxide (NO) with the oxygenated form of "truncated hemoglobin" N (trHbN) has been proposed to be responsible for the resistance mechanism by which this microorganism can evade the toxic effects of NO, by acting as NO-dioxygenase to yield the harmless nitrate ion.[3,4]

Truncated hemoglobins (trHb) build a distinct group within the hemoglobin (Hb) superfamily that is widely distributed in bacteria, unicellular eukaryotes, and higher plants.[5] The tertiary structure of trHbs consists of a 2-on-2 helical sandwich that is a subset of the 3-on-3 sandwich of the classical globin fold.[6] The proximal HisF8 heme-linked residue is conserved in both Hb and trHb families, and a distal tyrosine at position B10 is found in almost all the trHb family members sequenced to date. Despite their small size compared to vertebrate globins, several trHbs host a protein matrix apolar tunnel system that connects the heme pocket with the protein surface.[7–9] In trHbN from *M. tuberculosis* the tunnel system is built by two perpendicular branches,[8] of about 8 and 20 Å length, respectively (Fig. 1), that have been proposed to control diatomic ligand diffusion to/from the heme[10,11] as the rate-limiting step in NO conversion to nitrate.[12]

Despite the biophysical and structural characterization of trHbN and the large number of studies on ligand migration to the heme in related proteins,[13–17] no detailed information is available on the molecular mechanisms underlying diffusion of both O_2 and NO in trHbN. Additionally, nothing is known on how *M. tuberculosis* trHbN regulates ligand access to the heme to achieve NO detoxification and survival of the mycobacterium under the nitro-

---

The first two authors contributed equally to this work.

Grant sponsor: Fundación Antorchas, Universidad de Buenos Aires; Grant number: X038; Grant sponsor: ANPCYT; Grant number: 06-08447; Grant sponsor: Spanish Ministerio de Investigación y Ciencia; Grant number: SAF2002-02482; Grant sponsor: NIH postdoctoral fellowship to M.M.; Grant number: 1-R01-AI052258 (2004–2007); Grant sponsor: CIMAINA (Milano, Italy) to M.B.; Grant sponsor: Fondazione CARIPLO (Milano, Italy) to M.B.; Grant sponsor: the Italian Ministry for University and Scientific Research FIRB Project "Biologia Strutturale"; Grant number: RBLA03B3KC, to M.B.

*Correspondence to: Dario Estrin, University of Buenos Aires, Department of Chemistry, Ciudad Universitaria, Pab. 2, Buenos Aires, C1428EHA, Argentina or F. Javier Luque, University of Barcelona Av. Diagonal 643, 08028, Barcelona, Spain. E-mail: dario@qi.fcen.uba.ar or fjluque@ub.edu

Received 17 November 2005; Revised 3 February 2006; Accepted 15 February 2006

Published online 10 May 2006 in Wiley InterScience (www.interscience.wiley.com). DOI: 10.1002/prot.21004

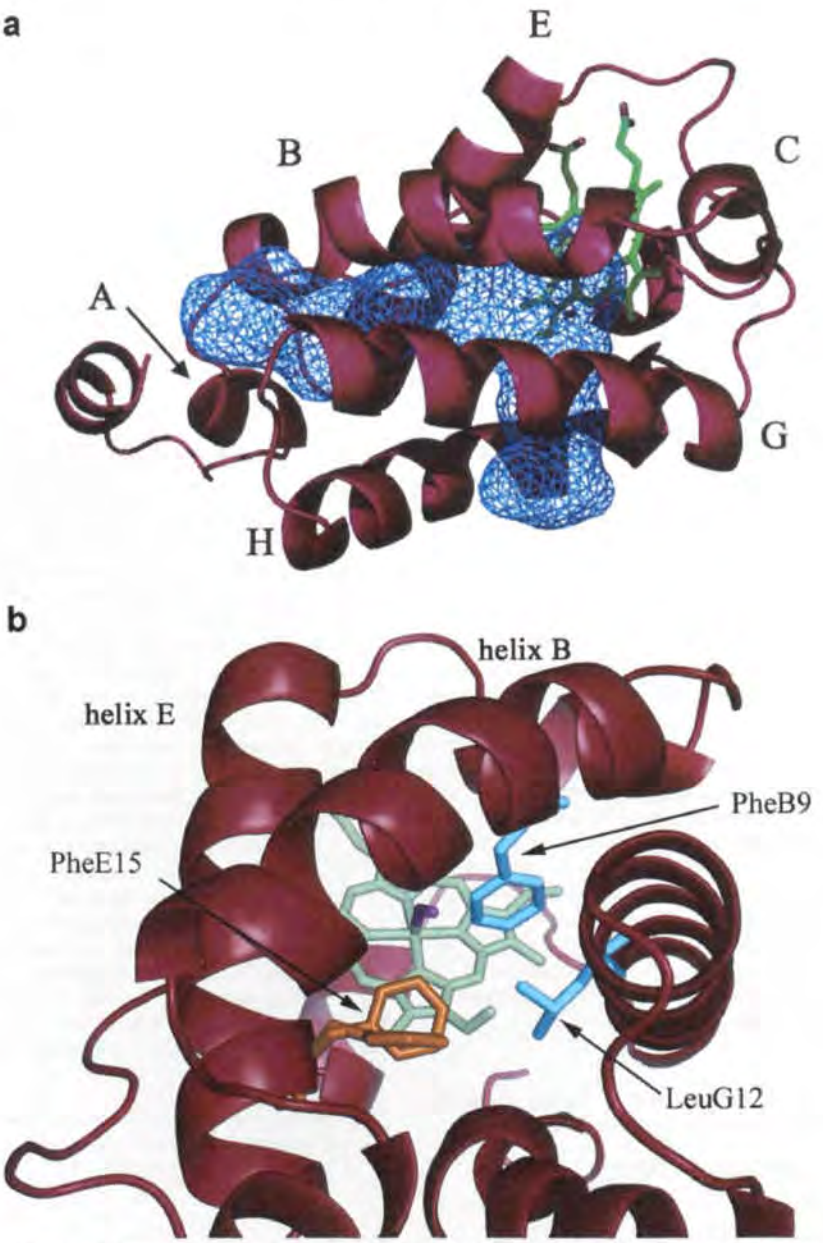

Fig. 1. (**a**) X-ray crystal structure of oxy-trHbN (PDB entry 1IDR) used in simulations, showing the labels of the helices, the location of the heme group (green) and the two branches of the tunnel system (blue mesh). The long branch (~20 Å long) is horizontal in the figure, and can be seen as roughly perpendicular to the heme distal face. The short branch (~8 Å long) lies roughly parallel to the heme plane (vertical in the figure), accessing the heme distal site pocket from the inner part of the heme crevice. Residues 1–15, building the N-terminal helix, are highlighted in purple. (**b**) Conformational change of PheE15 (orange) side chain along the C_α–C_β dihedral angle leading to *open* and *closed* states viewed along the tunnel long branch leading to the heme (green) in oxy-trHbN. The residues that define the bottleneck to ligand migration (PheB9, LeuG12; blue) in the *closed* state are also shown.

sative stress typical of latency conditions. Such mechanism issues are considered and explored in this work through extended 0.1-μs molecular dynamics (MD) simulations of both oxy and deoxy forms of trHbN.

MATERIALS AND METHODS

Molecular dynamics simulations were performed starting from the crystal structure of wild-type oxy-trHbN (PDB entry 1idr; monomer A at 1.9-Å resolution).[8] The enzyme was immersed in a preequilibrated octahedral box of TIP3P[18] water molecules. The standard protonation state at physiological pH was assigned to the ionizable residues. The final system contains the model protein, around 8600 water molecules and the added counterions, leading to a total of ~28,270 atoms. Simulations were performed in the NPT (1 atm, 298 K) ensemble.[19] The system was simulated employing periodic boundary conditions and Ewald sums (grid spacing of 1 Å) for treating long range electrostatic interactions.[20] All simulations were performed with the parmm99 force field[21] using Amber8.[22] The initial system was minimized using a multistep protocol. First, the position of all hydrogens in the protein was refined by using 2000 cycles of energy minimization (500 cycles of steepest descent + 1500 cycles of conjugate gradient). Then, water molecules were refined using 10,000 cycles of energy minimization (2000 cycles of steepest descent + 8000 cycles of conjugate gradient). Finally, the position of all atoms in the system was energy minimized (2000 cycles of steepest descent + 8000 cycles of conjugate gradient). The equilibration process was performed by heating from 100 to 298 K in four 100-ps steps, and the final structure was used as the starting point for a 0.1-μs MD simulation. To avoid a bias in the structure of the deoxy form of trHbN, it was built up by deleting the O_2 molecule from the X-ray crystallographic structure, and minimized and equilibrated following the same protocol mentioned above. The oxygenated and deoxygenated heme model system charges were determined by using RESP charges[23] and HF/6-31G(d) wave functions, according to the Amber standard protocol.

To study in detail the properties of the tunnel cavity system in trHb N from *M. tuberculosis*, we have calculated the diffusion free energy profiles for a diatomic neutral ligand along the tunnels for the oxy and deoxy proteins. The free energy profiles were constructed by performing constant velocity multiple steering molecular dynamics (MSMD) simulations, and using the Jarzynski's inequality,[24] which relates equilibrium free energy values with the irreversible work performed over the system that proceeds along a reaction coordinate from reactants to products. In the present study, the reaction coordinate λ was chosen as the iron–ligand distance. Calculations were performed using a force constant of 200 kcal · mol^{-1} $Å^{-1}$ and pulling velocities of 0.05 and 0.1 Å/ps, which yielded similar free energy profiles. The statistical error was calculated as the standard deviation between these two estimates. To reconstruct the free energy profile of ligand migration along the tunnels, a set of MSMD runs were performed starting from equilibrated MD structures with λ (t = 0) corresponding with the ligand in (1) the distal pocket, (2) the crystallographic Xe-binding sites, and (3) the ligand outside the tunnels. Ten MSMD simulations were performed in each direction (forward/exit and backward/entry) for each of the two pulling velocities. In cases in which two overlapping profiles were obtained (from entry and exit sets), we confirmed that both of them matched.

The role of PheE15 as gate residue along the long branch of the tunnel was investigated by computing the free energy profile using umbrella-sampling techniques[20] for the oxy and deoxy states of the proteins, using the PheE15 C_α–C_β dihedral angle as distinguished coordinate and a set of 12 windows of 1 ns each. Two independent sets of 12 windows each were employed to estimate the statistical error.

Finally, the set of structures collected along the 0.1-μs MD simulations were used to explore the dynamical behavior of the protein by determining the essential dynamics through principal component analysis,[25] conducted considering the backbone C_α atoms. Indeed, residues 1–15, which form the short N-terminal isolated helix (Fig. 1), were also excluded from the analysis because high flexibility in this region might mask the essential movements in the trHbN fold.

RESULTS AND DISCUSSION

To address the question of how NO can access the heme in oxy-trHbN, we analyzed a 0.1-μs trajectory of oxy-trHbN. The analysis revealed that only the long branch of the tunnel remains open for a significant fraction of time to allow diffusion of NO, and that opening of this path is controlled by residue PheE15, whose side chain mainly populates two conformations [characterized by average C_α–C_β torsional angles of about +40 and −50 degrees; Fig. 2(a)]. In the PheE15 *closed* state the side-chain phenyl ring protrudes into the tunnel long branch, preventing the access of incoming ligands to the heme distal cavity through this path. On the contrary, in the *open* state, PheE15 is roughly parallel to the tunnel long branch axis, enabling the transit of diatomic ligands, the narrowest tunnel width being ~3.4 Å.

The free energy profiles for ligand migration, obtained through steered MD simulations, indicated that in the *open* state NO diffusion is almost free of barriers, and access to the heme cavity is favored by 3–4 kcal/mol [Fig. 2(b)]. On the contrary, in the *closed* state the steric hindrance of PheE15 phenyl ring undermines ligand access, leading to a steady increase in the free energy profile [Fig. 2(b)]. Interestingly, the free energy minimum found at about 11 Å from the heme matches one of the Xe binding sites observed experimentally in *M. tuberculosis* trHbN.[9] Steered MD simulations also revealed that in oxygenated trHbN migration of NO through the tunnel short branch is not favored, related to a progressive rise in the free energy [Fig. 2(c)]. Taken together, the above results suggest that NO access to the heme distal cavity should preferentially occur through the long tunnel branch in oxy-trHbN.

Strikingly, the ligand migration pathway described above is drastically different in deoxy-trHbN. The analysis of the

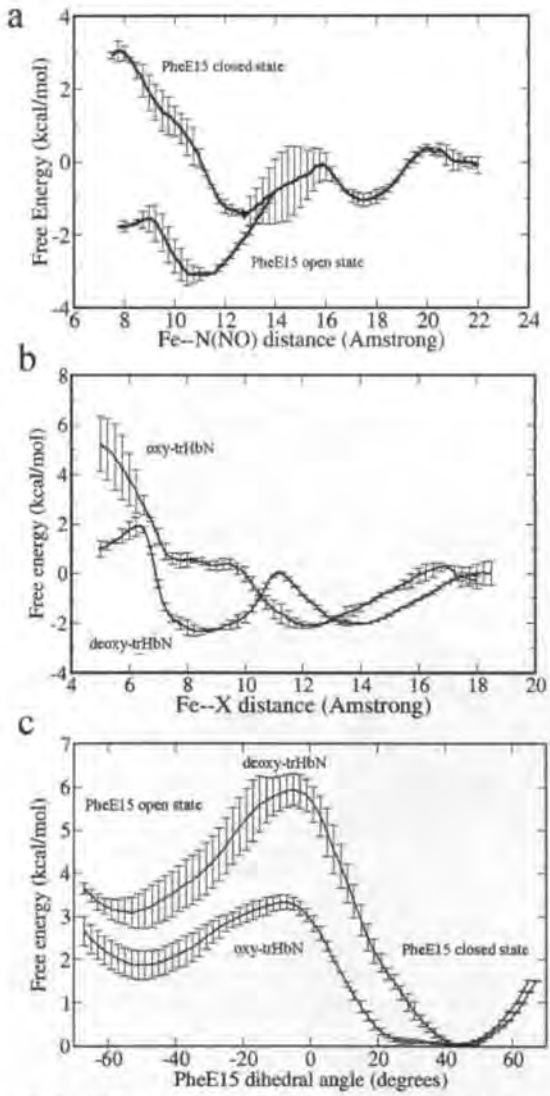

Fig. 2. (a) Free energy profile for NO migration along the long tunnel branch in both *open* and *closed* states of oxy-trHbN; the distance from the Fe atom to the nitrogen in NO is used as the driven coordinate. (b) Free energy profile for diatomic ligand (NO; O_2) migration along the short tunnel branch for oxy-trHbN (NO) and deoxy-trHbN (O_2); the distance from the Fe atom to either nitrogen (NO) or oxygen (O_2) atoms is used as the driven coordinate. (c) Potential of mean force for the conformational change in PheE15 C_α–C_β dihedral angle leading to conversion between open and closed states in deoxy- and oxy-trHbN. The statistical error bars were computed as stated in Material and Methods.

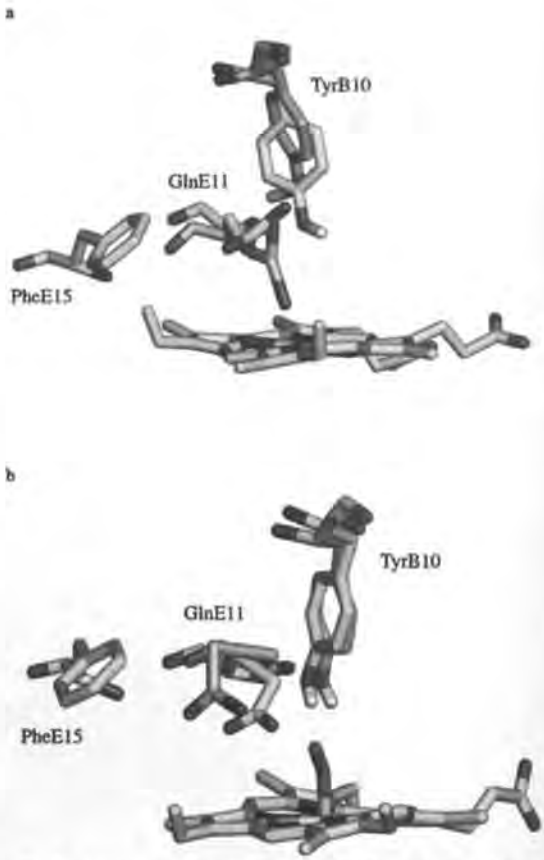

Fig. 3. Interactions between TyrB10 and GlnE11 in deoxy-trHbN and oxy-trHbN. (a) In deoxy-trHbN, the side chain of GlnE11 adopts an *all-trans* conformation (average torsions around C_α–C_β, C_β–C_γ, and C_γ–C_δ dihedrals of 40.2, 167.1, and 93.7 degrees), although the relative orientation of the amide group of GlnE11 and hydroxyl group of TyrB10 fluctuate along the trajectory. (b) In oxy-trHbN the side chain of GlnE11 populates two *staggered* conformation characterized by torsional angles around C_α–C_β, C_β–C_γ, and C_γ–C_δ bonds of (+45.0, −74.8, −99.3 degrees) and (−50.2, +67.2, +48.5 degrees), respectively. Transition of the former conformation to the latter one makes GlnE11 to approach PheE15 by ~1.5 Å.

0.1-μs MD trajectory for deoxy-trHbN showed that the long branch of the tunnel remains closed during the whole simulation time. In fact, the PheE15 torsional free energy profile, obtained using umbrella sampling calculations, reveals that in deoxy-trHbN the conformational transition between *open* and *closed* states of the tunnel gating residue PheE15 must overcome a free energy barrier higher than 6 kcal/mol (compared with the 3 kcal/mol barrier of oxy-trHbN; see Fig. 3). Moreover, the *open* state (less stable by ~2 kcal/mol relative to the *closed* state in oxy-trHbN) is further destabilized by 1.5 kcal/mol in deoxy-trHbN. In contrast, ligand migration through the short branch of the tunnel is now allowed, with a small free energy barrier [~2 kcal/mol; Fig. 2(c)] before reaching a flat minimum, which corresponds to a cavity formed by residues PheG5, AlaG9, and IleH11. In fact, this cavity is one of the Xe binding pockets observed by X-ray crystallography in the short tunnel branch.[6] Access to the Fe atom from this cavity requires overcoming a free energy barrier of ~4 kcal/mol [Fig. 2(c)], reflecting a narrow passage through the heme and ValG8.

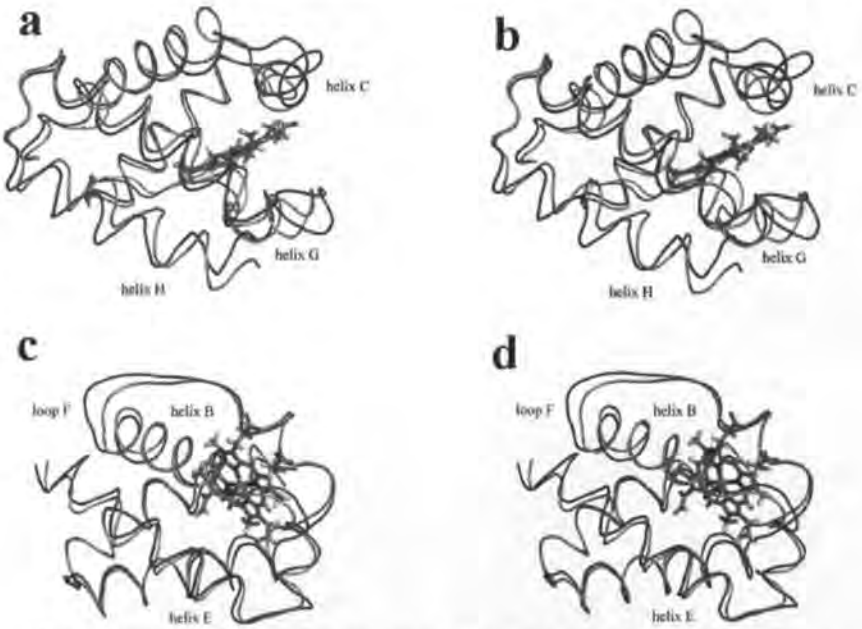

Fig. 4. Setereoview of the essential dynamics results of two different snapshots for deoxy-trHbN (**a** and **b**) and for oxy-trHbN (**c** and **d**). The largest motion leading to dynamical fluctuations in the protein backbone and the structural elements mainly involved in those fluctuations are shown.

The preceding results suggest that *M. tuberculosis* trHbN has evolved a molecular mechanism for ligand diffusion, whereby the coordination state of the heme group modulates the main path for ligand entry. Thus, access of an O_2 molecule to the heme through the tunnel short branch, and its coordination to the heme-Fe atom, would facilitate migration of the second ligand (NO; alternatively another O_2 molecule) through the tunnel long branch.

Such first set of conclusions raises the question of how does O_2 binding to the heme regulate the ligand access pathway. Our simulation results indicate that such regulation may be achieved through alteration of the heme distal site hydrogen-bonded network, a structural feature previously recognized to play a key role in trHbN heme/ligand stabilization.[7,10] In the deoxy-trHbN simulation, the side chain of GlnE11 adopts an extended *all-trans* conformation, allowing the terminal amido group to be hydrogen-bonded to the hydroxyl group of TyrB10. In addition, the simulation shows a dynamical fluctuation between (TyrB10)O—H · · · O=C(GlnE11) and (TyrB10)O · · · H—N(GlnE11) hydrogen bonds, such that TyrB10 hydroxyl group acts both as hydrogen-bond donor and acceptor in the 0.1-μs time frame (Fig. 4). In contrast, in oxy-trHbN the heme-Fe coordinated O_2 restricts the conformational freedom of TyrB10 through a hydrogen bond, thus allowing the phenolic hydroxyl group to act exclusively as hydrogen-bond acceptor for the amide-NH_2 group of GlnE11. Under these conditions GlnE11 side chain is forced to fluctuate between two *staggered* conformations (Fig. 4), and the distance between the side chains of GlnE11 and PheE15 is shortened by ~1.5 Å, due to different residue packing. Thus, GlnE11 might be viewed as an internal "switch" that would regulate the *open/closed* state of the PheE15 gate, within the tunnel long branch through a conformational compression mechanism (Fig. 4).

The changes in the heme distal site local structure, however, are also linked to alteration of the protein backbone motions. Thus, essential dynamics analysis shows that in deoxy-trHbN the major motions affect helices C, G, H, and the F extended region In contrast, when opening/closing events occur in the tunnel long branch, the major motion in oxy-trHbN involves the relative displacement of helices B and E (see Fig. 4). These findings therefore suggest that binding of O_2 to the heme group triggers a large-scale dynamical change that alters the natural fluctuations in the protein backbone, in agreement with the available experimental evidence indicating that ligand binding modulates trHbN structural plasticity.[26] In view of the specific location of GlnE11 within the protein structure, it can be speculated that the conformational "switch" described above for this residue may also play a role in facilitating the relative motion of helices B and E and the opening of the PheE15 gate.

The analysis of oxy-trHbN MD trajectory additionally revealed that the relative displacement of helices B and E is also regulated by the formation of a salt bridge between Arg10 (in the N-terminal region) and Glu70 (in the EF interhelical region) (Fig. 5), which promotes folding of the short A helix onto the EF hinge. As a result, helix E cannot

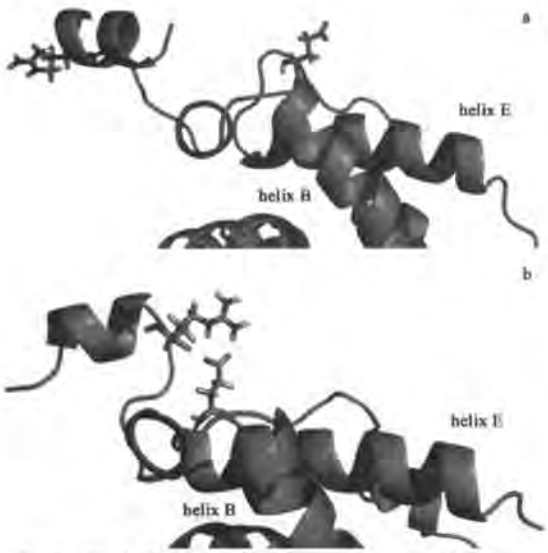

Fig. 5. The Arg10–Glu70 salt bridge interaction in trHbN. (a) In the absence of the salt bridge the dynamical fluctuations of the protein backbone facilitates the relative displacement of helices B and E, which should facilitate opening of the PheE15 gate in the tunnel long branch. (b) Formation of the salt bridge inhibits ligand migration through the tunnel long branch by increasing the friction between helices B and E.

be displaced relative to helix B, and the enhanced friction inhibits opening of the long tunnel branch. These results are consistent with the experimentally observed dependence of the kinetics of ligand diffusion in trHbN on the viscosity of the aqueous environment.[10,11]

On the basis of the preceding results, a dual-path ligand-induced regulation mechanism is proposed to be operative in *M. tuberculosis* trHbN. The key feature in such mechanism is the change of contacts formed by TyrB10 and GlnE11. Thus, O_2 binding to the heme would promote a *local* conformational change in the TyrB10–GlnE11 pair, in turn inducing compression on PheE15, facilitating the relative displacement of helices B and E and altering the *global* dynamical fluctuations of the protein. The alteration of the essential dynamics, in conjunction with rearrangements in the side chains that surround PheE15, would promote opening of the tunnel long branch, enhancing capture of NO from the aqueous phase. This mechanism partly relies on the very high oxygen affinity of the protein (O_2 binding affinity to ferrous trHbN of 8.0×10^{-9} M),[7] which guarantees that it is mainly loaded with O_2. The mechanism also benefits from the high hydrophobic character of the ligand diffusion tunnel, which can act as a potential reservoir to concentrate nonpolar diatomic ligands (possibly in the identified Xe sites), at the same time limiting the rate at which water may occupy the heme pocket, when vacated by the dissociated ligand. All these factors would contribute to enhance the efficiency of NO detoxification. The mechanism also provides a basis to rationalize why NO conversion to nitrate by oxy-trHbN occurs at a rate faster than O_2 binding to the deoxy protein (bimolecular rate constants of 745 and 25 $\mu M^{-1}\ s^{-1}$, respectively),[3,7] an explanation that cannot be extracted from the X-ray structures and from the kinetic data alone.

Our results are also consistent with recent studies of the modulation of the kinetics of CO recombination in trHbN, which suggest the existence of different ligand-dependent conformations with different kinetic behaviours.[11] Thus, these studies showed that the kinetic patterns observed for CO recombination to trHbN, which are atypical when compared with many other hemoglobins and myoglobins, exhibit up to three kinetic phases. It was shown that the time scale of the slowest phase is within experimental error consistent with the association of the binding of CO to deoxy trHbN, and that its amplitude increases with decreasing viscosity or increasing temperature. These experimental observations were interpreted by assigning the slowest phase to a CO rebinding process under conditions where the heme environment has fully relaxed to a conformation or distribution of conformations associated with the deoxy form of trHbN. In fact, it was concluded that a different range of conformations is accessible for the protein depending on the coordination state of the heme group, in agreement with our simulation results indicating that the dynamical fluctuations of trHbN are drastically altered upon binding of O_2 to the heme. It should also be noticed that the ligand-induced trHbN structural plasticity has also been highlighted by comparison of the UV Raman spectra of the w.t. protein with the TyrB10 → Phe mutant upon NO binding.[26] These spectrosocopic measurements clearly indicate that NO binding to the heme distal site triggers a large-scale conformational change that propagates through the pre-F helix to the E and B helices, in keeping with the large changes in the natural dynamics of the protein observed in the MD simulations of both deoxy- and oxy-forms of trHbN.

There are also relevant differences in the CO recombination process for w.t. trHbN and its TyrB10 → Phe mutant, which have been attributed to differences in the relaxation of the aromatic side chain at B10.[11] Whereas for the w.t. protein there is a phase corresponding to a viscosity-dependent relaxation initiated upon ligand dissociation, a single, faster, CO recombination process is experimentally observed for the mutant. This finding suggests a critical role played by TyrB10, which can be interpreted in terms of its hydrogen bond interaction with GlnE11. Thus, even though our results indicate that hydrogen bonding between these two residues is present in both deoxy- and oxy-states of trHbN, O_2 binding to the heme promotes a local conformational rearrangement of the TyrB10–GlnE11 pair, which ultimately modulates the conformational space accessible to the protein leading to the opening of the long branch tunnel. Replacement of TyrB10 by Phe removes such hydrogen bond, preventing the onset of the ligand-induced conformational switch mechanism; this

would also explain the different kinetic behavior seen in the TyrB10 → Phe mutant.

CONCLUSIONS

The present results suggest that a novel dual-path ligand-induced regulation mechanism is operative in *M. tuberculosis* trHbN, whereby the protein dynamics and the protein matrix tunnel system have evolved to allow the access of O_2 and NO ligands to the heme through distinct migration paths. The key feature in such mechanism is the change of contacts formed by TyrB10 and GlnE11, where GlnE11 acts as a switch regulating the ligand access pathway by altering the essential movements of the protein backbone. Thus, O_2 binding to the heme should induce compression of PheE15 by the side chain of GlnE11, and promote the relative displacement of helices B and E. These events, combined with local rearrangements in the side chains that surround PheE15, should open the tunnel long branch, facilitating capture of NO from the aqueous phase.

The detailed microscopic information obtained in these simulation studies suggests mutations that would significantly effect O_2/NO multiligand chemistry. Specifically, mutations of the gate amino acid PheE15 to Ala or Trp should promote full opening or permanent closing of the gate, respectively. Mutation of TyrB10 and GlnE11 should also greatly affect the conformational changes that lead to the opening of the tunnel long branch upon O_2 binding. Finally, to complete a full cycle, the nitrate anion produced should be removed form the heme cavity, and the Fe(III) protein should be reduced back to Fe(II). How these processes are accomplished is still unknown, although nitrate efflux to the solvent is expected to be fast, and probably limited by the heme–nitrate bond breaking. A suitable reductase system is expected to control the heme–Fe atom redox state in vivo, considering that steady conversion of NO to nitrate is an established protection mechanism in *M. tuberculosis*.[2,3]

As a final consideration, we note that other heme proteins have been proposed to perform multiligand chemistry. Among these, oxy-hemoglobin, oxy-myoglobin, and the recently discovered neuroglobin and cytoglobin.[27–29] Untangling the structural determinants of the interplay between ligand binding, protein dynamics and ligand migration will be essential to shed light on the emerging field of multiligand chemistry performed by heme proteins.

ACKNOWLEDGMENTS

Calculations were performed in the MareNostrum supercomputer at the Barcelona Supercomputing Center.

REFERENCES

1. Bloom BR. Tuberculosis: pathogenesis, protection and control. Washington, DC: ASM Press; 1994.
2. MacMicking JD, North RJ, LaCourse R, Mudgett JS, Shah SK, Nathan CF. Identification of nitric oxide synthase as a protective locus against tuberculosis. Proc Natl Acad Sci USA 1997;94:5243–5248.
3. Ouellet H, Ouellet Y, Richard C, Labarre M, Wittenberg B, Wittenberg J, Guertin M. Truncated hemoglobin HbN protects *Mycobacterium bovis* from nitric oxide. Proc Natl Acad Sci USA 2002;99:5902–5907.
4. Couture M, Yeh SR, Wittenberg BA, Wittenberg JB, Ouellet Y, Rousseau DL, Guertin M. A cooperative oxygen-binding hemoglobin from *Mycobacterium tuberculosis*. Proc Natl Acad Sci USA 1999;96:11223–11228.
5. Moens, L., et al. Globins in nonvertebrate species: dispersal by horizontal gene transfer and evolution of the structure–function relationships. Mol Biol Evol 1996;13:324–333.
6. Pesce A, Couture M, Dewilde S, Guertin M, Yamauchi K, Ascenzi P, Moens L, Bolognesi M. A novel two-over-two alpha-helical sandwich fold is characteristic of the truncated hemoglobin family. EMBO J 2000;19:2424–2434.
7. Milani M, Pesce A, Nardini M, Ouellet H, Ouellet Y, Dewilde S, Bocedi A, Ascenzi P, Guertin M, Moens L, Friedman JM, Wittenberg JB, Bolognesi M. Structural bases for heme binding and diatomic ligand recognition in truncated hemoglobins. J Inorg Biochem 2005;99:97–109.
8. Milani M, Pesce A, Ouellet Y, Ascenzi P, Guertin M, Bolognesi M. *Mycobacterium tuberculosis* hemoglobin N displays a protein tunnel suited for O_2 diffusion to the heme. EMBO J 2001;20:3902–3909.
9. Milani M, Pesce A, Ouellet Y, Dewilde S, Friedman JM, Ascenzi P, Guertin M, Bolognesi M. Heme-ligand tunneling in group I truncated hemoglobins. J Biol Chem 2004;279:21520–21525.
10. Samuni U, Dantsker D, Ray A, Wittenberg JB, Wittenberg BA, Dewilde S, Moens L, Ouellet Y, Guertin M, Friedman JM. Kinetic modulation in carbonmonoxy derivatives of truncated hemoglobins: the role of distal heme pocket residues and extended apolar tunnel. J Biol Chem 2003;278:27241–27250.
11. Dantsker D, Samuni U, Ouellet Y, Wittenberg BA, Wittenberg JB, Milani M, Bolognesi M, Guertin M, Friedman JM. Viscosity-dependent relaxation significantly modulates the kinetics of CO recombination in the truncated hemoglobin TrHbN from *Mycobacterium tuberculosis*. J Biol Chem 2004;279:38844–38853.
12. Crespo A, Martí MA, Kalko SG, Morreale A, Orozco M, Gelpi JL, Luque FJ, Estrin DA. Theoretical study of the truncated hemoglobin HbN: exploring the molecular basis of the NO detoxification mechanism. J Am Chem Soc 2005;127:4433–4444.
13. Schotte F, Lim M, Jackson TA, Smirnov AV, Soman J, Olson JS, Phillips GN Jr, Wulff M, Anfinrud PA. Watching a protein as it function with 150 ps time resolved X-ray crystallography. Science 2003;300:1944–1947.
14. Chu K, Vojtchovský J, McMahon BH, Sweet RM, Berendzen J, Schlichting I. Structure of a ligand binding intermediate in wild type carbonmonoxy myoglobin. Nature 2000;403:921–923.
15. Case DA, Karplus M. Dynamics of ligand binding to heme proteins. J Mol Biol 1979;132:343–368.
16. Bossa C, Anselmi M, Roccatano D, Amadei A, Vallone B, Brunori M, Di Nola A. Extended molecular dynamics simulation of the carbon monoxide migration in sperm whale myoglobin. Biophys J 2004;86:3855–3862.
17. Nutt DR, Meuwly M. CO migration in native and mutant myoglobin: atomistic simulations for the understanding of protein function. Proc Natl Acad Sci USA 2004;101:5998–6002.
18. Jorgensen WL, Chandrasekhar J, Madura JD, Impey RW, Klein ML. Comparison of sample potential functions for simulating liquid water. J Chem Phys 1983;79:926–935.
19. Berendsen HJC, Postma JPM, van Gunsteren WF, Di Nola A, Haak JR. Molecular dynamics with coupling to an external bath. J Chem Phys 1984;81:3684–3690.
20. Leach AR. Molecular modelling. 2nd ed. Englewood Cliffs, NJ: Prentice Hall; 2001.
21. Wang J, Cieplak P, Kollman PA. How well does a restrained electrostatic potential (RESP) model perform in calculating conformational energies of organic and biological molecules? J Comput Chem 2000;21:1049–1074.
22. Pearlman DA, Case DA, Caldwell JW, Ross WR, Cheatham TE III, DeBolt S, Ferguson D, Seibel G, Kollman P. AMBER, a computer program for applying molecular mechanics, normal mode analysis, molecular dynamics and free energy calculations to elucidate the structures and energies of molecules. Comp Phys Commun 1995;91:1–41.
23. Bayly CI, Cieplak, P, Cornell W, Kollman, PA A well behaved electrostatic potential based method using charge restraints for

deriving atomic charges: the RESP model J Phys Chem 1993;97: 10269–10280.
24. Jarzynski C. Non equilibrium equality for free energy differences. Phys Rev Lett 1997;78:2690–2693.
25. Amadei A, Linssen ABM, Berendsen HJC. Essential dynamics of proteins. Proteins 1993;17:412–415.
26. Mukai M, Ouellet Y, Guertin M, Yeh S-R. NO binding induced conformational changes in a truncated hemoglobin from *Mycobacterium tuberculosis*. Biochemistry 2004;43:2764–2770.
27. Ascenzi P, Salvati L, Brunori M. Does myoglobin protect *Trypanosoma cruzi* from the antiparasitic effects of nitric oxide? FEBS Lett 2001;501:103–105.
28. Eich RF, Li T, Lemon DD, Doherty DH, Curry SR, Aitken JF, Mathews AJ, Johnson KA, Smith RD, Phillips GN Jr, Olson JS. Mechanism of NO-induced oxidation of myoglobin and hemoglobin. Biochemistry 1996;35:6976–6983.
29. Brunori M, Giuffrè A, Nienhaus K, Ulrich Nienhaus G, Scandurra FM, Vallone B. Neuroglobin, nitric oxide, and oxygen: functional pathways and conformational changes. Proc Natl Acad Sci USA 2005;102:8483–8488.

4.2.2 Dynamical regulation of ligand migration in the Truncated Hemoglobin-N from Mycobacterium tuberculosis: assessment of the role of the TyrB10-GlnE11 pair

Axel Bidon-Chanal, Marcelo A. Martí, Darío A. Estrin, and F. Javier Luque

J. Am. Chem. Soc., 129, **2007**, 6782-6788.

J|A|C|S
ARTICLES
Published on Web 05/09/2007

Dynamical Regulation of Ligand Migration by a Gate-Opening Molecular Switch in Truncated Hemoglobin-N from *Mycobacterium tuberculosis*

Axel Bidon-Chanal,† Marcelo A. Martí,‡ Darío A. Estrin*,‡ and F. Javier Luque*,†

Contribution from the Departament de Fisicoquímica, Facultat de Farmàcia, Universitat de Barcelona, Avenida Diagonal 643, 08028, Barcelona, Spain, and Departamento de Química Inorgánica, Analítica y Química Física/INQUIMAE-CONICET, Facultad de Ciencias Exactas y Naturales, Universidad de Buenos Aires, Ciudad Universitaria, Pabellón 2, Buenos Aires, C1428EHA, Argentina

Received December 15, 2006; E-mail: fjluque@ub.es; dario@qi.fcen.uba.ar

Abstract: Truncated hemoglobin-N is believed to constitute a defense mechanism of *Mycobacterium tuberculosis* against NO produced by macrophages, which is converted to the harmless nitrate anion. This process is catalyzed very efficiently, as the enzyme activity is limited by ligand diffusion. By using extended molecular dynamics simulations we explore the mechanism that regulates ligand diffusion and, particularly, the role played by residues that assist binding of O_2 to the heme group. Our data strongly support the hypothesis that the access of NO to the heme cavity is dynamically regulated by the TyrB10−GlnE11 pair, which acts as a molecular switch that controls opening of the ligand diffusion tunnel. Binding of O_2 to the heme group triggers local conformational changes in the TyrB10−GlnE11 pair, which favor opening of the PheE15 gate residue through global changes in the essential motions of the protein skeleton. The complex pattern of conformational changes triggered upon O_2 binding is drastically altered in the GlnE11→Ala and TyrB10→Phe mutants, which justifies the poor enzymatic activity observed experimentally for the TyrB10→Phe form. The results support a molecular mechanism evolved to ensure access of NO to the heme cavity in the oxygenated form of the protein, which should warrant survival of the microorganism under stress conditions.

Introduction

Globins are found in all kingdoms of living organisms. Besides their function in assisting O_2 transport and storage, novel functions have been identified in the last years, such as control of nitric oxide (NO) levels in microorganisms. In *Mycobacterium tuberculosis*, which infects about one-third of the human population and causes more than a million deaths per year,[1] the NO resistance is based on the NO-dioxygenase activity of the oxygenated form of truncated hemoglobin-N (trHbN), which converts NO into nitrate anion,[2−4] thus contributing to induction and maintenance of bacilli latency.[5,6]

Truncated hemoglobins make up a distinct group within the hemoglobin superfamily.[7] Their tertiary structure consists of a 2-on-2 helical sandwich, which is a subset of the 3-on-3 sandwich of the classical globin fold.[8] Despite their small size, several truncated hemoglobins host an apolar tunnel that connects the heme pocket with the protein surface.[9−11] In trHbN from *M. tuberculosis* the tunnel system is built by two perpendicular branches of about 8 and 20 Å length, which differ from the cavities observed in sperm whale myoglobin. Moreover, it has been hypothesized to control diatomic ligand migration to the heme, which would be the rate-limiting step in NO conversion to nitrate.[2,3]

The role played by the ligand migration tunnel in trHbN has been explored by means of extended molecular dynamics (MD) simulations of both deoxygenated and oxygenated forms of trHbN, which have unraveled a dual-path ligand-induced regulation mechanism underlying diffusion of both O_2 and NO in trHbN.[12,13] According to this mechanism, ligand migration

† Universitat de Barcelona.
‡ Universidad de Buenos Aires.

(1) Bloom, B. R. *Tuberculosis: Pathogenesis, Protection and Control*; ASM Press: Washington D.C., 1994.
(2) Ouellet, H.; Ouellet, Y.; Richard, C.; Labarre, M.; Wittenberg, B.; Wittenberg, J.; Guertin, M. *Proc. Natl. Acad. Sci. U.S.A.* **2002**, *99*, 5902.
(3) Couture, M.; Yeh, S. R.; Wittenberg, B. A.; Wittenberg, J. B.; Ouellet, Y.; Rousseau, D. L.; Guertin, M. *Proc. Natl. Acad. Sci. U.S.A.* **1999**, *96*, 11223.
(4) Pathania, R.; Navani, N. K.; Gardner, A. M.; Gardner, P. R.; Dikshit, K. L. *Mol. Microbiol.* **2002**, *45*, 1303.
(5) MacMicking, J. D.; North, R. J.; LaCourse, R.; Mudgett, J. S.; Shah, S. K.; Nathan, C. F. *Proc. Natl. Acad. Sci. U.S.A.* **1997**, *94*, 5243.
(6) Shiloh, M. U.; Nathan, C. F. *Curr. Opin. Microbiol.* **2000**, *3*, 35.
(7) Moens, L.; Vanfleteren, J.; van de Peer, Y.; Peeters, K.; Kapp, O.; Czeluzniak, J.; Goodman, M.; Blaxter, M.; Vinogradov, S. *Mol. Biol. Evol.* **1996**, *13*, 324.
(8) Pesce, A.; Couture, M.; Dewilde, S.; Guertin, M.; Yamauchi, K.; Ascenzi, P.; Moens, L.; Bolognesi, M. *EMBO J.* **2000**, *19*, 2424.
(9) Milani, M.; Pesce, A.; Nardini, M.; Ouellet, H.; Ouellet, Y.; Dewilde, S.; Bocedi, A.; Ascenzi, P.; Guertin, M.; Moens, L.; Friedman, J. M.; Wittenberg, J. B.; Bolognesi, M. *J. Inorg. Biochem.* **2005**, *99*, 97.
(10) Milani, M.; Pesce, A.; Ouellet, Y.; Ascenzi, P.; Guertin, M.; Bolognesi, M. *EMBO J.* **2001**, *20*, 3902.
(11) Milani, M.; Pesce, A.; Ouellet, Y.; Dewilde, S.; Friedman, J. M.; Ascenzi, P.; Guertin, M.; Bolognesi, M. *J. Biol. Chem.* **2004**, *279*, 21520.
(12) Crespo, A.; Martí, M. A.; Kalko, S. G.; Morreale, A.; Orozco, M.; Gelpi, J. L.; Luque, F. J.; Estrin, D. A. *J. Am. Chem. Soc.* **2005**, *127*, 4433.
(13) Bidon-Chanal, A.; Martí, M. A.; Crespo, A.; Milani, M.; Orozco, M.; Bolognesi, M.; Luque, F. J.; Estrin, D. A. *Proteins* **2006**, *64*, 457.

10.1021/ja0689987 CCC: $37.00

is mediated by three main structural features. First, the tunnel system would have evolved to allow access of O_2 and NO ligands to the heme through distinct migration paths. Second, O_2 binding to the heme would facilitate access of NO by promoting opening of the tunnel long branch, where ligand diffusion is controlled by PheE15, which acts as a gate. Third, opening of PheE15 would be mediated by a subtle conformational change in the hydrogen-bonded network formed by TyrB10 and GlnE11, which act as a molecular switch.

Since residues TyrB10 and GlnE11 are crucial to facilitate opening of the tunnel gate upon O_2 binding to the heme, disruption of the molecular switch should lead to a substantial decrease in the biological activity. In this study we examine the structural and dynamical properties of the TyrB10→Phe and GlnE11→Ala mutants in order to investigate the reliability of the dual-path ligand-induced regulation mechanism mentioned above. In particular, the results provide a molecular basis to explain the dramatic decrease in NO consumption observed experimentally for the TyrB10→Phe mutant and predict a similar behavior for the GlnE11→Ala mutant.

Methods

MD simulations were performed from the crystal structure of the oxygenated form of the wild type (wt) trHbN (PDB entry 1IDR; monomer A at 1.9 Å resolution),[9] which was used to generate the starting structures of the TyrB10→Phe and GlnE11→Ala mutants. This procedure is supported by the close similarity observed between the structure of the wt protein and the recently reported X-ray crystallographic structures of the cyanide complexes TyrB10→Phe and GlnE11→Ala mutants (PDB entries 2GKM and 2GLN).[14] As noted in ref 14, which also reports the X-ray structures of the GlnE11→Val (2GKN) and TyrB10→Phe/GlnE11→Val (2GL3) mutants, the rmsd of the A chain in the different mutants and in the wt protein ranges from 0.23 to 0.41 Å, thus confirming that the mutations have little impact on the protein fold. Every mutated enzyme was immersed in a pre-equilibrated octahedral box of TIP3P[15] water molecules. The standard protonation state at physiological pH was assigned to the ionizable residues. The final system contains the mutated protein, around 8600 water molecules, and the added counterions, leading to a total of ~28 300 atoms. Simulations were performed in the NPT ensemble.[16] The system was simulated employing periodic boundary conditions and Ewald sums (grid spacing of 1 Å) for treating long-range electrostatic interactions.[17] All simulations were performed with the parmm99 force field[18] using Amber8.[19] For the oxygenated heme group RESP charges[20] and HF/6-31G(d) wave functions were used according to the Amber standard protocol. The initial system was minimized and equilibrated using the multistep protocol reported for the wt protein.[12] Then, 100 ns MD simulation was run for the two mutants. As a reference control, a 50 ns MD simulation was performed for the oxygenated form of the wt trHbN using the same protocol.

The role of PheE15 as gate residue in the tunnel long branch was examined by computing classical molecular interaction potential (CMIP)[21] energy isocontour profiles using a rigid NO probe characterized by RESP atomic charges and van der Waals parameters defined for equivalent atoms in the Amber force field (see Supporting Information). To this end, the protein was placed in a grid (spacing of 0.35 Å) centered at the active site (heme group) and large enough to cover the whole channel.

The dynamical behavior of the proteins was investigated by determining the essential dynamics through principal component analysis,[22] conducted considering the backbone C_α atoms. Indeed, residues 1−15, which form the short N-terminal isolated helix, were excluded from the analysis since the high flexibility of this region might mask the essential movements in the trHbN fold. The similarity between essential motions for the wt protein and the mutants was quantified using the similarity index defined in eq 1, which takes into account not only the nature of the essential movements but also their contribution to the structural variance of the protein.[23]

$$\xi_{AB} = \frac{2\sum_{i=1}^{i=z}\sum_{j=1}^{j=z}\left\{(\nu_i^A\nu_j^B)\frac{\exp\left[-\frac{(\Delta x)^2}{\lambda_i^A}-\frac{(\Delta x)^2}{\lambda_j^B}\right]}{\sum_{i=1}^{i=z}\exp\left[-\frac{(\Delta x)^2}{\lambda_i^A}\right]\sum_{j=1}^{j=z}\exp\left[-\frac{(\Delta x)^2}{\lambda_i^B}\right]}\right\}}{\sum_{i=1}^{i=z}\left\{\frac{\exp\left[-2\frac{(\Delta x)^2}{\lambda_i^A}\right]}{\left(\sum_{i=1}^{i=z}\exp\left[-\frac{(\Delta x)^2}{\lambda_i^A}\right]\right)^2}\right\}^2+\sum_{j=1}^{j=z}\left\{\frac{\exp\left[-2\frac{(\Delta x)^2}{\lambda_i^B}\right]}{\left(\sum_{j=1}^{j=z}\exp\left[-\frac{(\Delta x)^2}{\lambda_i^B}\right]\right)^2}\right\}^2} \quad (1)$$

where λ_i is the eigenvalue associated with a given eigenvector i whose unitary vector is ν_i, and the sum is extended to a given set (z) of relevant eigenvectors.

Results and Discussion

To the best of our knowledge, there is no experimental evidence for the viability of the GlnE11→Ala mutant to accomplish the O_2/NO chemistry. However, Guertin and co-workers have shown that the TyrB10→Phe mutation leads to a drastic reduction in the NO-consuming activity compared to wt trHbN, since the NO consumption rate was similar to that measured in buffer solution,[2] which demonstrates that TyrB10 is essential for NO detoxification by trHbN. The decrease in the biological activity cannot be attributed to the inability of the TyrB10→Phe mutant to bind O_2. In fact, resonance Raman spectra confirm that it binds O_2, as noted in the Fe−O_2 stretching mode detected at 570 cm^{-1}.[24] Compared to the wt protein, however, the frequency of the Fe−O_2 stretching mode is shifted by around 10 cm^{-1} due to the loss of the hydrogen bond formed between the bound O_2 and the hydroxyl group of TyrB10 in trHbN.

On the basis of the preceding experimental evidence, one might be tempted to attribute the reduced activity of the TyrB10→Phe mutant to a loss in the catalytic efficiency of the

(14) Ouellet, Y.; Milani, M.; Couture, M.; Bolognesi, M.; Guertin, M. *Biochemistry* **2006**, *45*, 8770.
(15) Jorgensen, W. L.; Chandrasekhar, J.; Madura, J. D.; Impey, R. W.; Klein, M. L. *J. Chem. Phys.* **1983**, *79*, 926.
(16) Berendsen, H. J. C.; Postma, J. P. M.; van Gunsteren, W. F.; Di Nola, A.; Haak, J. R. *J. Chem. Phys.* **1984**, *81*, 3684.
(17) Darden, T. A.; York, D.; Pedersen, L. *J. Chem. Phys.* **1993**, *98*, 10089.
(18) Wang, J.; Cieplak, P.; Kollman, P. A. *J. Comput. Chem.* **2000**, *21*, 1049.
(19) Pearlman, D. A.; Case, D. A.; Caldwell, J. W.; Ross, W. R.; Cheatham, T. E., III; DeBolt, S.; Ferguson, D.; Seibel, G.; Kollman, P. *Comp. Phys. Commun.* **1995**, *91*, 1.
(20) Bayly, C. I.; Cieplak, P.; Cornell, W.; Kollman, P. A. *J. Phys. Chem.* **1993**, *97*, 10269.
(21) Gelpí, J. L.; Kalko, S.; de la Cruz, X.; Barril, X.; Cirera, J.; Luque, F. J.; Orozco, M. *Proteins* **2001**, *45*, 428.
(22) Amadei, A.; Linssen, A. B. M.; Berendsen, H. J. C. *Proteins* **1993**, *17*, 412.
(23) Meyer, T.; Ferrer-Costa, C.; Pérez, A.; Rueda, M.; Bidon-Chanal, A.; Luque, F. J.; Laughton, C. A.; Orozco, M. *J. Chem. Theory Comput.* **2006**, *1*, 251.
(24) Yeh, S. R.; Couture, M.; Ouellet, Y.; Guertin, M.; Rousseau, D. L. *J. Biol. Chem.* **2000**, *275*, 1679.

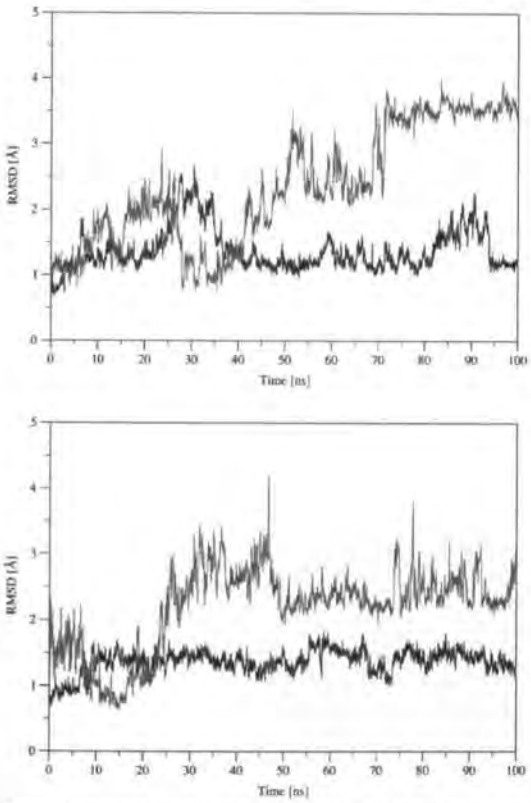

Figure 1. Positional root-mean-square deviation (Å) of the backbone atoms in the N-terminal (residues 1−15; gray) and core (residues 16−127; black) regions of the oxygenated forms of the TyrB10→Phe (top) and GlnE11→Ala (bottom) mutants determined relative to the X-ray structure of the wt protein (PDB entry 1IDR).

protein in the conversion of NO to nitrate anion. However, our previous studies of the chemical reaction in the wt protein and in the TyrB10→Phe mutant suggest that the replacement of Tyr by Phe does not exert a significant influence on the energetics of the reaction.[11] Then, it is unclear why the TyrB10→Phe mutant, which can bind O_2 and can accomplish the NO chemical conversion to nitrate anion, has an extremely low efficiency. It can be speculated that the low NO consumption of the TyrB10→Phe mutant stems from the disruption of the molecular mechanism that assists ligand diffusion to the O_2-bound heme, which presumably involves the TyrB10−GlnE11 pair. Analogously, it can be hypothesized that mutation of GlnE11 to Ala should also disrupt such a ligand migration mechanism.

MD Simulations of the oxy TyrB10→Phe and GlnE11→Ala Mutants. To explore the reliability of the preceding hypothesis, 100 ns MD simulations of the oxygenated form of the TyrB10→Phe and GlnE11→Ala mutants were performed. In the two cases stable trajectories, without large structural fluctuations, were obtained (rmsd for core residues (16−127) around 1.5 Å). The only noticeable displacements were found in the pre-helix A in the N-terminal region (rmsd for residues 1−15 in the range 2−3.5 Å; see Figure 1). Note that the same behavior was obtained in previous simulations of wt trHbN·O_2.[11]

Our previous studies[11,12] pointed out that PheE15 acts as the gate of the tunnel long branch in the wt trHbN·O_2, thus

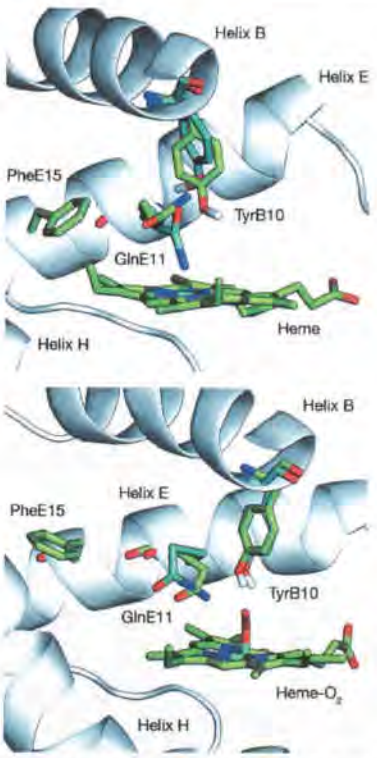

Figure 2. Hydrogen-bonded interactions between TyrB10 and GlnE11 in trHbN and trHbN·O_2 forms. (Top) In the deoxygenated form the side chain of GlnE11 adopts an *all-trans* conformation (average torsions around C_α−C_β, C_β−C_γ, and C_γ−C_δ dihedrals of 40.2°, 167.1°, and 93.7°), and the relative orientation of the amide group of GlnE11 and the hydroxyl group of TyrB10 fluctuates along the trajectory, so that the GlnE11 amide acts as either donor (NH_2) or acceptor (C=O) in the hydrogen bond formed with TyrB10. (Bottom) In trHbN·O_2 the heme-bound O_2 is hydrogen-bonded to the TyrB10 OH group, which forces the GlnE11 amide to act only as hydrogen-bond donor. To this end, the side chain of GlnE11 populates two *staggered* conformations (average torsional angles around C_α−C_β, C_β−C_γ, and C_γ−C_δ bonds of 45.0°, −74.8°, −99.3° and −50.2°, 67.2°, 48.5°, respectively). The conformational change of PheE15 leading to opening/closing of the tunnel long branch is illustrated by comparison of the structures (top: closed state; bottom: open state).

supporting the original proposal about the gating role of this residue made by Milani et al.[10] In fact, PheE15 populates two main conformations characterized by average C_α−C_β torsional angles of about +40° and −50° (see Figure 2; those dihedral angles, which are defined relative to the H_α−C_α−C_β−C_γ torsion, would be around −80° and 170° when the N−C_α−C_β−C_γ torsion is used). In the former, the phenyl ring protrudes into the tunnel branch, thus preventing access of incoming ligands to the heme distal cavity (*closed* state), but in the latter the benzene ring is roughly parallel to the axis of the tunnel, which enables the transit of diatomic ligands (*open* state). In fact, these conformational states are reflected in two distinct conformations observed for PheE15 in the X-ray crystallographic structure of the wt protein (unit A in the PDB entry 1IDR, where the N−C_α−C_β−C_γ torsional angle adopts values close to −91° and −155°, respectively, for the closed and open states).

The analysis of the 50 ns MD simulation of the wt trHbN·O_2 supported the ability of PheE15 to populate the two conforma-

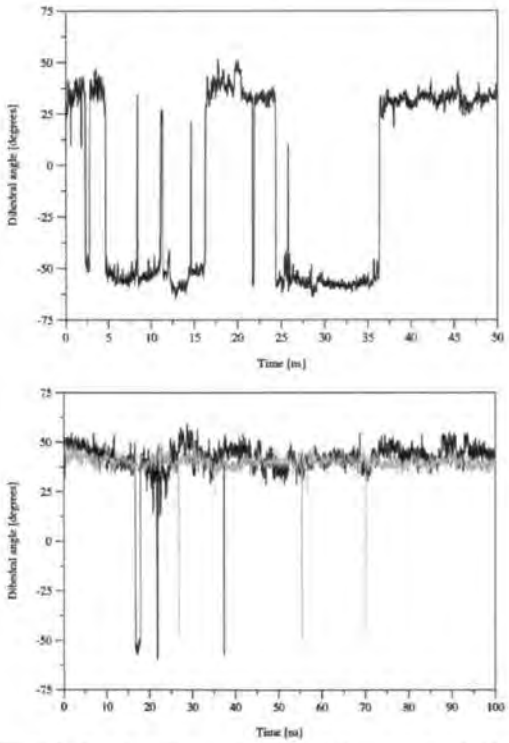

Figure 3. Time-dependence conformation of the torsional angle (deg) around the $C_\alpha-C_\beta$ bond of PheE15 along trajectories sampled for the oxygenated form of (top) the wt trHbN and (bottom) their TyrB10→Phe (black) and GlnE11→Ala (gray) mutants. The torsional angle $H_\alpha-C_\alpha-C_\beta-C_\gamma$ is used to follow the conformational fluctuations of PheE15. Note the different length of the MD simulations for the wt protein (50 ns) and the mutants (100 ns).

tional states. As noted in Figure 3, the trajectory reveals the occurrence of several transitions between *open* and *closed* states, the population of the *open* state being close to 53% (Figure 3). In fact, the analysis allowed us to identify the migration of a water molecule through the tunnel long branch, which transiently remained in the distal side of the heme pocket before being released to the bulk solvent. In contrast, the PheE15 conformational behavior observed for TyrB10→Phe and GlnE11→Ala mutants is drastically different. Thus, not only was a lower number of transitions between *open* and *closed* states detected (Figure 3), but the population of the *open* state was found to be negligible. In fact, PheE15 adopted a conformation defined by an average $C_\alpha-C_\beta$ ($H_\alpha-C_\alpha-C_\beta-C_\gamma$) torsional angle of about $+40°$ in the two mutants, which would impede migration of NO through the long channel (no water molecule was found to migrate along the tunnel even though the length of the MD simulations of the mutants was twice that used for the wt protein).

The blockade of the tunnel in the *closed* conformation of the PheE15 gate for the two mutants was supported by the CMIP isocontour plots for the interaction of a NO probe with the wt protein and their mutants. For a series of snapshots taken regularly along the trajectory, a favorable interaction energy region was identified in the distal side of the heme group (see Figure 4). Such a region protudes toward the intersection of

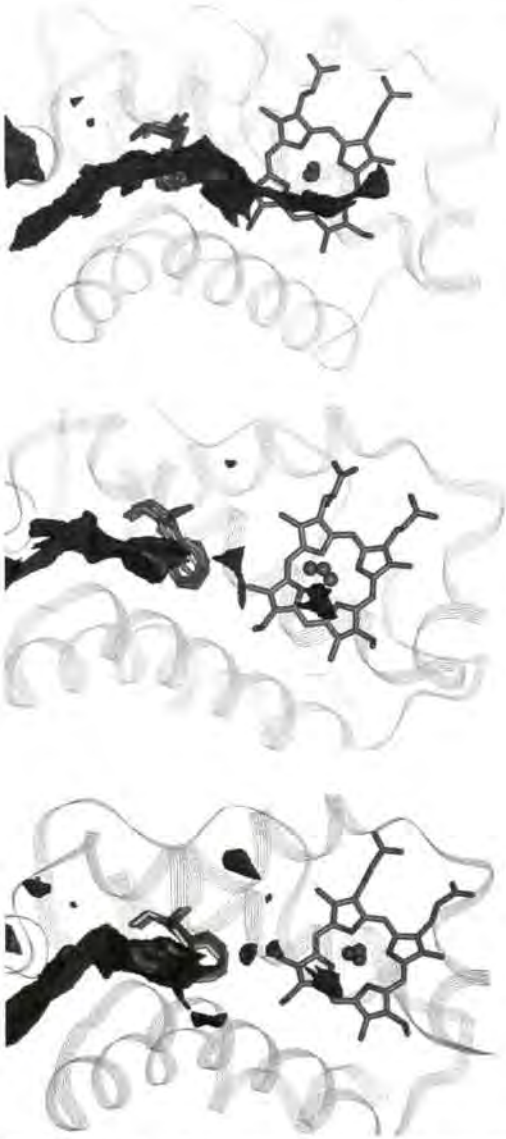

Figure 4. Classical molecular interaction potential isocontour plots determined for the interaction with a NO probe particle for the oxygenated form of the wt trHbN (top) and their TyrB10→Phe (middle) and GlnE11→Ala (bottom) mutants. The gate residue PheE15 obtained from five representative snapshots is also shown. The spheres stand for the heme iron and the bonded O_2 molecule.

the two tunnel branches, thus occupying a space in the cavity that coincides with one of the secondary Xe binding sites recently identified by Bolognesi's group upon treatment of trHbN crystals under Xe pressure.[10] For the mutants, however, the energy isocontour along the tunnel long branch is broken due to the presence of the PheE15 benzene ring (Figure 4, middle and bottom). In this case, the favorable interaction energy located near the benzene ring, but in the outer part of the tunnel, agrees with the main Xe binding site identified by Bolognesi et al.[10] In constrast, the CMIP isocontour determined for the

wt trHbN·O_2 (Figure 4, top) clearly delineates an energetically favorable path leading from the outer space to the heme cavity.

Essential Dynamics of the TyrB10→Phe and GlnE11→Ala Mutants. The preceding findings point out that the conformational flexibility of PheE15 is severely restricted in the oxy form of both TyrB10→Phe and GlnE11→Ala mutants. In trHbN·O_2 the transition between *open* and *closed* states of PheE15 is regulated by a salt bridge between Arg10 (in the N-terminal region) and Glu70 (in the EF interhelical region). This salt bridge is formed upon folding of the short A helix onto the EF hinge, which increases the friction between helices B and E, thus inhibiting opening of the tunnel long branch. The Arg10−Glu70 salt bridge is not observed in the X-ray crystallographic structure of the wt protein, even though this might simply stem from crystal packing. On the other hand, the physiological role of the pre-A region in trHbN remains unknown, thus making it necessary to be cautious in attributing a functional role to such an interaction. In any case, a similar folding effect might also justify the conformational restriction of Phe15 observed in the two mutants. However, the analysis of the whole trajectory revealed that this is not the case, since the salt bridge is not formed (the distance between Arg10 and Glu70 was in general larger than 20 Å; see Supporting Information). These findings, therefore, suggest that the reduced conformational flexibility of PheE15 must stem from the intrinsic inability of the mutant to induce the opening of the channel upon O_2 binding.

Our previous studies for wt trHbN·O_2 suggested that O_2 binding to the heme introduces a major change in the protein essential dynamics, which favors opening of the tunnel long branch by enhancing the relative displacement of helices B and E.[12] The essential dynamics analysis of the oxygenated forms of TyrB10→Phe and GlnE11→Ala mutants revealed a drastic difference in the natural movements of the protein backbone compared to the wt trHbN·O_2. Thus, the main contributions to the backbone structural fluctuations stems from helices G and H and the loop F in the TyrB10→Phe mutant (Figure 5, top) and from helices C, G, and H in the GlnE11→Ala mutant (Figure 5, bottom).

The difference in the main structural fluctuations of trHbN·O_2 and the two mutants can be measured by means of the similarity index ξ_{AB} (see eq 1 in Methods),[24] which takes into account not only the nature of the essential movements but also their contribution to the structural variance of the protein. Thus, for the 10 most relevant essential motions of the backbone skeleton in the core region of wt trHbN·O_2 and TyrB10→Phe·O_2, which account for around 70% of the structural variance, the similarity index only amounts to 0.48, which is clearly smaller than the self-similarities obtained for the wt protein and the TyrB10→Phe mutant (0.74 and 0.86, respectively; see Supporting Information). Interestingly, when such an analysis is performed separately for the pair of helices G−H, the similarity index is 0.45, whereas it only amounts to 0.26 for the pair of helices B−E. This indicates that the dynamical behavior of these two helices is highly different in wt trHbN·O_2 and the TyrB10→Phe·O_2 mutant.

Similar findings are obtained from the comparison of the essential dynamics of wt trHbN·O_2 and the GlnE11→Ala·O_2 mutant. In this case, the global similarity index (0.37, which compares with self-similarities of 0.74 and 0.89 for the wt and the GlnE11→Ala mutant; see Supporting Information) is larger than that obtained separately for helices B−E (0.30), but lower than that determined for the motion of helices G−H (0.52). Overall, these findings reveal the different nature of the motions in the wt protein and in the two mutants and particularly the disappearance of the relative displacement observed between helices B and E in wt trHbN·O_2, which is lost in the two mutants.

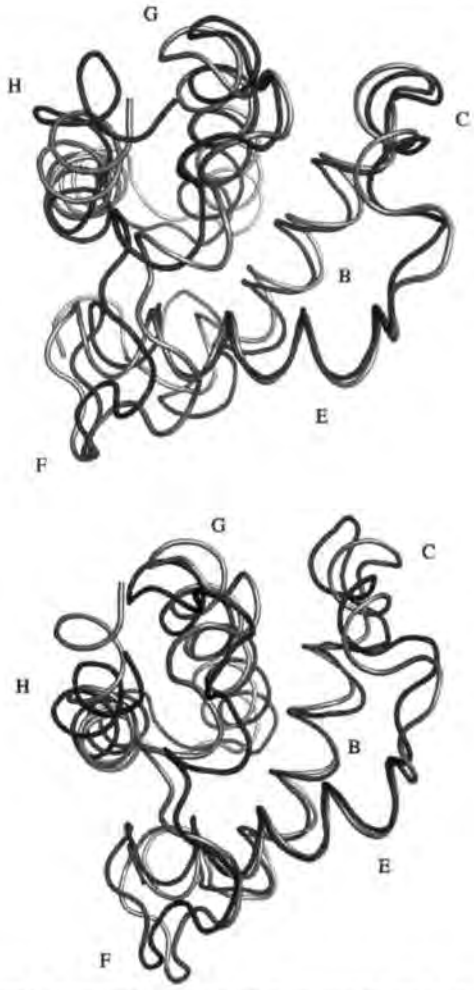

Figure 5. Representation of the backbone structural fluctuations due to essential dynamics motions in the oxygenated forms of TyrB10→Phe (top) and GlnE11→Ala (bottom) mutants. Structures in black and gray illustrate the regions in the peptide skeleton mostly affected by the essential movements (the labels denote the structural elements in trHbN).

Dynamical Behavior of the TyrB10(Phe) and GlnE11(Ala) Residues. The alteration in the essential dynamics of the protein backbone induced in trHbN upon O_2 binding to the heme is assisted by the hydrogen-bonded TyrB10−GlnE11 pair, which acts as a molecular switch.[12] In the deoxygenated trHbN, GlnE11 adopts an extended *all-trans* conformation, allowing the terminal amido group to be hydrogen-bonded to the hydroxyl group of TyrB10. In fact, there is a dynamical fluctuation between (TyrB10)O−H···O=C(GlnE11) and (TyrB10)O···H−N(GlnE11) hydrogen bonds, so that the hydroxyl group of TyrB10 acts as both hydrogen-bond donor and acceptor (Figure 2, top).

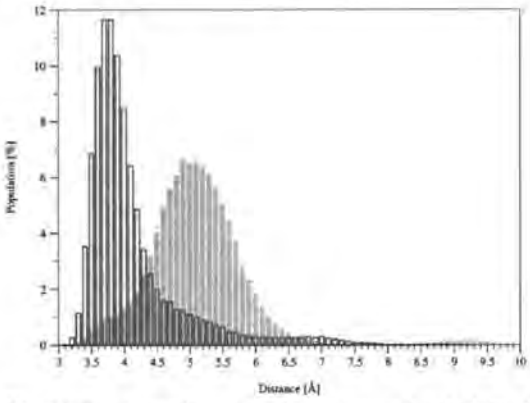

Figure 6. Distribution of interesidue distances between the side chains of GlnE11 and PheE15 in the oxygenated forms of the wt protein (white bars) and its TyrB10→Phe mutant (gray bars).

In contrast, since the heme-coordinated O_2 fixes TyrB10 through a hydrogen bond in trHbN·O_2, the TyrB10 hydroxyl group acts exclusively as hydrogen-bond acceptor for the amide NH_2 group of GlnE11, whose side chain populates two *staggered* conformations (Figure 2, bottom).

The transition between extended and staggered conformations of GlnE11 is associated with a notable variation in the separation between the side chains of GlnE11 and PheE15 (see Figure 6). The distance from the side chain of GlnE11 to the PheE15 benzene ring in trHbN·O_2 is, on average, close to 3.9 Å, but the contacts between the side chains of GlnE11 and PheE15 can be as short as 3.1 Å (Figure 6). In fact, there is a sizable fraction of structures (around 45%) having a separation contact below 3.9 Å (i.e., the van der Waals contact between $-CH_2-$ and >CH groups according to Pauling's radii). In contrast, in the deoxygenated form of trHbN, where GlnE11 adopts an extended conformation (see above), the average distance between GlnE11 and PheE15 is enlarged by around 1.5 Å. Therefore, it can be concluded that the alteration of the hydrogen-bonded interaction in the TyrB10−GlnE11 pair induced upon O_2 binding to the heme triggers a compression mechanism onto the benzene ring of PheE15, which is proposed to favor opening of the gate in the tunnel long branch.

The molecular switch formed by TyrB10−GlnE11 is greatly affected by the two mutations examined here. In the TyrB10→Phe mutant, GlnE11 forms a hydrogen-bond interaction with the heme-bound O_2. Such an interaction is maintained along the whole trajectory (average N···O distance of 3.0 Å) and forces GlnE11 to adopt an *all-trans* conformation. Inspection of the X-ray crystallographic structure of the cyanide complex of the TyrB10→Phe mutant[14] shows that GlnE11 also forms a hydrogen bond with the cyanide ligand. However, in the X-ray structure GlnE11 adopts a *staggered* conformation. This conformational difference can be mainly attributed to the different tilt of the two ligands, as noted in the angles formed by the diatomic molecules and the heme iron (values averaged for units A and B of 118.3° (Fe···O_2) and 168.3° (Fe···CN) in 1IDR and 2GKM, respectively), though it can also be affected, at least in part, by the steric hindrance due to PheB10, since the shortest contact between the carbon atoms in the benzene ring and the cyanide unit is 3.2 Å in the X-ray structure, which is around 1 Å lower than the average separation found in the MD simulation.

The direct interaction formed between GlnE11 and heme-bound O_2 makes the separation of the side chains of GlnE11 and PheE15 amount, on average, to 5.2 Å, which is notably larger than that found for the oxygenated wt protein (Figure 6). As a result, the conformational compression mechanism operative in wt trHbN·O_2 is completely lost in the TyrB10→Phe mutant, as noted in the fact that the population of structures with a separation between the side chains of GlnE11 and PheE15 lower than 3.9 Å is less than 4%. This effect, combined with the increased friction between helices B and E, should reduce the opening of the PheE15 gate.

In the case of the GlnE11→Ala mutant, where TyrB10 remains hydrogen-bonded to the heme-bound O_2 molecule (average O···O distance of 2.8 Å), the reduction in size and hydrogen-bond capability that accompanies the replacement of GlnE11 by Ala breaks the molecular switch that triggers opening of the PheE15 gate.

Functional Implications. The reduced catalytic activity observed for the TyrB10→Phe mutant can be ascribed to the inability of the PheB10−GlnE11 pair to trigger the local conformational change leading to (i) an increase in the local compression mechanism exerted by GlnE11 onto the side chain of PheE15 and (ii) the change in the global essential dynamics of the protein, which should favor the relative displacement of helices B and E. The ligand-induced regulation of the global structural plasticity of the protein is supported by experimental data indicating that NO-binding to the ferric heme group of the trHbN promotes a large-scale conformational change in the protein that propagates through the pre-F helix to the E and B helices.[25] Further support comes from the experimentally observed dependence of the kinetics of ligand diffusion in trHbN on the viscosity of the aqueous environment,[26] which suggests that the dynamical behavior of the protein is directly implicated in the regulation of ligand migration. In fact, the involvement of different conformational states in the dynamical modulation of ligand migration is also indicated by the different kinetic pattern observed in CO recombination assays in trHbN and its TyrB10→Phe mutant.[27]

Whereas the inability of the TyrB10→Phe mutant to capture NO can be ascribed to the direct hydrogen-bond interaction formed between GlnE11 and heme-bound O_2, which impedes the occurrence of the *local* conformational changes detected in the TyrB10−GlnE11 pair for the wt protein, our results also indicate that the oxygenated form of the GlnE11→Ala mutant should be inactive against NO consumption. In this case, despite the larger size of the heme pocket arising from the replacement of GlnE11 by Ala, the lack of NO-consumption activity should be attributed to the inability of Ala to compress *locally* the gate (PheE15) of the tunnel long branch and to promote the *global* change in the essential dynamics leading to motion of helices B and E.

On the basis of the preceding results, it can be concluded that the TyrB10−GlnE11 pair, besides their contribution to the high oxygen affinity of the protein (O_2-binding affinity to ferrous

(25) Mukai, M.; Ouellet, Y.; Guertin, M.; Yeh, S.-R. *Biochemistry* **2004**, *43*, 2764.
(26) Dantsker, D.; Samuni, U.; Ouellet, Y.; Wittenberg, B. A.; Wittenberg, J. B.; Milani, M.; Bolognesi, M.; Guertin, M.; Friedman, J. M. *J. Biol. Chem.* **2004**, *279*, 38844.
(27) Samuni, U.; Dantsker, D.; Ray, A.; Wittenberg, J. B.; Wittenberg, B. A.; Dewilde, S.; Moens, L.; Ouellet, Y.; Guertin, M.; Friedman, J. M. *J. Biol. Chem.* **2003**, *278*, 27241.

trHbN of 8.0×10^{-9} with a k_{off} of 0.2 s^{-1})[8] and to the correct positioning of the incoming NO ligand in the O_2-bound heme cavity, acts as a molecular switch that regulates opening of the tunnel long branch and facilitates ligand (NO) migration to the O_2-bound heme. In fact, since the NO conversion to nitrate by trHbN·O_2 occurs at a rate faster than O_2 binding to the deoxy protein (the bimolecular rate constants for these two processes are 745 and 25 μM^{-1} s^{-1}, respectively),[2,8] this role might be considered to be the most critical factor to warrant survival of *M. tuberculosis* under stress conditions.

Finally, in line with previous studies carried out to identify the factors that modulate ligand migration in heme proteins,[28-32] these results point out that the dual-path ligand-induced dynamical regulation mechanism in trHbN relies on a small number of key residues. This finding opens challenging questions relative to the involvement of similar ligand diffusion mechanisms in other truncated hemoglobins, whose activity might be regulated by motional fluctuations of certain structural domains[33] or even in the recently discovered neuroglobin and cytoglobin.[34-36] A particularly challenging case is trHbN of *M. smegmatis*, which has nearly 70% sequence similarity with trHbN of *M. tuberculosis* and retains most of the structural features crucial to attain the trHb fold.[37] In fact, PheE15, TyrB10, and GlnE11 are retained, and the protein binds oxygen reversibly with high affinity. Nevertheless, the NO-metabolizing activity of *M. smegmatis* trHbN is significantly lower than that of the *M. tuberculosis* protein.[37] It is not clear whether this functional difference might come from the lack of the highly polar and charged N-terminal sequence motif that constitutes the pre-A region in *M. tuberculosis* trHbN. Present results allow us to speculate that such a functional difference might also stem from an alteration in the dynamical behavior of the protein skeleton, which might affect the regulation mechanism that facilitates NO diffusion through the protein matrix. Clearly, untangling the structural basis of the interplay between ligand binding, protein dynamics, and ligand migration will shed light on the emerging field of multiligand chemistry in heme proteins.

Acknowledgment. We are grateful to Prof. M. Orozco for valuable discussions and suggestions. This work was partially supported by grants from Universidad de Buenos Aires (grant X038), ANPCYT (grant 25667), and the Spanish Ministerio de Educación y Ciencia (grant CTQ2005-08797-C02-01/BQU). Calculations were performed in the MareNostrum supercomputer at the Barcelona Supercomputing Center. Contribution dedicated to the memory of Prof. L. Pueyo.

Supporting Information Available: Parameters of the NO rigid probe used in CMIP computations. Plots for the probability distribution of the $C_\alpha-C_\beta$ dihedral angle of PheE15, and time dependence of the distance between Arg10 and Glu70. Tables reporting similarity indexes for the most relevant motions of the backbone and selected helices. This material is available free of charge via the Internet at http://pubs.acs.org.

JA0689987

(28) Schotte, F.; Lim, M.; Jackson, T. A.; Smirnov, A. V.; Soman, J.; Olson, J. S.; Phillips, G. N., Jr.; Wulff, M.; Anfinrud, P. A. *Science* **2003**, *300*, 1944.
(29) Chu, K.; Vojtchovský, J.; McMahon, B. H.; Sweet, R. M.; Berendzen, J.; Schlichting, I. *Nature* **2000**, *403*, 921.
(30) Case, D. A.; Karplus, M. *J. Mol. Biol.* **1979**, *132*, 343.
(31) Bossa, C.; Anselmi, M.; Roccatano, D.; Amadei, A.; Vallone, B.; Brunori, M.; Di Nola, A. *Biophys. J.* **2004**, *86*, 3855.
(32) Nutt, D. R.; Meuwly, M. *Proc. Natl. Acad. Sci. U.S.A.* **2004**, *101*, 5998.
(33) Marsella, L. *Proteins* **2006**, *62*, 173.
(34) Ascenzi, P.; Salvati, L.; Brunori, M. *FEBS Lett.* **2001**, *501*, 103.
(35) Eich, R. F.; Li, T.; Lemon, D. D.; Doherty, D. H.; Curry, S. R.; Aitken, J. F.; Mathews, A. J.; Johnson, K. A.; Smith, R. D.; Phillips, G. N., Jr.; Olson, J. S. *Biochemistry* **1996**, *35*, 6976.
(36) Brunori, M.; Giuffrè, A.; Nienhaus, K.; Nienhaus, G. U.; Scandurra, F. M.; Vallone, B. *Proc. Natl. Acad. Sci. U.S.A.* **2005**, *102*, 8483.
(37) Lama, A.; Pawaria, S.; Dikshit, K. L. *FEBS Lett.* **2006**, *580*, 4031.

Dynamical Regulation of Ligand Migration by a Gate-Opening Molecular Switch in Truncated Hemoglobin-N from *Mycobacterium tuberculosis*

Axel Bidon-Chanal,[1] Marcelo A. Martí,[2] Darío A. Estrin,[2] and F. Javier Luque[1]

1 Departament de Fisicoquímica, Facultat de Farmàcia, Universitat de Barcelona, Av. Diagonal 643, 08028, Barcelona, Spain.

2 Departamento de Química Inorgánica,Analítica y Química Física/ INQUIMAE-CONICET, Facultad de Ciencias Exactas y Naturales, Universidad de Buenos Aires, Ciudad Universitaria, Pabellón 2, Buenos Aires, C1428EHA, Argentina.

Supporting Information

Parameters of the NO rigid probe used in CMIP computations

Atomic charges are in units of electron and van der Waals hardness (kcal/mol) and radii (Å) are taken from the AMBER force field.

Atom	q	ε	r^*
N	**0.043**	**0.17**	**1.824**
O	**-0.043**	**0.21**	**1.661**

Table S1. Global similarity index determined by comparison of the most relevant essential motions of the peptide skeleton in the oxygenated form of wild type (wt) trHbN and its TyrB10→Phe and GlnE11→Ala mutants.

ξ_{AB}	wt	TyrB10→Phe	GlnE11→Ala
wt	0.74	0.48	0.37
TyrB10→Phe		0.86	0.42
GlnE11→Ala			0.89

Values determined by considering the 10 most relevant essential movements, which encompass 60-70% of the structural variance in the wild type protein and the two mutants.

Table S2. Similarity index determined by comparison of the most relevant essential motions of the backbone in helices B and E, and helices G and H in the oxygenated form of wild type (wt) trHbN and its TyrB10→Phe and GlnE11→Ala mutants.

ξ_{AB}	TyrB10→Phe	GlnE11→Ala
Helices B and E		
wt	0.26	0.31
TyrB10→Phe		0.29
Helices G and H		
wt	0.45	0.52
TyrB10→Phe		0.44

Values determined by considering the 10 most relevant essential movements, which encompass 60-70% of the structural variance in the wild type protein and the two mutants.

Figure S1. Normalized probability density distribution of the C_α-C_β (H_α-C_α-C_β-C_γ) dihedral angle of PheE15 along the trajectories for the oxygenated form of (*top*) the wild type trHbN and their TyrB10→Phe (*middle*) and GlnE11→Ala (*bottom*) mutants.

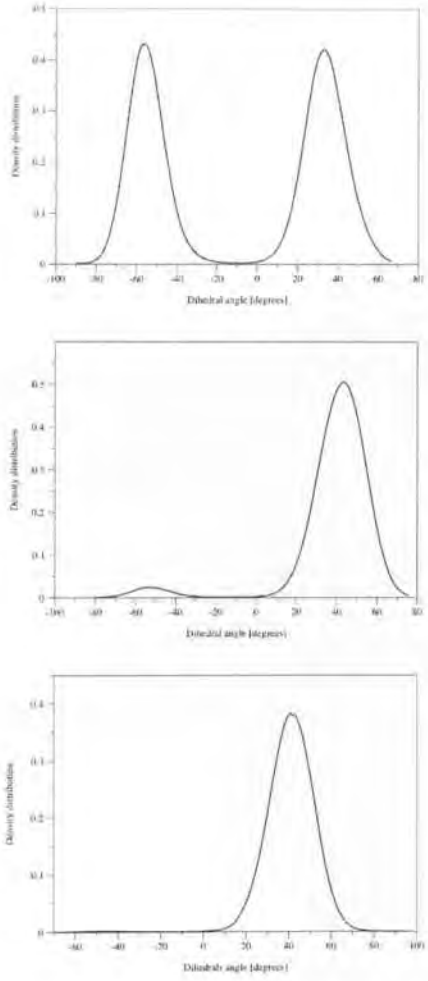

Figure S2. Time dependence of the distance between carbon atoms in the guanidinium and carboxy groups of Arg10 and Glu70 in the 100 ns molecular dynamics simulations of TyrB10→Phe (black) and GlnE11→Ala (gray) mutants.

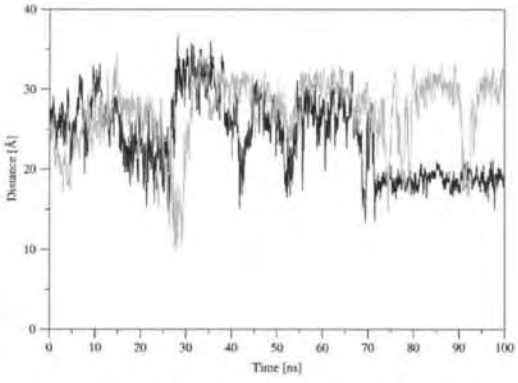

4.2.3 Mechanism of Product Release in NO detoxification from *Mycobacterium tuberculosis* Truncated Hemoglobin N

Marcelo A. Martí, **Axel Bidon-Chanal**, Alejandro Crespo, S. Yeh, V. Guallar, F. Javier Luque and Darío A. Estrin

J. Am. Chem. Soc., published online as ASAP article, january 2008, doi: 10.1021/ja076853+.

J|A|C|S
ARTICLES
Published on Web 01/12/2008

Mechanism of Product Release in NO Detoxification from *Mycobacterium tuberculosis* Truncated Hemoglobin N

Marcelo A. Martí,[†] Axel Bidon-Chanal,[‡] Alejandro Crespo,[†] Syun-Ru Yeh,[§] Victor Guallar,*[,∥] F. Javier Luque,*[,‡] and Darío A. Estrin*[,†]

Departamento de Química Inorgánica,Analítica y Química Física/INQUIMAE-CONICET, Facultad de Ciencias Exactas y Naturales, Universidad de Buenos Aires, Ciudad Universitaria, Pabellón 2, Buenos Aires, C1428EHA, Argentina, Departament de Fisicoquímica and Institut de Biomedicina (IBUB), Facultat de Farmàcia, Universitat de Barcelona, Av. Diagonal 643, 08028, Barcelona, Spain, Department of Physiology and Biophysics, Albert Einstein College of Medicine of Yeshiva University, Bronx, New York 10461, and ICREA, Computacional Biology Program, Barcelona Supercomputing Center, Edificio Nexos II, Barcelona 08028, Spain

Received September 10, 2007; E-mail: dario@qi.fcen.uba.ar; fjluque@ub.edu; victor.guallar@bsc.es

Abstract: The capability of *Mycobacterium tuberculosis* to rest in latency in the infected organism appears to be related to the disposal of detoxification mechanisms, which converts the nitric oxide (NO) produced by macrophages during the initial growth infection stage into a nitrate anion. Such a reaction appears to be associated with the truncated hemoglobin N (trHbN). Even though previous experimental and theoretical studies have examined the pathways used by NO and O_2 to access the heme cavity, the eggression pathway of the nitrate anion is still a challenging question. In this work we present results obtained by means of classical and quantum chemistry simulations that show that trHbN is able to release rapidly the nitrate anion using an eggression pathway other than those used for the entry of both O_2 and NO and that its release is promoted by hydration of the heme cavity. These results provide a detailed understanding of the molecular basis of the NO detoxification mechanism used by trHbN to guarantee an efficient NO detoxification and thus warrant survival of the microorganism under stress conditions.

Introduction

About one-third of the human population is infected by *Mycobacterium tuberculosis*.[1] During the initial growth infection stage, nitric oxide (NO) produced by macrophages contributes to restricting the bacteria in latency.[2,3] However, NO detoxification mechanisms have evolved in several pathogenic microorganisms to reduce the potential damage produced by the nitrosative stress. In *M. tuberculosis* such a mechanism appears to consist of the oxidation of NO with heme-bound O_2 to yield the harmless nitrate ion (eq 1),[4-6] a reaction associated with the truncated hemoglobin N (trHbN).

$$Fe(II)O_2 + NO \rightarrow Fe(III) + NO_3^- \qquad (1)$$

The trHbN pertains to a distinct group within the globin superfamily[7] and folds following a 2-on-2 helical sandwich motif instead of the 3-on-3 one of the classical globin fold.[8] The proximal HisF8 heme-linked residue is conserved in both Hb and trHb families, but a distal tyrosine at position B10, which contributes to modulating the oxygen affinity, is found in almost all the trHb family members sequenced to date.[9] Another relevant feature of trHbN from *M. tuberculosis* is that it displays a structurally conserved apolar tunnel system that connects the heme pocket with the protein surface, which consists of two perpendicular branches of about 8 and 20 Å in length, respectively.[10,11]

Experimental studies demonstrated that the NO-dioxygenase activity in trHbN is limited by the rate of ligand diffusion to the heme cavity,[4,5] which stimulated a variety of studies to identify the role of the tunnel in ligand migration. Previous studies suggested that the protein matrix tunnel follows a ligand-induced dynamical regulation mechanism,[12-14] where (i) O_2 and NO would access the heme cavity through the short and long

[†] Universidad de Buenos Aires.
[‡] Universitat de Barcelona.
[§] Albert Einstein College of Medicine of Yeshiva University.
[∥] Barcelona Supercomputing Center.

(1) Bloom, B. R. *Tuberculosis: Pathogenesis, Protection and Control*; ASM Press: Washington, DC, 1994.
(2) MacMicking, J. D.; North, R. J.; LaCourse, R.; Mudgett, J. S.; Shah, S. K.; Nathan, C. F. *Proc. Natl. Acad. Sci. U.S.A.* **1997**, *94*, 5243.
(3) Shiloh, M. U.; Nathan, C. F. *Curr. Opin. Microbiol.* **2000**, *3*, 35.
(4) Couture, M.; Yeh, S. R.; Wittenberg, B. A.; Wittenberg, J. B.; Ouellet, Y.; Rousseau, D. L.; Guertin, M. *Proc. Natl. Acad. Sci. U.S.A.* **1999**, *96*, 11223.
(5) Ouellet, H.; Ouellet, Y.; Richard, C.; Labarre, M.; Wittenberg, B.; Wittenberg, J.; Guertin, M. *Proc. Natl. Acad. Sci. U.S.A.* **2002**, *99*, 5902.
(6) Pathania, R.; Navani, N. K.; Gardner, A. M.; Gardner, P. R.; Dikshit, K. L. *Mol. Microbiol.* **2002**, *45*, 1303.
(7) Moens, L.; Vanfleteren, J.; van de Peer, Y.; Peeters, K.; Kapp, O.; Czeluzniak, J.; Goodman, M.; Blaxter, M.; Vinogradov, S. *Mol. Biol. Evol.* **1996**, *13*, 324.
(8) Pesce, A.; Couture, M.; Dewilde, S.; Guertin, M.; Yamauchi, K.; Ascenzi, P.; Moens, L.; Bolognesi, M. *EMBO J.* **2000**, *19*, 2424.
(9) Milani, M.; Pesce, A.; Nardini, M.; Ouellet, H.; Ouellet, Y.; Dewilde, S.; Bocedi, A.; Ascenzi, P.; Guertin, M.; Moens, L.; Friedman, J. M.; Wittenberg, J. B.; Bolognesi, M. *J. Inorg. Biochem.* **2005**, *99*, 97.
(10) Milani, M.; Pesce, A.; Ouellet, Y.; Ascenzi, P.; Guertin, M.; Bolognesi, M. *EMBO J.* **2001**, *20*, 3902.
(11) Milani, M.; Pesce, A.; Ouellet, Y.; Dewilde, S.; Friedman, J. M.; Ascenzi, P.; Guertin, M.; Bolognesi, M. *J. Biol. Chem.* **2004**, *279*, 21520.
(12) Crespo, A.; Martí, M. A.; Kalko, S. G.; Morreale, A.; Orozco, M.; Gelpi, J. L.; Luque, F. J.; Estrin, D. A. *J. Am. Chem. Soc.* **2005**, *127*, 4433.

10.1021/ja076853+ CCC: $40.75 © xxxx American Chemical Society

branches of the tunnel, respectively, and (ii) opening of the long branch is promoted upon O_2 binding to the heme through a local conformational change in the TyrB10-GlnE11 pair, which acts as a molecular switch that triggers a global change in the dynamical behavior of the protein. Accordingly, it can be speculated that such a regulation mechanism has evolved to optimize the efficiency of the O_2/NO chemistry, as the access of NO to the heme cavity should take place only upon binding of O_2 to the heme.

In this work the eggression pathway followed by the nitrate anion is examined by means of electronic structure, hybrid quantum mechanical−molecular mechanical, and classical molecular dynamics simulations. The critical role of trHbN as a NO-detoxifying enzyme demands that the nitrate anion formed in the heme cavity must be released efficiently to the aqueous solvent to enable the protein to start a new enzymatic cycle. However, the high hydrophobic character of the two branches of the tunnel makes it difficult to conceive that the nitrate anion might leave the heme cavity through the tunnel system. The results reveal that the nitrate anion is released rapidly through a distinct eggression pathway, which is not delineated in the X-ray crystallographic structure of the oxygenated form of trHbN.

Computational Methods

Classical Simulations. Molecular dynamics (MD) simulations were performed starting from the optimized trHbN·NO_3^- complex obtained in our previous work,[12] which in turn was based on the X-ray crystallographic structure of the oxygenated form of trHbN (PDB entry 1idr; chain A at 1.9 Å resolution). The enzyme was immersed in a preequilibrated octahedral box of TIP3P[15] water molecules. The final system contained the protein and around 8600 water molecules (ca. 28270 atoms). Simulations were performed in the NPT ensemble. The system was simulated employing periodic boundary conditions and Ewald sums for treating long-range electrostatic interactions (with the default Amber-9 parameters). All simulations were performed with the parmm99 force field of the Amber-9 package.[16] The atomic charges for the heme group were derived using the protocol reported in our previous works.[12] For the nitrate anion, charges of −0.437 *e* and 0.311 *e* were assigned to O and N atoms. For the heme-bound nitrate anion, the main differences in the partial charges concerned the oxygen atom linked to iron and the nitrogen atom, whose effect is attenuated by the restrain imposed to the Fe−O bond, but similar charges were obtained for the external oxygens. Finally, the Lennard−Jones parameters were taken from those assigned to negatively charged oxygen (similar to carboxylate oxygen) and sp^2 nitrogen.

The free energy profile for migration of the nitrate anion was determined by means of multiple steered molecular dynamics (MSMD) simulations. The free energy was obtained using Jarzynski's inequality.[17] The chosen reaction coordinate only pulls the nitrate anion from the heme active site, without imposing any constraint to a predefined eggression pathway. The free energy profile was built up by combining two independent free energy profile calculations which included 10 independent MSMD runs each.

Mixed Quantum Mechanics/Molecular Mechanics (QM/MM) Methods. QM/MM calculations were carried out with the QSite program.[18] Geometry optimizations were carried out using the B3LYP functional[19] in combination with the LACVP* and LACV3P* basis sets.[20] A frozen orbital was chosen at the QM/MM boundary, and classical mechanics were described with the AA-OPLS2001 force field.[21] A detailed description of the QM/MM methods and protocols can be found in previous studies.[22] The initial model for the QM/MM calculation was taken from a representative snapshot taken from the classical MD trajectory. Since the QM/MM protocol uses energy minimization, all water molecules beyond 10 Å from the protein surface were removed, and all water oxygen atoms beyond 6 Å from the protein surface were frozen in geometry minimizations and reaction coordinate computations. QM calculations were performed with the Jaguar program[23] using the same functional and basis set.

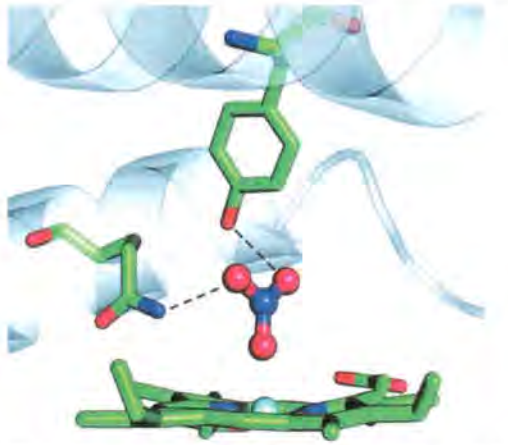

Figure 1. Representation of selected residues in the active site of the truncated hemoglobin N from *M. tuberculosis* for the state corresponding to the heme group bound to the nitrate anion. The hydrogen-bond interactions of the nitrate anion with TyrB10 and GlnE11 are shown by dashed lines.

Results and Discussion

The release of the nitrate anion to the aqueous environment can be limited by two processes: (i) the breaking of the bond between the anion and the heme group or (ii) the diffusion of the anion through the protein matrix. It can be anticipated that the former process will be penalized not only by the loss of the interaction energy between the anion and the Fe(III) atom but also by the loss of hydrogen-bond contacts with TyrB10 and GlnE11 (Figure 1).[12] On the other hand, though hydration by the bulk solvent can be conceived to be the driving force for the release of the anion, migration through the protein cannot be easily envisaged due to the hydrophobic character of the protein matrix tunnel, unless a distinct pathway mediates eggression of the anion. Under these circumstances, the release of the nitrate anion to the bulk solvent might be too slow, which could limit the efficiency of the NO detoxification mechanism associated with trHbN and therefore the survival of the microorganism. On the basis of these considerations, it is reasonable to expect that the protein has evolved an eggression

(13) Bidon-Chanal, A.; Martí, M. A.; Crespo, A.; Milani, M.; Orozco, M.; Bolognesi, M.; Luque, F. J.; Estrin, D. A. *Proteins* **2006**, *64*, 457.
(14) Bidon-Chanal, A.; Martí, M. A.; Estrin, D. A.; Luque, F. J. *J. Am. Chem. Soc.* **2007**, *129*, 6782.
(15) Jorgensen, W. L.; Chandrasekhar, J.; Madura, J. D.; Impey, R. W.; Klein, M. L. *J. Chem. Phys.* **1983**, *79*, 926.
(16) Pearlman, D. A.; Case, D. A.; Caldwell, J. W.; Ross, W. R.; Cheatham, T. E., III; DeBolt, S.; Ferguson, D.; Seibel, G.; Kollman, P. *Comp. Phys. Commun.* **1995**, *91*, 1.
(17) Jarzynski, C. *Phys. Rev. Lett.* **1997**, *78*, 2690.
(18) *Qsite*, 4.0; Schrodinger, LLC: New York, 2005.
(19) (a) Becke, A. D. *Phys. Rev. A* **1988**, *38*, 3098. (b) Lee, C.; Yang, W.; Parr, R. G. *Phys. Rev. B* **1988**, *37*, 785.
(20) Hay, P. J.; Wadt, W. R. *J. Chem. Phys.* **1985**, *82*, 270.
(21) Kaminski, G. A.; Friesner, R. A.; Tirado-Rives, J.; Jorgensen, W. L. *J. Phys. Chem. B* **2001**, *105*, 6474.
(22) Friesner, R. A.; Guallar, V. *Annu. Rev. Phys. Chem.* **2005**, *56*, 389.
(23) *Jaguar*, 6.5; Schrodinger, LLC: New York, 2005.

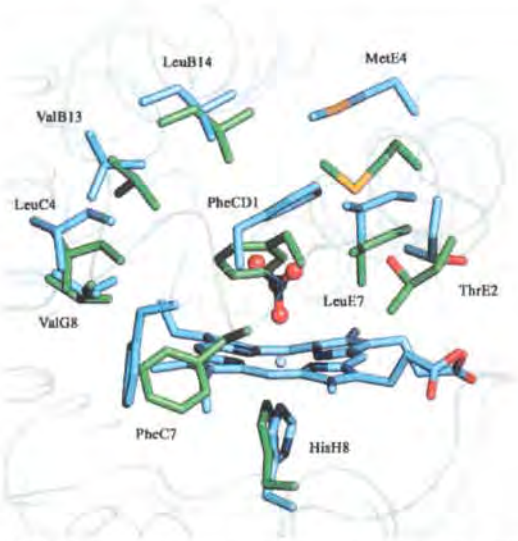

Figure 2. Representation of the average position adopted by selected residues at the heme cavity obtained upon superposition of representative structures of the wild type trHbN.O_2 protein (green) and the protein with heme-bound nitrate anion (blue).

mechanism to ensure an efficient turnover, which in turn should rely on the weakening of the interaction between Fe(III) and nitrate anion, and the delineation of an efficient eggression pathway from the heme cavity to the aqueous environment.

MD Simulation of the Nitrate-Anion-Bonded Protein. It might be hypothesized that the presence of the negative charge in the product formed from the reaction between the heme-bound O_2 and NO might disturb the structure of the cavity walls and eventually give rise to structural changes that facilitate the breaking of the bond between the heme group and the nitrate anion. To check this hypothesis, a 30 ns MD simulation of trHbN with a heme-bound nitrate anion was run. A stable trajectory was obtained with rmsd values for the backbone of the core residues (16−127) around 1.6 Å (see Figure S1 in the Supporting Information). The residues 32−58, which form the cavity walls, are the main contributors to the rmsd (by excluding these residues, the rmsd decreases to 1.2 Å).

Compared to O_2, the larger size of the nitrate anion and its negative charge induce a significant local rearrangement of residues TyrB10, ValB13, LeuB14, PheC7, PheCD1, MetE4, and LeuE7, which are pushed between 0.5 and 1.5 Å far away from the Fe atom relative to their position in the wild type trHbN oxygenated protein. As a result, the heme cavity is enlarged by a factor of ca. 2, as determined from the average volumes of the heme cavities measured[24] for a set of 50 snapshots taken randomly in the final part of the trajectory and from the simulation corresponding to the wild type trHbN oxygenated protein[14] (Figure 2).

Due to the conformational rearrangement, the compactness of the cavity walls is notably reduced, which facilitates the entry of water molecules to the interior of the cavity. Two distinct pathways by which water can access the cavity were detected along the trajectory. First, a fast rearrangement of MetE4 creates

(24) Kleywegt, G. J.; Jones, T. A. *Acta Crystallogr.* **1994**, *D50*, 1178.

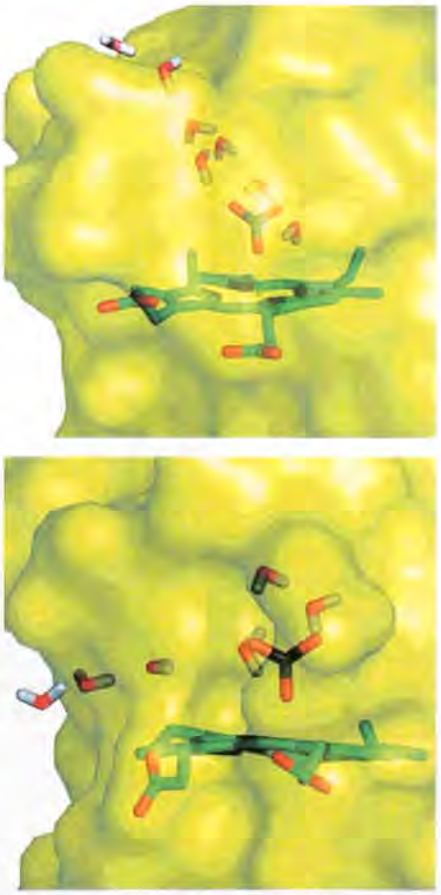

Figure 3. Representation of the pores formed in the cavity walls along the MD trajectory of the heme-bound nitrate anion. For the sake of clarity, protein residues have been omitted.

Table 1. High/low Spin Energy Gap (ΔE; kcal/mol) for the Different QM/MM Models, the Fe−O(Nitrate) Bond Distance (d; Å) for the Different Hexacoordinated Reactant Models (D, W, DL, and WL) and for the Penta-coordinated Products (PR)

	LACVP*		LACV3P*	
model	ΔE	d	ΔE	d
D	5.5	2.04	1.1	2.07
W	5.3	2.20	0.6	2.24
DL	4.5	2.13	0.9	2.15
WL	4.9	2.28	−3.1	2.32
PR	−1.0		−7.2	

a pore in the cavity as the residue moves away from the nitrate anion. Water molecules can then pass between residues TyrB10, LeuB14, MetE4, and LysE8 and solvate the nitrate anion (Figure 3). This water entry pathway is closed after 7 ns due to the rearrangement of the side chains of residues PheC7 and PheCD1, which in turn opens a new pathway between the backbone of helix C and the heme group, it being detected until the end of the trajectory (Figure 3). As a result, the nitrate anion interacts with a few water molecules (between 1 and 5, with a mean

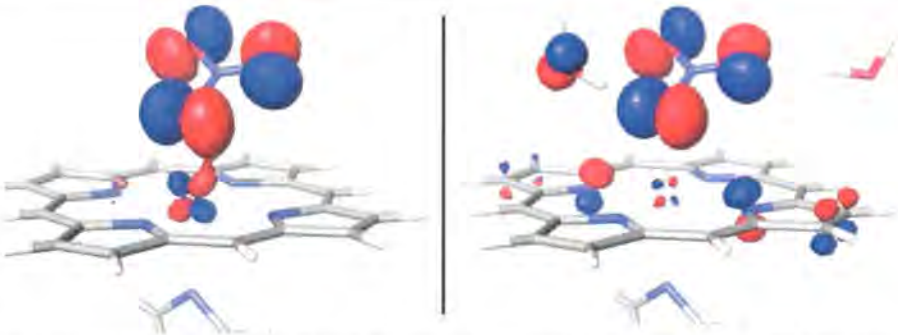

Figure 4. Molecular orbital for the iron(d_{z^2})-ligand π mixing in the reduced model without (left panel) and with (right panel) two water molecules.

value of 3), which are retained around the nitrate anion during the whole simulation (see Figure S2 in the Supporting Information).

Compared to the simulations run in previous studies[12-14] for trHbN with heme-bound O_2, where the presence of water molecules in the heme cavity was a rare, transient event, it is clear that the formation of the nitrate anion triggers a relevant structural rearrangement in the heme pocket, which increases the accessibility of water molecules to the heme cavity.

QM/MM Calculations of Fe−N Bond Breaking. In order to investigate the influence of the hydrating water molecules on the breaking of the bond between the nitrate anion and the heme group, QM/MM computations were performed to determine the effect of those water molecules in the geometrical and energetic features of the nitrate protein complex formed in the last step in the NO detoxification reaction (eq 2).

$$\text{Fe}-\text{ONOO} \rightarrow \text{Fe(III)} + \text{NO}_3^- \qquad (2)$$

The starting structure for the QM/MM model was derived from a representative snapshot taken from the final part of the MD trajectory. From this snapshot, four models named dry (D), large dry (DL), wet (W), and large wet (WL) were generated. In model D all the waters in the vicinity of the nitrate anion were deleted, and the quantum region simply included the heme group, the nitrate anion, and the axial histidine. In model W the water molecules around the nitrate anion were retained and included in the QM subsystem. Finally, the QM part in models DL and WL also included TyrB10 and GlnE11, which are hydrogen-bonded to the nitrate anion. Model WL, therefore, accounts for all the direct contacts between the nitrate anion and polar groups, including water molecules (see Figure S3 in the Supporting Information).

Table 1 shows the QM/MM energy difference between the high (sextet) and low (doublet) spin states for the different models and basis set, as well as the Fe−O(nitrate) distance for the sextet spin state. The results show that hydration weakens the Fe−O bond and decreases the energy gap between high and low spin states. Thus, the Fe−O distance increases by ca. 0.17 Å when water molecules are included in the QM subsystem, and the low and high spin states become almost degenerate when the LACV3P* basis is used (see models W and D in Table 1). Interestingly, the inclusion of TyrB10 and GlnE11 in the QM subsystem (models DL and WL) leads to an additional increase in the Fe−O distance (by 0.08 Å), and the high spin state is predicted to be the ground state according to the QM-(LACV3P*)/MM computations. Table 1 also shows the energy difference for the pentacoordinated product species (PR). As expected, the ground state is the sextet spin state, which is significantly stabilized as the basis set is enlarged.

These results point out that the electrostatic screening of the nitrate anion is crucial for a correct description of the spin state and the breaking of the Fe−O bond; as for the more complete QM subsystem (model WL) the length of the Fe−O bond is increased up to 2.32 Å, and the high spin state is predicted to be the ground state. This finding can be qualitatively realized from QM calculations performed on a reduced model consisting of a capped porphyrine, an imidazole, and a nitrate anion. For this model, the B3LYP/LACV3P* energy minimization of the sextet spin state gives an Fe−O distance of 1.97 Å, which is increased 0.11 Å upon addition of two water molecules hydrogen-bonded to the nitrate anion. Inspection of Mulliken, electrostatic potential-fitted, and natural bond orbital charges indicates that the charge of the nitrate anion increases by ~0.08 electron units upon addition of the water molecules. A molecular orbital analysis (Figure 4) indicates that the oxygen lone pairs of the nitrate anion are stabilized by the water molecules, decreasing the mixing between the iron d_{z^2} and ligand π orbitals and increasing the charge transfer from the iron center to the nitrate anion (similar trends are observed for the iron(d_{z^2})−nitrate bonding orbital; see Figure S4 in the Supporting Information).

By using model WL, QM(LACV3P*)/MM computations were performed to estimate the energy profile for the breaking of the Fe−O bond in the high spin state. The reaction coordinate was defined from the Fe−O bond distance, which was enlarged by increments of ~0.15 Å and constrained during energy minimizations. The large size of the system, about 1600 basis set functions, did not allow for more robust calculations, and the energy barrier determined by using this simple procedure must be interpreted as an upper limit. The energy barrier thus obtained amounts to ~4 kcal/mol at an Fe−O bond distance of 3.0 Å (Figure 5), where the release of the bond distance constraint drove the system downhill to the pentacoordinated product state. For the sake of comparison, the calculation for the dry model yielded a barrier close to 18 kcal/mol.

Overall, these results point out that the increase of hydration (polarity) in the active site stabilizes the nitrate species and facilitates the breaking of the Fe−O bond in the high spin state. The hydration level, therefore, appears to be a crucial factor in controlling the stability of the nitrate-bound species.

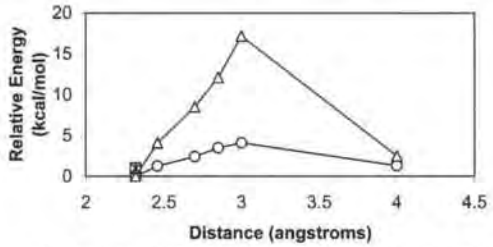

Figure 5. Energy profile (kcal/mol) obtained for the breaking of the Fe−O bond (distance in Å) for the heme-bound nitrate anion in the wet large (○) and dry (△) models.

Eggression of the Hydrated Nitrate Anion. The release of the solvated nitrate anion was examined by means of two MD simulations where the restraint imposed by the Fe−O(nitrate) bond was released. Figure 6 shows the time dependence of the distance between the heme Fe and nitrate anion for representative runs. In one case (black), the hydrated anion remains at about 6 Å from the heme iron during 2 ns due to hydrogen-bond interactions with TyrB10 and GlnE11. During the next nanosecond, it moves away passing close to MetE4 and forms a new interaction with the hydroxyl group of ThrE2. Such a position (located at around 9 Å from the heme iron) is also stabilized by interactions with the backbone amide groups of residues 47−49. After 1.5 ns, the nitrate anion leaves the protein matrix. In the other case (gray), the nitrate anion interacts with ThrE2 for 2 ns, being close to PheCD1, LeuE7, and MetE4, and then moves into the solvent through the loop formed by the backbone of residues 47 and 49 and the side chain of MetE4. Interestingly, the escape of the nitrate anion occurs in less than 5 ns in both runs, suggesting that the barrier for ligand eggression is quite low. To verify the reliability of the eggression pathway outlined above, we investigated the exit of the nitrate anion using PELE,[25] which produces a ligand random walk coupled to a side chain optimization and a minimization procedure, as an independent sampling protocol. The results fully supported the exit of the ligand toward the active site cavity defined by TyrB10, MetE4, PheCD1, and ThrE2 (see Figure S5 in the Supporting Information).

To further examine the feasibility of the nitrate eggression pathways, MSMD simulations were run to determine the free energy profile using Jarzynski's equality. By defining the reaction coordinate as the distance between the nitrate anion and the center of mass of TyrB10, in all cases the eggression of the nitrate anion followed the pathway shown in Figure 6. The resulting free energy profile (see Figure 6) shows that the transition from the heme site to the ThrE2-containing binding pocket is accompanied by a barrier of less than 1.0 kcal/mol. The interaction at the ThrE2 site corresponds to the minimum in the free energy profile, which is stabilized by about 1 kcal/mol, and the release of the anion into the solvent is accompanied by a barrier of up to 2 kcal/mol. It is interesting to note that the product release free energy barriers are similar to the barriers associated with the entry/exit of NO/O_2 through the hydrophobic tunnels. For example, the barrier for NO entrance along the long channel in the oxy protein is about only 1 kcal/mol, consistent with the fact that it is an almost diffusional process.[13] Our results

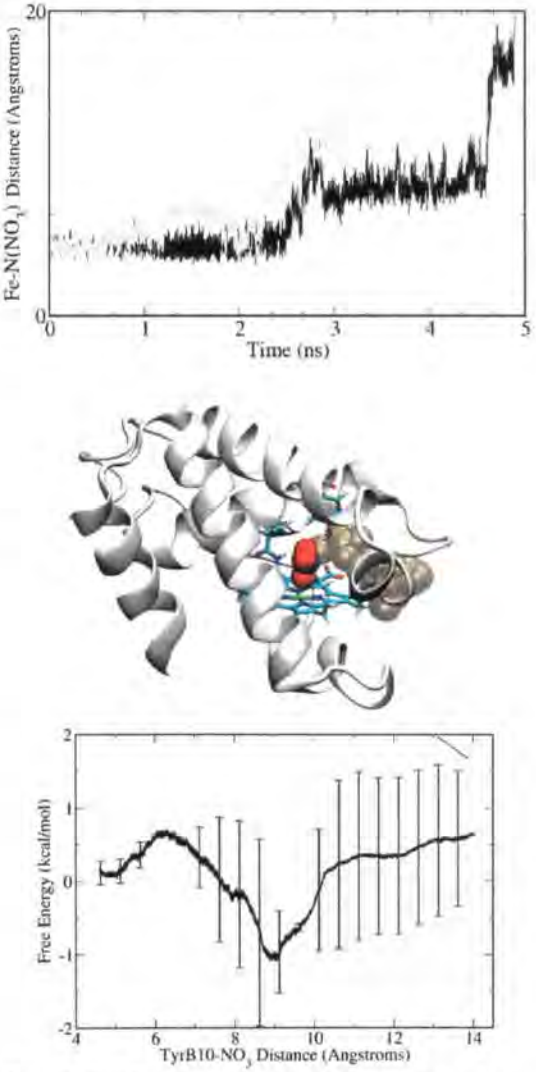

Figure 6. (Top) Time dependence of the Fe−N(nitrate) distance (Å) for two representative runs of the eggression pathways of the solvated nitrate ion in trHbN. (Middle) Representative eggression pathway of the solvated nitrate anion in trHbN. The heme group and TyrB10 are shown as sticks. The eggression pathways are shown in dark yellow. (Bottom) Free energy profile obtained for the release of nitrate anion (mean value and standard deviation derived from two different sets of MSMD runs are shown).

also suggest that ThrE2, which plays a key role in assisting the nitrate exit, may be an interesting target for site directed mutagenesis studies.

Functional Implications. The preceding results show that the overall barrier for eggression of the nitrate anion is small, as expected from the previous MD simulations performed for trHbN after having eliminated the bond restraint between the heme Fe atom and the nitrate anion. Accordingly, it can be concluded that the nitrate anion is released efficiently into the solvent once the Fe−O bond is broken. In contrast to the pathways followed by O_2 and NO to access the heme cavity, which are well-defined in the X-ray crystallographic structure

(25) Borrelli, K. W.; Vitalis, A.; Alcantara, R.; Guallar, V. *J. Chem. Theory Comput.* **2005**, *1*, 1304.

of trHbN,[10] the eggression pathway of the nitrate anion is not uniquely defined, as noted in the dispersion of free energy values obtained in MSMD simulations (see Figure 6). Clearly, this finding can be explained by the difference between the narrow, well delineated branches of the protein matrix tunnel involved for migration of diatomic ligands[8] and the broader pathway followed by the nitrate anion.

The crucial event in triggering the release of the nitrate anion can be attributed to the entry of water molecules to the heme cavity, which is facilitated by the structural destabilization of the cavity walls promoted by the formation of the nitrate anion. Among other residues, such a structural destabilization affects PheCD1, which has been identified as a heme-solvent shielding residue.[9] In contrast to the *dry* environment of the heme cavity observed in the MD simulations of the wild type trHbN in both deoxygenated and oxygenated forms,[12,13] those water molecules are retained along the simulation of trHbN with the heme−Fe(III)−NO_3^- complex due to the favorable electrostatic interactions with the negative charge of the anion.

The *wet* environment created by the presence of few water molecules has a decisive contribution to the weakening of the bond between the heme Fe atom and the nitrate anion. This is reflected in the enlargement of the Fe−O distance from a value of 1.97 Å for a simple *gas-phase-like* model to 2.32 Å for the QM/MM model of the complex in trHbN (see above). Furthermore, the small energy barrier obtained for the high spin state of the heme−Fe(III)−NO_3^- complex suggests that the breaking of the Fe−O bond should be thermally feasible, which is in agreement with the known difficulties in experimentally characterizing the heme-bound nitrate anion complex.

Overall, the results point out that trHbN is able to rapidly release the nitrate anion through an eggression pathway different than that used by the diatomic ligands O_2 and NO. Thus, previous studies[13] suggest that O_2 would access the heme cavity through the short branch of the tunnel with an associated barrier of ~4 kcal/mol, whereas migration of NO to the heme activity would take place through the long tunnel branch facilitated by the opening of the PheE15 gate upon binding of O_2 to the heme. The efficiency of the release of the nitrate anion is physiologically relevant, as it contributes to guarantee the survival of the microorganism, since it facilitates the turnover of trHbN with the concomitant uploading of O_2, and agrees with the experimental evidence that the rate of the NO detoxification is mainly limited by the access of the ligands to the heme cavity.

Conclusions

The results presented here permit us to reconcile the migration of the ligands O_2 and NO through the highly hydrophobic branches of the protein tunnel with the larger size and charged nature of the nitrate anion, as the product of the reaction leaves the enzyme using a different pathway. The migration of the nitrate anion is promoted by the increase in the hydration of the heme binding site, which contributes to the weakening of the Fe−O bond and facilitates the transition to the high spin state. In turn, the results also show that entry of the water molecules to the heme binding site is related to the structural distortion of the cavity walls induced upon formation of the product (i.e., the nitrate anion), which gives rise to the formation of different pores that allow the entrance of water molecules.

These findings complement previous experimental[4−6,8−11] and theoretical[12−14] work on the NO detoxification mechanism by trHbN from *M. tuberculosis*. Taken together, this information permits identifying certain residues that play a crucial role in the NO-dioxygenase activity of trHbN, such as PheE15, which acts as the gate of the long tunnel branch, the pair TyrB10-GlnE11, which not only modulates the O_2 binding affinity and the correct positioning of NO in the heme-bound O_2 cavity but also contributes to facilitating the opening of the gate by combining both local and global conformational changes, and ThrE2, which assists the nitrate anion along the eggression pathway. The knowledge gained from the detailed analysis of these results should be valuable to suggest possible mutations, which should affect the efficiency of the NO-detoxification mechanism by trHbN, to explain the differences in activity between related truncated hemoglobins and eventually to provide a basis for the design of a pharmacological strategy against tuberculosis based on the definition of trHbN as a potential therapeutic target.

Acknowledgment. This work was supported by grants from the ANPCYT (National Science Agency of Argentina), CONICET, and University of Buenos Aires to D.A.E, from the Spanish Ministerio de Educación y Ciencia to F.J.L. (Grant CTQ2005-08797-C02-01/BQU) and V.G. (Grant CTQ2006-10262). Calculations were performed in the *Marenostrum* Supercomputer at the Barcelona Supercomputer Center. M.A.M. thanks CONICET for a doctoral fellowship. We thank Dr. S. Kalko for a valuable discussion of the manuscript.

Supporting Information Available: Complementary figures are available free of charge via the Internet at http://pubs.acs.org.

JA076853+

Supporting Information

Mechanism of Product Release in NO detoxification from *Mycobacterium tuberculosis* Truncated Hemoglobin N

Marcelo A. Martí,[1] Axel Bidon-Chanal,[2] Alejandro Crespo,[1] Syun-Ru Yeh,[3] V. Guallar,[4*] F. Javier Luque[2*] and Darío A. Estrin[1*]

1 Departamento de Química Inorgánica,Analítica y Química Física/ INQUIMAE-CONICET, Facultad de Ciencias Exactas y Naturales, Universidad de Buenos Aires, Ciudad Universitaria, Pabellón 2, Buenos Aires, C1428EHA, Argentina.

2 Departament de Fisicoquímica and Institut de Biomedicina (IBUB), Facultat de Farmàcia, Universitat de Barcelona, Av. Diagonal 643, 08028, Barcelona, Spain.

3 Department of Physiology and Biophysics, Albert Einstein College of Medicine of Yeshiva University, Bronx, New York, 10461, USA

4 ICREA, Computacional Biology Program. Barcelona Supercomputing Center. Edificio Nexos II. Barcelona 08028. Spain

* Corresponding author: D. A. E. (dario@qi.fcen.uba.ar), F. J. L. (fjluque@ub.edu), V. G. (victor.guallar@bsc.es)

Figure S1. Representation of the time dependence of (top) the potential energy (E_{pot}; kcal/mol) and (bottom) the root-mean.square deviation (rmsd; Å) for the MD simulation of the trHbN with heme-bound nitrate anion. The gray line corresponds to the rmsd determined for the alpha carbon atom of the core region (residues 16-127), and the black line corresponds to the values obtained after excluding the contribution of those atoms pertaining to the residues 32-58, which form the walls of the heme cavity.

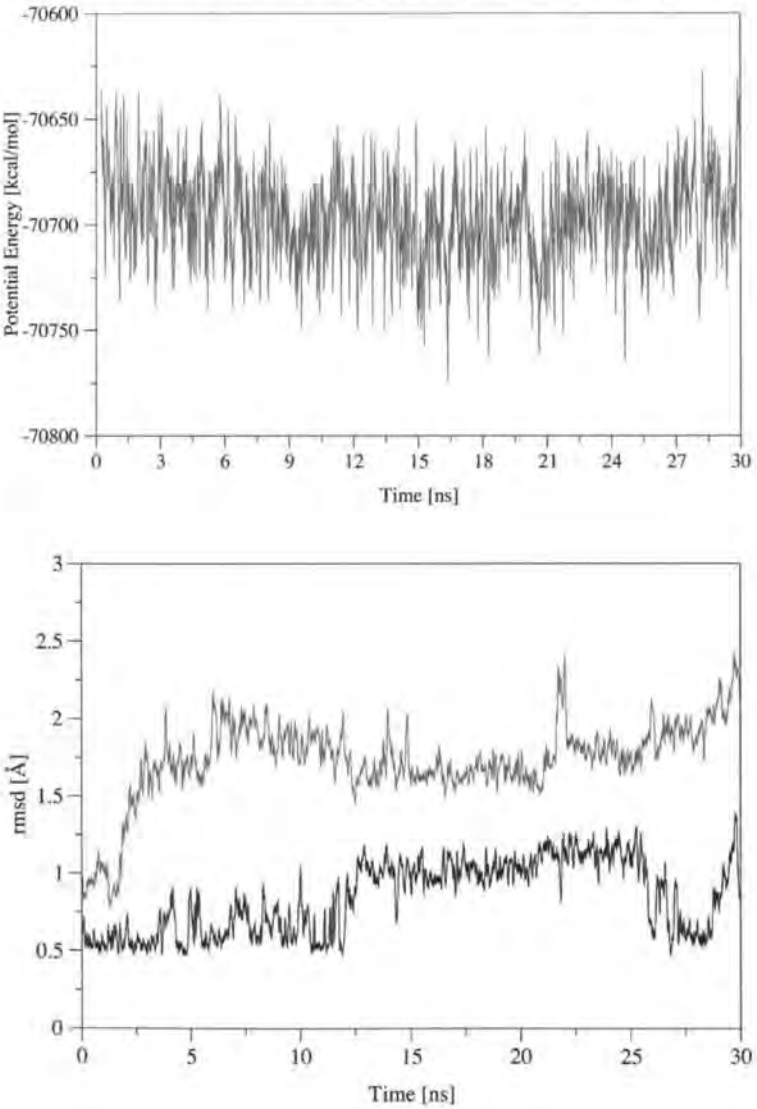

Figure S2. Representation of the water density (isodensity contour of 0.8) determined for the trajectory obtained for the trHbN with heme-bound nitrate anion.

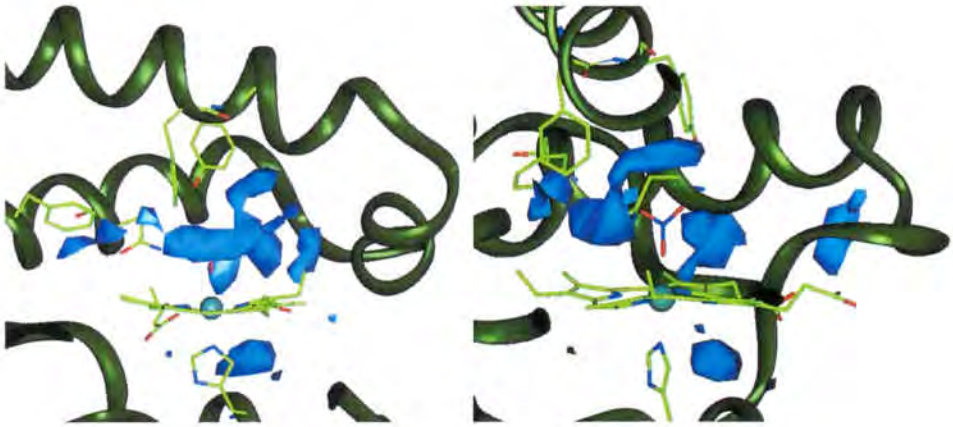

Figure S3. Representation of the quantum mechanical subsystem used in model WL.

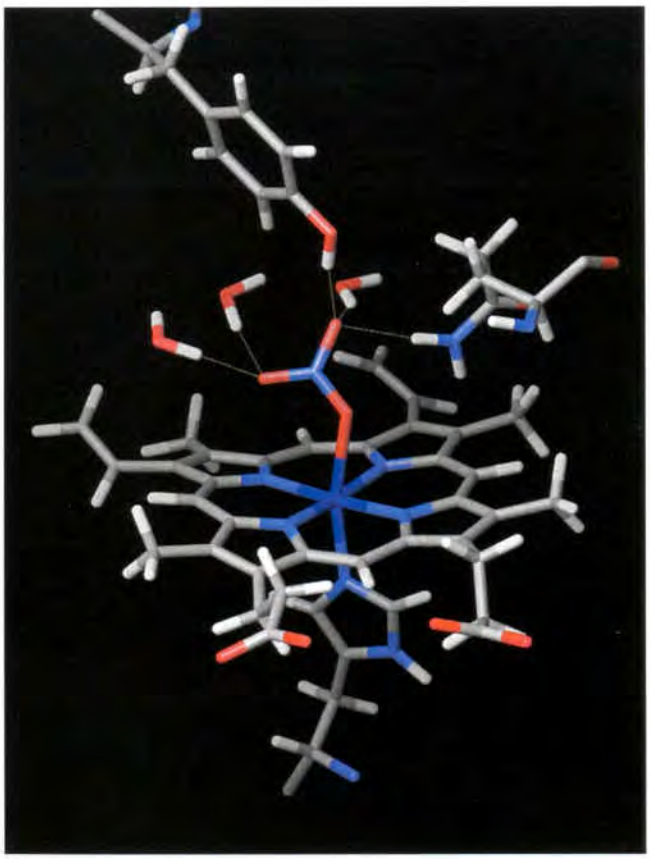

Figure S4. Molecular orbital for the iron(d_{z^2})-ligand π mixing in the reduced model without (left panel) and with (right panel) two water molecules.

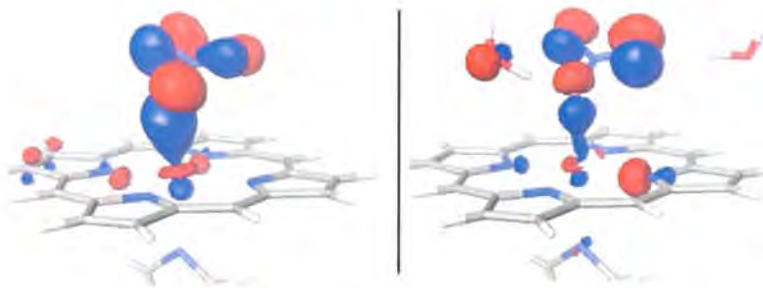

Figure S5. Pathway for the eggression of the nitrate anion determined from PELE computations.

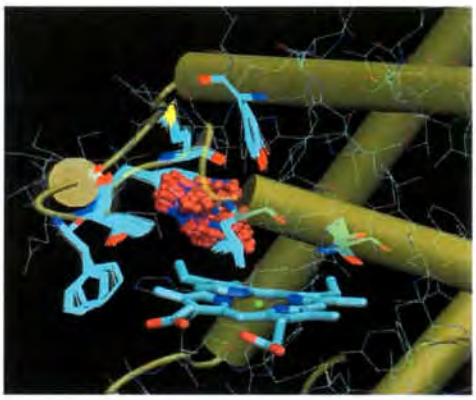

Figure S6. Individual works for the two sets (top and bottom) of 10 MSMD runs from 5 to 11 Å for the release of the solvated nitrate anion.

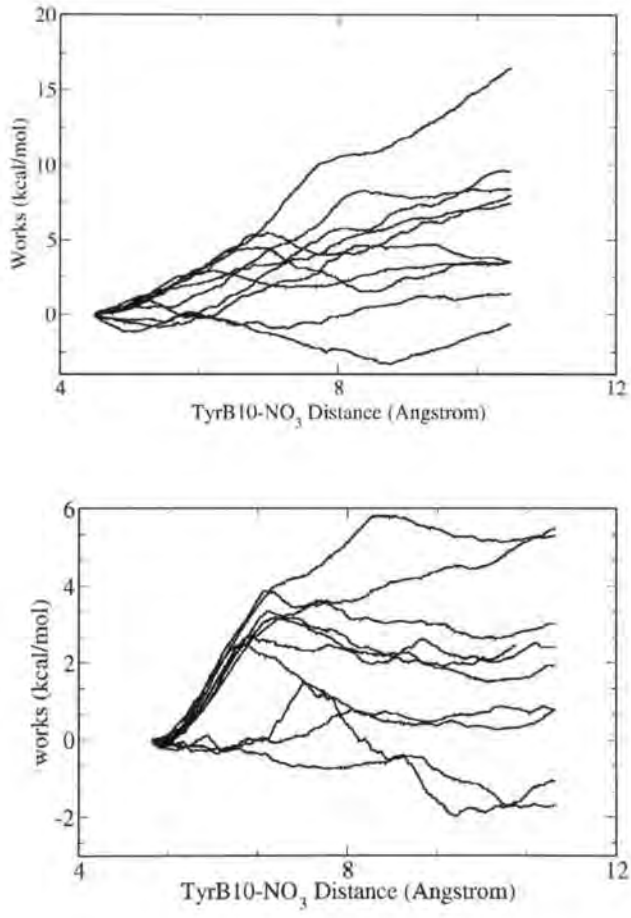

Figure S7. Individual works for the two sets (top and bottom) of 10 MSMD runs from 10.5 to 14.5 Å for the release of the solvated nitrate anion.

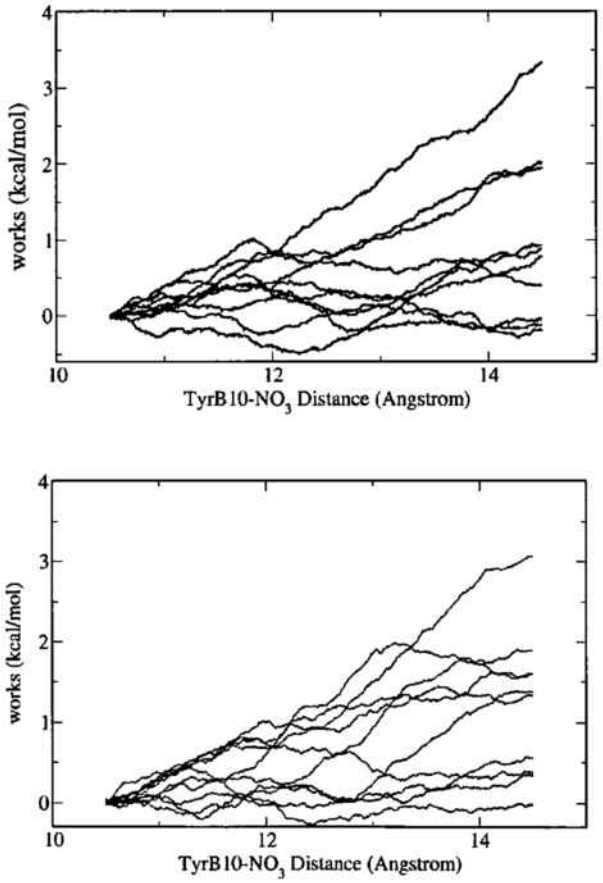

Figure S8. Connoly surfaces of the heme cavity in the oxy and nitrate bound proteins, depicted in the left and right panels, respectively.

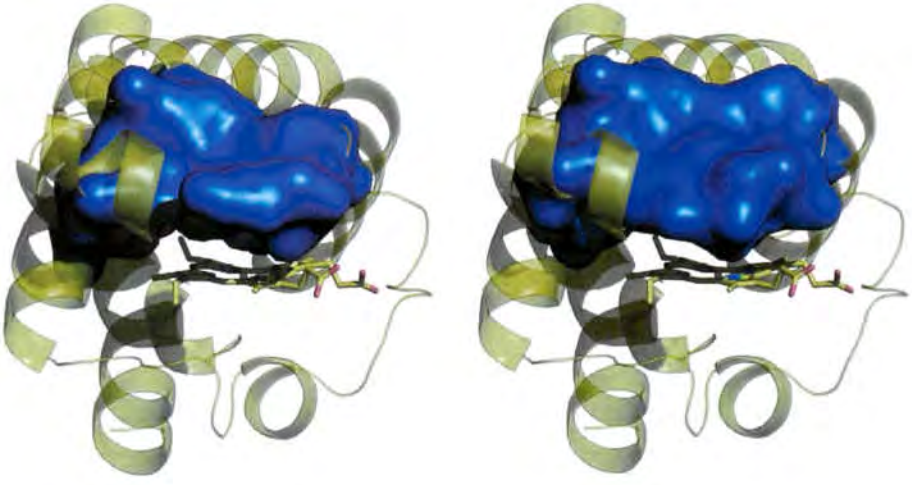

Inhibidores duales de Acetilcolinesterasa

- La unión del anillo de tacrina o clorotacrina presenta un elevado grado de conservación en cuanto a las interacciones establecidas con el receptor, lo cual puede atribuirse a la elevada complementariedad entre la unidad 6-clorotacrina y los residuos que conforman el centro catalítico de acetilcolinesterasa.

- Si bien las propiedades morfológicas del canal están altamente conservadas entre los distintos inhibidores, se aprecian diferencias en la orientación de las cadenas laterales de los residuos que lo conforman, lo cual refleja la capacidad del canal para adaptarse a las diferencias en la estructura química de la cadena carbonada que conecta las unidades situadas en los centros catalítico y periférico. Las interacciones establecidas con los residuos del canal modulan la capacidad del anillo heteroaromático terminal para interaccionar en el centro periférico.

- La interacción del anillo heteroaromático terminal con el centro periférico no se limita únicamente a la formación de apilamientos π-π con el anillo indol de Trp279, sino que involucra alteraciones en la orientación de la cadena lateral de dicho residuo, lo cual puede repercutir en otras posibles funciones biológicas, como la capacidad de acetilcolinestarasa para afectar la agregación del péptido β-amiloide.

- Los resultados sugieren que los residuos que conforman la garganta participan de forma activa en la formación del complejo. En consecuencia, el diseño de nuevos inhibidores duales debería considerar no sólo los factores responsables de la unión al centro catalítico y periférico, sino también optimizar la interacción del inhibidor con los residuos del canal.

Mecanismo de regulación de la proteína trHbN de *M. tuberculosis*

- Si bien la estructura cristalográfica de la proteína revela la existencia de un túnel formado por dos canales ortogonales de distinta longitud, nuestros estudios permiten apuntar que ambos canales presentan funciones diferenciadas, por cuanto uno de ellos es utilizado para la entrada de O_2, mientras que el otro debería estar principalmente involucrado en la captación de NO. La entrada de los dos ligandos no se produce de manera coordinada, entrando primero O_2 a través del canal corto, mientras el canal largo se mantiene obstruido por el residuo PheE15, que actúa como puerta de acceso a lo largo del canal largo.

- La unión de O_2 al grupo hemo desencadena cambios conformacionales locales, que afectan principalmente a la conformación de los residuos TyrB10 y GlnE11, cuya cadena lateral adopta una conformación plegada. A su vez, ello incrementa la presión ejercida por GlnE11 sobre PheE15, lo cual debe favorecer el cambio conformacional de la cadena lateral de PheE15 y el acceso de NO al centro activo.

- Asimismo, la unión de O_2 al grupo hemo promueve un cambio en las propiedades dinámicas globales de la proteína, manifestado esencialmente en un aumento de la movilidad de las hélices B y E, que definen mayoritariamente el túnel principal. Ello debería contribuir a facilitar la apertura del canal principal y por lo tanto el acceso de NO a la cavidad del grupo hemo.

- Al formarse el producto de la reacción, el anión nitrato, la cavidad del centro activo se ensancha para acomodar la carga negativa. Dicho ensanchamiento posibilita la apertura no simultánea de dos canales nuevos, que permiten la entrada de agua y la consecuente solvatación del anión. La distancia del enlace Fe–ONOO aumenta en un ~12% al solvatarse el anión, disminuyendo la barrera enérgéitca para la rotura del enlace de ~18 kcal/mol a solamente ~4 kcal/mol. Una vez roto el enlace Fe–ONOO, la salida del anión se produce de forma rápida y prácticamente sin barrera a lo largo de un camino completamente diferente al de entrada de los ligandos diatómicos.

Apéndice A: otras publicaciones

- F. Javier Luque, C. Curutchet, J. Muñoz, **A. Bidon-Chanal**, I. Soteras, A. Morreale, J.L. Gelpi and M. Orozco *Continuum Solvation Models: Dissecting the Free Energy of Solvation*, Physical Chemistry Chemical Physics, vol. 5, **2003**, pág. 3827 3.343 03-2 1.5159

- C. Curutchet, **Axel Bidon-Chanal**, Modesto Orozco, and F. Javier Luque *MST study of group contributions for alkane derivatives:effect of the charge normalization*, Chemical Physics Letters, 384, **2004**, 299-305

- F. Javier Luque, **A. Bidon-Chanal**, J. Muñoz, I. Soteras, C. Curutchet, A. Morreale and M. Orozco, *Solute-Solvent interactions from QM SCRF methods: Analysis of group contributions to solvation*, Fundamental World of Quantum Chemistry: A tribute volume to the memory of Per-Olov Löwdin, Volume 3. Eds: E. Brandas, E. Kryachko. Kluwer Academic Publishers.

- C. Curutchet, **Axel Bidon-Chanal**, Ignacio Soteras, M. Orozco and F. Javier Luque, *MST Continuum Study of the Hydration Free Energies of Ionic Species*, J. Phys. Chem. B, 109. **2005**, 3565-3574

- Ignacio Soteras, Carles Curuchet, **A. Bidon-Chanal**, Modesto Orozco, F. Javier Luque, *Extension of the MST model to the IEF formalism: HF and B3LYP parametrizations*. Journal of molecular structure: THEOCHEM., **2005**, 727 (2005), 29-40

- Meyer T., Ferrer-Costa C., Pérez A., Rueda M., **Bidon-Chanal A.**, Luque F.J., Orozco M., *Essential dynamics: a tool for efficient trajectory compression and management*, J. Chem. Theory Comput., 2, **2006**, 251-258

- Ignacio Soteras, Carles Curutchet, **Axel Bidon-Chanal**, François Dehez, Jnos G. ngyn, Modesto Orozco, Christophe Chipot, and F. Javier Luque. *Derivation of Distributed Models of Atomic Polarizability for Molecular Simulations*. J. Chem. Theory Comput., 3, **2007**, 1901-1913.

- Marcelo A. Martí, Luciana Capece, **Axel Bidon-Chanal**, Alejandro Crespo, Víctor Guallar, Francisco Javier Luque and Dario Estrín, *NO reactivity with globins as investigated through computer simulation*. Submited to Methods in Enzymology.

- Ignacio soteras, Damián Blanco, Oscar Huertas, **Axel Bidon-Chanal**, F. Javier Luque, *Solvent Effects in Chemical Equilibria*, Continuum Solvation Models in Chemical Physics: From Theory to Applications, Benedetta Mennucci (Editor), Roberto Cammi (Co-Editor), Wiley, UK, pp. 323-337.